Fachbereich Mathematik und Naturwissenschaften
Fachgruppe Physik
Bergische Universität Wuppertal

Studies on Resonances of Top Quark Pairs and Development of a Grid Expert System

Dissertation zur Erlangung des Doktorgrades
vorgelegt von
Markus Mechtel

February, 2011

“Reality is that which,
when you stop believing in it,
doesn’t go away.”

— Philip K. Dick

Contents

1 Introduction

"Reality is merely an illusion,
albeit a very persistent one."
— Albert Einstein

The central question that drives all science is:

Why is the world the way it is ?

Particularly particle physics aims at describing the most fundamental building blocks of our world, down to the fabric of time and space itself. The Standard Model of elementary particle physics has proved to be a reliable and accurate description of all known subatomic processes. Despite its success, the Standard Model cannot be the final theory describing our world. On the one hand the Standard Model has some shortcomings and uncomfortable aspects that we would like to see resolved in a more advanced theory, e.g. the unification of forces, the fine tuning and hierarchy problem or a connection between leptons and quarks. On the other hand, the Standard Model is unable to describe gravity, nor can it explain its weakness. The Standard Model only describes the strong and electroweak interactions of elementary particles. Therefore, we eventually need a theory of quantum gravity that goes far beyond the validity of the Standard Model.

Although we do not have a reliable theory of quantum gravity yet, there are many extensions beyond the Standard Model (called BSM models) which provide mechanisms

to solve some of its problems. There is hardly a model that does not require the existence of new undiscovered particles in addition to the particles already covered by the Standard Model. Determination of the properties of these additional particles is the best way to distinguish between the different models and to possibly exclude most of them. In addition, already the Standard Model itself predicts a yet unobserved particle, the Higgs boson.

Current and future experiments at particle colliders intensively search for these predicted particles and try to find evidence for them. Colliders are designed to provide enough centre-of-mass energy to produce these particles in a reasonable number and detectors are laid out to measure all kinds of particles as precisely as possible. This means that, if not even the Higgs boson can be found at the Large Hadron Collider (LHC), the Standard Model has to be modified in order to match the new results from measurement.

Particle detectors deliver a huge amount of data that has to be analysed for evidence for predicted phenomena. In order to provide the needed computing power, a global batch system, called the Grid, has been developed to distribute the analysis over all offered computing clusters, globally. Connecting all sorts of computing clusters to form a globally uniform computing interface is still a complicated and error-prone technology, although it is already used heavily in many kinds of scientific research.

This work covers two topics connected to the experiments at the LHC. The first part of this work is an effort to improve the quality and usability of the Grid. Based on an earlier development for a Job Execution Monitor (JEM), a Grid expert system (GridXP) has been developed to classify and categorise error messages collected from grid jobs. By supervising the status of many grid jobs, it is possible to draw conclusions about the origin of certain job failures, which could not be determined by a single user or with the information from a single grid site. If a certain grid job fails, the grid expert system tries to find an explanation for this failure. In some cases, even a solution can be given to fix the error so that it does not have to occur again.

The second part studies different extensions of the standard model. A new model for the event generator HERWIG++ has been developed which adds an additional heavy particle to the Standard Model that decays into a top- and an anti-top (t, $\bar{t}$) quark. Therefore, this particle is called a $t\bar{t}$ resonance. As a special feature, this model respects the interference of all implemented Feynman diagrams. This includes diagrams for Standard Model $t\bar{t}$ production as well as $t\bar{t}$ pairs from decaying resonances. Depending on the properties of the resonance, the $t\bar{t}$ invariant mass distribution is altered characteristically compared to the pure Standard Model $t\bar{t}$ production. For some models the interference has notable influence on $t\bar{t}$ events. This study compares some BSM models and the effect of interferences on the invariant mass distribution.

Chapter 2 of this work gives a short outline of theoretical aspects of the Standard Model and some extensions introducing new heavy particles that could decay into top quark pairs. Features of proton-proton interactions and their description by event generators for high energy particle collisions are described in chapter 3. The subsequent chapter 4 describes the design of the ATLAS detector at the LHC as a typical general purpose detector for high energy particle collisions.

Short descriptions of the Job Execution Monitor and the grid expert system, which was developed as part of this work, are presented in chapter 5. The outline and methods for the study of models of $t\bar{t}$ resonances is shown in chapter 6. Finally, this is followed by the results of the study on $t\bar{t}$ resonances respecting their interferences with QCD $t\bar{t}$ production in chapter 7.

As mentioned before, this work consists of two main parts. As a result, there is no common conclusion about both parts. Instead, Chapters 5 and 7 contain their respective conclusions as separate sections.

2 Theoretical Foundations of Elementary Particle Physics

"If I could explain it to the average person,
I wouldn't have been worth the Nobel Prize."
— Richard Phillips Feynman

In the 20th century, great success has been achieved in describing the interactions of elementary particles. The description of these processes has condensed into a commonly accepted theoretical model that is called the Standard Model of elementary particle physics. This chapter summarises the key elements of the Standard Model (SM). In a second part, special emphasis is put on the production and decay of top quark pairs, as described not only by the Standard Model but also by some of its extensions, including yet undiscovered resonances predicted by these extensions.

2.1 The Standard Model of Elementary Particle Physics

The Standard Model of elementary particle physics describes the currently known elementary particles and their interactions. The interactions of elementary particles are described by two fundamental forces that dominate the microscopic world. These are the strong and the electroweak interaction. Although there is a third fundamental interaction, gravity, there is yet no satisfying theory to describe it on a quantum level.

The Standard Model is a quantum field theory based on the local gauge symmetry group

$$SU(3)_C \times SU(2)_L \times U(1)_Y$$

that can be decomposed into the $SU(3)_C$ colour symmetry for the strong interaction and the $SU(2)_L \times U(1)_Y$ symmetry for the electroweak interaction. The theory of the strong interaction is called Quantum Chromodynamics (QCD). The electroweak symmetry is spontaneously broken down to a residual $U(1)_{em}$ symmetry for the electromagnetic force, which emerges from a mixture of the original symmetry groups and cannot be identified with the original $U(1)_Y$ of weak hypercharge. The quantum theory of electromagnetism is called *Quantum Electrodynamics* (QED). Therefore, the weak and electromagnetic force are often treated as two independent interactions, which is not exactly true, because there is no consistent quantum theory of the weak interaction alone. A pure $SU(2)_L$ symmetry is not able to describe the different couplings of neutral and charged weak currents to fermions.

The Standard Model describes the interactions of 12 elementary fermions, which are shown in figure 2.1. Their masses are listed in table 2.1. Fermions are responsible for the stability of all observable matter. They can only be created or annihilated with their corresponding anti-fermions, resulting in a conservation of the total fermion number, which is even valid for some sub-sorts of fermions separately like baryons and leptons. Additionally, as particles with half-integer spins, fermions obey Fermi-Dirac statistics and thus the Pauli exclusion principle, i.e. two fermions cannot occupy the same quantum state. Therefore, matter containing a number of fermions is forced to occupy a minimum amount of space.

Fermions can be divided into quarks and leptons. Additionally, fermions can be arranged in three generations of equal quantum numbers. Each generation consists of two quarks, a charged lepton and its respective neutrino. Quarks take part in the strong interaction whereas leptons do not. Interactions of particles are determined by their quantum numbers summarised in table 2.2. Colour charge makes a particle responsive to the strong interaction whereas the weak isospin T lets the particle take part in the weak interaction. The 3-component of the isospin distinguishes between up- and down-type quarks or charged leptons and neutrinos respectively. The weak hypercharge Y is introduced to give all fermions their observed electrical charge Q in units of the elementary electrical charge e according to the Gell-Mann–Nishijima formula [1, 2, 3]

$$Q = \left(T_3 + Y\right) e\,.$$

Fermions occur in two chirality states which are labelled as their *left-* and *right-handed* components. Only right-handed neutrinos are special because they take part neither

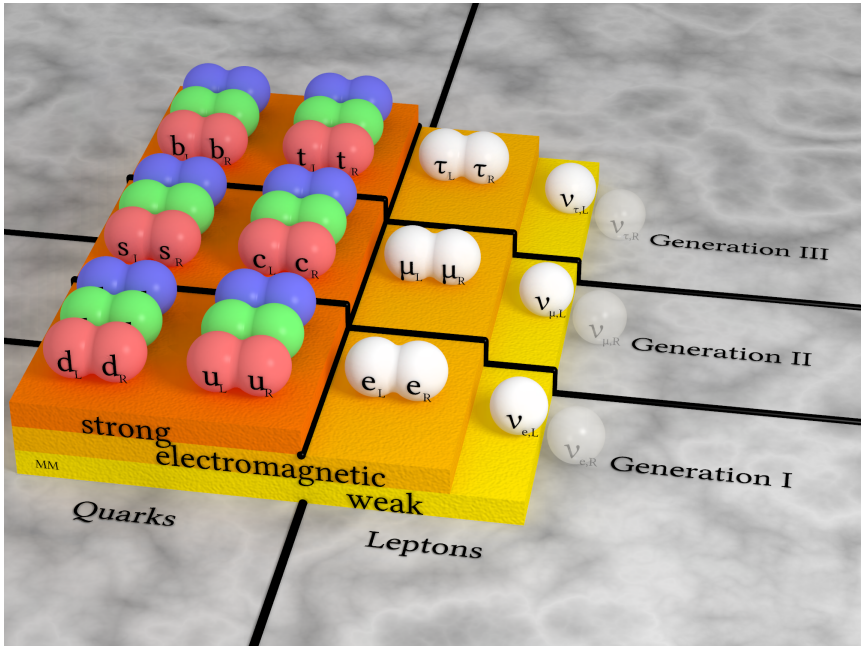

Figure 2.1: *Fermions of the Standard Model and their interactions. Each of the three generations contains a neutrino, a charged lepton and two quarks in three colours. Every fermion occurs with its left- and right-handed spin component. Neutrinos are the only exception as right-handed neutrinos have not been observed.*

in the strong nor in the electroweak interaction. In fact, right-handed neutrinos have never been observed in experiment, yet.

By construction, the Standard Model considers neutrinos as being massless. Nevertheless, measurements of solar and atmospheric neutrino fluxes [6, 7] clearly indicate neutrino oscillations which are only possible if neutrinos have a non-vanishing rest mass. In this case, neutrinos can be Dirac or Majorana particles or a mixture of both. If they are (at least partially) Dirac particles, they have a right-handed component which has to be much heavier than the left-handed one and/or does not interact with other Standard Model particles. A light right-handed neutrino would occur in decays of the Z^0 boson and experiments would observe a larger decay width. If neutrinos

quark		mass $[\mathrm{MeV}/c^2]$	lepton		mass $[\mathrm{MeV}/c^2]$
down	d	$4.1 - 5.8$	electron	e^-	0.510998910(13)
up	u	$1.7 - 3.3$	e-neutrino	ν_e	$< 2 \cdot 10^{-6}$ (95 % CL)
strange	s	101^{+29}_{-21}	muon	μ^-	105.658367(4)
charm	c	1270^{+70}_{-90}	μ-neutrino	ν_μ	< 0.19 (90 % CL)
bottom/beauty	b	4190^{+180}_{-60}	tauon	τ^-	1776.82 ± 0.16
top/truth	t	173300 ± 1100	τ-neutrino	ν_τ	< 18.2 (95 % CL)

Table 2.1: *Fermions of the Standard Model and their masses. The u-, d-, and s-quark masses are estimates of so-called* current-quark masses*, in a mass-independent subtraction scheme such as $\overline{\mathrm{MS}}$ at a scale $\mu \approx 2$ GeV. The c- and b-quark masses are the* running *masses in the $\overline{\mathrm{MS}}$ scheme [4]. The top quark mass is taken from direct measurement at the Tevatron [5]. Only upper limits can be given for neutrino masses. Their masses could not be determined in direct measurement, yet.*

are pure Majorana particles, they are their own anti-particles and do not have a right-handed component. As neutrinos are the lightest type of fermions, their rest mass can be ignored in high energy collider experiments without any negative effects.

Interactions between fermions are transmitted by gauge bosons. Their properties are determined by the underlying symmetry group of the interaction. The strong interaction is mediated by 8 gluons, whereas the carriers of the electroweak force are the Photon γ, the Z^0 and the $W^\pm$ bosons. Their quantum numbers are summarised in table 2.3. Additionally, there is the Higgs boson, responsible for giving all particles their respective rest masses. This particle is necessary in electroweak symmetry breaking by the Higgs mechanism [8]. In theories of quantised gravity, the graviton is the hypothetical particle needed to transmit the gravitational force.

particle			spin $[\hbar]$	electrical charge $[e]$	colour representation	weak isospin T_3	weak hypercharge Y
$\begin{pmatrix} u \\ d \end{pmatrix}_L$	$\begin{pmatrix} c \\ s \end{pmatrix}_L$	$\begin{pmatrix} t \\ b \end{pmatrix}_L$	$1/2$	$2/3$ $-1/3$	[3]	$\begin{pmatrix} 1/2 \\ -1/2 \end{pmatrix}$	$1/6$
u_R	c_R	t_R	$1/2$	$2/3$	[3]	0	$2/3$
d_R	s_R	b_R	$1/2$	$-1/3$	[3]	0	$-1/3$
$\begin{pmatrix} \nu_e \\ e^- \end{pmatrix}_L$	$\begin{pmatrix} \nu_\mu \\ \mu^- \end{pmatrix}_L$	$\begin{pmatrix} \nu_\tau \\ \tau^- \end{pmatrix}_L$	$1/2$	0 -1	[1]	$\begin{pmatrix} 1/2 \\ -1/2 \end{pmatrix}$	$-1/2$
e_R^-	μ_R^-	τ_R^-	$1/2$	-1	[1]	0	-1

Table 2.2: *Fermions of the Standard Model and their quantum numbers. Left- and right-handed spin components are treated separately to account for the $SU(2)_L$ symmetry of the weak interaction.*

particle	mass $[\mathrm{GeV}/c^2]$	spin $[\hbar]$	electrical charge $[e]$	colour representation	weak isospin T_3	weak hypercharge Y
Gluon (g)	0	1	0	[8]	0	0
Photon (γ)	0	1	0	[1]	0	0
Z^0	91.1876(21)	1	0	[1]	0	0
$W^\pm$	80.399(23)	1	± 1	[1]	± 1	0
Higgs (h)	> 114.4 (95 %CL)	0	0	[1]	$-1/2$	$1/2$
Graviton (G)	0	2	0	[1]	0	0

Table 2.3: *Bosons of the Standard Model and their quantum numbers [4]. The Higgs boson and the graviton are still hypothetical particles, because there is no evidence for their existence, yet.*

2.1.1 Quantum Chromodynamics

The theory of Quantum Chromodynamics describes the strong interaction of quarks. Every quark occurs in three colour charges [9, 10, 11], labelled *red*, *green* and *blue*. The force is transmitted via 8 gluons, that carry a colour charge and a colour anti-charge [12]. Thus, they change the colour charge of quarks. Its theoretical description is based on the local gauge group $SU(3)_C$ [13].

The only free parameters of QCD are the quark masses m_f, the strong coupling parameter α_s and a phase factor for violating the CP symmetry, which has been determined in experiment to be $< 10^{-10}$ [4]. Thus, QCD seems to be fixed completely by setting these values.

Renormalisation group equations induce a variation of α_s at different energy scales Q according to the differential equation [14]

$$\frac{Q^2}{4\pi}\frac{\partial\alpha_s(Q)}{\partial Q^2} = \beta(\alpha_s) = -\sum_{n=0}^{\infty}\beta_n\left(\frac{\alpha_s}{4\pi}\right)^{n+2},$$

where the first coefficients of the Taylor expansion of the β function

$$\begin{aligned}
\beta_0 &= \frac{11C_A - 2n_f}{3} = 11 - \frac{2}{3}n_f \\
\beta_1 &= \frac{2}{3}\left(17C_A^2 - 5C_A n_f - 3C_F n_f\right) = 102 - \frac{38}{3}n_f \\
\beta_2 &= \frac{1}{54}\left[2857C_A^3 + (54C_F^2 - 615C_F C_A - 1415C_A^2)n_f + (66C_F + 79C_A)n_f^2\right] \\
&= \frac{2857}{2} - \frac{5033}{18}n_f + \frac{325}{54}n_f^2 \\
\beta_3 &= \left(\frac{149753}{6} + 3564\zeta(3)\right) - \left(\frac{1078361}{162} + \frac{6508}{27}\zeta(3)\right)n_f \\
&\quad + \left(\frac{50065}{162} + \frac{6472}{81}\zeta(3)\right)n_f^2 + \frac{1093}{729}n_f^3 \\
&\vdots
\end{aligned}$$

can be determined from renormalisation and group theory. Characteristic values for $SU(3)$ have been inserted for the Casimir factors $C_A = 3$ and $C_F = 4/3$. n_f is the number of relevant flavours of fermions and $\zeta(3)$ is the Riemann Zeta function $\zeta(x)$ at $x = 3$. The form of β_3 given above is specific to $SU(3)$.

In next-to-leading order, i.e. up to β_1, the solution of this differential equation can be expressed as

$$\alpha_s(Q) = \frac{4\pi}{\beta_0 \ln\left(\frac{Q^2}{\Lambda^2_{\mathrm{QCD}}}\right)} \left[1 - \frac{\beta_1}{\beta_0^2} \frac{\ln\left(\ln\left(\frac{Q^2}{\Lambda^2_{\mathrm{QCD}}}\right)\right)}{\ln\left(\frac{Q^2}{\Lambda^2_{\mathrm{QCD}}}\right)}\right],$$

where Λ_{QCD} occurs as an integration constant, representing the energy which α_s diverges at. Its numerical value depends on the order of perturbation theory and the so called *renormalisation scheme* and is about $\Lambda_{\mathrm{QCD}} \approx 200\,\mathrm{MeV}$ for the $\overline{\mathrm{MS}}$ scheme. With this quantity matched to measured data, figure 2.2 shows the running coupling parameter α_s as a function of momentum transfer Q.

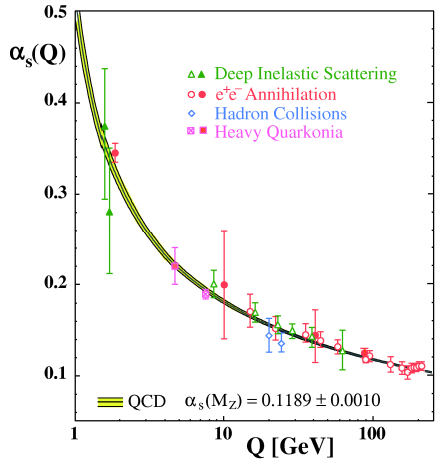

Figure 2.2: *Running coupling parameter $\alpha_s(Q)$ as a function of the energy scale Q from [15]. Open symbols show analyses using (resummed) next-to-leading order (NLO) perturbation theory calculations, filled symbols analyses using next-to-next-to-leading order (NNLO) calculations. The curves indicate QCD predictions for the combined world average value of $\alpha_s(M_{Z^0})$.*

This behaviour of the coupling parameter leads to two characteristic properties of QCD. In the high energy or large momentum transfer region, the coupling gets small, so that QCD processes may be calculated perturbatively by Taylor expansion. In this

case, quarks behave more and more like free particles. Interactions between them get weaker and weaker. This property is called *asymptotic freedom*, i.e. at infinite energy, quarks behave as free, non-interacting particles.

At small momentum transfer, the QCD coupling parameter gets large, so that perturbation theory is not applicable at low energy. On the other hand, this region is accessible with calculations on a spacetime lattice. QCD interactions get so strong that quarks are inescapably coupled to each other to form mesons and baryons, i.e. quarks cannot occur as free particles but only as a quark-antiquark pair or a couple of three quarks. This property of QCD is called *confinement*. A strong confirmation of QCD recently was achieved by successfully calculating hadron masses with a QCD prescription on a space-time lattice [16]. This effort confirms QCD as an accurate description of the strong interaction.

2.1.2 The electroweak Interaction

The electroweak interaction is described by the Glashow-Salam-Weinberg model [17, 18, 19]. It is based on a local $SU(2)_\mathrm{L} \times U(1)_\mathrm{Y}$ gauge symmetry that is broken down to the $U(1)_\mathrm{QED}$ symmetry of quantum electrodynamics (QED) via the Higgs mechanism.

This complicated symmetry group is needed because the weak interaction treats left- and right-handed fields differently, but charged currents do not distinguish between up- and down type (electron- and neutrino type) fermions. These properties can be explained with the $SU(2)_\mathrm{L}$ symmetry, which leads to three vector bosons $W_{1,2,3}$ coupling to left-handed fermions. The additional $U(1)_\mathrm{Y}$ symmetry introduces a new coupling parameter g' and a fourth vector boson B.

None of these boson fields can be identified with observable particles because electromagnetic and weak neutral currents also couple to right-handed fermions. The coupling strength of the photon is not equal to the coupling parameters of either gauge group, but can be identified with the electrical charge. Additionally, none of the fields are eigenstates of mass and the electrical charge operator Q.

The four observable electroweak gauge bosons originate non-trivially from the gauge fields $W_{1,2,3}$ of the $SU(2)_\mathrm{L}$ symmetry group and the field B of the $U(1)_\mathrm{Y}$ group. The $W^\pm$, Z^0 bosons and the photon A emerge as charge and mass eigenstates of the fundamental

fields:

$$
\begin{aligned}
W^{\pm} &= \frac{1}{\sqrt{2}} \left(W_1 \mp i \cdot W_2 \right) \\
\begin{pmatrix} A \\ Z^0 \end{pmatrix} &= \begin{pmatrix} \cos\vartheta_{\mathrm{W}} & \sin\vartheta_{\mathrm{W}} \\ -\sin\vartheta_{\mathrm{W}} & \cos\vartheta_{\mathrm{W}} \end{pmatrix} \begin{pmatrix} B \\ W_3 \end{pmatrix} \\
&= \frac{1}{\sqrt{g^2 + g'^2}} \begin{pmatrix} g & g' \\ -g' & g \end{pmatrix} \begin{pmatrix} B \\ W_3 \end{pmatrix} .
\end{aligned}
$$

At this point, the Weinberg mixing angle ϑ is introduced still as a free parameter. The last equality only emerges after symmetry breaking by identifying the Z^0 and the photon as mass eigenstates of the electroweak gauge fields.

The photon interaction is constrained by the electrical elementary charge. The electromagnetic coupling parameter is introduced to be

$$
e = \frac{g\, g'}{\sqrt{g^2 + g'^2}} ,
$$

which turns out to be $e = g \sin\vartheta_W$ after symmetry breaking.

The missing feature is a lack of any massive particle. In the Standard Model, a solution to this issue is achieved by the Higgs mechanism.

2.1.3 The Higgs Mechanism

The Higgs mechanism [8] is a method to give all massive particles their masses. The ad hoc way to introduce fermion masses for a particle φ with mass m via the expression

$$
m^2 \varphi\overline{\varphi} = m^2 \left(\varphi_{\mathrm{L}} \varphi_{\mathrm{R}}^{\dagger} + \varphi_{\mathrm{R}} \varphi_{\mathrm{L}}^{\dagger} \right)
$$

is not allowed because it is not invariant under local $SU(2)_{\mathrm{L}}$ gauge transformations. Only left-handed components are being transformed and right-handed components remain unchanged.

Nevertheless, particles can be given masses by introducing two additional complex scalar fields that form a doublet concerning the weak isospin, called the Higgs field

$$
\Phi = \begin{pmatrix} \Phi_1 + i\Phi_2 \\ \Phi_3 + i\Phi_4 \end{pmatrix} . \tag{2.1}
$$

With the Higgs field the electroweak $SU(2)_{\mathrm{L}} \times U(1)_{\mathrm{Y}}$ symmetry can be broken down to the remnant $U(1)_{\mathrm{em}}$ symmetry of quantum electrodynamics.

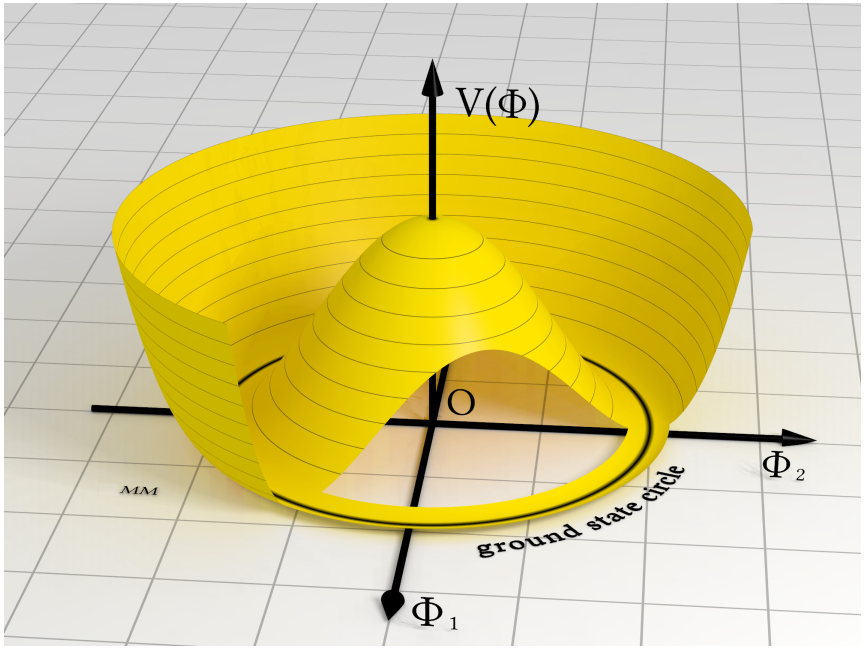

Figure 2.3: *2-dimensional representation of the Higgs potential. Only two components of the Higgs field (equation 2.1) have been drawn. The picture shows the Higgs potential for* $\Phi_3 = \Phi_4 = 0$.

The potential of the Higgs field is introduced as

$$V(\Phi) = \mu^2 \Phi^* \Phi + \lambda (\Phi^* \Phi)^2 ,$$

where the parameter λ can be interpreted as the strength of the Higgs self-coupling.

By defining the parameter μ^2 to be negative, the Higgs potential takes on a form equivalent to the potential shown in figure 2.3, giving the Higgs field a non-vanishing vacuum expectation value

$$\langle \|\Phi\| \rangle = \sqrt{-\frac{\mu^2}{2\lambda}} \stackrel{\text{def}}{=} v > 0 .$$

A field in a potential like this does not have a single ground state but a continuum of equivalent ground states, connected by suitable gauge transformations. Implications of this kind of potential can be most conveniently calculated in unitary gauge by expanding the Higgs field around its vacuum expectation value $\Phi = (0, v + h(x))^{\mathsf{T}}$. The spacetime dependence is contained in $h(x)$.

With this special choice of parametrisation, three degrees of freedom are transferred from the Higgs doublet to the weak gauge bosons. A mass expression emerges for the $W^{\pm}$ and Z^0 bosons and accordingly they acquire a longitudinal wave function component. The Higgs field h only keeps one degree of freedom which appears to be a neutral scalar boson.

By diagonalising the weak boson mass matrix, it is possible to express the masses of the electroweak gauge bosons in terms of the Higgs field vacuum expectation value v and the two electroweak coupling constants g and g' as

$$m_{W^{\pm}} = \frac{1}{2} v g$$
$$m_{Z^0} = \frac{1}{2} v \sqrt{g^2 + g'^2}.$$

At the same time the photon turns out to stay massless. The Higgs boson gets a mass of $m_H = v\sqrt{8\lambda}$. Its numerical value is unknown, because the Higgs self-coupling parameter λ can assume an arbitrary value. In fact, the easiest way to determine the parameter λ is by measuring the Higgs boson mass.

Fermion masses are introduced by coupling them to the Higgs boson. This is done by $\lambda_f \overline{U_{\mathrm{L}}} \Phi U_{\mathrm{R}}$ for the up-type fermion fields U and by $\lambda_f \overline{D_{\mathrm{L}}} \epsilon \Phi D_{\mathrm{R}}$ for the down-type fermion fields D. Here, λ_f is a free coupling parameter for the respective fermion to the Higgs boson and ϵ is the totally antisymmetric tensor in two dimensions. This results in fermion mass terms of the form $m_f = \frac{1}{\sqrt{2}} v \lambda_f$. Thus, fermion masses are not fixed by theory but only translated into coupling parameters to the Higgs field.

By measuring the $W^{\pm}$ and Z^0 masses, the electroweak mixing angle can be determined to be $\sin^2 \vartheta_{\mathrm{W}} = \frac{g'^2}{g^2 + g'^2} = 0.23108(5)$ [4]. The Higgs vacuum expectation value can be evaluated from measuring the weak Fermi constant

$$G_F = (\hbar c)^3 \frac{\sqrt{2}}{8} \left(\frac{g}{m_W} \right)^2 = (\hbar c)^3 \frac{\sqrt{2}}{8} \left(\frac{2}{v} \right)^2 = 1.166364(5) \cdot 10^{-5} \frac{1}{\mathrm{GeV}^2}$$

to be $v = 246\,\mathrm{GeV}/c^2$.

2.1.4 Diagonalising the Mass Matrices

After electroweak symmetry breaking via the Higgs mechanism all particles have acquired their respective masses. Still the three generations of particles remain unrelated as there is no interaction between particles of different generations. The following considerations are expressed for quarks, but are valid for leptons as well.

The nine orthonormal fields of the left- and right-handed up-type fermions $U_{i,L}$ and $U_{i,R}$ as well as the right-handed down-type fields $D_{i,R}$ may be chosen arbitrarily. The index $i = 1,2,3$ denotes the generation of the respective field. The remaining fields are then fixed by the lowering operators of the $\mathfrak{su}(2)_L$ and $\mathfrak{su}(3)_C$ algebras. This leaves the complete Standard Model Lagrangian density with a $U(3)^3$ symmetry for the quarks. This symmetry can be used to choose appropriate fermion fields, that are mass eigenstates and interaction eigenstates at the same time.

The Higgs field couples differently to up-type and down-type fermions. Thus, there are two 3×3 complex mass matrices M and M', one for the up-type and one for the down-type quarks. Each of them can be diagonalised by two unitary matrices $UMV^\dagger$ and $U'M'V'^\dagger$.

But the $U(3)^3$ symmetry allows of choosing only three matrices, i.e. there have to be three types of quarks for which the interaction eigenstates cannot be identified with their mass eigenstates. This discrepancy usually is focused on the left-handed down-type fermions, where the Cabibbo-Kobayashi-Maskawa (CKM) matrix [20, 21] parametrises the composition of interaction eigenstates d', s', b' from mass eigenstates d, s, b via

$$\begin{pmatrix} d' \\ s' \\ b' \end{pmatrix}_L = \underbrace{\begin{pmatrix} V_{ud} & V_{us} & V_{ub} \\ V_{cd} & V_{cs} & V_{cb} \\ V_{td} & V_{ts} & V_{tb} \end{pmatrix}}_{V_{CKM}} \cdot \begin{pmatrix} d \\ s \\ b \end{pmatrix}_L .$$

It is possible to formulate the Standard Model Lagrangian density in terms of mass eigenstates. In this case, the CKM matrix is transferred to the couplings to the $W^\pm$ bosons. This shows that only $W^\pm$ bosons are able to mediate a change in particle flavour, i.e. they are the only bosons which couple to different types of fermions at the same time. A squared matrix element $\left|V_{ij}\right|^2$ is proportional to the probability of a flavour change from quark type i to j. A remarkable feature of the Standard Model is the complete suppression of *flavour changing neutral currents* (FCNCs), because the CKM matrix turns out to cancel when coupling a quark and an antiquark of same flavour.

With the evidence for neutrino oscillations, neutrinos also have to be given masses, which implies a flavour mixing matrix for leptons, called the Maki-Nakagawa-Sakata-Pontecorvo (MNSP) matrix [22, 23]. Measured values of most matrix elements still contain large errors. Both matrices can be parametrised by three mixing angles and one CP violating complex phase parameter. In case neutrinos have a Majorana component, the MNSP matrix contains two additional CP violating phases. The two mixing matrices still are subject to current investigation.

2.1.5 Unresolved Aspects of the Standard Model

The Standard Model is able to consistently describe elementary particle physics with a remarkable amount of precision. Some of its greatest achievements are the prediction of the bottom and top quarks, the τ-neutrino and the $W^{\pm}$ and Z^0 bosons. Nevertheless, there are some shortcomings arising, that cannot be explained by the Standard Model. Some examples follow.

- The Standard Model does not describe *gravity*. A satisfying description of gravity, that is consistent with the Standard Model, has not been achieved, yet. The most accurate formulation is the theory of general relativity, which is based on a classical picture of spacetime. Quantisation of gravity leads to severe theoretical problems that make it impossible to calculate predictions, which can be tested in experiment.
- A related issue is the *hierarchy problem*. Gravity is about 44 orders of magnitude weaker then the electromagnetic force, when comparing forces between two protons. For this reason, gravity is ignored in most calculations. Effects of gravity only become important at the *Planck scale* at energies of about 10^{19} GeV.
- The *finetuning problem* also relates to a large difference in scales. Loop diagrams from higher order perturbation theory induce large corrections to the Higgs mass

  $$\Delta m_h^2 = -\frac{\left|\lambda_f\right|^2}{8\pi^2}\Lambda_{\mathrm{SM}}^2\,,$$

  where Λ_{SM} is the scale to which the Standard Model is valid. These loop corrections are quadratically divergent. If Λ_{SM} is taken to be the Planck scale, the bare Higgs mass has to be adjusted up to 16 digits in order to retain a physical Higgs mass of the order of $\sim 100\,\mathrm{GeV}/c^2$.
- The *symmetry between quarks and leptons* is not explained by the Standard Model. Both kinds of fermions occur in three generations with a pair of par-

ticles each. Additionally, the electrical charge of each generation adds up to zero, when counting all quarks with their three states of colour.

- Also the *origin of the Higgs mechanism* is left unexplained by the Standard Model. The Higgs boson is the only scalar particle in the Standard Model. The choice of one Higgs doublet seems to be arbitrary.
- The coupling of the Higgs boson to fermions is proportional to the respective fermion mass. The *top quark mass* is given in terms of the Higgs boson vacuum expectation value

$$m_t = \underbrace{\frac{v}{\sqrt{2}}}_{\approx 175\,\mathrm{GeV}/c^2} \cdot \underbrace{\lambda_t}_{\approx 1},$$

  where the coupling constant $\lambda_t \approx 1$. This special value may indicate a close connection between the top quark and the Higgs boson.

Many extensions of the Standard Model address these topics, often with the necessity of introducing new heavy particles, which are potential candidates for $t\bar{t}$ resonances.

2.2 Production and Decay of Top Quark Pairs

The top quark was discovered in 1995 at the Fermilab by the CDF and DØ experiments [24, 25]. With a mass of $m_t = 173.3\,\mathrm{GeV}/c^2$ the top quark is the heaviest elementary particle, currently known. It has a lifetime of $\tau_t \lesssim 5 \cdot 10^{-25}\,\mathrm{s}$. This makes it the only quark that decays before it can be captured in hadrons by the strong force, because the typical timescale of QCD interactions is $\hbar/\Lambda_{\mathrm{QCD}} \approx 10^{-24}\,\mathrm{s}$. The decay of top quarks is determined by the CKM matrix elements $|V_{tb}| = 0.88 \pm 0.07$, $|V_{ts}| = (38.7 \pm 2.1) \cdot 10^{-3}$ and $V_{td} = (8.4 \pm 0.6) \cdot 10^{-3}$ [4], where all values where obtained from measurements under the assumption of three generations of fermions. The first element completely dominates the top quark decay whereas the other ones are small. Therefore, a top quark decays almost exclusively into a bottom quark by emitting a $W^{\pm}$ boson.

As heaviest elementary particle, the top quark has a privileged role in probing the Standard Model Higgs boson as well as physics beyond the Standard Model. With a mass close to the scale of electroweak symmetry breaking, this property inspired many alternative or extended models for electroweak symmetry breaking and mass generation, e.g. *Little Higgs* [26, 27], *Topcolour* [28, 29, 30] or *top-seesaw* [31, 32, 33]. Some models predict the existence of additional gauge bosons with enhanced couplings to the third generation of quarks. Some of these models include excitations

of electroweak [34] or strong [35, 36, 37, 38, 39, 40, 41, 42] gauge bosons coupling to top quarks.

2.2.1 Top Quark Pair Production

Pairs of top and antitop quarks ($t\bar{t}$) can be produced via Standard Model QCD processes. Leading order contributions are shown in figure 2.4. $t\bar{t}$ pairs can be produced by quark-antiquark annihilation or by gluon scattering. The latter one is possible via three different production mechanisms, called the s-, t- and u-channels, whereas the former one can only be possible via the s-channel. These processes do not include a heavy $t\bar{t}$ resonance. Therefore, the centre-of-mass energy of the top quark pair is distributed continuously.

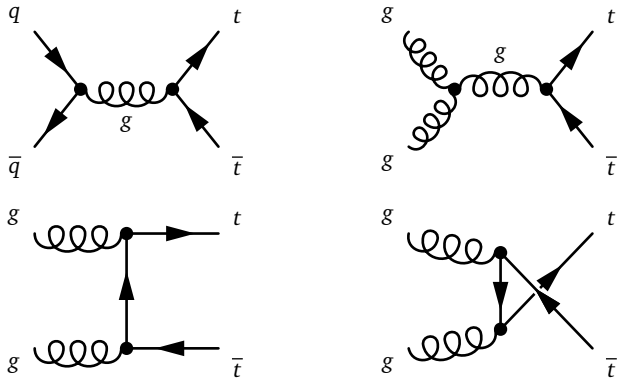

Figure 2.4: *Standard Model $t\bar{t}$ production. Top quark pairs can either be produced in quark-antiquark annihilation (top left) or via gluon scattering. For gluon scattering, there is one Feynman diagram for the s-, t- and u-channel whereas $q\bar{q}$ annihilation is only possible in the s-channel.*

Resonant production of $t\bar{t}$ pairs requires the existence of an undiscovered particle. Candidates for $t\bar{t}$ resonances are any kind of neutral bosons that are heavier than twice the top quark mass. Undetermined quantum numbers are spin, colour charge, and coupling strengths to left- and right-handed components of fermions. Couplings are related to the *parity* and γ_5*-parity* of a resonance. These quantum numbers determine the effect of a parity transformation on a wave function, i.e. how a wave function behaves after a reflection of coordinates.

As no such resonance is known to exist yet, it makes sense to look for resonances with any possible combination of these quantum numbers. Table 2.4 shows some of these combinations along with some examples of theories predicting these resonances.

spin [$\hbar$]	colour representation	parities $(1,\gamma_5)$	type	example
0	[1]	(1,0)	scalar colour singlet	SM, MSSM, 2HDM
0	[1]	(0,1)	pseudoscalar colour singlet	MSSM, 2HDM
0	[8]	(1,0)	scalar colour octet	techni-π^0
0	[8]	(0,1)	pseudoscalar colour octet	techni-π^0
1	[1]	(SM,SM)	excitation of Z^0	sequential Z'
1	[1]	(1,0)	vector colour singlet	
1	[1]	(0,1)	axial vector colour singlet	
1	[1]	(1,1)	left-handed vector colour singlet	
1	[1]	(1,-1)	right-handed vector colour singlet	
1	[8]	(1,0)	vector colour octet	coloron, KK gluon
1	[8]	(0,1)	axial vector colour octet	axigluon
2	[1]	–	tensor colour singlet	KK graviton

Table 2.4: *Some possible combinations of quantum numbers for $t\bar{t}$ resonances [43]. Most combinations are predicted by some extensions of the Standard Model. Some types of resonances occur in more than one model.*

Standard Model Higgs Boson Production

The Standard Model Higgs boson may be a $t\bar{t}$ resonance if the Higgs boson mass is greater than twice the top quark mass $m_h > 2m_t$. Earlier measurements at the Large Electron-Positron Collider (LEP) already exclude the low mass region up to $m_h < 114.4\,\mathrm{GeV}/c^2$ [44]. Recent results from the two experiments DØ and CDF at the Tevatron collider additionally exclude a Higgs boson mass of $158\,\mathrm{GeV}/c^2 < m_h < 175\,\mathrm{GeV}/c^2$ with 95 % confidence level [45]. These limits are shown in figure 2.5. Although elec-

troweak fits of Standard Model parameters favour a light Higgs boson, a Higgs boson mass above $2m_t$ is not strictly excluded.

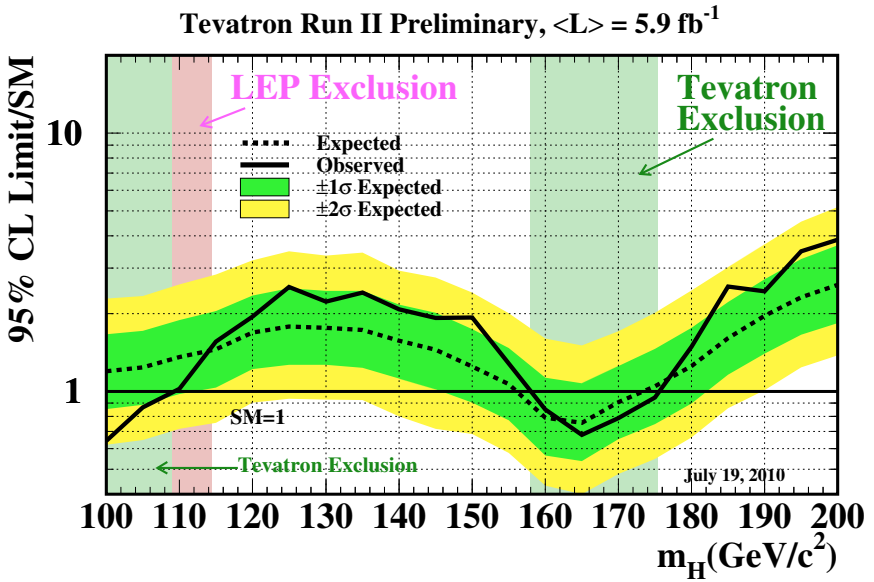

Figure 2.5: *Higgs boson exclusion limits from* LEP *and Tevatron [46]. Existence of a Standard Model Higgs boson can be excluded for mass ranges* $m_h < 114.4\,^{\mathrm{GeV}}/_{c^2}$ *and* $158\,^{\mathrm{GeV}}/_{c^2} < m_h < 175\,^{\mathrm{GeV}}/_{c^2}$ *with 95 % confidence level.*

Multi Higgs Doublet Models (MHDM)

According to its name the Two-Higgs-Doublet model [47] contains an additional doublet of Higgs fields, compared to the Standard Model with only one doublet. With four additional degrees of freedom there are many ways to couple the additional fields to the Standard Model particles and different ways of electroweak symmetry breaking, but the general features of this model remain the same.

There are also some extensions of the Two-Higgs-Doublet model, e.g. the Three-Higgs-Doublet Model (3HDM) [48, 49, 50], or extensions of the Standard Model also requiring two Higgs doublets, e.g. supersymmetry [51]. Some of these models predict even

more than five Higgs bosons and many other undiscovered particles, but all of them require at least the ones mentioned above. The 2HDM can be considered as a minimal extension of the Standard Model concerning the Higgs sector.

After electroweak symmetry breaking, three degrees of freedom have moved to the electroweak gauge bosons $W^{\pm}$ and Z^0 which acquire a longitudinal component of polarisation like in the Standard Model. The remaining five degrees of freedom manifest as five different Higgs bosons which acquire their masses through self-interactions with each other. Among these Higgs bosons, there is the Standard Model Higgs boson h, a second scalar Higgs boson H, a pseudoscalar boson A and a pair of electrically charged Higgs bosons $H^{\pm}$. All of them are colour-neutral particles of spin $s = 0\hbar$. The three neutral Higgs bosons h, H and A are candidates for $t\bar{t}$ resonances. Their quantum numbers are summarised in table 2.5.

Higgs boson	electrical charge $[e]$	parities $(1, \gamma_5)$
h^0	0	(1,0)
H^0	0	(1,0)
A^0	0	(0,1)
$H^{\pm}$	± 1	(1,0)

Table 2.5: *Higgs bosons in the Two-Higgs-Doublet Model. The 2HDM includes five different Higgs bosons, two scalars, one pseudoscalar and a pair of electrically charged Higgs bosons.*

In Multi Higgs Doublet Models each Higgs doublet Φ_i has its own vacuum expectation value v_i and may couple in its own way to up- and down-type fermions U and D respectively. With two Higgs doublets, the ratio of both vacuum expectation values are usually denoted by $\tan(\beta) = \frac{v_2}{v_1}$ and the mass ratio of the two scalar Higgs bosons is defined as $\tan(\alpha) = \frac{m_{h^0}}{m_{H^0}}$. Two extreme models are the following.

- Φ_1 does not couple to fermions at all.
  Φ_2 couples equally to up- and down-type fermions.

In this case, the couplings are given by

$$\begin{aligned}\mathscr{L}_{Hf\overline{f}} = &-\frac{g}{2m_{W^\pm}\sin\beta}\overline{D}M_D D\left(H^0\sin\alpha + h^0\cos\alpha\right) - \frac{ig\cot(\beta)}{2m_{W^\pm}}\overline{D}M_D\gamma_5 DA^0 \\ &-\frac{g}{2m_{W^\pm}\sin\beta}\overline{U}M_U U\left(H^0\sin\alpha + h^0\cos\alpha\right) + \frac{ig\cot(\beta)}{2m_{W^\pm}}\overline{U}M_U\gamma_5 UA^0 \\ &+\frac{g\cot\beta}{2\sqrt{2}m_{W^\pm}}\left(H^+\overline{U}\left[M_U V_{\mathsf{CKM}}\left(1-\gamma_5\right) - V_{\mathsf{CKM}}M_D\left(1+\gamma_5\right)\right]D + \text{h.c.}\right).\end{aligned}$$

- Φ_1 couples only to down-type fermions.
  Φ_2 couples only to up-type fermions.

  In this case, couplings are given by

$$\begin{aligned}\mathscr{L}_{Hf\overline{f}} = &-\frac{g}{2m_{W^\pm}\cos\beta}\overline{D}M_D D\left(H^0\cos\alpha + h^0\sin\alpha\right) - \frac{ig\tan(\beta)}{2m_{W^\pm}}\overline{D}M_D\gamma_5 DA^0 \\ &-\frac{g}{2m_{W^\pm}\sin\beta}\overline{U}M_U U\left(H^0\sin\alpha + h^0\cos\alpha\right) + \frac{ig\cot(\beta)}{2m_{W^\pm}}\overline{U}M_U\gamma_5 UA^0 \\ &+\frac{g}{2\sqrt{2}m_{W^\pm}}\left(H^+\overline{U}\left[\cot\beta M_U V_{\mathsf{CKM}}\left(1-\gamma_5\right) + \tan\beta V_{\mathsf{CKM}}M_D\left(1+\gamma_5\right)\right]D \right. \\ &\left. + \text{h.c.}\right).\end{aligned}$$

Exclusion limits on Higgs bosons from a non-minimal Higgs sector are less tight than limits on the Standard Model Higgs boson. Measurements at the Large Electron Positron Collider (LEP) exclude neutral Higgs bosons from the Minimal Supersymmetric Model (MSSM) up to masses of $m_{h^0} < 92.8\,\mathrm{GeV}/c^2$ and $m_{A^0} < 93.4\,\mathrm{GeV}/c^2$ [52]. Experiments at Tevatron do not quote explicit exclusion limits on masses of Higgs bosons, but only limits on $\tan\beta$ as a function of the Higgs mass [53].

Apart from Higgs doublet models there are even more elaborate models, e.g. the Higgs Triplet Model (HTM) [54, 55], which also contain many Higgs bosons, but are not considered in this study.

Technicolour

The technicolour model (TC) [56, 57] considers the Higgs boson as a composite particle. Its constituents, called techni-fermions, are confined by a new strong interaction. The Higgs boson is formed during a dynamical breaking of the new gauge symmetry.

At low energy, the Higgs boson appears as a condensate of techni-fermions which develops a non-vanishing expectation value $\left\langle f\overline{f'}\right\rangle \neq 0$, just like mesons emerge after chiral symmetry breaking as a quark condensate in low energy QCD. The simplest model of technicolour is not able to give masses to leptons and quarks. To make this possible, the technicolour gauge group has to be extended, introducing new gauge bosons which are able to couple to Standard Model fermions. This model is called *extended technicolour* (ETC) [58, 59].

Nevertheless, ETC still has problems with flavour changing neutral currents and generating the extremely heavy top quark mass. A *topcolour* extension of the model leads to the *topcolour assisted extended technicolour* model [29]. In this model, techni-fermions do not only form the Higgs boson, but also produce many other particles by building condensates and by interacting with Standard Model particles.

One of these new particles emerging from the model is a heavy copy of the Z^0 boson, called Z'. The Z' boson can be heavy enough to decay into a top quark pair. The easiest channel to detect this particle would be its decay into a pair of charged leptons. On the other hand, there are some models with a leptophobic Z' boson, that does not couple to leptons. In this case, the search for it as a $t\bar{t}$ resonance is a good channel for its discovery.

Leptophobic Z' bosons as a $t\bar{t}$ resonance have already been studied at the DØ and the CDF experiments at Tevatron. Existence of this type of resonance could be excluded with 95 % confidence level up to a mass of $m_{Z'} < 820\,{}^{\mathrm{GeV}}/_{c^2}$ [60] and $m_{Z'} < 805\,{}^{\mathrm{GeV}}/_{c^2}$ [61] respectively.

The Coloron and Axigluon Model

Inspired by the spontaneous electroweak symmetry breaking, the QCD symmetry group $SU(3)_C$ is extended to a product of gauge groups $SU(3) \times SU(3)$ [62]. In the axigluon model [63, 64], these two symmetry groups act on left- and right-handed quarks, separately, so that it can also be labelled $SU(3)_L \times SU(3)_R$. For the coloron model, the two coupling constants may be different. Their ratio is usually written as ${}^{g_1}/_{g_2} = \cot\theta$.

The Standard Model gauge group $SU(3)_C$ remains after spontaneous symmetry breaking as the diagonal subgroup. Similar to the Higgs mechanism, some of the gauge bosons acquire a mass. The eight massless gauge bosons are identified with gluons from QCD. The remaining eight bosons emerge as an octet of colour charged heavy particles. Just like the gluon, these particles cannot be distinguished by their colour charge, which makes them appear as different states of the same particle.

Depending on the details of the gauge symmetry and the respective couplings to quarks, this particle is called a *coloron* or *axigluon*. Colorons are colour octet vector bosons and can be imagined as heavy gluons. Axigluons instead are colour octet axial vector bosons. Both particles interact strongly with quarks, which also includes a strong coupling to top quarks. Their strong coupling to quarks and gluons leads to a high production rate and a large expected signal.

Both models have already been studied at the Tevatron without any significant findings, resulting in quite high exclusion limits between 800 GeV/c^2 and 3.2 TeV/c^2 depending on the respective type of coupling. Respective exclusion limits are summarised in table 2.6

particle	coupling	confidence level	excluded mass range $[\mathrm{GeV}/c^2]$
axigluon	-	95 %	$m_A < 910$
	-	90 %	$m_A < 920$
coloron	$\cot\theta = 1$	95 %	$m_C < 800$, $895 < m_C < 1960$
		90 %	$m_C < 805$, $880 < m_C < 2470$
coloron	$\cot\theta = 1.5$	95 %	$150 < m_C < 950$
coloron	$\cot\theta = 2$	99.99 %	$m_C < 930$, $1110 < m_C < 1860$
		95 %	$m_C < 955$, $1030 < m_C < 3200$
		90 %	$m_C < 960$, $1020 < m_C < 3250$

Table 2.6: *Coloron and axigluon exclusion limits [65]. The coloron model provides the coupling strength relative to the Standard Model strong coupling as a free parameter. This coupling is fixed to the Standard Model value in models of axigluons.*

Extra Dimensions

The theory of extra dimensions is based on the assumption that at microscopic scales there are more than the ordinary four dimensions of space and time [66, 67]. The reason why these extra dimensions have not been noticed yet is because they have periodic boundary conditions and their length is of a microscopic scale. Effects of extra dimensions can easily been seen in the Klein-Gordon equation

$$\left(\partial^\mu \partial_\mu - m^2\right)\psi = 0\,,$$

which describes the propagation of a scalar particle ψ with mass m.

The d'Alembert operator ($\Box = \partial^\mu \partial_\mu$) in d dimensions can be split into the ordinary 4-dimensional d'Alembert operator plus the second derivatives in the extra dimensions.

$$\begin{aligned} &\left(\Box^{(d)} - m^2\right)\psi = 0 \\ \Leftrightarrow &\left(\Box^{(4)} + \sum_{\mu=5}^{d} \partial_\mu \partial^\mu - m^2\right)\psi = 0\,. \end{aligned}$$

The sum over the momenta in direction of the extra dimensions plus the rest mass squared of the described particle can be summed up to an effective mass visible in four dimensions. As an effect of periodic boundary conditions of the extra dimensions momentum in these directions is quantised. If n_μ denotes the order of excitation and R the radius of the extra dimension, the Klein-Gordon equation can be written as

$$\left(\Box^{(4)} \underbrace{- \sum_{\mu=5}^{d} \frac{n_\mu^2}{R^2} - m^2}_{-m^2_{\text{visible}}}\right)\psi = 0\,.$$

This equation describes an infinite number of particle excitations. The ground state still is a particle of rest mass m of the Standard Model particle. By moving along the extra dimension, a particle can acquire additional visible mass. With one extra dimension, there are excitations of this particle with equidistant mass gaps. This periodic spectrum is also called the *Kaluza-Klein* (KK) *tower* of particle excitations. With more extra dimensions, the spectrum gets denser with increasing masses, i.e. more and more excitations can be produced with increasing energy until the spectrum looks almost continuous. The number of excitations increases as $\sim E^{d-4}$.

The model described above is only the simplest model of extra dimensions. There are also more complex models involving dimensions of different sizes, curved or warped extra dimensions or models without periodic boundary conditions. All these model differ in their phenomenology, but most of them provide excitations of some Standard Model particles.

The most promising Kaluza-Klein excitations of Standard Model particles are excitations of massless particles. These are the first particles that can be excited at low energy scales. With heavy Standard Model particles, some energy is lost for their rest mass, before they can gain momentum in the extra dimensions.

Candidates for $t\bar{t}$ resonances can be Kaluza-Klein gluons or Kaluza-Klein gravitons. Kaluza-Klein gluons have already been studied at the Tevatron without any evidence of their existence. A lower mass limit of $m_{\mathrm{KKg}} > 800\,{}^{\mathrm{GeV}}/_{c^2}$ has been set for the Kaluza-Klein gluon of the bulk Randall-Sundrum model [68].

2.2.2 Decay Channels of Top Quark Pairs

In a $t\bar{t}$ decay, the two occurring $W^{\pm}$ bosons decay each into a pair of quarks or leptons. Depending on the $W^{\pm}$ decays, a $t\bar{t}$ event is called either *fully hadronic*, *semileptonic* or *dileptonic*. In fully hadronic events, both $W^{\pm}$ bosons decay into quarks. In the semileptonic case, one $W^{\pm}$ boson decays into quarks, the other one into leptons. The dileptonic channel contains two decays into leptons. Their respective branching ratios are depicted in figure 2.6.

The fully hadronic channel has the largest branching fraction of 64.8 %, but is hard to distinguish from a QCD event with only lighter quarks. The final state only consists of jets which hide the presence of an electroweak decay and make all events appear like processes of light quarks in QCD. Therefore the fully hadronic channel is difficult to study and needs a large suppression of different processes.

The dileptonic channel has a clean signature, which is faked by only a small fraction of similar processes. Two leptons of opposite signs can be easily identified and distinguished from pure QCD events. A drawback of this channel comes from the two neutrinos which cannot be detected. Thus, the event cannot be reconstructed completely with all particle momenta. An additional difficulty arises from $\tau^{\pm}$ decays, because $\tau^{\pm}$ leptons decay into hadrons in 64.8 % [4] and cannot be unambiguously identified as leptons. Therefore, the $W^{\pm}$ decay into a $\tau^{\pm}$ and its τ-neutrino is usually ignored, leaving the dileptonic channel with a usable branching fraction of only 4.4 %.

The semileptonic channel provides a compromise between a high usable branching fraction (28.6 %) and a moderate amount of non-$t\bar{t}$ processes with a similar final state. Although it contains one neutrino from the leptonic $W^{\pm}$ decay, the kinematics of the event can be completely reconstructed by posing a mass constraint on the reconstructed $W^{\pm}$. With one hadronic $W^{\pm}$ decay and one decay into an $e^{\pm}$ or $\mu^{\pm}$ plus the respective neutrino, the semileptonic channel still holds a branching fraction of 28.6 %, which makes it the favoured channel for many $t\bar{t}$ studies. Also this study considers the semileptonic decay of top quark pairs.

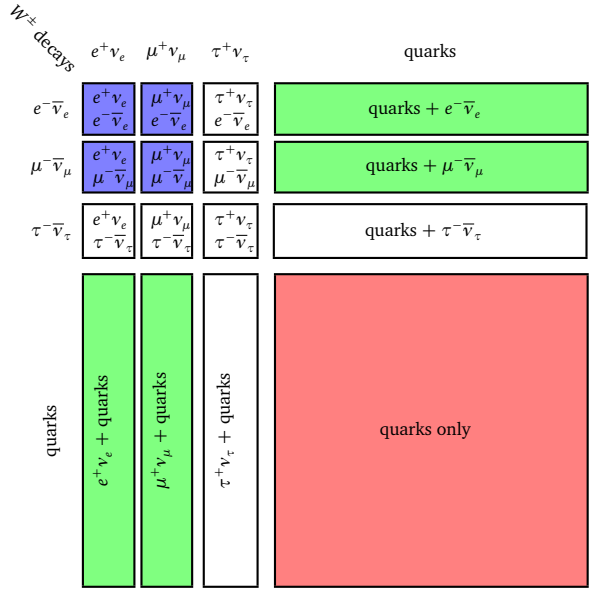

Figure 2.6: *Branching fractions of two $W^{\pm}$ bosons. The fully hadronic channel (red) has the largest branching ratio of 46.7 %. Studies of leptonic channels usually omit the $\tau^{\pm}$ decays because $\tau^{\pm}$ leptons decay before they can reach the detector. In 64.8 % [4] it decays into hadrons, which can be misidentified as QCD jets. Therefore, the usable branching fraction into the semileptonic channel (green) is 28.6 % and 4.4 % into the dileptonic channel (blue).*

2.2.3 Interferences in Top Quark Pair Production

An additional heavy resonance decaying into a $t\bar{t}$ pair opens a new production channel for top quark pairs. In order to get accurate predictions for physical observables, resonant production processes have to be treated equally like ordinary QCD production channels if initial and final states are the same.

In the operator formalism, the S matrix contains all transition amplitudes between an arbitrary initial and a final state. Therefore, transition amplitudes from initial to final states are also called *matrix elements*, denoted by $\mathscr{M}$. The transition probability from the initial to final state is given by its absolute square $|\mathscr{M}|^2$.

A resonance process with transition amplitude $\mathscr{M}_{\text{Res}}$ can interfere with $t\bar{t}$ production via QCD processes $\mathscr{M}_{\text{QCD}}$. The total $t\bar{t}$ production rate is proportional to the absolute square of matrix elements

$$|\mathscr{M}|^2 = \left|\mathscr{M}_{\text{QCD}} + \mathscr{M}_{\text{Res}}\right|^2 = \left|\mathscr{M}_{\text{QCD}}\right|^2 + \left|\mathscr{M}_{\text{Res}}\right|^2 + \underbrace{2 \cdot \text{Re}\left(\mathscr{M}_{\text{QCD}}\overline{\mathscr{M}_{\text{Res}}}\right)}_{\text{Interference}} . \tag{2.2}$$

For many models the interference is small and can be ignored. In this case, processes can be divided into a *signal* contribution of interesting events and a *background* contribution from similar events of other processes. Often signal events include yet undiscovered phenomena like particles predicted from extensions of the Standard Model. Then, background events are well known Standard Model processes with an equal or similar final state. The total observed cross section is just the sum of signal and background contributions. This is shown in figure 2.7

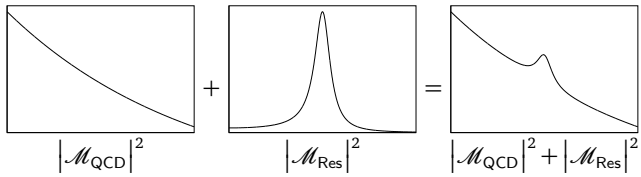

Figure 2.7: *Example of signal and background contributions to a given process. With negligible interference, the full process is the sum of both types of events.*

If the interference is large, i.e. comparable in size with the signal contribution, it cannot be ignored any more. In this case, a full simulation is necessary, respecting all Feynman diagrams at the same time, contributing to the total cross section. The interference can have a strong impact on the shape of observable quantities. This influence is shown schematically in figure 2.8.

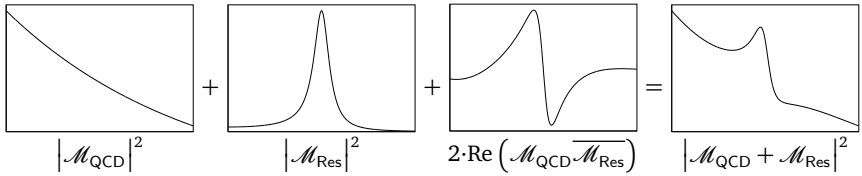

Figure 2.8: *Example of background, signal and interference contributions to a given process. The interference can give a substantial contribution to the full process.*

In case of a full simulation, distinction between $t\bar{t}$ production in QCD or via a resonance is not allowed any more, because all production channels together contribute to the whole process. Also the branching ratio of a resonance decaying into a pair of top quarks is already included in the transition amplitude for $t\bar{t}$ production.

3 Event Generators for high Energy Particle Collisions

"First Commandment of Event Generation:
Thou shalt never believe event generation is easy."
— Leif Lönnblad

Comparisons between theoretical predictions and experimental measurements are a non-trivial task. On the one hand distributions of observable quantities can only be calculated analytically for partons. On the other hand experiments can only detect hadrons and leptons with a sufficiently long lifetime. Additionally, detectors have a limited resolution in space and momentum. In order to compare continuous theoretical distributions with measurements of discrete events, a large number of events is needed to reduce statistical errors. In order to achieve an accurate theoretical prediction of expected measurements, the full process of measurement is simulated on an event-by-event basis by *event generators* for different extensions of the Standard Model.

This chapter describes the different stages of a hadron-hadron collision and their implementation in event generators. As a part of this work, a new model was implemented for the event generator HERWIG++. Properties of this model are described in the last section.

3.1 Proton-Proton Interactions

Heavy particles such as resonances of top quark pairs can only be produced and studied directly at high energy particle colliders, e.g. the Large Hadron Collider (LHC) or the Tevatron. High energy collisions of two protons are rather complex processes, mostly because protons are composite objects of quarks and gluons, generally called *partons*. The major theoretical issue is the confinement property of QCD, which prevents partons described by theory from being observed as free particles. Yet, the relation between stable final states and fundamental partonic states can only be described by empirical quantities and phenomenological processes like parton distribution functions (PDFs), fragmentation functions or hadronisation models.

Many observable variables are expressed as total or differential *cross sections*. In particle collisions, a cross section is imagined as a hypothetical area representing the projection of the target particle. If a particle collides with the target and crosses this area, both particles interact. Otherwise, the particle misses the area without any reaction. The total cross section of hadron-hadron collisions can be divided into contributions from different processes, where a specific cross section is proportional to the probability or frequency of the respective process. Figure 3.1 shows a summary of some prominent processes.

For lepton-lepton, e.g. e^+-e^-, collisions and deep inelastic scattering (DIS), i.e. lepton-hadron scattering, a factorisation theorem [70, 71, 72] states, that particle collisions can be described by a decomposition into several independent processes for calculating cross sections, e.g. *initial state radiation* (ISR), a *hard process*, *final state radiation* (FSR) and hadronisation. This is possible because processes at high energy scales hardly interfere with processes of low energy scales. For hadron-hadron collisions this theorem has been explicitly disproven [73], which means that processes at all energy scales may interfere and influence the full process. Despite this fact, the factorisation theorem is nevertheless applied regularly to hadron-hadron collisions because correlations of processes at different energy scales are expected to be small. Thus, the factorisation theorem is considered to be a good approximation to actual hadron-hadron collisions.

Differential cross sections $\frac{d\sigma}{dX}$ of any observable final state X can be related to parton-level differential cross sections $\frac{d\hat{\sigma}_{ab}}{d\hat{X}}$ by

$$\frac{d\sigma}{dX} = \sum_{a,b} \int \underbrace{f_a(x_a, Q_i)}_{\text{PDF}} \underbrace{f_b(x_b, Q_i)}_{\text{PDF}} \cdot \frac{\hat{\sigma}_{ab}}{d\hat{X}} \cdot F_{\hat{X}\to X}(Q_i, Q_f)\, dx_a dx_b \,.$$

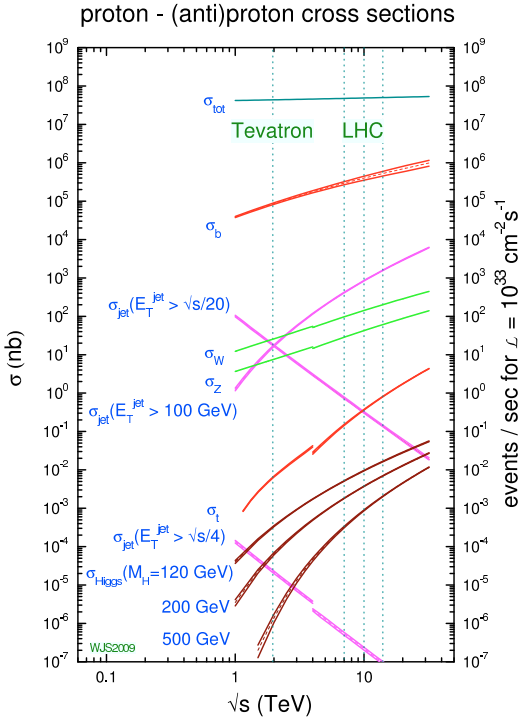

Figure 3.1: *Cross sections of some interesting processes as a function of centre-of-mass energy [69]. Vertical dashed lines show energies of the two major hadron-hadron colliders, the Tevatron at 1.96 TeV and the Large Hadron Collider (LHC) at 7, 10 or 14 TeV, depending on future upgrades in energy. Cracks in plotted lines indicate a transition from $p\bar{p}$ at the Tevatron to pp collisions at the LHC. All cross sections of interesting processes rise with increasing energy, raising the signal/background ratio.*

Here, $f_j(x_j, Q_i)$ is the parton distribution function for a parton of type j with momentum fraction x_j for a given momentum transfer of Q_i. The probability or frequency for different initial state partons is determined according to the relative values of their parton distribution functions. The partonic cross section $\hat{\sigma}_{jk}$ for the hard process can be calculated analytically by perturbation theory. The function $F_{\hat{X}\to X}$ evolves the partonic final state from a scale Q_i to the observable final state at scale Q_f. It describes processes like production of jets, hadronisation or hadron decays, which subsequently take place at different energies until the scale Q_f is reached. These steps are shown in figure 3.2.

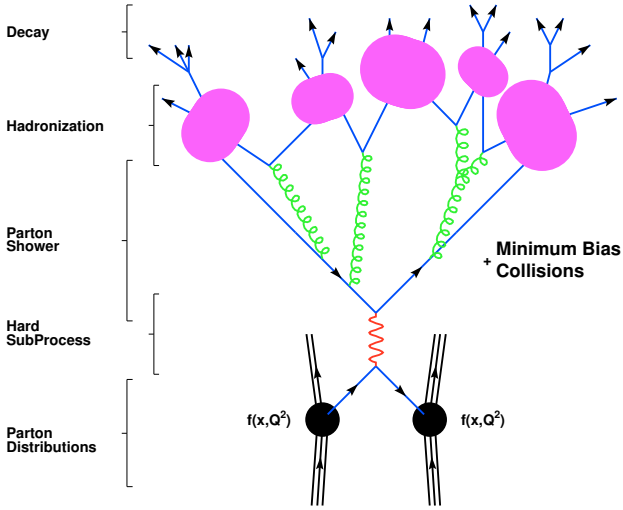

Figure 3.2: *Factorisation steps of a high energy collision event [74]. Parton distribution functions determine the probability for one parton from each colliding proton to enter into the hard process. Outgoing partons radiate gluon bremsstrahlung in the parton shower. All created partons get confined into hadrons, which decay into stable particles.*

Actual proton-proton collisions include an additional complication as there may be other partonic interactions apart from the hard process, the so called *underlying event* as well as many pairs of protons colliding at the same time, called *multiple proton interactions*.

3.1.1 The hard Process

The partonic interaction with the highest energy scale during a particle collision is called the *hard process*. This most interesting interaction is described by Feynman diagrams like in figure 3.3 can be calculated perturbatively up to a given order in the strong and electroweak coupling parameters.

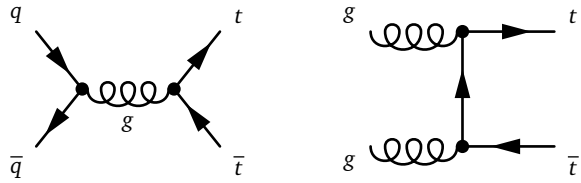

Figure 3.3: *Two example diagrams of a hard process for $t\bar{t}$ production. The initial state in the left diagram is a quark-antiquark pair whereas in the right diagram it consists of two gluons. Both diagrams have the same final state consisting of a pair of top-antitop quarks.*

The hard process is the transition from a given partonic initial state into a predefined final state of partons. In a hadron-hadron collision, the initial state may consist of a quark/antiquark or a gluon from each of the initial hadrons.

The hadronic cross section into a partonic final state is given by

$$\sigma = \sum_{a,b} \int f_a(x_a, Q_i) f_b(x_b, Q_i) \cdot \frac{1}{\hat{s}} \cdot \Theta(\text{cuts}) \cdot \overline{\sum} \left| \mathscr{M}\left(p_a p_b \to p_1 p_2 \ldots p_n\right) \right|^2 dx_a dx_b d\Phi_n \,,$$

where the Mandelstam variable $\hat{s} = E_{\text{cm}}^2 = (p_a + p_b)^2 c^2$ is the squared partonic centre-of-mass energy. $\overline{\sum}$ denotes the sum over all final state quantum numbers and the average over all initial state quantum numbers such as spin and colour degrees of freedom. The matrix element is a function of the momenta p_i of all incoming and outgoing partons. $d\Phi_n$ is the Lorentz invariant phase space element of the n outgoing partons. The Heaviside function Θ accounts for kinematic cuts applied to the outgoing particles.

The diagrams in figure 3.3 only show contributions in leading order (LO) perturbation theory. In order to achieve more accurate results, higher order diagrams are required, which include additional loops or outgoing partons, like the ones in figure 3.4. Diagrams without any loops are also called *tree level* diagrams.

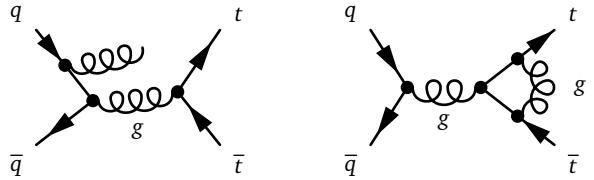

Figure 3.4: *Two example diagrams of a hard process for $t\bar{t}$ production in next-to-leading order. The left diagram shows an additional gluon radiation from an initial state quark, which adds a third parton to the final state. The right diagram shows an additional gluon exchange by the two outgoing top quarks.*

3.1.2 Parton Distribution Functions

Protons are not elementary particles, but consist of three valence quarks, which are coupled together by gluons. As a property of QCD, these gluons can interact with each other, split into two or three gluons or a quark/antiquark pair. As a consequence, a proton consists not only of three valence quarks, but also a huge number of gluons and sea quarks. Each of these partons can take part in the hard process.

Parton distribution functions $f_a(x,Q)$ tell the probability to find a parton of type a with a momentum fraction x of the total hadron momentum at a scale Q. In general, this probability is different for each parton type and depends on the energy scale Q. Thus, PDFs tell the probability distribution for all matrix element initial states. Figure 3.5 shows the MSTW 2008 [75] set of PDFs at two different energy scales at leading order in α_s.

For small Q, the contribution of the valence quarks can be seen clearly, producing a bump in the u and d quark distributions. At high scales Q and low momentum fractions x, contributions from the sea quarks become more important. Also contributions from other quark flavours arise, ordered inversely by their respective masses. The region of small momentum fractions is completely dominated by the gluon distribution. Therefore, about half of the proton momentum is carried by gluons.

The energy dependence of parton distribution functions f is given by the Dokshitzer-Gribov-Lipotov-Altarelli-Parisi (DGLAP) [76, 77, 78] evolution equation

$$Q \cdot \frac{df}{dQ} = \frac{\alpha_s}{\pi} \int_x^1 P(z) \cdot f\left(\frac{x}{z}, Q\right) \frac{dz}{z}$$

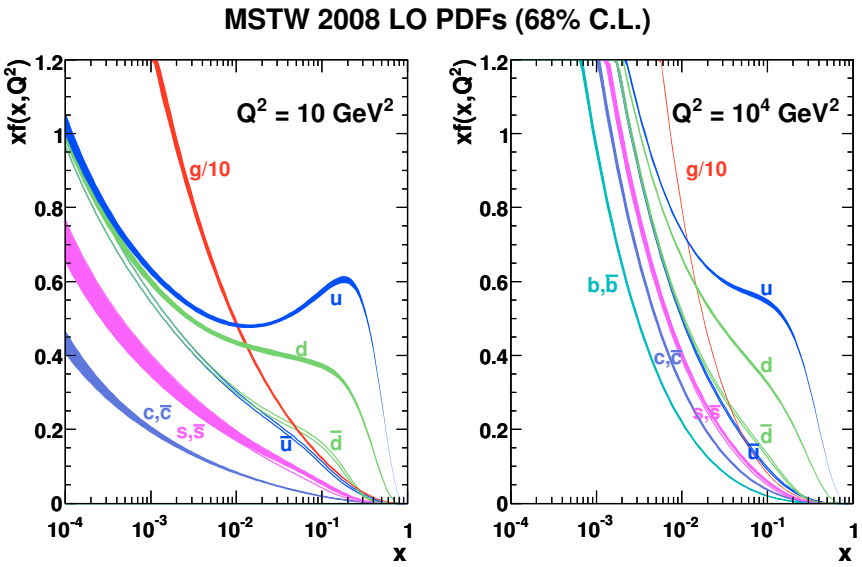

Figure 3.5: *Parton distribution functions for two different energy scales at leading order in α_s [75]. The widths of the bands indicate theoretical and experimental uncertainties from various sources.*

where $P(z)$ is called the splitting kernel. The splitting kernel gives the probability of a parton to split into two partons with one of them carrying the momentum fraction z of the original parton. The three splitting processes of QCD in leading order of α_s are shown in figure 3.6.

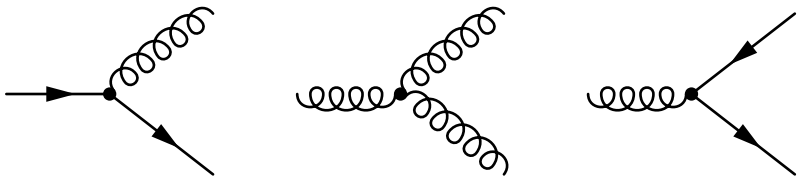

Figure 3.6: *Elementary QCD processes representing splitting kernels for gluon radiation (left), gluon splitting into two gluons (middle) and quark pair production (right).*

Splitting kernels determine the probabilities of the respective splitting processes. In leading order of α_s they are given analytically by

$$\begin{aligned} P_{q\to qg}(z) &= C_\mathsf{F}\frac{1+z^2}{1-z} \\ P_{g\to gg}(z) &= C_\mathsf{A}\frac{(1-z(1-z))^2}{z(1-z)} \\ P_{g\to q\bar{q}}(z) &= n_\mathsf{f}T_\mathsf{F}(z^2+(1-z)^2)\,. \end{aligned} \tag{3.1}$$

Here, $T_\mathsf{F} = 1/2$ is the normalisation of group generators, $C_\mathsf{F} = 4/3$ and $C_\mathsf{A} = 3$ are the Casimir factors characteristic for the $SU(3)$ symmetry of QCD.

3.1.3 The Parton Shower

Despite the outgoing partons from the hard process are assumed to not interact with each other any more, they still undergo particle reactions. Quarks radiate gluons via QCD bremsstrahlung, gluons split into two gluons or into a quark-antiquark pair, all charged partons and particles radiate photons as electromagnetic bremsstrahlung and quarks decay via the weak interaction.

With possibly hundreds of participating partons these processes are extremely complicated. To reduce their complexity, they are usually divided into a hard interaction with only a few final state partons and a parton shower, where each parton radiates additional partons, increasing the number and reducing the average energy of final state partons until it reaches a predefined energy threshold. The distinction between parton radiation from the matrix element or the parton shower is artificial because both stages are only approximations to the real complex process. The transition energy is not unique, but has to be chosen when calculating particle interactions.

Radiation processes can again be expressed in terms of the splitting kernels from equations 3.1 depicted in figure 3.6. The *Sudakov form factor* [79]

$$\Delta(t,t_0) = \exp\left[-\sum_j \int_{t_0}^{t}\int_{z_{\min}(t')}^{z_{\max}(t')} \frac{\alpha_s(t')}{\pi} P_{i\to j}(z)dz\frac{dt'}{t'}\right] \tag{3.2}$$

expresses the probability of no radiation between the scales t and t_0. The Sudakov form factor describes the emission pattern of partons and their energy loss. An example of parton radiation is shown in figure 3.7.

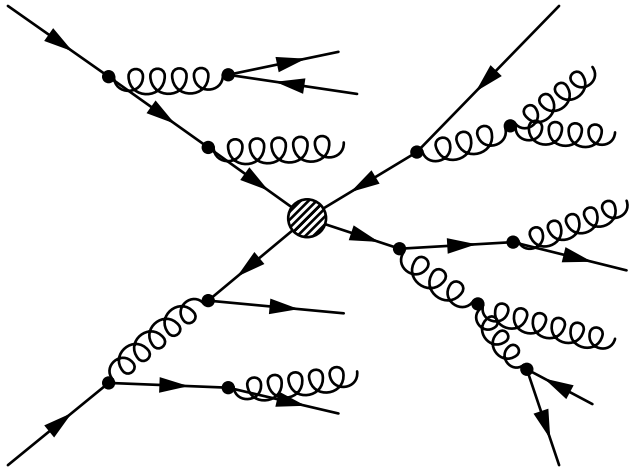

Figure 3.7: *Example parton shower from initial and final state partons. The blob in the middle contains the hard process. This diagram only shows QCD reactions as they are the most dominant processes. Weak particle decays and electromagnetic radiation are also possible.*

Initial state partons radiate gluons or split into quark-antiquark pairs until two partons from the initial state radiation (ISR) interact with each other and become the initial state particles for the hard process. Final state partons from the hard process then also split into two partons iteratively, loosing energy until they reach the QCD hadronisation scale.

Result of the parton shower is a large number of partons. In general, the outgoing particles carry a colour charge and, thus, cannot exist as free particles. Quarks and gluons have to form colour neutral hadrons. Parton showers generally exhibit a property of *preconfinement* [80, 81, 82], which means that colour singlet pairs of coloured partons end up with a small distance in phase space. This property establishes the preconditions for the hadronisation.

3.1.4 Hadronisation

Hadronisation generally is a low energy effect, that sets in at energies corresponding to typical hadron masses of $E_{\text{had}} \approx m_{\text{Hadron}}c^2 \approx 200 - 1500\,\text{MeV}$. The property of confinement of QCD makes quarks and gluons not occur as free particles.

Nonperturbative QCD simulations on a spacetime lattice determine the confinement/deconfinement transition at a temperature of about T_c =146-170 $^{\text{MeV}}/_{k_B}$ [83, 84, 85] for an infinite volume. The specific temperature strongly depends on the respective observable and can be higher for a smaller system, because the transition is only an analytic cross over of different states, but not a phase transition.

Below the transition temperature a gluon string of constant energy density is formed between two quarks when their distance is increased above the typical diameter of a hadron which is about 1 fm. When the string contains enough energy to create an additional quark-antiquark pair which can act as endpoints of the gluon string, the string breaks apart and the original hadron splits up into two or more hadrons, effectively reducing the energy stored in the string and confining all quarks into hadrons [86, 87]. Similar arguments hold for strings between gluons.

The property of confinement is closely related to the emergence of *jets* in high energy particle collisions. Escaping quarks and gluons from an event radiate additional partons which remain colour-connected through gluon strings. If the relative momentum of two connected partons $\Delta p \gtrsim m_{\text{Hadron}}c$, the string may be broken by creating a new quark-antiquark pair where each of the new quarks is again colour-connected to one of the original partons, but not necessarily connected among each other. All relative and transverse momenta of colour-connected partons are effectively reduced to $p_\perp \leq \Delta p \approx 1\,^{\text{GeV}}/_c$, which corresponds to typical hadron masses. Below this scale, partons are not able to break their colour-connections. As a result, colour-connected partons end up with a small distance in phase space, which is the reason for the property of *preconfinement*.

Transverse momenta of emerging hadrons are limited to $p_\perp \lesssim 1\,^{\text{GeV}}/_c$, but the original parton can have a large momentum $p \gg 1\,^{\text{GeV}}/_c$. In this case, hadron momenta are highly boosted into the direction of flight of the original parton. Their trajectories appear to be collimated into a bundle of tracks, called *jet*.

In general, produced hadrons are unstable. Their decays are well understood from direct measurements at all kinds of accelerator experiments. A quite complete list of hadron decay channels can be found in [4]. All subsequent particles in a decay chain approximately keep their direction of flight, because of momentum conservation and the original particles may be highly boosted. Therefore, hadrons from a specific

parton are collimated into the same direction and form a jet. Its properties reflect the properties of the original parton. Therefore, it is possible to study partonic properties by measuring the properties of jets.

3.1.5 Additional Interactions

Apart from the hard process, there are always additional interactions that contribute additional final state particles to the event. The following list contains some commonly used categories of additional interactions, some of which have a similar meaning, but have to be distinguished carefully.

Multiple Parton Interactions Measurements of QCD jet production indicate a rapid rise in jet cross sections with increasing centre-of-mass energy which eventually may exceed the total pp or $p\overline{p}$ cross section and violate unitarity. This effect is initiated by a rapid rise of parton distribution functions for decreasing momentum fraction x, which indicates an increasing probability of more than one partonic interaction during the same hadron-hadron collision.

Multiple Proton Interactions Real particle colliders do not collide single particles, but dense packets, so called *bunches*, of up to 10^{11} hadrons. During a collision of bunches, many pairs of hadrons may interact independently at the same time.

Pile-up This type of events includes all additional interactions apart from the primary collision. Apart from Multiple Proton Interactions, this also includes interactions with particles from other sources, e.g. with beam gas.

Minimum Bias This expression refers to a single particle-particle, i.e. proton-proton interaction. This includes all possible types of interactions, such as elastic scattering, single-, double- and non-diffractive events as well as hard scatterings. As hard scatterings are rare, Minimum Bias events are dominated by soft interactions.

Underlying Event This component of an event includes all particles from a single particle collision except those from the process of interest. The Underlying Event may also contain particles from a hard scattering, if there is a second hard interaction parallel to the main hard process of interest.

Final state particles from additional interactions contribute as background to a measurement of the hard process. They raise occupancies of most parts of the detector, which increases the difficulty to detect the interesting final state objects of the hard process.

3.2 Implementations of Event Generators

Simulations of high energy particle collisions are done with *event generators*. There is a large number of event generators, some for simulating special processes or steps in an event, or general purpose event generators, which simulate complete events of all kinds. Examples of specialised generators just for the hard process are AcerMC, AlpGen, Ariadne, CompHEP, MC@NLO and MadEvent/MadGraph.

There are mainly three common general purpose event generators: Herwig++, Pythia and Sherpa.

All specialised event generators have to be interfaced with the parton shower and hadronisation component of a general purpose generator in order to obtain realistic events. For each step there are several models or algorithms that concentrate on different aspects of the simulation or are optimised to reproduce certain observable quantities accurately. This work makes use of the general purpose event generator Herwig++. This generator was chosen for the following reasons

- As a general purpose event generator Herwig++ provides the complete chain of steps of an event simulation. No external module is needed. Consistency of all participating parts is guaranteed. Especially, this means a consistent transition between hard process and parton shower. The available phase space of incoming and outgoing partons is sampled consistently and unambiguously, which can be an issue when using an external matrix element generator.

- Herwig++ was rewritten from scratch based on the preceding event generator Herwig. In this process, several improvements over the previous version where included, e.g. a new ordering variable for its parton shower implementation, which accounts for effects of massive partons.

- Herwig++ offers some advantages compared to Pythia, e.g. the automatic application of spin correlations. Herwig++ includes spin correlations for all its matrix elements without any additional setup. This makes matrix element predictions more realistic.

- Although the Sherpa approach of automatic matrix element code generation seems quite advanced and comfortable, it makes studies of many particles with different properties difficult. Sherpa determines possible Feynman diagrams from properties of a particle and its couplings to other particles. For this study of many different types of $t\bar{t}$ resonances this means many different configurations and initialisation steps, which would be too time-consuming for purposes of mass production with current versions of this generator.

The following sections describe some of the concepts in greater detail that are used by HERWIG++.

3.2.1 Matrix Element Calculation

Matrix element calculations with event generators have to deal with divergences in cases when partons radiate gluons of small energy or collinearly to another outgoing parton. This configuration has to be excluded from matrix elements. The missing region in phase space is handled by the parton shower.

Care has to be taken on the one hand not to double count regions in phase space that are handled in the matrix element as well as in the parton shower and on the other hand not to skip a region of phase space completely. Matrix element calculation and parton shower have to fit together to cover all possible regions of phase space. The corresponding procedure of dividing phase space is called *matching* between matrix element and parton shower.

In NLO calculations the occurring divergences are cancelled by diagrams with additional loops. In this case, algorithms have to be implemented in a way to avoid large contributions leading to numerical instabilities, i.e. all integrals have to be split into parts of finite size. This procedure sometimes leads to events of negative weights which have to be treated carefully during an analysis.

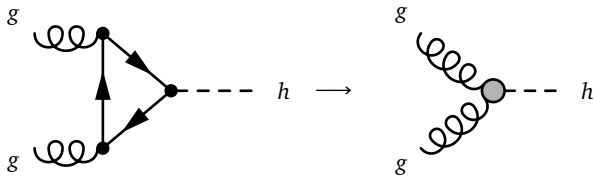

Figure 3.8: *Contraction of a loop contribution into an effective vertex. Higgs bosons couple to gluons only via a quark loop. This loop contribution can be calculated analytically. Thus, it is possible to establish an effective vertex where the Higgs boson is able to couple to gluons directly.*

HERWIG++ is a tree level, fixed order event generator, i.e. available matrix elements do not have any loops and must always provide a fixed final state. Exceptions are possible with effective vertices, where a loop contribution can be described as single vertex like in figure 3.8.

Matrix elements for HERWIG++ require two particles in the initial state and can handle an arbitrary number of partons in the final state. There are many existing matrix

elements included in HERWIG++ for a wide range of processes. Many Standard Model processes and a lot of processes beyond the Standard Model are provided for, e.g. supersymmetry, universal extra dimensions or new gauge bosons and resonant graviton production.

As part of this work, a new matrix element was implemented for HERWIG++, which is able to calculate pair production of heavy quarks in hadron-hadron collisions. Besides standard QCD processes, also resonant $q\bar{q}$ production via additional production channels is handled, including an arbitrary resonance with configurable quantum numbers. This new matrix element was developed with the requirement of respecting all possible interferences between QCD $q\bar{q}$ production and production via an intermediate resonance. Details of this matrix element are described in section 3.3.

3.2.2 Parton Distribution Functions

Parton distribution functions are not uniquely determined. Distributions of partons inside a proton are functions of the considered factorisation scale Q and the longitudinal momentum fraction x of the total proton momentum. As a proton is a bound state, parton and momentum distributions inside a proton are low energy properties where the strong coupling parameter gets large. Thus, these quantities are inaccessible to perturbation theory. Colliding particles probe the composition of a proton at a specific energy scale Q, which is also interpreted as the momentum transfer between two colliding partons. This scale also determines the resolution to which the structure of the proton can be resolved.

The strong coupling region of QCD is in general accessible via calculations on a space-time lattice, but these calculations are still far too expensive for today's computers. Parton distribution functions therefore have been measured in deep inelastic scattering experiments. Some fits of different parametrisations to measured data exist. The two most common fits are the CTEQ [88] and the MSTW [75] PDF sets.

Depending on the matrix element, different PDF sets have to be used. There are PDFs for use with leading order calculations and sets for NLO or NNLO matrix elements. By default, HERWIG++ uses the MSTW 2008 LO** PDF set, which is a PDF set tuned to reproduce NLO cross sections with leading order matrix elements. To determine uncertainties in the fits, PDF groups also provide error PDFs which deviate one standard deviation from the central value. The MSTW group provides a set of 20 pairs of PDF eigenvector sets, which have been orthogonalised to provide approximately uncorrelated errors to determine PDF errors. Each pair is normalised to an error of one standard deviation.

Most event generators, and also HERWIG++, provide an interface to externally defined parton distribution functions. This interface follows the *Les Houches Accord Parton Distribution Function* (LHAPDF) standard [89]. All major PDF sets are available via this library and can be easily selected and changed.

3.2.3 The Parton Shower

For the evaluation of parton showers the Sudakov form factor in equation 3.2 is not determined analytically. In order to obtain a probability of a parton splitting, its Taylor expansion is truncated after the first non-trivial order, which is called *leading logarithmic approximation* (LLA). In this approximation, only one parton emission at a time has to be respected with no interference between two emitted partons. For an application of next-to-leading logarithmic approximation (NLLA), the splitting kernels have to be adjusted to include splittings at next-to-leading order in α_s. In any case, the evaluation of Sudakov form factors can be precalculated for all values of ordering parameters, so that integrals only have to be determined once.

In the prescription of the Sudakov form factor in equation 3.2, there is some degree of freedom in choice of the ordering parameter t. Different implementations use different ordering parameters, such as transverse momentum or virtuality to cover the complete available phase space of emitted partons (see figure 3.9). These approaches have to be extended to respect the effect of *colour coherence* [90]. Gluon radiation from child partons after a splitting looks like radiation from the parent parton on its mass shell. This effect leads to an *angular ordering* of parton radiation, i.e. the angle of a subsequent parton radiation has to be smaller than the angle of any previous radiation.

To account for colour coherence, the HERWIG++ parton shower [92, 93] implemented its ordering variable

$$t^2 = \frac{2E_{ij}^2 \left[1-\cos\left(\theta_{ij}\right)\right]\left[1+\cos\left(\theta_{\tilde{ij}}\right)\right]^2}{\left[1+\cos\left(\theta_i\right)\right]\left[1+\cos\left(\theta_j\right)\right]}$$

with respect to the original final state parton from the matrix element, called the *progenitor*. θ_i and θ_j are the angles between the progenitor and the respective child particle i or j. $\theta_{\tilde{ij}}$ is the angle between the parent and the progenitor, and θ_{ij} is the angle between the two children. E_{ij} denotes the energy of the parent.

When a branching occurs, the starting evolution scales of the child partons i and j with momentum fractions z and $1-z$ are set to $zt \approx E_i\theta_{ij}$ and $(1-z)t \approx E_j\theta_{ij}$

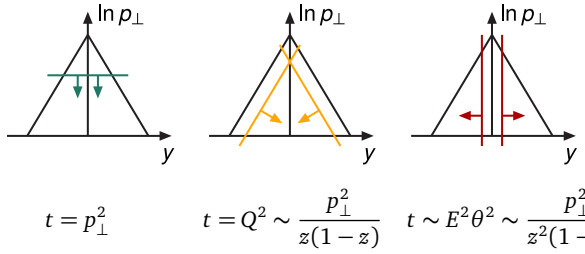

Figure 3.9: *Ordering variables of parton showers [91]. p_T ordering (left), virtuality ordering (middle) and angular ordering (right) cover the accessible phase space of rapidity y and transverse momentum $p_\perp$ of emitted partons from different directions.*

respectively. The maximum opening angle of any subsequent branching is θ_{ij}, which ensures angular ordering explicitly.

Further features of the HERWIG++ parton shower implementation are its Lorentz invariance under boosts along the jet axis and the treatment of heavy quark fragmentation through the use of mass-dependent splitting functions [94] and kinematics, providing a complete description of the *dead-cone* region [95], i.e. gluon radiation from a quark is kinematically forbidden for angles $\theta < \frac{m_q c^2}{E_q}$. This relation originates from the condition that velocities of quarks and gluons have to obey $v_q < v_g = c$.

3.2.4 String and Cluster Hadronisation Models

Mechanisms of hadronisation are not well understood from first principles. Only effective models exist for transformations of colour charged partons into colour neutral hadrons. Types and quantum numbers of the resulting hadrons are determined by the quantities of the originally available partons, because all conservation laws have to be respected, e.g. conservation of colour and electrical charge, momentum or spin. Examples of how to combine partons to hadrons is given in figure 3.10. There are two main models for hadronisation, the cluster model [96] and the Lund string model [97].

The Lund string model constructs strings of colour flow spanning from a quark across colour-connected gluons to an appropriate antiquark. Gluons from the parton shower act as fixed points for the quark-antiquark connection that change the direction of the string. At some points, the string may break, reducing the total energy stored in the string. A new quark-antiquark pair with suitable colour charges is produced at the

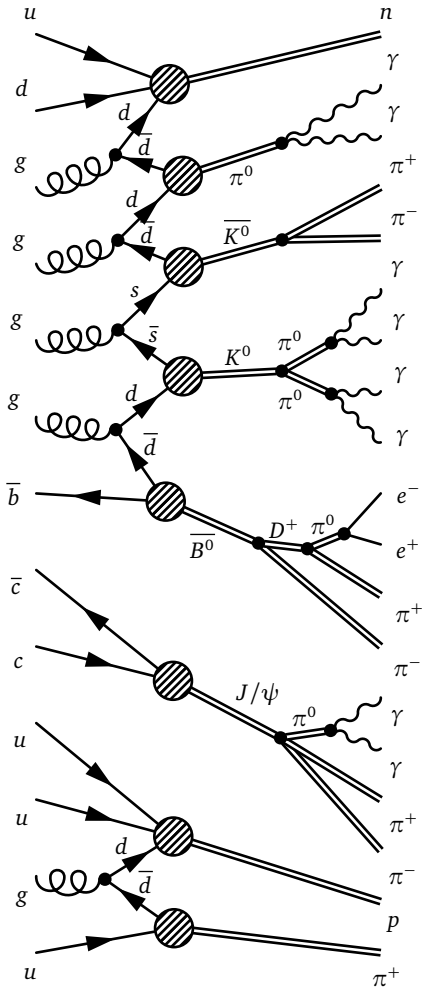

Figure 3.10: *Example for hadronisation and hadron decays. Partons from the parton shower enter the diagram from the left. Before hadronising, gluons split up into pairs of quarks and antiquarks. Respecting their colour charges and flavours, all quarks are coupled to mesons and baryons (hatched blobs). On the right hand side of the diagram, these hadrons decay.*

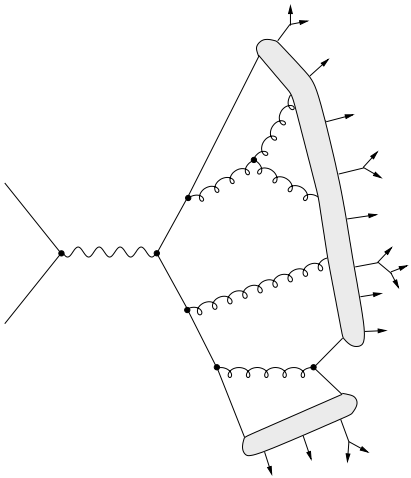

Figure 3.11: *Illustration of the Lund string model of hadronisation [98]. The shaded areas represent strings as intermediate states between partons and hadrons.*

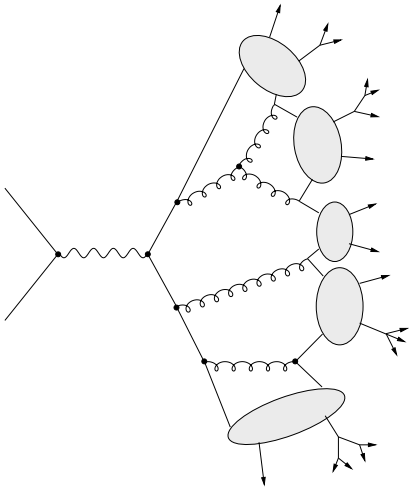

Figure 3.12: *Illustration of the cluster model of hadronisation [98]. The shaded areas represent clusters as intermediate states between partons and hadrons.*

new endpoints. When the energy of a string is too small to generate an additional quark-antiquark pair, it is transformed into a hadron.

In contrast, as a first step, the cluster model splits gluons from the parton shower into quark-antiquark pairs. After that, pairs of colour-connected quarks and antiquarks are collected into *clusters*, which are guaranteed to be close in phase space because of the preconfinement property of the parton shower. Eventually, all clusters are transformed into hadrons, respecting the given quantum numbers of original partons and according to available phase space.

The main advantage of the cluster model compared to the string model is a small number of parameters which makes the cluster model simpler and more intuitive. On the other hand, the string model is able to adapt to measured data more easily. In fact, there are some observables that are not described accurately with the cluster model. As a disadvantage, the string model needs many abstract parameters with no physical interpretation.

Hadrons produced during the hadronisation can be unstable and highly excited. They are finally being decayed according to their respective branching ratios into stable particles.

3.2.5 The Underlying Event

Multiple parton interactions can be implemented as many independent scattering processes as long as some physical constraints are respected for all extracted partons, e.g. total energy and flavour conservation. The total momentum of all partons cannot be larger than the original (anti)proton momentum. The sum of all parton flavours has to match the flavour content of the (anti)proton.

In HERWIG++ these constraints are matched by ignoring events violating energy or momentum conservation. Only one parton is evolved backwards to a valence quark during the initial state radiation parton shower. Partons for multiple interaction processes are always evolved back to a gluon.

In addition to these semi-hard processes, HERWIG++ implemented a second component of multiple interactions. Soft scatterings are modelled by elastic collisions of soft gluons. Motivated by the pomeron-like structure of these scatterings, the two colliding gluons are colour-connected to each other so that the outgoing proton remnants are not affected.

3.3 The heavy Quark Resonance Model for HERWIG++

Current event generators are able to simulate a wide variety of processes, also including many undiscovered particles predicted by extensions of the Standard Model, such as Z' bosons, supersymmetric particles or Kaluza-Klein excitations of Standard Model particles. Usually, these processes are simulated independently of each other using distinct matrix elements even if they have the same initial states and result in the same final states, which can easily be mixed up. In this case, interferences of diagrams with equal initial and final states are ignored. As explained in section 2.2.3, such an interference can provide a significant contribution to the full process, i.e. interferences have to be taken into account for some models [99]. Considering this aspect, only few existing event generators are available to simulate a heavy quark resonance interfering with QCD production of heavy quarks.

As part of this work, a new model was implemented for HERWIG++, which extends the Standard Model by one additional resonance decaying into a pair of quarks. The

matrix element is designed with a resonance of heavy quarks in mind, especially top quarks. The final state quarks, therefore, are generally labelled with Q and $\overline{Q}$. The model is designed as flexible as possible to simulate resonances with arbitrary quantum numbers.

Some constraints are implied by a forced decay of the resonance into a $Q\overline{Q}$ pair. Its electrical charge has to be 0, its spin has to be integer and the resonance cannot be a stable particle. Resonant quark pair production further implies a resonance mass $m_{\text{Res}} > 2 \cdot m_Q$, otherwise only continuum production is possible, e.g. like $t\bar{t}$ production in Standard Model QCD.

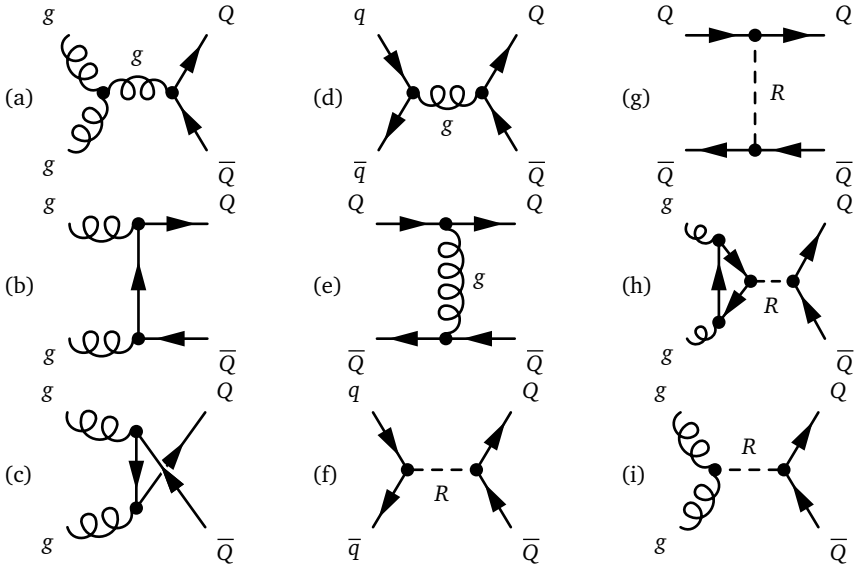

Table 3.1: *Feynman diagrams implemented in the heavy $Q\overline{Q}$ resonance matrix element. The diagrams show quark-antiquark production via gluon scattering (a)–(c) and quark-antiquark scattering (d), (e) in QCD and similar production channels via gluon scattering (f), (g) and quark-antiquark scattering (h), (i) including a resonance R.*

The matrix element provides nine Feynman diagrams shown in table 3.1. Diagrams (a)–(c) show heavy quark pair production in QCD via gluon scattering. The three diagrams show the s-, t- and u-channel respectively. Diagrams (d) and (e) present the

s- and *t*-channel diagrams for quark-antiquark scattering in QCD. Diagrams (f) and (g) represent the *s*- and *t*-channel diagrams including the resonance in quark-antiquark scattering. Resonance production in gluon scattering is shown in diagrams (h) and (i).

As a quark-antiquark resonance, it couples directly to quarks, i.e. diagrams (f) and (g) directly follow from the definition of the resonance. Couplings to gluons are not covered by this definition, but depend on the properties of the resonance. For resonances coupling only to quarks, but not to gluons, diagram (h) is the leading order production diagram for gluon scattering. For instance, this applies for production of Higgs bosons in the Standard Model. Although the loop diagram is suppressed by two additional vertices, corresponding to two additional orders of coupling parameters, the diagram may give a significant contribution, if the coupling parameter is large. This is the case for the coupling of a top quark to the Standard Model Higgs boson and may also be valid for other types of resonances.

HERWIG++ implements the coupling via a quark loop with an effective vertex, such that the loop contribution is calculated analytically and matched to the remaining tree level simulation. This also implies a sum over contributions from all types of quark loops.

Diagram (h) is not used for vector resonances. The Furry theorem [100, 101] forbids the production of a vector particle from two vector partons via a fermion loop. Colour-charged resonances are able to couple to gluons directly. Diagram (i) can be applied for these types of resonances. As a result, colour-neutral vector resonances, such as the Z' boson, do not couple to gluons and can only be produced in quark-antiquark annihilation.

HERWIG++ calculates transition amplitudes of Feynman diagrams using the HELAS formalism [102] to determine wave functions of particles and values of vertices. The matrix element module of the heavy quark resonance model calculates transition amplitudes explicitly for all 16 combinations of helicities of incoming and outgoing partons so that spin degrees of freedom are propagated correctly between initial and final state partons.

Treatment of colour degrees of freedom is not implemented explicitly. Transition amplitudes include the colour average of initial state partons and the sum of final state colours. In determination of the absolute square of transition amplitudes, colour degrees of freedom induce further constraints on the matrix element. Flows of colour charges have to be consistent also in interferences between each pair of Feynman diagrams. To account for conserved colour flows, a weight, called *colour factor*, is applied to each pair of Feynman diagrams, which can be calculated algebraically from the

property	value	description
particle name	`HeavyQQbarResonance`	name of the resonance
PDGID	9900000	PDG particle ID [4]
short name	`HeavyQQbarResonance`	abbreviation
mass	> 0	resonance mass
width	> 0	resonance decay width
cut off	float	Breit-Wigner resonance cut off
$c \cdot \tau$	0	speed of light · lifetime automatically calculated from width
electrical charge [$e/3$]	0	has to be 0 for $q\overline{q}$ resonances
colour representation	1	colour singlet
	8	colour octet
spin representation	1	spin 0
	3	spin 1
stable	0	$q\overline{q}$ resonance has to be unstable

Table 3.2: *Configurable parameters of the $q\overline{q}$ resonance. Its mass, decay width, colour and spin representations determine the physical properties of the resonance.*

properties of the $SU(3)_c$ gauge symmetry. A detailed derivation of all colour factors for a general $\mathfrak{su}(N)$ algebra is listed in appendix A.4. Full matrix elements in terms of individual transition amplitudes, including all interferences, as implemented in the heavy quark resonance model are given in appendix A.5.

In case the above considerations are applied to top quark pair production, the model simplifies because Feynman diagrams (e) and (g) do not apply any more. The parton distribution function of top quarks is negligible. Therefore, none of the available fits of PDFs include contributions of top quarks. For this reason, initial state top quarks do not occur and calculated transition amplitudes for Feynman diagrams (e) and (g) always vanish.

3.3.1 Parameters

A list of configurable quantum numbers of the resonance is presented in table 3.2, such as the mass and width of the resonance as well as spin and colour charge.

In order to couple the resonance to other particles, the Heavy Quark Resonance Model includes four vertex objects which implement couplings of a spin-0 or spin-1 resonance

to quarks or gluons respectively. Couplings to leptons is not necessary because all initial and final state partons are always quarks or gluons. Available options of the model are listed in table 3.3.

Each vertex can be set up to provide one of the following types of couplings between the resonance and quarks or gluons:

em coupling parameter of the electromagnetic interaction $\alpha_{\mathrm{em}}(Q)$

strong coupling parameter of the strong interaction $\alpha_{\mathrm{s}}(Q)$

Z equal coupling parameters as the Z^0 boson to fermions, i.e. $\frac{\alpha_{\mathrm{em}}(Q)}{4\sqrt{\sin^2\vartheta_{\mathrm{W}}\cdot\left(1-\sin^2\vartheta_{\mathrm{W}}\right)}}$

higgs equal coupling parameters to fermions as the Higgs boson in the Standard Model $\frac{g\cdot m_{\mathrm{f}}(Q)}{2\cdot m_{W^\pm}}$

constant constant coupling parameter with a configurable value.

In addition, two parameters (`ResonanceParity`, `ResonanceGamma5Parity`) specify the parity p and γ_5-parity p_5 of the resonance in each vertex object. These parameters are used to define its couplings to the left- and right-handed components of quarks which are scaled by $\left(p-p_5\right)$ and $\left(p+p_5\right)$ respectively. In case of a Z^0 boson coupling, the parities are multiplied by the vector or axial vector couplings of fermions to the Z^0 boson. The parity parameters may also be used to scale up or down the coupling strength. This way, enhanced or decreased couplings can be studied which deviate from the respective coupling strength of the Standard Model.

Additional parameters are provided to define the type of outgoing quarks (`QuarkType`) or switch on or off some of these diagrams. It is possible to switch off all Standard Model QCD processes (`QCDdiagrams`), so that only resonance diagrams are included. On the other hand, if the resonance is switched off (`Resonance`), only QCD production processes of heavy quark pairs are included. Interferences between both types of processes can only occur if both types are switched on. Two options specify which initial states to be included, one switch for gluon-gluon scattering (`GluonScattering`) and one for quark-antiquark scattering (`QQbarScattering`).

Remaining options specify the minimal value of the invariant mass of the outgoing quarks (`InvMassLimit`) and the verbosity of output of the different modules of the Heavy Quark Resonance Model (`DebugLevel`).

module	parameter	values	description
model	`DebugLevel`	0–3	verbosity level
vertices	`CouplingType`	`em`	electromagnetic coupling
$q\bar{q} \to R$ / $gg \to R$		`strong`	strong coupling
scalar/vector		`higgs`	SM Higgs coupling
		`Z`	Z coupling
		`constant`	constant coupling
	`ResonanceParity`	float	strength of vector coupling
	`ResonanceGamma5Parity`	float	strength of axial vector coupling
	`DebugLevel`	0–3	verbosity level
matrix element	`QuarkType`	1–6	type of outgoing quarks (1: down, ..., 6: top)
	`QCDdiagrams`	`on/off`	switch for QCD diagrams
	`Resonance`	`on/off`	switch for resonance diagrams
	`GluonScattering`	`on/off`	switch for gluon scattering
	`QQbarScattering`	`on/off`	switch for $q\bar{q}$ annihilation
	`InvMassLimit`	float	minimum invariant mass
	`DebugLevel`	0–3	verbosity level

Table 3.3: *Configurable parameters of the $q\bar{q}$ resonance model. These options determine couplings of the resonance to gluons and quarks of the Standard Model.*

4 Proton-Proton Collisions at the Large Hadron Collider

"The real voyage of discovery consists of
not in seeking new landscapes
but in having new eyes."
— Marcel Proust

High energy particle collisions with a centre-of-mass energy of several T*e*V require extraordinary effort. There are only few research facilities being able to address all technical and logistic difficulties, the two most important ones being Fermilab near Chicago in the United States of America and CERN near Geneva in Switzerland. The task is usually divided into several portions. The research facility provides the accelerator and high energy particle beams colliding at defined interaction points. Research institutes from all over the world cooperate to build particle detectors at these interaction points to measure, reconstruct and analyse these collisions. Simulations of particle collisions and the analysis of gathered data is processed in a large distributed computing network called the *grid*.

4.1 The Large Hadron Collider

The *Large Hadron Collider* (LHC) [103] at CERN near Geneva is one of the most complex machines ever built in human history. It is able to collide two beams of protons with

a centre-of-mass energy of $\sqrt{s} = 7\,\text{TeV}$, but is even designed for $\sqrt{s} = 14\,\text{TeV}$. The accelerator will reach its design energy after a future upgrade.

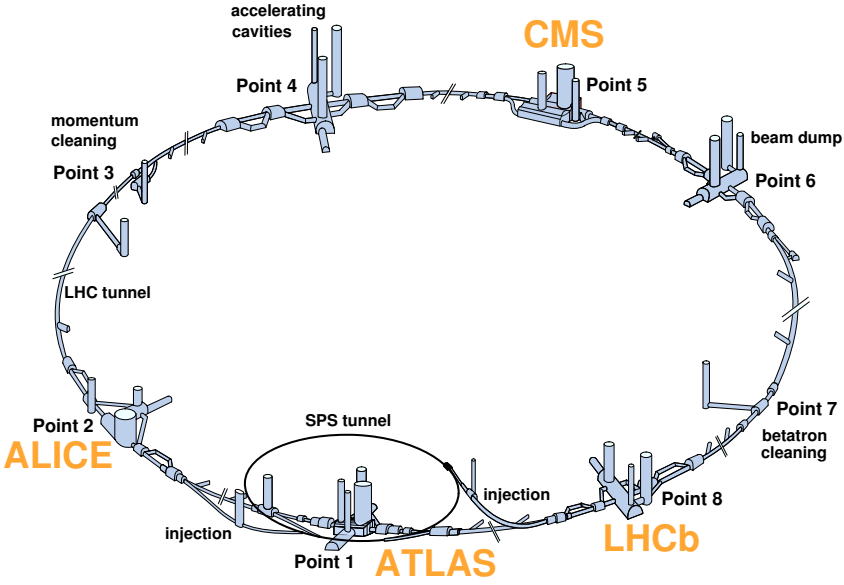

Figure 4.1: *Schematic layout of the* LHC *accelerator ring [104]. Protons are injected in opposite direction from the* SPS *accelerator via two transition lines. The two beams collide inside the four main detectors* ATLAS, ALICE, CMS *and* LHC*b. When needed, the beams are extracted into two beam dump areas, preventing any damage to the infrastructure.*

The Large Hadron Collider as shown in figure 4.1 is the last piece in a chain of accelerators. Each machine accelerates protons to higher energies. The LHC gets its protons from the *Super Proton Synchrotron* (SPS) with an initial energy of 450 GeV. The Large Hadron Collider is a circular syncho-cyclotron accelerator of 26.66 km in circumference, located in a tube 100 m underground in average. It accelerates two beams of protons, running in opposite directions through separate beam pipes. They are kept on circular tracks by 1232 superconducting dipole magnets with a magnetic field of up to $B = 8.6\,\text{T}$. They are cooled down to a temperature of $T = 1.9\,\text{K}$ with superfluid helium. A cross section of a typical dipole magnet is shown in figure 4.2. In addition, there

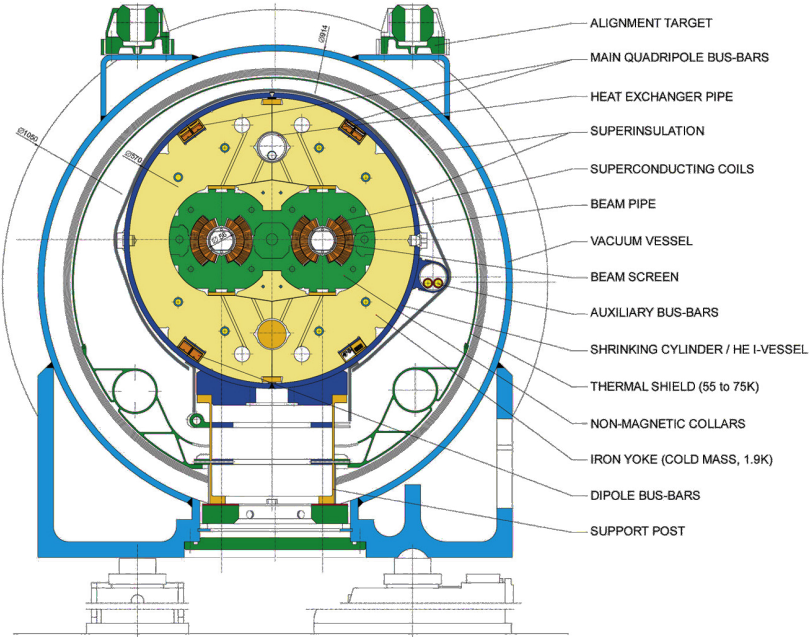

Figure 4.2: *Cross section of a typical* LHC *dipole magnet [105]. The proton beams circulate in two separate beam pipes. Superconducting magnets keep them on a circular orbit. All dipole magnets provide an iron yoke to insulate the magnetic field and several layers of thermal shielding to keep all magnets at a temperature of 1.9 K.*

are more than 6000 quadrupole, sextupole, octopole and decapole magnets building a magnetic lensing system to focus the beams.

The collider ring is divided into eight sectors connecting eight special insertions (IR) in the beam line, each one dedicated to the ATLAS and LHCf experiments (IR1), the ALICE experiment (IR2), momentum cleaning (IR3), accelerating cavities (IR4), the CMS and TOTEM experiments (IR5), the beam dumps (IR6), betatron cleaning (IR7) and the LHCb experiment (IR8).

The protons are bundled in 2808 *bunches* of about 10^{11} particles each. At four interaction points (IPs) these bunches are squeezed to a diameter of 20 µm and a length of 8 cm and brought to collision at a crossing angle of 300 µrad. Subsequent bunches

are displaced by a distance of about 7.5 m, resulting in a collision rate of 40 MHz, i.e. every 25 ns.

The performance of an accelerator is summarised in a quantity called *instantaneous luminosity* $\mathscr{L}_{\text{inst}}$. It is a measure for the number of collisions per area and time interval. Multiplied with a cross section for a specific type of process, the instantaneous luminosity relates to the expected rate of events of this type

$$\frac{dN}{dt} = \mathscr{L}_{\text{inst}} \cdot \sigma \,.$$

The LHC accelerator is designed to provide proton-proton collisions with an instantaneous luminosity of $\mathscr{L}_{\text{inst}} = 10^{34} \frac{1}{\text{cm}^2 \cdot \text{s}}$. At a centre-of-mass energy of 14 TeV the cross section for top quark pairs is estimated to be $\sigma_{t\bar{t}}(14\,\text{TeV}) \approx 880\,\text{pb}$. Given these numbers, the LHC will produce 10 $t\bar{t}$ events per second which is more than any other accelerator in the world is able to provide, which is why the LHC is often called a "top quark factory".

Pairs of top quarks can be produced either via quark-antiquark annihilation or gluon scattering. With two proton beams at the LHC top quark pair production is dominated by gluon scattering as the contribution of antiquarks in a proton has to be provided completely from sea quarks (cf. figure 3.5). Therefore, top quark pairs at the LHC originate from quark-antiquark annihilation in only about 10 % whereas gluon scattering contributes with about 90 %.

The six main experiments at the LHC are built at four interaction points. The ATLAS detector and the CMS experiment are general purpose detectors surrounding their respective interaction points. They are designed to track all fragments of a collision to achieve a reconstruction of all events provided by the accelerator.

The ALICE detector is a specialised experiment for heavy ion collisions, which replace the proton collisions in regular intervals. Collisions of heavy ions provide a high density of nuclear matter. The experiment will study the plasma of quarks and gluons where even coloured partons are able to behave as free particles.

The LHCb detector is specialised to processes including bottom quarks. Among other topics, LHCb will studies the asymmetry between matter and antimatter and CP violating processes induced by the complex phase parameter of the CKM matrix.

Two smaller experiments are located at a greater distance to IP1 and IP5. The LHCf experiment studies particle scattering at small angle and the TOTEM detector measures the total elastic and diffractive cross sections.

4.2 The ATLAS Experiment

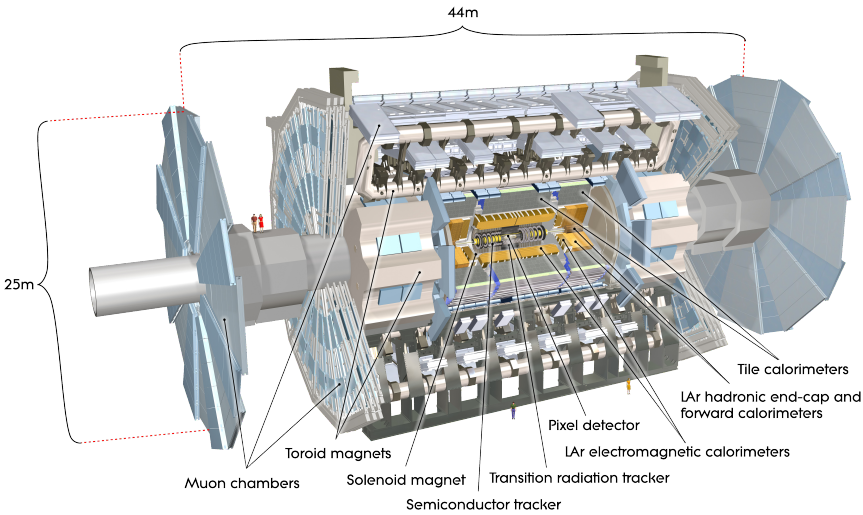

Figure 4.3: *Elevation of the ATLAS detector [106]. Most of its volume is occupied by the large magnetic coils for the toroidal magnetic field and the muon spectrometer system. The big wheels of muon detectors give ATLAS an overall length of 44 m and a diameter of 25 m.*

The ATLAS experiment is located at interaction point 1 (IP1) of the LHC ring, 100 m below surface. The detector is 44 m long and spans 25 m in diameter as shown in figure 4.3. It is designed as a cylindrical structure with several layers of subdetectors for different purposes surrounding the beam pipe. This central part of the detector is called the *barrel* region. At both ends, additional cylindrical *end-caps* cover the forward regions close to the beam pipe.

According to the cylindrical layout of the detector, two common coordinate systems have been introduced to identify positions relative to the interaction point. The right-handed Cartesian coordinate system (x, y, z) is defined by the positive x-axis pointing from the interaction point to the centre of the LHC ring and the positive y-axis pointing upwards. In this system the z-axis is identical with the beam axis.

The second, cylindrical coordinate system (ϱ, η, φ) is motivated by kinematic properties of massless particles. ϱ is the distance from the beam pipe. The azimuthal angle

particle	tracking system	electromagnetic calorimeter	hadronic calorimeter	muon spectrometer
muon	✓	✓	–	✓
photon	–	✓	–	–
charged hadron	✓	–	✓	–
neutral hadron	–	–	✓	–
electron	✓	✓	–	–
neutrino	–	–	–	–

Table 4.1: *Signatures of particles in the subdetectors. Different types of particles leave a characteristic combination of signals in the subdetectors. Neutrinos leave the detector without any signals.*

φ relates to the direction orthogonal to the beam axis with $\varphi = 0$ pointing in the direction of the positive x-axis. The polar angle ϑ is measured towards the positive z-axis. The *pseudorapidity* is defined as

$$\eta = -\ln\left[\tan\left(\frac{\vartheta}{2}\right)\right].$$

For massless particles the pseudorapidity is identical with the rapidity $y = \operatorname{artanh}\frac{v}{c}$, for which differences in rapidity are invariant under Lorentz boosts along the beam axis.

Figure 4.4 illustrates the structure of different shells of ATLAS and the different signatures of particles passing through the detector. The innermost component is the tracking system. It determines the tracks of charged particles in an axial magnetic field of $B = 2\,\mathrm{T}$ which is generated by a solenoid coil. The charge/mass ratios and momenta of charged particles can be determined from the curvature of their tracks.

The calorimeter system determines the kinetic energies of particles and can distinguish between hadrons on the one hand and leptons or photons on the other hand. The outermost part of ATLAS is a special spectrometer for muons. It is embedded in large toroidal magnetic fields of $B = 0.5\,\mathrm{T}$ in the barrel region and $B = 1\,\mathrm{T}$ in the end-cap region. The large coils for the toroidal magnetic field of ATLAS are the main reason for the huge dimensions of the whole detector.

Types of detected particles can be determined from the combination of signals they leave in the different subdetectors. Table 4.1 shows the characteristic combinations for different types of particles. Neutrinos are the only type of particle that cannot be detected by any subdetector. Nevertheless, their momentum component transverse

to the beam can be calculated from a momentum imbalance of all detected particles because total transverse momentum of all final state particles has to vanish.

4.2.1 The Tracking System

The tracking system depicted in figure 4.5 consists of three subdetectors, the Pixel detector, the *Semiconductor Tracker* (SCT) and the *Transition Radiation Tracker* (TRT). Each subdetector provides a number of points in space where a charged particles has generated a signal. These so called *hits* along the paths of particles are used to calculate their trajectories, also called *tracks*.

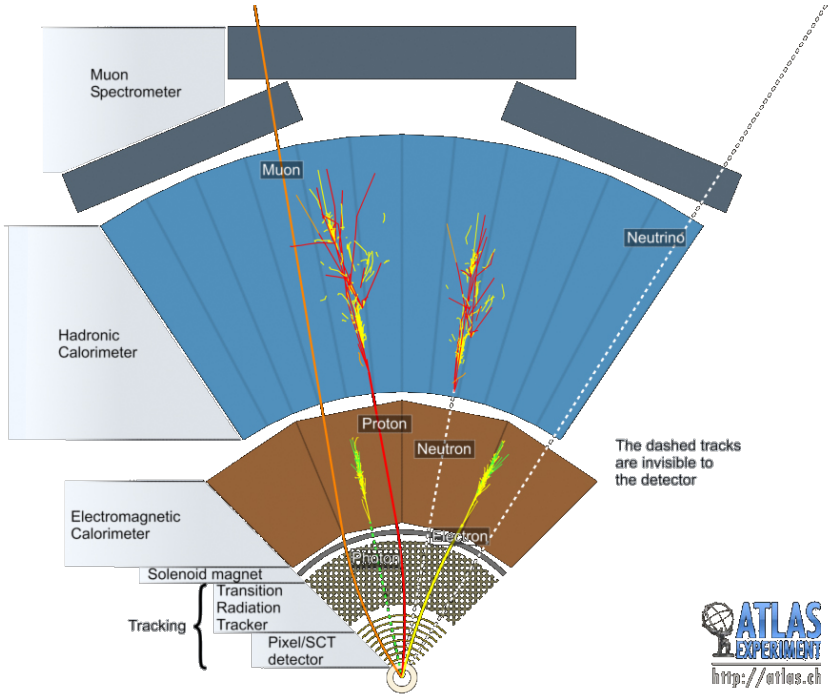

Figure 4.4: *Signatures of different types of particles in the* ATLAS *detector [107, 106]. All types of particles leave a characteristic combination of signals in the subdetectors.*

The Pixel detector has three layers of silicon semiconductor pixels, operated as diodes in reverse direction, which are 400 µm×50 µm in size. Particles passing through the material produce pairs of electrons and holes. These can be measured as an electrical signal. As the innermost subdetector the Pixel detector provides three hits close to the primary collision vertex for each charged particle. With this information it is possible to reconstruct the origins of charged particle tracks with an accuracy of about 11 µm [106] in the x-y-plane. This resolution is especially needed for studies involving bottom quarks. Because of their long lifetime, hadrons with bottom quarks are able to decay several millimetres away from the primary vertex. A secondary vertex indicates the presence of heavy particles decaying via the weak interaction. As bottom quarks, which may originate from top quark decays, have a rather long lifetime, a secondary vertex from their decay is useful to identify top quark events.

The Semiconductor Tracker consists of similar silicon semiconductor cells, of which each is about 60 µm×10 cm in size. The operating principle is the same as for the Pixel detector. The SCT provides four additional hits in the central region of the detector and up to nine hits in the end-cap region.

The Transition Radiation Tracker consists of about 170000 straw tubes of 4 mm in diameter, i.e. gas-filled drift chambers, with intermediate layers of polypropylene as

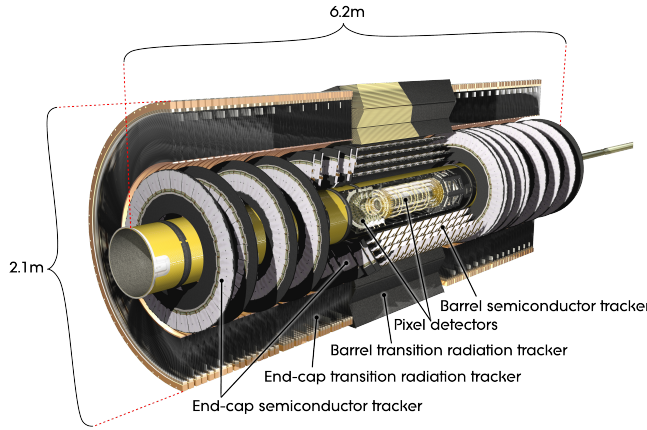

Figure 4.5: *Elevation of the ATLAS inner detector [106]. It consists of the Pixel detector, surrounded by the Semiconductor Tracker and the Transition Radiation Tracker as the outermost subdetector.*

radiator material. Charged Particles ionise gas atoms. Released electrons are accelerated by a high electrical voltage. An avalanche of electrons is produced which can be detected as an electrical signal. Electrons additionally are able to emit transition radiation. When they pass the border of the radiator material, transition radiation is emitted because of a change in the optical refraction index. Generated photons also produce a measurable signal inside the straw tubes. The Transition Radiation Tracker is able to provide an average of 36 additional hits for track reconstruction. As electrons emit more radiation than other types of charged particles, the TRT is also used to identify electrons.

4.2.2 The Calorimeter System

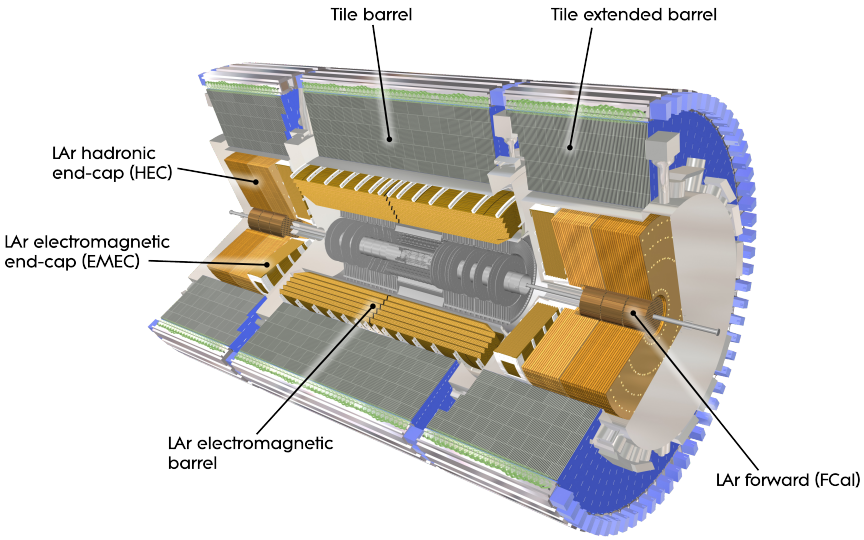

Figure 4.6: *Elevation of the ATLAS calorimeters [106]. The electromagnetic calorimeter is surrounded by the hadronic calorimeter. Both types of calorimeters consist of a barrel and an end-cap part. Forward calorimeters cover the the region of small scattering angles near the beam pipe. The grey part in the centre is the tracking system.*

The ATLAS calorimeters shown in figure 4.6 determine the total energies of electrons, photons and hadrons. They are all designed as *sampling calorimeters*, i.e. they consist

of several layers of absorber material with intermediate layers of detection material. The absorber generates showers of particles which are detected by the detection layers. The combinations of absorber and detector materials for the different parts of the calorimeters as well as their energy resolutions are summarised in table 4.2.

calorimeter	absorber	detector material	energy resolution $\frac{\sigma_E}{E}$
EM barrel [108]	lead	liquid argon	$10.1\,\% \frac{\sqrt{\text{GeV}}}{\sqrt{E}} \oplus 0.17\,\%$
EM end-cap [108]	lead	liquid argon	$10.1\,\% \frac{\sqrt{\text{GeV}}}{\sqrt{E}} \oplus 0.17\,\%$
FCal1 [109]	copper	liquid argon	$28.5\,\% \frac{\sqrt{\text{GeV}}}{\sqrt{E}} \oplus 3.5\,\%$
hadronic Tile [110]	steal	plastic	$159\,\% \frac{\text{GeV}}{E} + 52.05\,\% \frac{\sqrt{\text{GeV}}}{\sqrt{E}} \oplus 3.02\,\%$
hadronic end-cap [106]	copper	liquid argon	$70.6\,\% \frac{\sqrt{\text{GeV}}}{\sqrt{E}} \oplus 5.8\,\%$
FCal2 [109]	tungsten	liquid argon	$94.2\,\% \frac{\sqrt{\text{GeV}}}{\sqrt{E}} \oplus 7.5\,\%$
FCal3 [109]	tungsten	liquid argon	$94.2\,\% \frac{\sqrt{\text{GeV}}}{\sqrt{E}} \oplus 7.5\,\%$

Table 4.2: *Components of the ATLAS Calorimeter and their energy resolutions [106]. Relative energy resolutions as a function of energy is given by a constant, a stochastic term ($\sim 1/\sqrt{E}$) and a noise term ($\sim 1/E$).*

In general, electromagnetic calorimeters have a better energy resolution than hadronic calorimeters, because electrons and photons interact extensively with the electrons in the detector material via the electromagnetic force. By scattering with electrons from the absorber or detector material, they are rapidly decelerated, distributing their kinetic energy among many electrons of the material. While being decelerated, they heavily radiate electromagnetic bremsstrahlung. The emitted photons produce more electrons and positrons by pair production until their available energy is smaller than $2m_e$.

Calorimetry of hadrons in general is more difficult than for electrons or photons. Although hadrons also scatter with electrons of the material, they hardly loose energy, because hadrons are several hundred times heavier than electrons. Thus, they also hardly radiate bremsstrahlung.

Hadrons most efficiently loose energy in inelastic reactions with nuclei of the absorber material via the strong interaction. As the hadronic interaction length is in general larger than the electromagnetic radiation length, hadronic calorimeters have to be larger than electromagnetic calorimeters in order to capture all secondary particles produced in the shower.

Products of nuclear reactions contain many secondary hadrons such as π^0 mesons which mostly decay into photons. Thus, a hadronic shower is often accompanied by an electromagnetic shower from decaying pions. These sub-showers are much easier to detect than hadronic showers. Measured signals from electromagnetic showers have to be corrected in order not to overestimate determined hadronic energies. In hadronic showers, a part of the initial energy cannot be measured because it is lost for nuclear fissions or in neutrinos and muons leaving the active detector volume. These effects further reduce the resolution of hadronic calorimeters.

4.2.3 The Muon Spectrometer

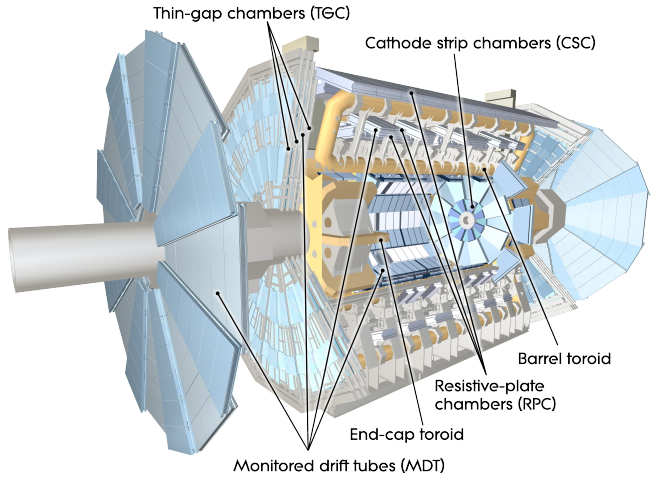

Figure 4.7: *Elevation of the* ATLAS *muon chambers [106]. Four types of detectors are used to account for different intensities of radiation and focus on spacial or temporal resolution.*

Muons are long lived particles which, in general, are not stopped by the inner detector or the calorimeters. As such, their energy cannot be determined by the electromagnetic or hadronic calorimeter. The muon chambers are the outermost part of the ATLAS detector. To determine the energies and momenta of muons accurately three layers of muon chambers are embedded into a large toroidal magnetic field to bend the trajectories of the muons.

type	function	spacial resolution			temporal resolution
		R	z	φ	[ns]
MDT	tracking		35 µm		≈700
CSC	tracking	40 µm	–	5 mm	7
RPC	trigger	–	10 mm	10 mm	1.5
TGC	trigger	2-6 mm	–	3-7 mm	4

Table 4.3: *Spacial and temporal resolutions of the muon detectors [106]. Specifications of spacial resolutions depend on the orientation of the chambers. Components in the barrel region measure (z, φ) coordinates whereas detectors in the end-cap region measure (R, φ) coordinates. Only one spacial resolution is given for the MDTs because they are used in the barrel as well as in the end-cap region.*

In different regions of the detector different techniques and geometries are used to accommodate varying particle fluxes, accuracy and timing constraints. Figure 4.7 shows the position of the *Monitored Drift Tubes* (MDTs), the *Cathode-Strip Chambers* (CSCs), the *Resistive Plate Chambers* (RPCs) and the *Thin Gap Chambers* (TGCs). All muon detectors operate as charged capacitors in which a crossing muon causes a discharge, generating a measurable electrical signal. Their spacial and temporal resolutions are listed in table 4.3.

The MDTs and CSCs offer a precise spacial resolution, but a limited temporal resolution, which is why they are used primarily for tracking paths of traversing muons. On the other hand, RPCs and TGCs provide precise timing information, but offer limited spacial resolutions. They are used to associate detected muons to specific events.

Among other parts of the detector, e.g. the calorimeter towers, the TGCs are part of a large trigger system that rapidly selects interesting events from a huge amount of Minimum Bias events. The muon chambers trigger on events with an electromagnetic component.

4.3 The Anti-$k_\perp$ Jet Algorithm

Measured events from a detector consist of several hits of charged particles in the tracking system and energy depositions from electrons, photons and hadrons in the calorimeter system. Muons are detected via hits in the muon chambers. Depositions of energies from the hard process are concentrated in small distinct regions of the detector because of the underlying jet structure of QCD interactions. As these regions spread across many cells of the calorimeter, a clustering algorithm has to identify

groups of adjacent calorimeter cells that have received energy from jets. Such clustering algorithms are called *jet algorithms*.

There are many different jet algorithms and implementations being used by different experiments. They all face two major difficulties when searching for clusters of energy depositions. On the one hand jets have to be stable against small disturbances, i.e. jet clusters should not change under small variations of measured energies in the calorimeter cells. Such disturbances may be caused by additional soft radiation from minimum bias events or finite resolution in energy of the detector. As shown in figure 4.8, soft disturbances are able to change the jet structure of the event. Robust jet algorithms have to be stable against this effect.

On the other hand, as shown in figure 4.9 particles may decay into two particles that deposit their energies into separate calorimeter cells. This may lead to a different configuration of found jets. Nevertheless, the total deposited energy remains the same and reconstructed jets have to remain unchanged. The *Anti-$k_\perp$* jet clustering algorithm [111] is stable against both effects, soft radiation and collinear splitting. Therefore it has been chosen to be used for this study.

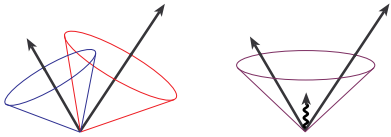

Figure 4.8: *Jet clustering differences with soft radiation [112]. Additional soft particles are able to establish a connection between otherwise distinct jet candidates.*

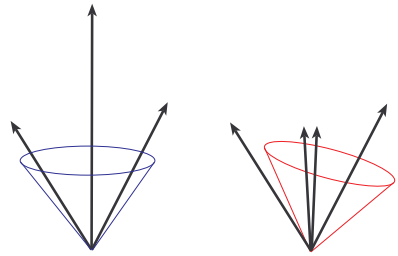

Figure 4.9: *Jet clustering differences with collinear splitting [112]. Splittings are able to shift the direction of jet candidates.*

Jet clustering algorithms can not only be applied to distributions of energy depositions in calorimeter cells but also on lists of particle momenta. During its application momenta are merged iteratively. Resulting jet candidates often are also called *pseudojets*. As particles and pseudojets are treated equally within the algorithm the name *entities* is common as a general expression. The clustering is performed in two steps.

1. All possible distances between all entities and the beam are calculated by

$$\Delta_{ij}^2 = \left(y_i - y_j\right)^2 + \left(\varphi_i - \varphi_j\right)^2 ,$$
$$d_{ij} = \min\left(k_{\perp,i}^{2p}, k_{\perp,i}^{2p}\right) \frac{\Delta_{ij}^2}{R^2} ,$$
$$d_{i\mathrm{B}} = k_{\perp,i}^{2p} .$$

   The distance Δ_{ij} is measured between two entities in the plane spanned by their rapidities y and azimuthal angles φ. Distances are defined in terms of transverse momenta $k_\perp$. The parameter p determines the properties of the metric and is set to $p = -1$ for the Anti-$k_\perp$ algorithm. The parameter R is a weight for the distance between two entities compared to their distance to the beam. A common value is $R = 0.4$, which has also been used for this study.

2. The smallest distance d_{ij} or $d_{i\mathrm{B}}$ is determined. If it is a distance between two entities i and j, they are combined by adding their momenta. If the smallest distance comes out between an entity and the beam, the object i is fixed to be called a jet and removed from the list of entities for the next iteration.

These two steps are repeated until no entities are left and all jets have been defined. The result is a list of momenta of all calculated jets.

4.4 The DELPHES Detector Simulation

The DELPHES [113] package is a free, open source implementation of a detector simulation for general detectors. Its parameters can be adjusted to match the layout of existing and future particle detectors. DELPHES is able to simulate all crucial elements and subtleties of a generic detector, such as

- geometry of both central and forward detectors
- limited energy and spacial resolution of trackers and calorimeters
- the effect of magnetic fields on tracks
- the reconstruction of tracks of photons and charged leptons as well as jets, b-jets, $\tau^\pm$-jets and missing transverse momentum
- a lepton isolation criterion
- a trigger emulation.

It already includes a predefined layout for the ATLAS detector, which has been used for the studies in this work. This setup has been validated to match the expectations to the real ATLAS detector. Although DELPHES does not respect all details of the ATLAS detector, results are comparable to the complete detector simulation with the GEANT simulation software [114], but offers the advantage of being several 100 times faster.

For the reconstruction of jets, DELPHES is able to apply several different algorithms commonly used in collider experiments:

- Cone jet algorithm [115]
- Midpoint Cone algorithm [112]
- Seedless Infrared Safe (SIS) Cone algorithm [116]
- Longitudinally invariant $k_\perp$ jet algorithm [117, 118]
- Cambridge/Aachen jet algorithm [119, 120]
- Anti-$k_\perp$ jet algorithm [111].

For this study, the Anti-$k_\perp$ jet algorithm has been used, because it supersedes the other available algorithms as explained in the previous section.

4.5 The LHC Computing Grid

In recent years the connection of computer clusters into a global computing *grid* has become an important and indispensable tool for many fields of modern science research. Current experiments in high energy physics, such as the ATLAS experiment at the LHC, deliver a huge amount of data that has to be processed and analysed. At its designed performance the ATLAS experiment will create 8 Petabytes of data in each year of operation. In addition, the same amount of data is needed for simulated events from event generators. An efficient analysis would be impossible without a distributed processing as there is no single institute being able to provide all the needed computing power.

The LHC *Computing Grid* (LCG) [121] currently provides the computing power of over 100000 CPUs distributed over 170 participating institutes. Provided storage for data accumulates to several Petabytes of hard disk space.

The general idea behind the grid follows the concept of the grid for electrical power. Computing power should be available everywhere via an ordinary network connection. Computers for the actual calculations are provided by large computing farms, in analogy to electrical power plants. The user just has to specify a task to be processed, the grid takes care of all the management in the background and just provides the final result.

The software providing the connection to and the management of the grid is called *middleware*. The LHC Computing Grid is based on the *gLite* middleware distribution [122]. Tasks of sophisticated or time-consuming calculations are called *jobs*. Each job is described via the *Job Description Language* (JDL). A job description includes an executable file and supplementary input files which are packaged into the *input sandbox*. Additional input parameters as well as output files can be specified as a result of the calculation. These can be received via the *output sandbox*. The Job Description Language also provides the possibility to package many sub-jobs into one job description so that a large computation can be checkpointed or split into smaller parts. There are also various additional options to further constrain the computing task, but they are usually not needed for an average job.

Access to all grid resources is provided by a special front end computer called the *user interface* (UI). Figure 4.10 illustrates the different stages of a job in the grid.

- The job is first submitted to the *Workload Management System* (WMS) which holds a list of all *Computing Elements* (CEs) available in the grid, along with their current workload and usage.
- The WMS selects a suitable computing element with a low workload to process the job. The WMS holds a job status for each of its jobs, so that users can query the current status of their jobs. Additional information is provided by the *Logging and Bookkeeping Service* (LB) which is also useful for debugging purposes in case of errors with aborted jobs.
- The Computing Element is connected to a Batch System which holds one or more queues of jobs to be processed. The CE can be considered a a front end interface which connects the Batch System to the grid.
- The Batch system is able to schedule jobs according to different criteria of priority. A *fair share algorithm* is used with the goal to distribute available computing time fairly among all users or groups of users.
- When a free slot in the computing cluster is available, the Batch System sends the job to a *Worker Node* (WN) which reads the information from the job description file, unpacks the input sandbox and starts processing the task. If needed, the job is able to fetch additional files of data from a *storage element* which provides large amounts of disk space.
- After the job has finished, the output sandbox is sent back to the Workload Management System where the user can fetch the final result from.

With growing capacity and user communities, called *virtual organisations* (VOs), security of data is an important topic. Security is provided by the requirement of authenticated network connections in every action in the grid framework. Every user, service

and host has to authenticate himself/itself towards any other participant or component via certificates following the X509 standard [123]. This way, every instance is able to check the identity of other participants of the grid infrastructure.

Each user has to authenticate himself in order to submit jobs to the grid. Furthermore, also the job itself has to provide a certificate to the grid infrastructure in order to get the permission of being executed. This is done via *proxy certificates*, which are derived from the user's private certificate, but have a restricted time of validity. By

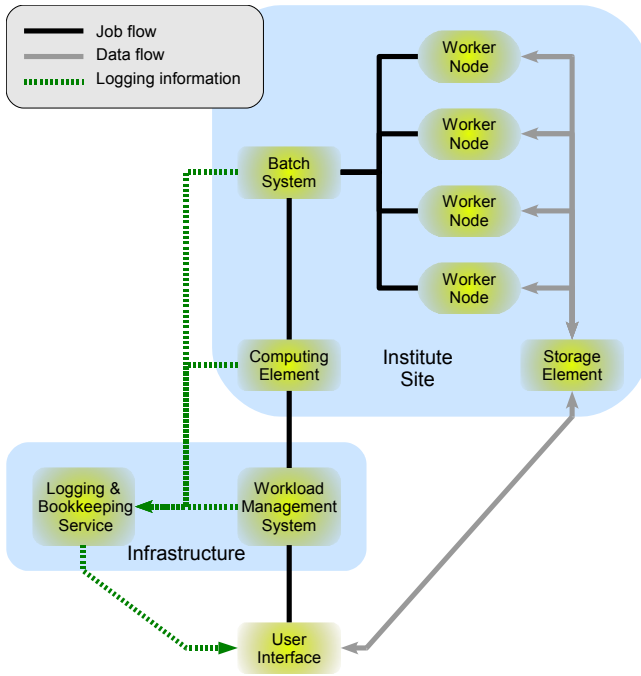

Figure 4.10: *Overview of components of the grid. Jobs are submitted to the Workload Management System (WMS) which delivers them to a suitable Computing Element (CE). A Batch System spreads jobs among available Worker Nodes (WN). Generated data can be stored on attached Storage Elements (SE) from where they can be requested and fetched by users or subsequent jobs.*

default, proxy certificates are only valid for 12 hours after which they cannot be used for authentication any longer.

4.5.1 Data Distribution

Although the idea of the grid is to have no single points of failure, large experiments such as ATLAS are forced to introduce some kind of hierarchy, because huge amounts of data are produced by the experiment which has to be distributed among participating institutes. Therefore, the LCG introduced a hierarchy of distribution centres called *Tiers*. CERN is the Tier-0 centre which stores all raw data of all LHC experiments. For ATLAS these data are stored as *Raw Data Objects* (RDOs). After reconstruction, the event information is converted into *Event Summary Data* objects (ESDs). A fraction of all RDOs and all ESDs are transferred to national Tier-1 centres, where events are filtered and shrunk into *Analysis Object Data* (AOD). All AODs and a fraction of all ESDs is distributed to national Tier-2 institutes, where they are available for user analyses. Event information is further condensed into *Derived Physics Data* (DPD) objects which contain compressed information for final analyses. These small objects make it easy to quickly analyse a large number of events. Table 4.4 shows a list of all Tier-1 and the German Tier-2 centres.

4.5.2 GANGA

The GANGA tool [124] is a front end to manage a list of jobs on the user interface. GANGA is already being widely used in the ATLAS and LHCb communities. It provides an easy to use interface for all common grid actions, including job submission, download of results and job monitoring. GANGA is built in a modular way, so that its functionality can be easily extended via plugins. Extension plugins exist to support the software framework of different experiments, such as ATHENA [125] for the ATLAS collaboration or Gaudi [126] for the LHCb experiment. It also provides options for different grid middlewares, e.g. gLite, Unicore or even a local execution on a user's desktop computer.

Another kind of plugin extends monitoring capabilities. By default, GANGA only checks the status of each job. Other plugins provide a fine-grained monitoring ability, even down to the execution of a single command. The package providing this functionality is the *Job Execution Monitor* (JEM) [127, 128, 129, 130], developed entirely at the University of Wuppertal. It is able to supervise the execution of single commands in script files or binary executables and provides information on running jobs nearly in

Tier 0	Tier 1	German Tier 2
CERN	SARA-NIKHEF (Amsterdam, NL)	Albert-Ludwig University Freiburg
	IN2P3 (Lyon, FR)	University of Wuppertal
	INFN CNAF (Bologna, IT)	DESY Hamburg
	RAL (Didcot, UK)	DESY Zeuthen
	TRIUMF (Vancouver, CA)	Institute for Algorithms and Scientific Computing (St. Augustin)
	FNAL (Chicago, USA)	ITWM (Kaiserslautern)
	GridKa (Karlruhe, DE)	Georg-August University Göttingen
	PIC (Barcelona, ES)	GSI (Darmstadt)
	ICEPP (Tokyo, JP)	Ludwig-Maximilian University & Leibniz Centre for Computing (Munich)
	CERN (Geneva, CH)	Institute for nuclear physics (Heidelberg)
	ASGC (Taipei, TW)	Institute for physics & Computing centre (Garching)
	BNL (Berkeley, USA)	RWTH Aachen University
	NDGF (Scandinavia)	Friedrich-Wilhelm University Bonn
		Technical University Dortmund

Table 4.4: *LCG model of hierarchical analysis centres. Subsequent fractions of data are distributed among 12 national Tier-1 centres. In Germany, the Karlsruhe analysis centre distributes event files among 14 Tier-2 centres at various institutes.*

realtime. This function is provided also as an independent package, so that JEM can be used as a standalone monitoring application.

5 The Job Execution Monitor and the Grid Expert System

"When we dream alone it is only a dream
but when many dream together
it is the beginning of a new reality."
— Friedensreich Hundertwasser

The grid approach of connecting thousands of computers is a powerful tool for providing huge amounts of computing power and data storage to a large number of users. Nevertheless, all components of such a complex compound have to be maintained continuously as they are at risk to a wide variety of errors. The task of discovering such errors and quickly finding solutions to fix them is split into two parts. The first step consists of gathering of information about running jobs and their environment. The *Job Execution Monitor* (JEM) has been developed to supervise the execution of jobs on a Worker Node as well as the status of the Worker Node itself while the job is running.

In a second step, collected information is fed into an expert system which has been developed as part of this work. It is able to find correlations between different jobs and localise the sources of occurring errors. It is also able to suggest possible solutions in case of discovered error conditions.

5.1 Job Monitoring

The grid is an accumulation of a huge number of different computers with different setups, scattered across the world. With large differences among all components of the grid, there are many possibilities of upcoming error conditions which influence the successful processing of jobs.
The available grid middleware offers only limited capabilities for monitoring jobs. The main purpose of the middleware is the transport of the job from a user interface to a worker node and backtransport of its result.
As such, the middleware does not evaluate the result of a processed job. Among the 10 defined states of jobs, shown in figure 5.1, the middleware only knows four possible states for finished jobs which have the following meaning.

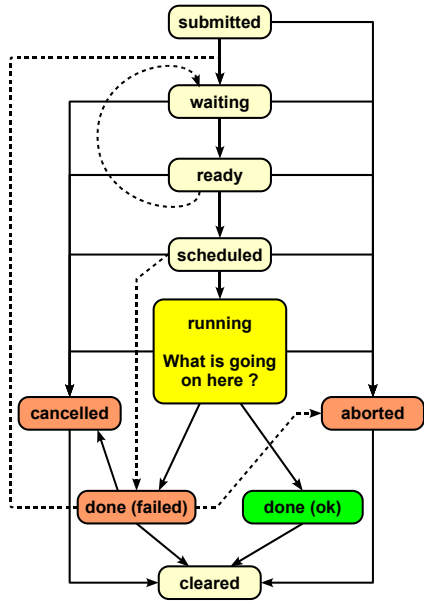

Figure 5.1: *States of a grid job. Successful jobs have to finish into the* ok *state. Error conditions lead to failed jobs.*

ok The job finished successfully. No error was encountered. Nevertheless, it is possible for some commands to fail, but the job is able to continue. A possible scenario is a job of an event generator that wants to copy the generated events to a storage element. If the storage element is unreachable, the file transfer will fail. As the file transfer is not critical to the execution of the job, it could exit successfully although the task is not completed.

failed The job ended in an error condition. If the error did not affect the result of the job or the error occurred after the result was generated successfully, the error could be ignored. This could be the case if the job in the above scenario checked the success of the file transfer. In case of a failed transfer the job could exit with an error message and a non-zero exitcode.

cancelled The job was cancelled by the user before it was finished. This is not a severe error condition because the user knows the reason for cancelling the job.

aborted An error condition occurred which prevented the job from being executed. This is the most severe error condition because all data of a job is deleted. No output sandbox can be received and no further information is available about the status of the job. A possible scenario for this condition is an expired proxy certificate. After expiration the job has lost its permission to receive grid resources and is aborted.

In about 15-20 % of all cases, a job is not able to finish successfully. Job errors can be divided into two categories, depending on who is responsible for the failure. Job errors may be caused by fault-intolerant programs that do not check for unexpected conditions. Such programs quickly run into error conditions that cannot be recovered any more, e.g. a *segment violation*. A second source of errors comes from the environment, which can run out of resources, e.g. a worker node does not have any space left on a hard drive. Such site errors may indicate a failure in hardware or the need for a reconfiguration of the system infrastructure. Both types of errors cause the job to be aborted because the failure prevents a further execution. In case of aborted jobs, the output sandbox cannot be retrieved, so that no information is available on the actual reason for a failed job.

5.2 The Job Execution Monitor

In order to determine the source of an error, detailed information about the execution of the job is needed. This information has to be collected and made available during the runtime of the job, because it is not possible to recover any information from an aborted job. For this purpose, the Job Execution Monitor [131, 127, 128, 129, 130] was developed at the University of Wuppertal. It is a tool that is able to monitor and keep track of the execution of single commands of a job. Initially designed to execute script files command by command, it is now also able to monitor the execution of precompiled binary programs at the level of single commands. With these features, every command can be checked on its success while it is executed. In case of a failed command, detailed information can be provided on the history of preceding commands so that the source of the failure can be easily traced and identified.

5.2.1 Requirements

The Job Execution Monitor is a tool intended to be used by an ordinary grid user. As such, it has to meet several requirements in order to be accepted.

transparency All jobs monitored by JEM have to run in exactly the same way as without JEM. The Job Execution Monitor is not allowed to change the behaviour or the result of a job. In an ideal situation, the user does not even notice his jobs being monitored.

robustness It is the aim of JEM to discover and report failures in a user's job. As the error rate does not have to be increased by JEM, it has to be prevented from generating additional errors. For this reason, there is a *fallback mode* in case of errors with JEM itself. An internal error forces JEM to be disabled and the job is executed without additional monitoring. This ensures a safe job execution without additional failures.

user-friendliness An important criterion for the acceptance of JEM is its ease of use. All controls have to be kept as simple as possible so that users can learn quickly how to use it. With the integration into the GANGA environment, initially implemented by Martin Rau [132], JEM can be invoked by just one switch in the GANGA interface. Job information is collected in the background and provided to the user.

modularity With future extensions in mind, e.g. additional features or bugfixes, the system had to be built in a modular way so that changes to one module do not affect other modules. Another advantage is an easy way to add or remove different components such that the user has the option to choose which components of his job should be supervised, i.e. it is possible to define which script languages should be monitored.

shell scripts A typical job usually does not start with a binary executable, but with a shell script which is responsible for setting up the environment for the main executable. This includes setting environment variables or downloading files of data. As many errors are known to occur in this setup, JEM has to be able to supervise the success of shell script commands.

Python scripts The ability of monitoring Python scripts was a request of the High Energy Physics Community Group (HEPCG). A large fraction of analysis frameworks of the LHC experiments, such as ATHENA or Gaudi, are written in Python. There are also many modules written or modified by users, which are therefore prone to errors. Thus, the JEM substantially benefits from the ability of monitoring Python scripts.

In its current state, all of these requirements have been fulfilled and even surpassed in some aspects.

5.2.2 Structure

The Job Execution Monitor consists of two main parts, one on the user interface and another part which is submitted together with the job to the worker node, like it is shown in figure 5.2. The JEM introduces several new actions to the usual processing of a job. When JEM is used, a job is processed according to the following steps which are presented for an ATHENA job, but are also valid for any other type of job.

- The user defines a job. This can be done with a framework like GANGA or by writing the JDL file by hand.
- Before submission, the job description is modified. The worker node modules of JEM are added to the input sandbox and the initial command of the job is changed to first execute JEM which in turn starts the user's job. After job modifications are complete, the job is submitted to the WMS as usual.
- A receiver for monitoring information has to be started on the user interface. This is either done automatically by GANGA or can be done manually. The receiver records monitoring information and provides it to subsequent modules for further processing or analysis.

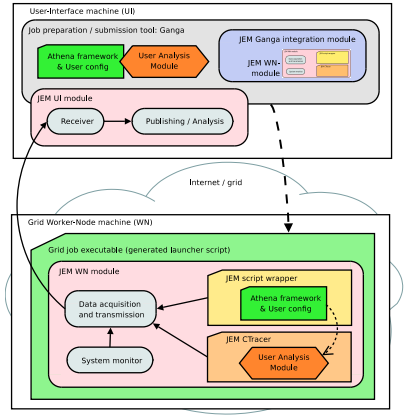

Figure 5.2: *Scheme of the Job Execution Monitor [133]. Monitoring modules are added to a job on the user interface, which supervise the execution of the job on a worker node.*

- On the worker node, JEM is started as the first executable. Before the actual job is launched, JEM starts the system monitors to record resources of the worker node and the module for data acquisition and transmission.

- JEM starts the user's job. Script files are executed and supervised by the script wrapper module where all parameters and return values of script commands can be monitored. Binary executables written in C/C++ can be supervised by the CTracer module if they have been compiled accordingly.

- Monitored information is collected by the acquisition and transmission module which sends it to the appropriate receiver on the user interface. This way, the user can get realtime information about all jobs currently executed. In case of an error, the user can revisit the last commands, their parameters and return values which can give hints about the reason for the failure.

The current structure of JEM consists of many modules of which each is responsible for a special task. The main modules are described briefly in the following list.

Bash Wrapper After first implementations of a Bash interpreter by Dimitri Igdalov [134] and Ahmad Hammad [135], Andreas Baldeau introduced a new approach to monitor Bash scripts with a slightly modified version of the Bash shell [136]. It is extended with a module that reports all commands to be executed in advance and after they have finished along with all input variables, command line arguments, return values, exitcodes, inputs from the `stdin` and outputs to the `stdout` and `stderr` streams.

Python Wrapper The Python wrapper originally was introduced by Joachim Clemens. It is able to monitor a given Python script through the tracing capability of Python. Available types of monitoring data include function calls and returns, exceptions, current values of local variables, and the currently executed line of code.

GANGA interface The integration of JEM into the GANGA framework has been achieved by Martin Rau [132]. When defining a job description, an additional option has been introduced to automatically include JEM with the job.

CTracer Tim dos Santos extended the ability of JEM to not only monitor the execution of script files, but also supervise the execution of binary executables, written in C/C++.

System Monitor The System Monitor is a component which runs in parallel to the user's job. It is responsible for watching the environment and system resources. Monitored quantities include

- processor workload,
- incoming network traffic (summed over all network interfaces),
- outgoing network traffic (summed over all network interfaces),
- available memory,
- available space in home directories,
- available space in `/tmp`,
- available space in the current working directory,
- partitions with less than 100 kBytes of available space.

```
mame@charm:~> voms-proxy-init --voms atlas
Enter GRID pass phrase:
Your identity: /O=GermanGrid/OU=UniWuppertal/CN=Markus Mechtel
Creating temporary proxy ..................................................... Done
Contacting  voms.cern.ch:15001 [/DC=ch/DC=cern/OU=computers/CN=voms.cern.ch] "atlas" Done
Creating proxy ................................................................ Done
Your proxy is valid until Mon Sep  6 23:37:11 2010

mame@charm:~> export GANGA_CONFIG_PATH=GangaJEM/JEM.ini

mame@charm:~> /griddata/gridsoft/local/muenchen/ganga/install/5.5.12/bin/ganga

*** Welcome to Ganga ***
Version: Ganga-5-5-12
Documentation and support: http://cern.ch/ganga
Type help() or help('index') for online help.

This is free software (GPL), and you are welcome to redistribute it
under certain conditions; type license() for details.

In [1]:
```

Figure 5.3: *Initialisation of* GANGA. *A proxy certifivate is needed to submit jobs to the grid.* GANGA *provides a comfortable command line interface, which supports Python syntax for commands.*

With this information it is possible to discover job failures which may not be caused by the job itself, but because of insufficient system resources.

The core system in its current state has been implemented by Stefan Borovac. Collected data of all components are sent to the central communications module which sends all information to a listener module on the user interface where messages are decoded and provided to the user.

5.2.3 Usage

The integration of the Job Execution Monitor into the GANGA framework makes it easy to use. The following steps show how to define, run and monitor a simple job with JEM using GANGA.

Starting Ganga Initial steps are shown in figure 5.3. First a grid proxy certificate has to be derived from the user's grid certificate. This is done via the `voms-proxy-init` command on the user interface. The job is allowed to run as long as the proxy certificate is valid. The optional argument `--voms atlas` stores the user's membership in the virtual organisation `atlas` inside the proxy certificate. Additionally, the environment variable `GANGA_CONFIG_PATH` has to be set, so that GANGA is able to find the configuration file of JEM. After that, GANGA can be started from the command line as usual.

Job Definition The job has to be defined in GANGA as shown in figure 5.4. The first step is to define the middleware. In this case, the job is submitted to the grid

```
In [1]:j = Job()

In [2]:j.backend = LCG()

In [3]:j.backend.middleware = 'glite'

In [4]:j.application = Executable()

In [5]:j.application.exe = File("test-prime-numbers.sh")

In [6]:j.application.args = ["100"]

In [7]:j.inputsandbox = ["test-prime-numbers.py"]

In [8]:j.info.monitor = JobExecutionMonitor()

In [9]:j.info.monitor.realtime = True

In [10]:j.info.monitor.advanced.bashmonitor.disable = False

In [11]:j.info.monitor.advanced.pythonmonitor.disable = False

In [12]:j.info.monitor.advanced.ctracer.disable = True

In [13]:j.submit()
Ganga.GPIDev.Lib.Job               : INFO     submitting job 27
Ganga.GPIDev.Lib.Job               : INFO     job 27 status changed to "submitting"
GangaJEM.Lib.JEM.out               : INFO     Enabling JEM monitoring for job 27.0
Ganga.GPIDev.Adapters              : INFO     submitting job 27 to LCG backend
GangaJEM.Lib.JEM.out               : INFO     The Job Execution Monitor is active for this job.
GangaJEM.Lib.JEM.out               : INFO       Please consider providing (positive and/or negative) feedback of your user experience
GangaJEM.Lib.JEM.out               : INFO       with GangaJEM - visit https://svn.grid.uni-wuppertal.de/trac/JEM for that. Thanks :)
GangaJEM.Lib.JEM.out               : INFO     The JEM realtime monitoring listener has been started for job 27.
Ganga.GPIDev.Lib.Job               : INFO     job 27 status changed to "submitted"
Ganga.GPIDev.Lib.Job               : INFO     job 27 status changed to "submitted"
Out[13]: 1

In [14]:
```

Figure 5.4: *Job definition and submission via* GANGA. *After the job is defined, the Job Execution Monitor is added to the job description.*

via the gLite middleware. Secondly, the job itself is configured by defining the executable file, the command line arguments to the executable and additional files to put into the input sandbox. After that, the job monitoring is configured by activating the Bash and Python monitors of JEM. Finally, the job is submitted to the grid.

Job Monitoring Running jobs can be monitored within GANGA. Apart from the usual commands of GANGA for monitoring jobs, JEM provides mechanisms to view job outputs, executed commands, occurring exceptions and other data at runtime. Figure 5.5 just shows three possible monitoring commands including a snapshot of the current job output.

The Job Execution Monitor provides the ability to monitor the execution of every command executed on the worker node. This information provides valuable data to check the state of jobs while they are still running. Future versions of JEM, as they are being developed by Tim dos Santos, are planned to provide also a graphical view of monitoring information. With this tool, it is also possible to check system resources during

```
In [69]:jobs
Out[69]:
Registry Slice: jobs (8 objects)
--------------
    fqid |    status |      name | subjobs |    application |        backend |                            backend.actualCE
-------------------------------------------------------------------------------------------------------------------------
      20 | completed |           |         |     Executable |            LCG |gridittce01.na.infn.it:2119/jobmanager-lcgpbs-
      21 | completed |           |         |     Executable |          Local |                charm.physik.uni-wuppertal.de
      24 |   running |           |         |     Executable |            LCG |lcgceatlas.dnp.fmph.uniba.sk:2119/jobmanager-
      26 | completed |           |         |     Executable |            LCG |lcg-ce.rcf.uvic.ca:2119/jobmanager-lcgpbs-gen
      27 | submitted |           |         |     Executable |            LCG | ce07.pic.es:2119/jobmanager-lcgpbs-glong_sl5

In [70]:jobs(26).info.monitor.getStatus()
GangaJEM.Lib.JEM.out                : INFO     Job execution finished. No new data will be received.
GangaJEM.Lib.JEM.out                : INFO     current job status
-------------------------------------------------------------------------------------------------------------------------
status (middleware)                 : Done (Success)
status (user application)           : Finished
job-id                              : https://glite-wms.physik.uni-wuppertal.de:9000/PrEyXwXSjjjkxUrI4ZSniQ
compute element                     : lcg-ce.rcf.uvic.ca:2119/jobmanager-lcgpbs-general
exceptions logged                   : 1


In [71]:jobs(26).info.monitor.peek(50)
GangaJEM.Lib.JEM.out                : INFO     Job execution finished. No new data will be received.
GangaJEM.Lib.JEM.out                : INFO     peeking at output (last 50 of stdout, skipping 0)
-------------------------------------------------------------------------------------------------------------------------
(31   ) 12:27:36.344 | calculating prime numbers from 1 to 100
(30   ) 12:27:36.731 | Initialising...
(29   ) 12:27:36.752 | Running...
(28   ) 12:27:36.757 | prime numbers from 1 to 100
(27   ) 12:27:36.763 | 2
(26   ) 12:27:36.768 | 3
(25   ) 12:27:36.773 | 5
(24   ) 12:27:36.778 | 7
(23   ) 12:27:36.783 | 11
(22   ) 12:27:36.788 | 13
(21   ) 12:27:36.793 | 17
(20   ) 12:27:36.798 | 19
(19   ) 12:27:36.803 | 23
(18   ) 12:27:36.808 | 29
(17   ) 12:27:36.813 | 31
(16   ) 12:27:36.818 | 37
(15   ) 12:27:36.823 | 41
(14   ) 12:27:36.828 | 43
(13   ) 12:27:36.833 | 47
(12   ) 12:27:36.838 | 53
(11   ) 12:27:36.843 | 59
(10   ) 12:27:36.848 | 61
(9    ) 12:27:36.853 | 67
(8    ) 12:27:36.858 | 71
(7    ) 12:27:36.863 | 73
(6    ) 12:27:36.868 | 79
(5    ) 12:27:36.873 | 83
(4    ) 12:27:36.878 | 89
(3    ) 12:27:36.883 | 97
(2    ) 12:27:36.888 | Finished
(1    ) 12:27:36.893 | calculation finished
```

Figure 5.5: *Job monitoring in* GANGA *with* JEM. *The Job Execution Monitor provides access to job output, even while the job is still running.*

the complete runtime of a job so that their development in time can also give hints for reasons of job failures.

5.3 The Grid Expert System

With many thousands of CPUs, the Worldwide LHC Computing Grid (WLCG) is the largest compound of computers in the world. In such a complex system, there are unfortunately many sources of failures and errors. In many cases, the origin of an error is difficult to determine, but the combination of information from many failed jobs may help to find the real source of an error.

The most important indicator of a failure is a large number of jobs not finishing successfully. The next piece of information to determine is, whether the failure was caused by an error in the job itself or in the environment where the job was executed. This question is often difficult to answer for a single job and can only be estimated when a large number of failed jobs from different users are taken into account.

Two scenarios can be taken as templates for these two types of job failures:

job error The job is misconfigured, e.g. the proxy certificate of a job is invalid or the job tries to access a non-existent file. In this case the job will fail, regardless of the worker node it is tried to run on. As a typical user usually submits many jobs at the same time, all jobs of this user will fail.

infrastructure error A worker node is misconfigured, e.g. one of its hard disks has run out of space. In this case all jobs run on this specific worker node will fail, because they cannot store needed information on disk.

Although real situations may be more involved than these two cases, in principle they can be divided into these two types of errors. Jobs of a specific user may fail on many sites, but may also be successful at other sites because each site may have a special setup preventing a specific error scenario. On the other hand, jobs may fail on a worker node only if they come from a specific VO. Tracking of errors may be difficult in these cases.

The Grid Expert System [127, 130], which was developed as part of this work, is a tool to address these kind of problems in the grid or in user's jobs. In addition, it provides the ability to suggest suitable actions to solve a given problem. It is built to support users as well as site administrators to trace sources of error conditions and help them to correct encountered errors.

5.3.1 Expert Systems

Expert systems are complex computer systems which are able to draw conclusions from a given set of input data, based on a predefined set of rules. They conserve

knowledge about a specific domain where no human expert is available or the specific system is too large to be covered by only one expert. The knowledge is provided to ordinary users who are not familiar with the topic.

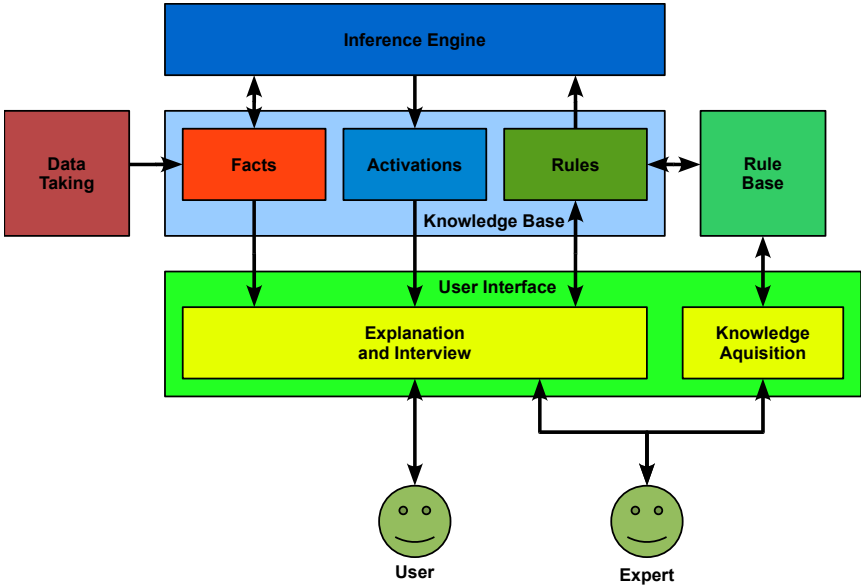

Figure 5.6: *Structure of an expert system. Data is fed into the system as facts by a data taking component. Rules determine all conclusions drawn from known facts. The inference engine matches rules against available facts. Users may view and manipulate facts and rules through a user interface, which can have a specialized mode for experts.*

Expert systems consist of many interacting components. A schematic diagram of these components and their relations is shown in figure 5.6. The expert system collects raw data about the considered system via the *data taking* component. Gathered information is stored as *facts* in the *knowledge base*. The knowledge base holds all variable data of the expert system. Apart from the currently relevant facts, there are also the known rules and their current activations.

The rules represent all knowledge of the expert system about the specific domain. Each rule consist of a condition that has to be matched by facts and a conclusion, which is an

action to be performed. If all conditions of a rule are satisfied, the condition becomes active and is appended to a list of all *activations*.

The component to process all rules and match them against all known facts is called *inference engine*. This part is the core of every expert system. It implements the *Rete algorithm* [137], which is an efficient method to match a large number of conditions and facts against each other. The Rete algorithm recognises equal parts in conditions of different rules and evaluates them efficiently so that the number of comparisons is optimised and reduced significantly.

Results after evaluation of all rules are presented to the user, which may by a solution to a current problem. It is also possible to request additional information from a user, if the system has not enough information to draw a conclusion. Experts may also add new rules to extend the abilities of the expert system. These rules are stored in a *rule base* until they are confirmed and inserted into the expert system. Thus, the knowledge and characteristics of the expert system are given completely by the set of defined rules.

5.3.2 Requirements

The grid expert system is a tool meant to be used by the ordinary grid user as well as site administrators. To reach this goal, it has to match some design criteria, which help users accept the new tool as well as its developers to quickly implement new features and fix experienced shortcomings. Among these requirements are the following.

modularity The expert system has to be able to retrieve its information from several different sources in order to gather as much information as possible about failed jobs. On the other hand, it is necessary to provide several different user interfaces, depending on who is using the system, a typical user or an expert maintaining the system. As every component should be able to be replaced or changed separately, the core system also has to manage all these components separately, which means that all components have to be built as modules or plugins, communicating via a common, standard interface. With this approach, each component can be changed independently, without influencing other components.

user-friendliness In order to be easily usable, there has to be only a small number of possible commands with which the system can be controlled completely. As much as possible has to be done automatically by the expert system, because the user does not want to deal with technical details, but is only interested in

the result. The system has to deal automatically with obvious tasks, without disturbing the user.

clear interface The user interface has to be designed to allow an easy and quick access to all available functions and information. Suggested solutions have to be presented clearly and easily understandable. They have to be explained in detail. A possible solution could include a list of actions necessary to implement the solution.

partial diagnostics As not all possible solutions can be known to the system from the beginning, the list of known solutions has to be extended with time. Thus, at the beginning, only few solutions are known. The system has to provide its current information to the user, even though a complete solution is not known, because it may be possible to exclude some sources of errors or get hints from known information. In this case, the system could present a list of sources which still can cause the problem after consideration of all known information.

security It is necessary for the expert system to gather information about all kinds of jobs from many different users. Therefore, it could be possible for a user to retrieve information about other users' jobs. As these data are potentially critical, the grid expert system has to ensure, only authorised users are able to retrieve information about their own jobs.

client/server architecture Not every computer is allowed to connect and retrieve information from the grid. In order to provide a way to monitor grid jobs from everywhere, the grid expert system is divided into a client and a server component. The server collects all information and runs the actual expert system. The client just connects to the server and displays its information. With this approach, information also has to be processed once on the server. The client can be a simple machine without any special requirements.

The grid expert system shares some of these requirements with a second expert system developed in parallel by Tobias Henß for the ATLAS detector control system. The purpose of the *Pixel Advisor* expert system [138] is to help the responsible shifter for the ATLAS pixel detector spot possible problems in its operation and advice him to take appropriate actions.

Despite both expert systems have many requirements in common, the task of the Pixel Advisor expert system differs significantly from the purpose of the grid expert system in some aspects. Important difference between both systems are the following.

protection The Pixel Advisor assists the current shifter to handle problems in the operation of the ATLAS pixel detector. This piece of hardware is the innermost part of the ATLAS detector. It can be controlled completely from the ATLAS control

room. Thus, it is also possible to set up dangerous environmental conditions, that could damage the hardware without a possibility to replace a failed component. Therefore, the Pixel Advisor has to be extremely careful in its suggestions in order not to give an advice that could be dangerous to the detector. This is also the reason why the Pixel Advisor is not allowed to take automatic actions that have not been controlled by a human expert.

On the other hand, the grid expert system only gives advice about some pieces of software. Advice given by the grid expert system could also be dramatic, e.g. if a site fails to be operational after applying a solution suggested by the expert system. Nevertheless, such a failure could always be recovered as no critical component can be damaged permanently.

security Access to grid resources is always authenticated via a valid grid certificate. No action can be performed without such a certificate. Thus, the grid expert system and its users have to authenticate themselves in order to access grid-related information. This has to be done twofold. On the one hand, the grid expert system has to provide a certificate for itself in order to access and collect information about grid jobs. On the other hand, the expert system has to check the identity of a potential user, who has to provide a certificate to the expert system in order to retrieve its collected information. As the user may contact the grid expert system from any computer, any connection between the client and the server has to be encrypted, so that information can only be read by authenticated people.

In contrast, the Pixel Advisor does not need any authentication or encryption, because the pixel detector can only be accessed from dedicated servers in the ATLAS control room. As access to these computers is already controlled by the ATLAS collaboration and the CERN infrastructure, no additional effort is needed to protect these computers from unauthorised access.

In order to minimise work on the expert system and to prevent double developments of the same features, it has been decided to develop a common core system for both expert systems, called *UnifiedXP*. With this approach, only data taking components and specific sets of rules have to be developed separately, but both systems can combine their best features.

5.3.3 Structure of the Grid Expert System

As expert systems are being used in many different areas, there are also many different implementations of basic functionalities. These packages are called *expert system shells*

and can be used to set up actual expert systems. After comparison of several expert system shells, it was decided to build the grid expert system as well as the Pixel Advisor on *JBOSS Rules* [139] which is part of the free JBOSS software repository, written in Java and maintained by the RedHat Company.

On top of the basic expert system shell, further components have been developed in collaboration with Tobias Henß, Denis Huning and Frank Iker, which unify the core of the expert system and its handling of input data and facts via common interfaces. With this approach, also the user interface could be unified so that it is able to display all relevant data of both expert systems, the Pixel Advisor as well as the grid expert system. The only two components that cannot be unified among different expert systems remain to be the data taking component and the specific set of rules. Detailed information about the unification of expert systems can be found in the theses of Tobias Henß [138], Dennis Huning [140] and Frank Iker [141]. Core features of UnifiedXP are the following.

unification of data handling All facts are stored in a common structure, which is called `Storeable` and allows to represent all needed types of data. This enables a standardised interface for inserting data into and retrieving data from the UnifiedXP. Thus, it is possible to easily exchange all components interfacing the expert system such as data taking and graphical interfaces. Unified objects for data exchange are the basic structures which make a unification of expert systems possible.

user interface With unified data handling, also a unified representation of these data becomes possible, i.e. the user interface can be developed such that it can represent data of any expert system built upon UnifiedXP.

client/server architecture As a requirement for the grid expert system, the client and server components are split into two independent parts which communicate via network connections. Data is exchanged in form of `Storeable` objects. With this architecture, the client is able to handle all types of data and can be used for any kind of expert system.

encrypted data transfer Separate client and server components which communicate over network make it necessary to encrypt their exchange of data so that no information can leak to unauthorised listeners. Encryption is realised by a usual Secure Socket Layer (SSL) protocol, after the client has authenticated itself with the user's grid certificate.

Although a client/server architecture and encryption was not necessary for the Pixel Advisor, it benefits from these features such that it is now in principle possible to monitor the ATLAS pixel detector from any computer through a secure connection.

Nevertheless, this opportunity is strictly limited by CERN and ATLAS security policies. Internet connections from the control server of the ATLAS pixel detector are strictly forbidden to prevent any intrusion from outside which could lead to a severe damage to the detector.

In addition to these features, which the grid expert system inherits from UnifiedXP, system-specific components of GridXP provide following features.

data taking The main source of data for the expert system is the Relational Grid Monitoring Architecture R-GMA [142]. This distributed database collects information about all jobs processed in the grid. Information can be retrieved by queries following the Structured Query Language (SQL) [143, 144].

As a distributed database, R-GMA has to collect requested information from several different sites, which may take a considerable amount of time. Therefore, information required by the expert system cannot be fetched as needed, because it could take an undetermined time until the piece of information actually can be retrieved. For this reason, there are always some requests running in parallel tasks to the expert system. They continuously retrieve information from R-GMA and feed it into the expert system as new facts.

rule base The above constraint on information retrieval has a significant influence on conclusions that can be drawn from available information. As it is not possible with R-GMA to request a specific piece of information when it is needed, the expert system often has to deal with limited data about job failures at all times. Thus, conclusions can be rather unspecific. In some cases, no conclusions can even be drawn at all.

In general, implementation of a new expert system has become relatively simple when building it upon the developed UnifiedXP base. From a user's perspective, all expert systems based on UnifiedXP can be handled in the same way as described in [138]. Thus, for an extensive description on the user interface of the expert system and more details about UnifiedXP, the reader is referred to that document.

5.4 Conclusion

Monitoring grid jobs has become an important task to determine problems in the grid infrastructure. The Job Execution Monitor provides a large amount of information about running and also failed jobs. With JEM it is possible to trace back error conditions to their sources. It is then possible to prevent similar errors from occurring again.

With its integration into the GANGA framework, adding and using JEM with a user's job has become an easy task which can be done with just a few lines of GANGA commands. With its modular structure and possibilities to monitor bash and Python scripts as well as precompiled programs, it exceeds monitoring capabilities of all other monitoring packages.

When run with a large number of jobs, it also provides useful information about the status of grid sites which the jobs run at. Therefore, also site administrators can benefit from using JEM, if information from many grid jobs is analysed with respect to site-specific problems.

Analysis of grid job failures is done by the grid expert system, which tries to find sources and also solutions to encountered job errors. To minimise necessary development, most components of the grid expert system have been unified with the Pixel Advisor. Unification has been a large effort for building new expert systems. Only the data taking component and rules have to be built from scratch. All other parts can be reused without any changes for every expert system. The client/server architecture makes it possible to run the user interface on almost every computer with an internet connection. Encryption and authentication provide a secure way of handling collected information.

Although the Pixel Advisor is still being developed and used to help controlling the ATLAS Pixel detector, the grid expert system has undergone a focus shift. Instead of having an independent expert system for analysing data of all grid jobs it appeared appealing to merge the expert system with the ATLAS Dashboard [145] project, which already collects large amounts of job and site specific information and presents it in a summarising collection of web pages. This way, the system does not analyse all grid jobs any more, but only ATLAS-specific jobs. On the other hand, the dashboard already grants access to a huge amount of collected data from simulation jobs as well as users' analysis jobs in the ATLAS community.

Currently, the Job Execution Monitor and the analysis of grid failures and their solutions are maintained and further developed by Tim dos Santos and Frank Volkmer, respectively, during their PhD theses.

6 General Strategy of the $t\bar{t}$ Resonance Analysis

"The difference between fiction and reality?
Fiction has to make sense."
— Tom Clancy

There are many theoretical models predicting heavy particles decaying into a $t\bar{t}$ pair of quarks. Depending on its quantum numbers, a $t\bar{t}$ resonance may exhibit strong patterns of interference with top quark pair production in QCD. Such interferences may alter the strength of a signal for the respective resonance. In some cases, the interference enhances handles for distinguishing the resonance from $t\bar{t}$ production in QCD. The significance of these models is increased by the interference. In other cases, an interference may have a negative effect on the significance of a model. The interference can decrease the strength of a signal.

As a result, predictions from studies ignoring any interference have to be adjusted. Exclusion limits have to be revised with respect to changed significances. This study investigates effects of interferences on exclusion limits for various $t\bar{t}$ resonances.

6.1 Search Strategies for Fermion-Antifermion Resonances

Studies of resonant fermion-antifermion production have a long tradition, beginning with the lightest mesons π^0, η and ϱ. Discoveries of heavier quark-antiquark resonances like the ϕ, J/ψ and Υ mesons lead to evidence for the strange, charm and

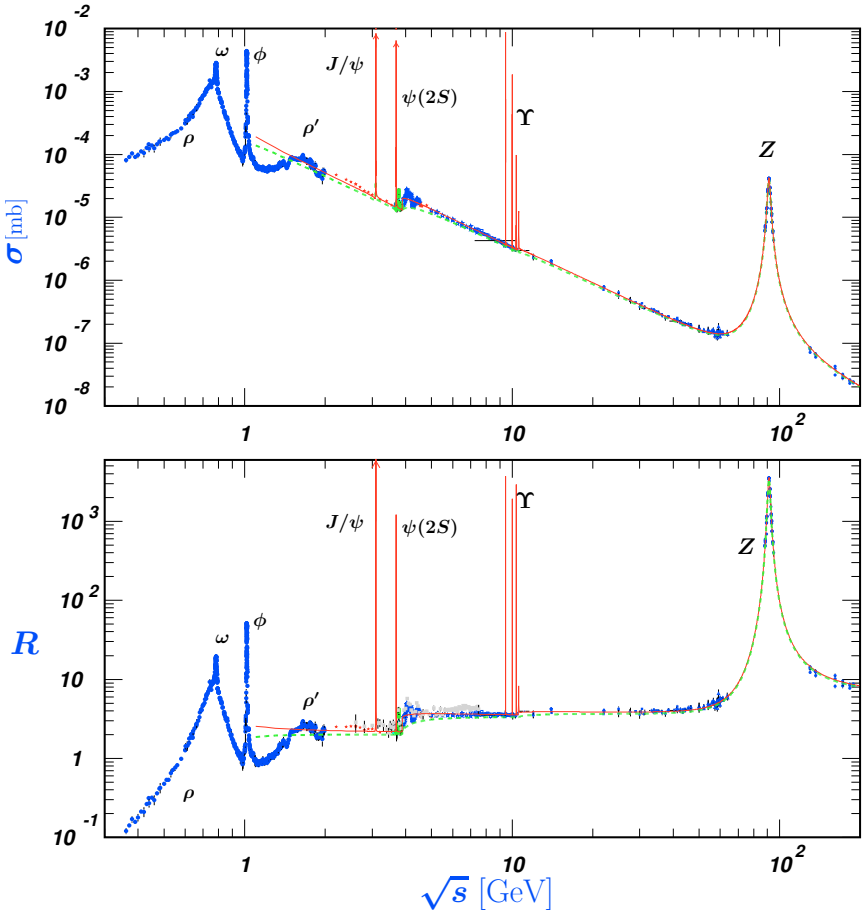

Figure 6.1: *Total cross section of $e^+e^- \to$ hadrons and the ratio $R = \frac{\sigma(e^+e^- \to \text{hadrons})}{\sigma(e^+e^- \to \mu^+\mu^-)}$ [4]. Resonances like the ϕ, J/ψ, Υ mesons or the Z^0 boson are visible as sharp peaks in both distributions.*

bottom quarks respectively. Finally, the discovery of the Z^0 boson was a great success for the Standard Model.

Figure 6.1 shows the total cross section for hadron production in e^+e^- collisions. All resonances mentioned above can be clearly identified as outstanding peaks in the spectrum.

Unfortunately, in hadron collisions the partonic centre-of-mass energy cannot be determined precisely like in e^+e^- collisions. All partons of a proton carry only a fraction of the total proton momentum, but the exact amount is unknown. In most cases, colliding partons have different momenta such that their centre-of-mass system is not at rest and the hard event is Lorentz-boosted along the beam axis.

Additionally, the final state contains many particles from minimum bias and underlying events. Cross sections for interesting processes are orders of magnitude lower than the total cross section, as can be seen from figure 3.1. Therefore, studies of $t\bar{t}$ resonances first have to sufficiently suppress background events before a significant contribution from an unknown resonance can be revealed. In this case, the mass equivalent of the partonic centre-of-mass energy $\sqrt{\hat{s}}$ is also called the *invariant mass* of the $t\bar{t}$ pair

$$m^2c^4 = \hat{s} = \left(p_t + p_{\bar{t}}\right)^2 c^2 .$$

Here, m is the rest mass of a potential particle decaying into the top quark pair. If a large range of $\sqrt{\hat{s}}$ is scanned, an unknown particle would reveal itself as a peak in the invariant mass distribution also denoted as the differential cross section $\frac{d\sigma}{dm_{t\bar{t}}}$.

To effectively select $t\bar{t}$ events and also reject non-$t\bar{t}$ events at the same time, the events have to match certain criteria, called *cuts*, which require characteristic features of the interesting processes and distinguishes them from background events. These criteria often require a minimal number of jets with a minimal transverse momentum. If electroweak processes are involved, the requirement of at least one charged lepton is a good method to suppress pure QCD reactions. The next section describes the selection and analysis technique used in this study.

6.2 Reconstruction of Semileptonic Decays

In order to determine the invariant mass of a Top-Antitop pair of quarks, the events have to be selected among a huge background of other processes and the final state objects in each event have to be reconstructed and identified.

The selection is done by application of suitable cuts which are determined by the characteristics of a semileptonic $t\bar{t}$ event. As can be seen from figure 6.2, the final

state of a semileptonic $t\bar{t}$ decay contains a charged lepton, a neutrino, two b quarks and a pair of quarks from the hadronic $W^{\pm}$ decay.

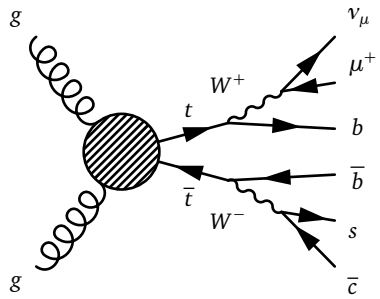

Figure 6.2: *Structure of a typical semileptonic $t\bar{t}$ process. Both top quarks produced in the hard process (blob) decay into a $W^{\pm}$ and a $b/\bar{b}$ quark. One of the $W^{\pm}$ bosons decays into a charged lepton and its respective (anti-)neutrino. The other $W^{\pm}$ boson decays into two different quarks.*

These final state particles determine the required cuts. A typical semileptonic $t\bar{t}$ selection requires the following features for an event.

- At least one charged lepton. A lower limit is required for its transverse momentum to raise the probability of it coming from a $W^{\pm}$ decay and to guarantee an accurate energy measurement.

- The neutrino also carries away a similar amount of energy and momentum as the charged lepton, but it cannot be detected in the experiment. Therefore, a large amount of missing transverse momentum is a second criterion.

- The four quarks manifest themselves as jets with high transverse momentum. Often only three jets are required by the selection in order to keep events where two jets are boosted into the same direction or one jet is lost in an insensitive region of the detector. Usually, jets with the highest transverse momentum are selected, assuming they originate from the hard process and have a transverse momentum higher than a certain threshold.

Major background events faking a $t\bar{t}$ signature come from processes like $W^{\pm}$+jets production or QCD multi-jet processes, where one jets is misidentified as a charged lepton. Existing studies of $t\bar{t}$ events show, that these backgrounds can be sufficiently suppressed and handled appropriately, so that it is appropriate to concentrate on the actual $t\bar{t}$ channel in this study.

cut	threshold	efficiency
no cut	—	100 %
1 isolated $e^{\pm}$ or $\mu^{\pm}$	$p_{\perp} > 25\,{}^{\mathrm{GeV}}/_{c}$ $\lvert\eta\rvert < 1.37$ or $1.57 < \lvert\eta\rvert < 2.47$	34.36 %
missing momentum	$p_{\perp} > 25\,{}^{\mathrm{GeV}}/_{c}$	63.7 %
3 jets	$p_{\perp} > 40\,{}^{\mathrm{GeV}}/_{c}$ $\lvert\eta\rvert < 2.5$	71.83 %

Table 6.1: *Cuts applied to all simulated $t\bar{t}$ events. Selected objects have to exceed certain thresholds in transverse momentum to suppress similar events from non-$t\bar{t}$ processes. Cuts in η are applied to exclude regions of the detector with reduced sensitivity to the respective objects.*

Cuts used in this work are summarised in table 6.1, together with a graphical representation of their efficiencies in figure 6.3 and the number of events surviving each cut in figures 6.4.

The major issue in a reconstruction of a semileptonic $t\bar{t}$ event arises from the undetectable neutrino. It carries away a large momentum, which is considered to be the largest contribution to measured missing transverse momentum. Only the transverse component of missing momentum, which is perpendicular to the beam axis can be used in reconstruction, because the Lorentz boost of the event along the beam axis is not known as described above. Thus, the z component of the neutrino is a priori unknown. It can be calculated under the assumption that the charged lepton and the neutrino come from a $W^{\pm}$ decay, imposing a $W^{\pm}$ mass constraint on its decay products. With momentum conservation, the equation

$$m_{W^{\pm}}^2 c^2 = p_{W^{\pm}}^2 = \left(p_{l^{\pm}} + p_{\nu}\right)^2$$

has to hold, where the p_i stand for the 4-momenta of the $W^{\pm}$ boson, the charged lepton and the neutrino respectively. By inserting all known momentum components, this quadratic equation can be solved for the z component of the neutrino $p_{\nu,z}$. The

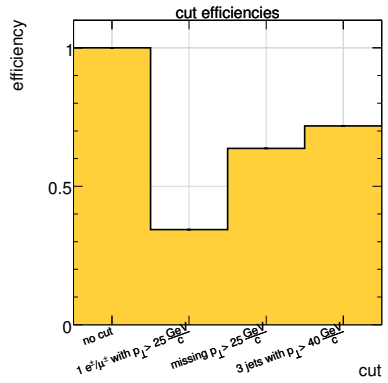

Figure 6.3: *Graphical illustration of cut efficiencies for $t\bar{t}$ events in QCD. Efficiencies are determined for each cut independent from other cuts such that all bins are uncorrelated to each other.*

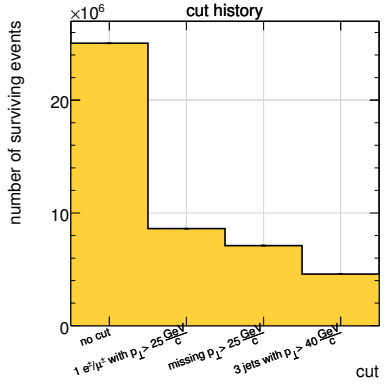

Figure 6.4: *Graphical illustration of the cut flow for $t\bar{t}$ events in QCD. The number of surviving events depends on efficiencies of all previous cuts. Final events have to match all criteria of all cuts.*

exact solution is given by

$$
\begin{aligned}
q :=& \frac{c^2}{2}\left[m_{W^\pm}^2 - m_{l^\pm}^2 - m_\nu^2\right] + \vec{p}_{l^\pm,\perp}\cdot\vec{p}_{\nu,\perp} \\
r :=& \frac{E_{l^\pm}^2}{c^2} - p_{l^\pm,z}^2 = p_{l^\pm,\perp}^2 + m_{l^\pm}^2 c^2 \\
s :=& -2qp_{l^\pm,z} \\
t :=& \frac{E_{l^\pm}^2}{c^2}\left(\vec{p}_{\nu,\perp}^2 + m_\nu^2 c^2\right) - q^2 \\
p_{\nu,z} =& \frac{1}{2r}\left[-s \pm \sqrt{s^2 - 4rt}\right],
\end{aligned}
$$

where $E_{l^\pm}$ is the total energy of the charged lepton.

In case the quadratic equation does not have a solution, $p_{\nu,z}$ is set to zero and the missing transverse momentum of the event is adjusted accordingly in order to keep

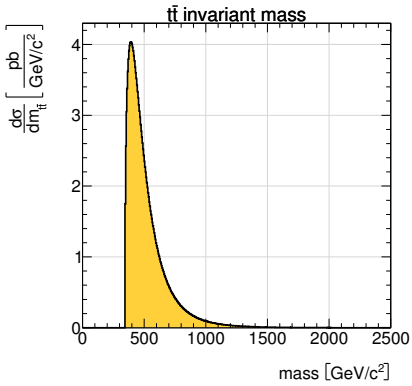

Figure 6.5: *Example $t\bar{t}$ invariant mass spectrum on parton level. The sharp edge at $2m_t$ is clearly visible.*

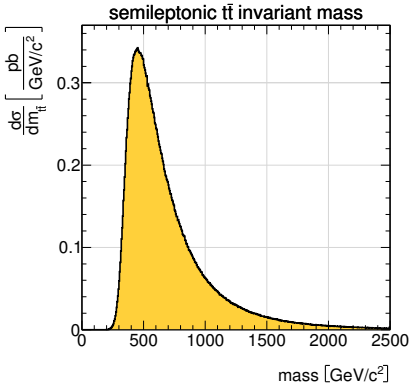

Figure 6.6: *Example $t\bar{t}$ invariant mass spectrum after semileptonic reconstruction. The distribution is smeared by detector effects and the semileptonic reconstruction of $t\bar{t}$ events. The expected total cross section is reduced by applied cuts.*

the whole event consistent. In case of two possible solutions, the smaller z-momentum is chosen, which has been checked in simulations to provide the correct solution in the majorityof all cases.

With known momentum of the neutrino, the invariant mass of the $t\bar{t}$ pair can simply be calculated as the sum of all 4-momenta of the jets and leptons

$$m_{t\bar{t}}^2 c^2 = \left(p_{l^\pm} + p_\nu + \sum_{i=1}^{4} p_i \right)^2 ,$$

where p_i is now the 4-momentum of the i-th jet. Figures 6.5 and 6.6 show the $t\bar{t}$ invariant mass distribution on parton level and after semileptonic reconstruction with the above cuts applied.

Applied cuts reduce the number of expected events and, therefore, lower observed total cross sections. The original distribution of the $t\bar{t}$ invariant mass shows a sharp edge at $2m_t = 345\,\mathrm{GeV}/c^2$, which is because the pair of top quarks has to have an invariant mass of at least twice the top quark mass. In this case, both top quarks are produced at

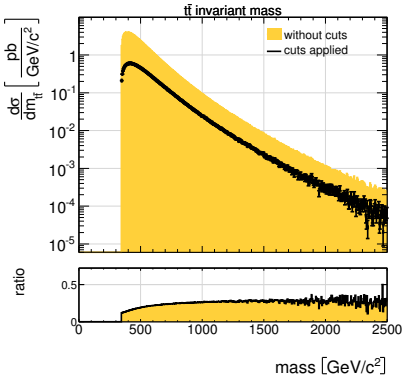

Figure 6.7: *Comparison of $t\bar{t}$ invariant mass distributions before and after application of cuts. The selection efficiency of cuts rises from 12.5 % at the threshold of the distribution up to 29 % for invariant masses above $2\,^{TeV}/_{c^2}$.*

rest. Any additional amount of energy in an event is used to increase the momenta of the top quarks. The distribution peaks at an invariant mass of about $400\,^{GeV}/_{c^2}$, which means that most probably the two top quarks share a kinetic energy of about 50 GeV.

Compared to the original $t\bar{t}$ invariant mass distribution, figure 6.6 shows that the observable distribution after a semileptonic reconstruction is broadened and smeared by detector effects and the semileptonic reconstruction of $t\bar{t}$ events. The expected total cross section is reduced by applied cuts.

Cuts do not affect all regions of the invariant mass spectrum in a similar way. Figure 6.7 shows that events in the threshold region are only selected with an efficiency of 12.5 %, whereas events above an invariant mass of $2\,^{TeV}/_{c^2}$ are selected with an efficiency of 29 %. This is because events with higher $t\bar{t}$ invariant masses also have jets and leptons with higher transverse momenta. Therefore, they are more likely being selected by the above cuts.

6.3 Scaling of Coupling Parameters

The most remarkable sign of a heavy $t\bar{t}$ resonance is a peak in the invariant mass spectrum of the top-antitop pair. With negligible interference, the total distribution is just the sum of a resonance and a QCD $t\bar{t}$ contribution. As the $t\bar{t}$ resonance may be produced via a new force of unknown strength, its couplings and cross section are a priori unknownand have to be treated variably. In the simplest case without interfer-

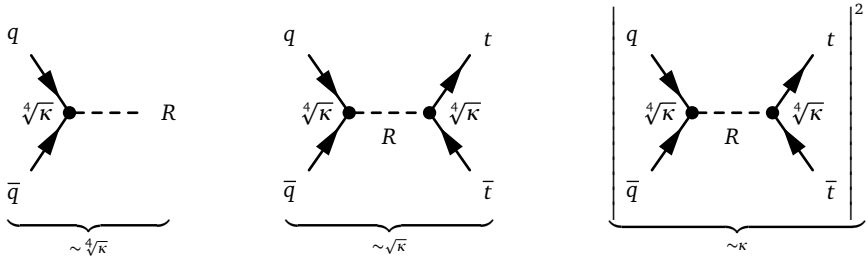

Figure 6.8: *Scaling of resonance contribution. The coupling described by a vertex is scaled by $\sqrt[4]{\kappa}$. The transition amplitude is then scaled by $\sqrt{\kappa}$, because it contains two vertices. Any observable is scaled by κ because it is proportional to the absolute square of the amplitude.*

ence, the signal can just be scaled accordingly by a scale parameter κ. This leads to a peak of variable height, corresponding to a scaled cross section of the resonance.

In cases of a non-negligible interference, the distinction between a signal and a background contribution is no longer valid. The interference closely couples both channels into a *full* $t\bar{t}$ production process. Scaling the resonance contribution cannot be done simply by scaling final distributions any more. In general, as shown in figure 6.8, couplings are scaled by a factor of $\sqrt[4]{\kappa}$ in each vertex, depending on the types of particles the resonance couples to. As every resonance has a production and a decay vertex, Feynman diagrams and matrix elements with exactly one resonance can be scaled by $\sqrt{\kappa}$. Accordingly, this translates into cross sections and other observables being scaled by κ for processes with exactly one resonance.

Scaling of the resonance contribution in the full samples is more difficult, because the QCD channel, the pure resonance channel and the interference contain different contributions of resonances. In general, Feynman diagrams with a different number of resonances have to be scaled separately and differently.

For this study, relevant Feynman diagrams are summarised in appendix A.2. They only contain one or no resonances. Thus, the absolute square of the matrix element splits only into three parts, the pure QCD processes which do not depend on the scale parameter, the pure resonance with linear dependence on κ and the interference, which scales according to $\sqrt{\kappa}$. Cross sections decomposed into these contributions can

be written as

$$\begin{aligned}\sigma_{t\bar{t}} \sim |\mathcal{M}|^2 &= \left|\mathcal{M}_{\mathrm{QCD}} + \sqrt{\kappa}\mathcal{M}_{\mathrm{Res}}\right|^2 \\ &= \left|\mathcal{M}_{\mathrm{QCD}}\right|^2 + \kappa\left|\mathcal{M}_{\mathrm{Res}}\right|^2 + \underbrace{2\sqrt{\kappa}\cdot\mathrm{Re}\left(\mathcal{M}_{\mathrm{QCD}}\overline{\mathcal{M}_{\mathrm{Res}}}\right)}_{\text{Interference}}. \end{aligned} \tag{6.1}$$

The interference can be calculated from the unscaled calculations of the pure resonance, the pure QCD $t\bar{t}$ and a calculation of the full process, schematically described in figure 6.9. After the interference has been determined, a new full spectrum can be calculated with the resonance, QCD $t\bar{t}$ and interference components scaled separately. This procedure relies on a consistent prediction of all total cross sections. As inter-

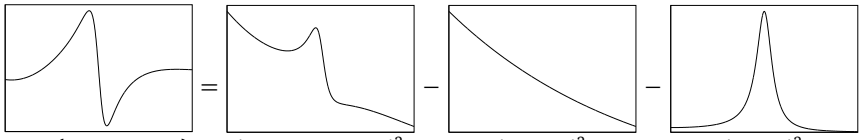

Figure 6.9: *Sketch for determination of an interference. The signal and background components are subtracted from the calculation of a full process. The remainder represents the interference.*

ferences are calculated as a difference of three independent simulations, all further calculations rely on an accurate prediction of cross sections by the event generator. There is no possiblility to vary cross sections of single channels! Calculated cross sections by the event generator have to be accepted. Nevertheless, it is possible to obtain distributions with a scaled resonance contribution with the above scaling procedure.

The interference is not directly available as an independent sample, but it can be determined from the three simulated types of events. To obtain a scaling prescription containing only the three available types of simulations, the interference is inserted into equation 6.1. A distribution with a scaled contribution of the resonance can then be calculated by

$$\begin{aligned}&\left|\mathcal{M}_{\mathrm{QCD}} + \sqrt{\kappa}\mathcal{M}_{\mathrm{Res}}\right|^2 \\ &\quad= \left|\mathcal{M}_{\mathrm{QCD}}\right|^2 + \kappa\left|\mathcal{M}_{\mathrm{Res}}\right|^2 + 2\sqrt{\kappa}\cdot\mathrm{Re}\left(\mathcal{M}_{\mathrm{QCD}}\overline{\mathcal{M}_{\mathrm{Res}}}\right) \\ &\quad= \left|\mathcal{M}_{\mathrm{QCD}}\right|^2 + \kappa\left|\mathcal{M}_{\mathrm{Res}}\right|^2 + \sqrt{\kappa}\left(\left|\mathcal{M}_{\mathrm{QCD}} + \mathcal{M}_{\mathrm{Res}}\right|^2 - \left|\mathcal{M}_{\mathrm{QCD}}\right|^2 - \left|\mathcal{M}_{\mathrm{Res}}\right|^2\right) \\ &\quad= \left(1-\sqrt{\kappa}\right)\left|\mathcal{M}_{\mathrm{QCD}}\right|^2 + \left(\kappa-\sqrt{\kappa}\right)\left|\mathcal{M}_{\mathrm{Res}}\right|^2 + \sqrt{\kappa}\left|\mathcal{M}_{\mathrm{QCD}} + \mathcal{M}_{\mathrm{Res}}\right|^2. \end{aligned} \tag{6.2}$$

With this decomposition it is possible to generate distributions of the $t\bar{t}$ invariant mass with an arbitrary strength of a resonance, if only the three components are known, i.e. the QCD $t\bar{t}$ distribution, the pure resonance distribution and the full distribution including the interference. This method is used later on to reweight events in the full simulation according to their partonic $t\bar{t}$ invariant masses in order to obtain scaled distributions.

The weight of an event is calculated using equation 6.2 divided by the unscaled contribution $\left|\mathscr{M}_{\mathrm{QCD}} + \mathscr{M}_{\mathrm{Res}}\right|^2$. The distribution of event weights is calculated from the three distributions of invariant masses at parton level. The resulting distribution is used as a lookup table of event weights. Therefore, bin sizes have to be balanced between two extreme cases. High accuracy of event weights require a small bin size and many bins. On the other hand, this leads to large statistical errors, because each bin only contains few events. As a compromise, bin sizes have been chosen to span a width of only 5 $^{\mathrm{GeV}}/_{c^2}$ for parton level distributions.

In order to cover a large range of scaling parameters, each generated sample has been processed with signal contributions reduced by factors of 0.5, 0.2, 0.1, 0.05, 0.02 and 0.01. Additionally, all signal contributions have been enhanced by factors of 2, 5, 10, 20, 50 and 100. In total, this means, every sample of generated events was processed 13 times, each with a different scaling of the resonances contribution.

Scaling of resonance contributions on parton level exactly follows equation 6.2. On the other hand, in nature, all interference occurs between the observable initial and final states, i.e. between the initial protons and measured long-living particles in the detector, which usually are photons, charged pions, protons, neutrons, electrons and muons.

This total interference includes the partonic interference as a major part, but also incorporates further contributions from many different processes. If the factorisation theorem is applied, these contributions can be assumed to be small. Thus, they merely have a negligible impact on the full process. Nevertheless, the unusual treatment of signal scaling makes it necessary to apply a sophisticated way to calculate sensitivities.

6.4 Statistical Analysis

In order to confirm or falsify a theoretical model, it has to state distinguishable predictions compared with other models that are visible in measurable quantities. In experiment, the true distribution of measured quantities can never be determined because of the limited number of events, i.e. measured quantities always suffer from

statistical and also systematic uncertainties. It is therefore necessary to determine the magnitude of how well a prediction of a certain model matches the measured distribution. This can be interpreted as a probability of the model describing measured data.

In the modified frequentistic approach [146], probabilities are interpreted as relative fractions of different results in a large number of measurements. The $\mathsf{CL_S}$ method determines the quality of predictions of different models compared with predictions of a reference model which usually is the Standard Model. The *likelihood ratio*

$$\exp\left(-\frac{1}{2}Q\right) = \frac{L(D|H_S)}{L(D|H_0)}$$

is proven by the Neyman-Pearson-Lemma [147] to be the optimal quantity to distinguish predictions of a signal hypothesis H_S from a null hypothesis H_0 with respect to a sample of measured data D. The likelihood $L(D|H)$ denotes a measure for a hypothesis or a theoretical model H to describe measured quantities D.

In experiments with a limited number of measurements, discrete results usually are distributed according to the Poisson distribution

$$P(x|\lambda) = \frac{\lambda^x}{x!}e^{-\lambda},$$

where x is the measured value and λ is the expectation value of the probability distribution. If more than one quantity is available for comparison, e.g. in a histogram of a binned distribution, the likelihood is given as the product of all probabilities in each bin

$$L = \prod_{i=1}^{N} P(x_i|\lambda_i)\,.$$

To speed up computations, usually the logarithmic likelihood

$$\ln(L) = \sum_{i=1}^{N} x_i \ln(\lambda_i) - \lambda_i - \ln(x_i!)$$

is calculated. The absolute value of a likelihood is difficult to interpret by itself. It becomes more relevant in comparison with likelihood values for different measurements or different theoretical predictions.

A measure to quantify differences in predictions of different models is the *significance*. In order to quantify discrepancies in predictions of different models, their respective likelihood ratios are calculated with respect to simulated pseudodata from each of both

models. Usually, the Standard Model prediction is considered as the null hypothesis without signal.

For each model, its respective Q value is calculated as

$$\begin{aligned} Q_0 &= -2 \cdot \ln \frac{L(D_0|H_S)}{L(D_0|H_0)} \\ Q_S &= -2 \cdot \ln \frac{L(D_S|H_S)}{L(D_S|H_0)}, \end{aligned} \tag{6.3}$$

where D_0 and D_S are ensembles of pseudodata, generated under the assumtion of the H_0 and H_S hypotheses, respectively. The distributions of Q values for a large number of ensembles of pseudodata contain information how the two specific models can be distinguished. The p value of a model with respect to the null hypothesis is defined as

$$p = \frac{\int_{-\infty}^{Q_S^{\text{median}}} Q_0 dQ}{\int_{-\infty}^{\infty} Q_0 dQ},$$

where Q_S^{median} is the expected median Q value of the signal model. The p value is a number between 0 and 1. It expresses the probability of a background Q value to be smaller than the median Q value of the signal distribution, i.e. for a background ensemble to look like a signal ensemble. If two models cannot be distinguished, they both have a value of $p = 1/2$ with respect to each other.

The p value can be converted into an expected *significance* or *sensitivity* for an exclusion limit. The frequentistic confidence level (CL) of excluding a certain model is just $1 - p$. A common convention is to quote exclusion limits for a confidence level larger than 95 %, which can be interpreted meaning the following: If there is no resonance present in nature, measurements of the pure QCD $t\bar{t}$ distribution imitate the presence of the considered resonance in only 5 % of all cases. On the other hand, if there was a resonance actually existing in nature, the conclusion is more difficult. In this case, an existing resonance can nevertheless be excluded by 95 % CL, but only with a probability of less than 50 %. Thus, the probability of excluding a resonance, although it actually exists, drops below 50 %.

Expressed in terms of Gaussian standard deviations, the sensitivity S is given as

$$S = \sqrt{2} \cdot \text{erf}^{-1}(2p - 1).$$

Table 6.2 shows a list of corresponding values for common limits.

p	confidence level	standard deviation
0.5	50 %	$0\,\sigma$
0.1587	84.13 %	$1.0\,\sigma$
0.1	90 %	$1.28\,\sigma$
0.05	95 %	$1.64\,\sigma$
$1.35 \cdot 10^{-3}$	99.865 %	$3.0\,\sigma$
$3 \cdot 10^{-7}$	99.99997 %	$5.0\,\sigma$

Table 6.2: *Commonly used values for one-sided limits. Exclusion limits usually are given with 95 % CL. Evidence for new signals has to exceed $3\,\sigma$. Discoveries of new phenomena have to exceed $5\,\sigma$.*

6.4.1 Determination of Significances

Two model predictions are compared by generating pseudodata for each model and comparing them with both exact model predictions. Pseudodata is generated in form of histograms, simulating a measurement of the respective model with a predefined integrated luminosity, also called *ensemble*. This is done in two steps:

- determination of the expected total number of events,
- filling the histograms according to the theoretical prediction.

The expected total number of events N is calculated from the integrated luminosity $\mathscr{L}$ and the total cross section σ of the process via

$$N = \mathscr{L} \cdot \sigma \cdot \varepsilon\,, \tag{6.4}$$

where ε is the efficiency of all selection cuts, which reduce the number of observed events. As the number of observed events in experiment is a discrete number, its value follows a Poisson distribution. Therefore, N is smeared accordingly in all bins of generated ensembles.

The determined number of events is filled randomly into histograms for the signal ensemble D_S and the ensemble for the null hypothesis D_0, distributed according to the exact predictions of the respective models H_S and H_0. This procedure automatically generates Poisson distributed numbers of entries in each bin of the ensembles.

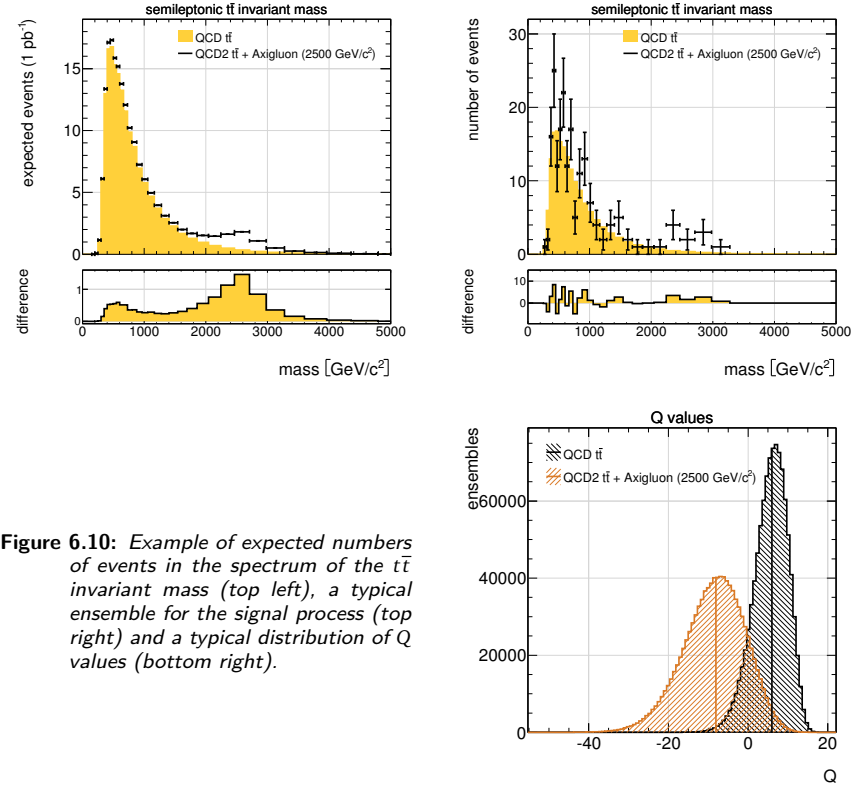

Figure 6.10: *Example of expected numbers of events in the spectrum of the $t\bar{t}$ invariant mass (top left), a typical ensemble for the signal process (top right) and a typical distribution of Q values (bottom right).*

The logarithmic likelihood values are calculated by

$$\ln\left[L(D_0|H_0)\right] = \sum_{i\in\text{bins}} -H_0(i) + D_0(i)\cdot\ln\left[H_0(i)\right]$$

$$\ln\left[L(D_0|H_S)\right] = \sum_{i\in\text{bins}} -H_S(i) + D_0(i)\cdot\ln\left[H_S(i)\right]$$

$$\ln\left[L(D_S|H_0)\right] = \sum_{i\in\text{bins}} -H_0(i) + D_S(i)\cdot\ln\left[H_0(i)\right]$$

$$\ln\left[L(D_S|H_S)\right] = \sum_{i\in\text{bins}} -H_S(i) + D_S(i)\cdot\ln\left[H_S(i)\right]$$

Finally, the Q values and sensitivities can be calculated with equations 6.3 and the formulae thereafter. An example of an ensemble for the $t\bar{t}$ invariant mass distribution and a typical distribution of Q values is shown in figure 6.10.

An advantage of this method is its widely accepted validity. In contrast to Bayesian methods, no prior assumptions about probabilities of considered models have to chosen. All models are treated equally and symmetrically.

On the other hand, a disadvantage of this method is its intensive need of computing power. The p value expresses the probability of a given ensemble to be described by a given model. This probability is determined as a fraction of generated test ensembles. Therefore, the probability can never be smaller than one ensemble out of the complete set of ensembles. Thus, the achievable exclusion limit depends on the number of generated ensembles.

For this study, all determinations of sensitivities are based on 10000 ensembles, which is equivalent with an achievable sensitivity of at most $3.89\,\sigma$. Higher sensitivities can be assessed, but their value cannot be determined. This study focuses on an exclusion limit of 95 % CL for all described models compared to the Standard Model $t\bar{t}$ production. Although this could already be achieved with 20 ensembles, the result would not be reliable, because statistical fluctuations are large with such a small number of ensembles. Therefore, 10000 ensembles have been generated to determine each sensitivity.

6.4.2 Statistical Independence

The above method to determine the significance of a model has a special property, which is convenient for most comparisons of models. If a distribution is compared with itself, the Q value always vanishes, which is why the significance of a model is determined only by its differences to distributions of other models. This can be seen by comparing two distributions where one contains only QCD $t\bar{t}$ production and the other is the sum of this same distribution and a pure $t\bar{t}$ resonance contribution. Figure 6.11(a) shows a comparison of these two distributions for an example of a Z' boson with a mass of $m_{z'} = 1000\,\mathrm{GeV}/c^2$.

The *pull* p of two quantities x_1 and x_2 is defined as

$$p = \frac{x_2 - x_1}{\sqrt{\sigma_2^2 + \sigma_1^2}},$$

with σ_1 and σ_2 the respective errors of x_1 and x_2. The pull distribution reveals the region of large contributions of the resonance. As expected, the pull distribution shows

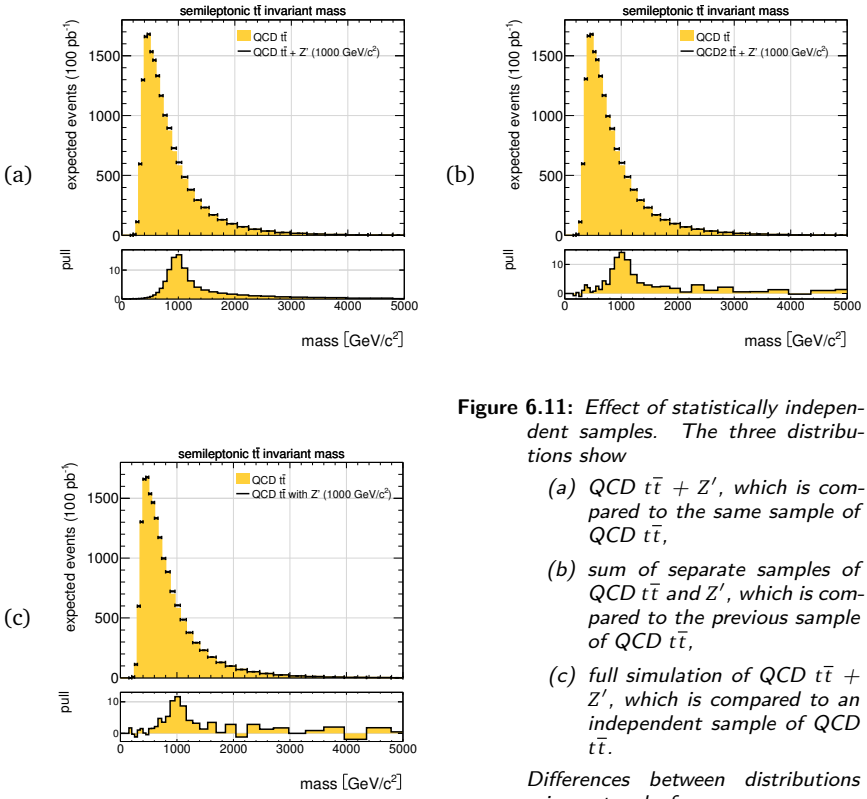

Figure 6.11: *Effect of statistically independent samples. The three distributions show*

(a) QCD $t\bar{t}$ + Z', which is compared to the same sample of QCD $t\bar{t}$,

(b) sum of separate samples of QCD $t\bar{t}$ and Z', which is compared to the previous sample of QCD $t\bar{t}$,

(c) full simulation of QCD $t\bar{t}$ + Z', which is compared to an independent sample of QCD $t\bar{t}$.

Differences between distributions arise not only from resonance contributions, but also from statistical fluctuations.

the largest deviations at the Z' mass where the differences to the QCD $t\bar{t}$ distribution are the largest.

Despite this pronounced and smooth distribution, this comparison represents the ideal case where the resonance distribution includes a QCD $t\bar{t}$ contribution and is afterwards compared to the same QCD $t\bar{t}$ distribution. In this case, when calculating the pull, the difference between both distribution reveals the original resonance distribution again. In a more realistic scenario, the true $t\bar{t}$ distribution of QCD is not known.

To account for this, the resonance distribution has to be added upon one QCD $t\bar{t}$ distribution and compared with a different QCD $t\bar{t}$ sample, such that the two distributions are completely independent. This has been done in figure 6.11(b).

A different way to account for statistical fluctuations can be a fit to the pure QCD $t\bar{t}$ distribution. This has the advantage, that this fit could be used easily for all samples to determine the background of QCD $t\bar{t}$ events from the full simulation. A suitable fit function has to be found, which accurately describes the distribution. On the other hand, if the function does not exactly describe the $t\bar{t}$ spectrum, there are always regions where the fitted function lies above the distribution of events and other regions where the function lies below. Unfortunately, this is just a pattern which is expected from interferences. Thus, an improper fit function can always fake patterns of interferences, even for plain QCD $t\bar{t}$ events. Therefore, this work concentrates only on spectra of generated $t\bar{t}$ events alone.

The independent sample of QCD $t\bar{t}$ production gives rise to additional statistical fluctuations which are present across the complete range of the distribution, not just in the region of the resonance mass. As such fluctuations add an additional source of differences also between similar distributions, they may also increase the significance of a sample compared to any other sample, even if the contribution of a resonance is arbitrarily small. Therefore, statistical fluctuations have to be reduced to prevent fake significances. Although they can never be completely suppressed, they can be smoothed by choice of reasonable bin sizes. Therefore, sizes of bins have been chosen to be 10 % of their lower edge value, but at least $50\,\mathrm{GeV}/c^2$. These values have been chosen because they are large enough to smooth the distributions, but still smaller than the experimental mass resolution, which has been determined in section 7.2.

For the special topic of the study, it is unavoidable to have two distinct samples to be compared. In cases of models with a significant interference between QCD diagrams and resonance diagrams of $t\bar{t}$ production, both channels cannot be simulated separately without loosing the interference. Therefore, the full process has to be simulated at once, including all QCD processes. As a consequence, all events are completely independent from a simulation of $t\bar{t}$ events in QCD alone.

An example of such a *full* simulation is shown in figure 6.11(c), where the included resonance has again been chosen to be a Z' boson with a mass of $m_{z'} = 1000\,\mathrm{GeV}/c^2$. This distribution looks similar to the one in figure (b). Some bins even seem to show the same fluctuations in both distributions, which is because both simulations are compared to the same sample of $t\bar{t}$ events in QCD.

In order to compare models in two cases where a possible interference is either respected or ignored, it is necessary to use two samples of QCD $t\bar{t}$ events. When the

interference is ignored, one of these samples is used to create the resonance distributions by adding events with a resonance. The other sample is then used for comparison in order to determine the significance of the resonance model compared to the pure QCD $t\bar{t}$ sample. In case the resonance is included in the full simulation, the sample already includes $t\bar{t}$ events from QCD. Then, only one QCD $t\bar{t}$ sample is needed for comparison.

It may be noted that these two samples of $t\bar{t}$ events from QCD could be two extreme example distributions with exceptionally large statistical fluctuations. It could be possible they enhance or soften signals of certain resonances during the statistical analysis. If this is to be avoided, many samples of QCD $t\bar{t}$ production would have to be produced. The resonance distribution would have to be compared with a large number of QCD distributions of $t\bar{t}$ production. In this case, all statistical fluctuations would eventually cancel, revealing the significance compared to an average QCD distribution.

For the present situation, this would have meant a huge amount of additional events to be generated, which was not appropriate for this study. Instead, it is assumed that the two independent samples of QCD $t\bar{t}$ production lead to typical distributions of invariant masses.

In summary, the ideal way to determine the significance of a independent full model including interference compared to model of QCD $t\bar{t}$ production only is the following.

- Generation of several QCD distributions. These are needed, so that statistical fluctuations of a single distribution are compensated by the other distributions. With many independent distributions, the statistical spread of samples can be estimated and taken into account.

- Only one signal distribution is needed, because it can be determined sufficiently accurate. Statistical uncertainties usually are much smaller than the accuracy of the QCD distribution.

- One distribution of the full model is needed, which has to be determined to a high degree of precision. This distribution usually contains only a small contribution of resonances. To distinguish this distribution from a typical QCD distribution, statistical uncertainties of the full model have to be much smaller than the expected excess, caused by the resonance.

- For a comparison with QCD $t\bar{t}$ production, the pure resonance distribution has to be added on top of an arbitrary QCD distribution. The distribution of the full model already includes the contribution of QCD by construction. To determine the expected significance of such distributions, they have to be compared with an independent distribution of QCD $t\bar{t}$ production. To minimise effects of

statistical fluctuations, this comparison has to be done with many independent distributions so that statistical uncertainties are respected properly.

This study only uses two independent samples of QCD $t\bar{t}$ production. A larger number of samples would have exceeded capabilities of the currently available computer clusters.

6.4.3 Treatment of Systematic Uncertainties

All parameters of an experiment are only known to a certain degree of precision. Among the most important uncertainties for this study are the absolute scale of jet energies (JES), the form of parton distribution functions, the values of total cross sections or the total integrated luminosity of an experiment. These systematic uncertainties have to be taken into account when calculating exclusion limits for an experiment. They enter the calculation of significances at two points:

- Uncertainties affecting the expected total number of events are treated in the determination of the number of events of an ensemble. Before calculating the expected number of events, the luminosity $\mathscr{L}$ and the total cross section σ are smeared with a Gaussian distribution according to the *rate uncertainties* of all systematic errors. The resulting expected number of events is again smeared with a Poisson distribution to account for statistical fluctuations in the number of measured events. The final number is the number of events for the respective ensemble.

- *Shape uncertainties* affect only the form of a distribution, but not the number of events. They are treated similarly as rate uncertainties, but they may affect each bin of a distribution differently. Each uncertainty is represented by a distribution E containing one standard deviation from the model prediction. A random variable δ is determined for each uncertainty, representing how many standard deviations the current ensemble differs from the central model prediction for the respective uncertainty. In most cases the variable is distributed according to a Gaussian normal distribution, although there are also rare cases with different properties. The final ensemble is the sum of the original ensemble and all weighted uncertainties

$$D^{\text{syst}} = D + \sum_i \delta_i \cdot E_i \,,$$

  where i is just a counter for all uncertainties.

Shape uncertainties for the QCD channel, the pure resonance and the full channel are calculated as just described.

$$D^{\text{syst}}_{\text{QCD}} = D_{\text{QCD}} + \sum_i \delta_i \cdot E_{\text{QCD},i}$$
$$D^{\text{syst}}_{\text{Res}} = D_{\text{Res}} + \sum_i \delta_i \cdot E_{\text{Res},i}$$
$$D^{\text{syst}}_{\text{QCD+Res}} = D_{\text{QCD+Res}} + \sum_i \delta_i \cdot E_{\text{QCD+Res},i}$$

The δ parameter is always the same for all contributions because they are affected equally by systematic errors.

If a resonance distribution is to be compared with another distribution, is has to be added on top of the QCD $t\bar{t}$ distribution. In this step the resonance can also be scaled with a parameter κ in order to account for an unknown strength of coupling to Standard Model particles. The full resonance distribution is then calculated by

$$\begin{aligned} D^{\text{syst}}_{\text{QCD}} + \kappa D^{\text{syst}}_{\text{Res}} &= D_{\text{QCD}} + \sum_i \delta_i \cdot E_{\text{QCD},i} + \kappa \left(D_{\text{Res}} + \sum_i \delta_i \cdot E_{\text{Res},i} \right) \\ &= D_{\text{QCD}} + \kappa D_{\text{Res}} + \sum_i \delta_i \cdot \left(E_{\text{QCD},i} + \kappa E_{\text{Res},i} \right) . \end{aligned}$$

In case of a large interference between an unknown resonance and the QCD $t\bar{t}$ processes, the invariant mass spectrum can no longer be split into two independent parts and the resonance contribution cannot be scaled arbitrarily without also scaling the QCD contribution. Therefore, systematic uncertainties are decomposed into three components, a QCD part, a resonance part and an interference part. Afterwards, systematic uncertainties are scaled to different resonance strengths just like described above in sections 2.2.3 and 6.3.

The full distribution with a scaled resonance including systematic errors is calculated by

$$
\begin{aligned}
D^{\text{syst}}_{\text{QCD}+\kappa\text{Res}} &= D^{\text{syst}}_{\text{QCD}} + \kappa D^{\text{syst}}_{\text{Res}} + \sqrt{\kappa} D^{\text{syst}}_{\text{Int}} \\
&= D^{\text{syst}}_{\text{QCD}} + \kappa D^{\text{syst}}_{\text{Res}} + \sqrt{\kappa} \left(D^{\text{syst}}_{\text{QCD+Res}} - D^{\text{syst}}_{\text{QCD}} - D^{\text{syst}}_{\text{Res}} \right) \\
&= \sqrt{\kappa} D^{\text{syst}}_{\text{QCD+Res}} + (1-\kappa) D^{\text{syst}}_{\text{QCD}} + \left(\kappa - \sqrt{\kappa} \right) D^{\text{syst}}_{\text{Res}} \\
&= \left(1 - \sqrt{\kappa} \right) \left(D_{\text{QCD}} + \sum_i \delta_i \cdot E_{\text{QCD},i} \right) \\
&\quad + \left(\kappa - \sqrt{\kappa} \right) \left(D_{\text{Res}} + \sum_i \delta_i \cdot E_{\text{Res},i} \right) \\
&\quad + \sqrt{\kappa} \left(D_{\text{QCD+Res}} + \sum_i \delta_i \cdot E_{\text{QCD+Res},i} \right) \\
&= \left(1 - \sqrt{\kappa} \right) D_{\text{QCD}} + \left(\kappa - \sqrt{\kappa} \right) D_{\text{Res}} + \sqrt{\kappa} D_{\text{QCD+Res}} \\
&\quad + \sum_i \delta_i \cdot \left[\left(1 - \sqrt{\kappa} \right) E_{\text{QCD},i} + \left(\kappa - \sqrt{\kappa} \right) E_{\text{Res},i} + \sqrt{\kappa} E_{\text{QCD+Res},i} \right]
\end{aligned}
$$

With this method it is possible to treat processes equally where interferences are either ignored or not. Thus, this method is suitable to compare both kinds of processes.

7

Studies on $t\bar{t}$ Resonances

"Reality is determined not by what scientists
or anyone else says or believes
but by what the evidence reveals to us."
— Alan Hale

In order to provide realistic exclusion limits for various types of $t\bar{t}$ resonances, a chain of mathematical methods and calculations has to be established and checked for plausibility. Calculation of simulated events from an event generator have to agree with similar calculations. In case of the new Heavy Quark Resonance Model for HERWIG++, the calculation has to match results with existing matrix elements.

Resonances of top-antitop quark pairs have been previously studied by many people [60, 148, 149, 150]. Also interferences of resonances with QCD continuum production of $t\bar{t}$ pairs have been explicitly investigated [43, 99]. Results of this work are also compared to these studies.

Finally, simulated events are fed into a simulation of the ATLAS detector to receive pseudodata as a basis for a realistic reconstruction and investigation of sensitivities to different types of $t\bar{t}$ resonances. With this information, the importance of interference can be evaluated compared to the strength of the pure resonance. Exclusion limits can be set, depending whether interference between the resonance and the QCD continuum are taken into account or ignored.

7.1 Consistency Checks of the Heavy Quark Resonance Model

Every new model for an event generator has to be checked for accuracy of its predictions. The most important test is a comparison with measured data. As measurement at the LHC only has started recently at $\sqrt{s} = 7\,\mathrm{TeV}$ no data is available for $\sqrt{s} = 14\,\mathrm{TeV}$. In order to check consistency of the Heavy Quark Resonance Model, its predictions are compared to results obtained with existing processes already implemented in HERWIG++.

As only the matrix element has been changed, it is sufficient to check only its outgoing particles to match properties with outgoing particles of existing matrix elements. All subsequent steps are equal for all matrix elements and do not need to be checked. Therefore, only distributions of the outgoing top and antitop quarks have to be compared with outputs of different matrix elements. Distributions to be compared are the spectra of invariant masses of the top quark pairs, the transverse momenta and the pseudorapidity of the top and antitop quarks. Distributions of the azimuthal angle have also been checked to be flat in all cases, so that they are not shown explicitly.

7.1.1 Top Quark Pair Production in QCD

The new model is based on the existing matrix element for production of heavy quark pairs. Originally this matrix element of HERWIG++ was able to calculate the five QCD Feynman diagrams including gluon-gluon and quark-antiquark scattering (a)–(e) of table 3.1. The behaviour of this matrix element can be reproduced in the Heavy Quark Resonance Model by switching off all diagrams including a resonance (`set MEpp2HeavyQQbar:Resonance off`).

A comparison between both models is shown in figure 7.1. The six diagrams show comparisons in five different quantities. In the top row, Figures (a) and (b) show the distributions of transverse momenta for the top and anti-top quarks respectively. In the middle row, Figures (c) and (d) show the distributions of transverse momenta for the top and anti-top quarks respectively.

Distribution (e) shows the invariant mass spectrum of the top quark pairs up to $5\,{}^{\mathrm{TeV}}/_{c^2}$ in logarithmic scale. Errors of all entries are small enough to be only visible in the highest bins of the logarithmic representation. The distribution rises from $2m_t = 345\,{}^{\mathrm{GeV}}/_{c^2}$ and reaches its maximum at about $400\,{}^{\mathrm{GeV}}/_{c^2}$. At high invariant masses the spectrum falls off almost exponentially.

Distributions of both models are equal in all quantities. Differences arise from statistical fluctuations only. Generation of $t\bar{t}$ pairs in QCD is reproduced accurately by the

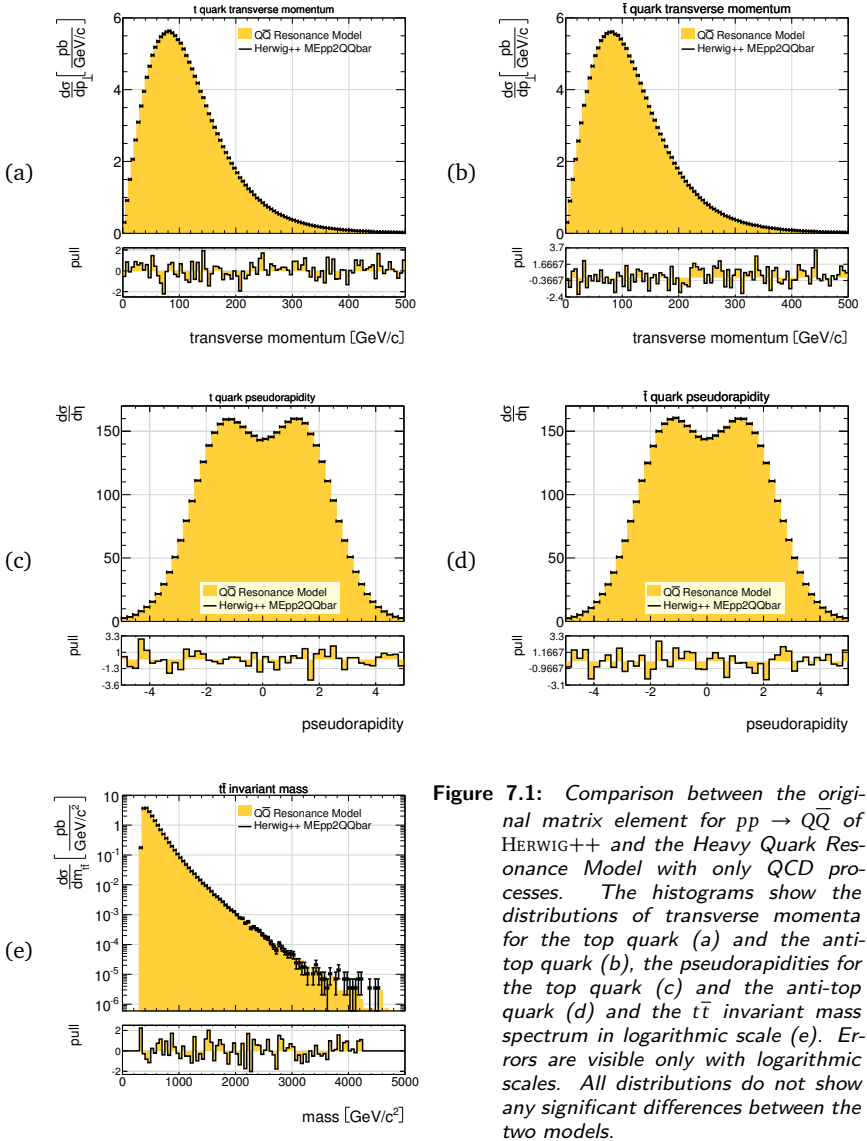

Figure 7.1: *Comparison between the original matrix element for $pp \to Q\overline{Q}$ of* HERWIG++ *and the Heavy Quark Resonance Model with only QCD processes. The histograms show the distributions of transverse momenta for the top quark (a) and the anti-top quark (b), the pseudorapidities for the top quark (c) and the anti-top quark (d) and the $t\bar{t}$ invariant mass spectrum in logarithmic scale (e). Errors are visible only with logarithmic scales. All distributions do not show any significant differences between the two models.*

Heavy Quark Resonance Model. This should be the expected behaviour, because the Heavy Quark Resonance Model was built with the `MEpp2QQbar` matrix element as a template.

7.1.2 Standard Model Higgs Boson Production

As a second test, production of Standard Model Higgs bosons is investigated which decay into a pair of top quarks. QCD diagrams are switched off and the parameters of the resonance are set to the quantum numbers of the SM Higgs boson. Three different masses of 400, 500 and 600 GeV/c^2 are used with their respective decay widths of 27.44, 63.14 and 113.70 GeV/c^2.

The matrix element for Higgs boson production provided by HERWIG++ is called `MEHiggs`. It only calculates the production of Higgs bosons from protons. Masses of Higgs bosons are distributed according to a Breit-Wigner function. Their decays follow the SM branching ratios of Higgs bosons into all possible types of SM fermions as well as $W^{\pm}$ and Z^0 bosons. As the decay into a pair of top quarks is implicit in the Heavy Quark Resonance Model, events from the `MEHiggs` matrix element have to be selected only if the Higgs boson decays into top quarks.

Figures 7.2, 7.3 and 7.4 compare the Heavy Quark Resonance Model with the `MEHiggs` matrix element for Higgs boson production of $m_h = 400$, 500 and 600 GeV/c^2 respectively. The histograms show the $t\bar{t}$ invariant mass spectrum with linear and logarithmic scales, the distributions of transverse momenta for the top quark and the anti-top quark and pseudorapidities for the top quark and the anti-top quark.

All distributions show differences in the total cross section as well as different shapes. Differences in shape can be explained with a cut-off in the original `MEHiggs` matrix element, where the Higgs propagator is cut off for values greater than a predefined threshold, which is usually set to $m_h + 10 \cdot \Gamma_h$. This cut off can be seen in histograms (a) and (b) of figures 7.2 and 7.3. In figure 7.4 the cut-off is not visible because it lies at the boundary of the the shown mass range.

For this reason, events with high $t\bar{t}$ invariant mass are missing in the sample of the `MEHiggs` matrix element. This also leads to a reduced number of particles with high transverse momentum.

Differences in total cross sections are a second issue. They are unrelated to the differences in shape because they remain similar although the cut-off gets less important for larger masses. This discrepancy can easily be corrected by rescaling distributions. As leading order calculations, like the present one, are known to underestimate total

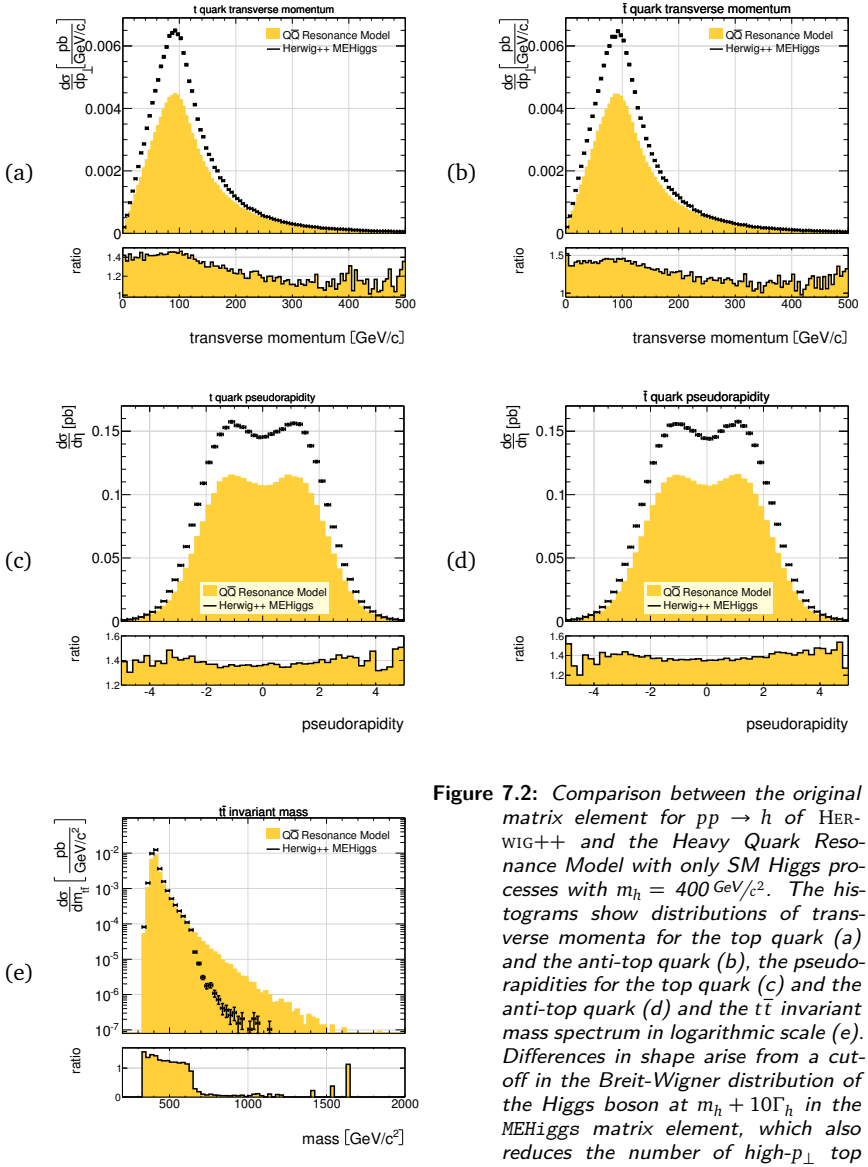

Figure 7.2: *Comparison between the original matrix element for $pp \to h$ of* HERWIG++ *and the Heavy Quark Resonance Model with only SM Higgs processes with $m_h = 400\,\mathrm{GeV}/c^2$. The histograms show distributions of transverse momenta for the top quark (a) and the anti-top quark (b), the pseudorapidities for the top quark (c) and the anti-top quark (d) and the $t\bar{t}$ invariant mass spectrum in logarithmic scale (e). Differences in shape arise from a cut-off in the Breit-Wigner distribution of the Higgs boson at $m_h + 10\Gamma_h$ in the* `MEHiggs` *matrix element, which also reduces the number of high-$p_\perp$ top quarks.*

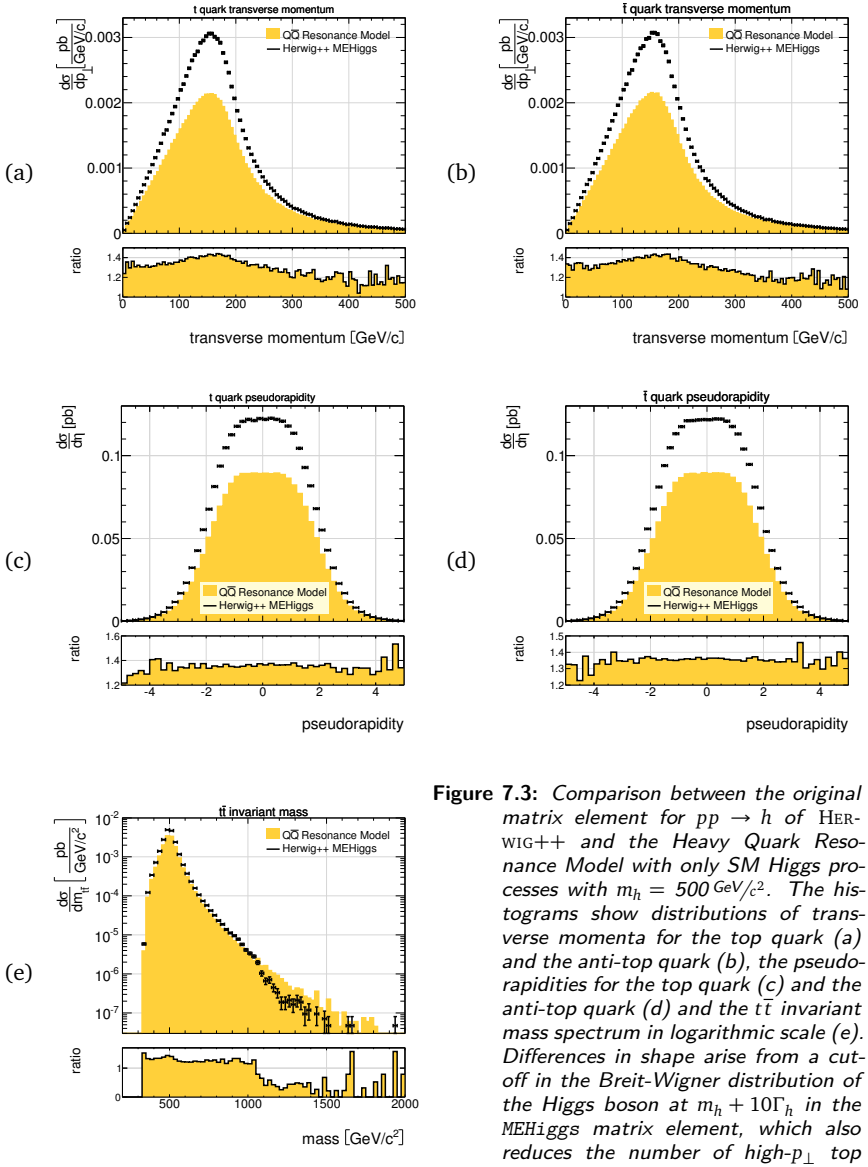

Figure 7.3: *Comparison between the original matrix element for $pp \to h$ of* HERWIG++ *and the Heavy Quark Resonance Model with only SM Higgs processes with $m_h = 500\,\mathrm{GeV}/c^2$. The histograms show distributions of transverse momenta for the top quark (a) and the anti-top quark (b), the pseudorapidities for the top quark (c) and the anti-top quark (d) and the $t\bar{t}$ invariant mass spectrum in logarithmic scale (e). Differences in shape arise from a cut-off in the Breit-Wigner distribution of the Higgs boson at $m_h + 10\Gamma_h$ in the* `MEHiggs` *matrix element, which also reduces the number of high-$p_\perp$ top quarks.*

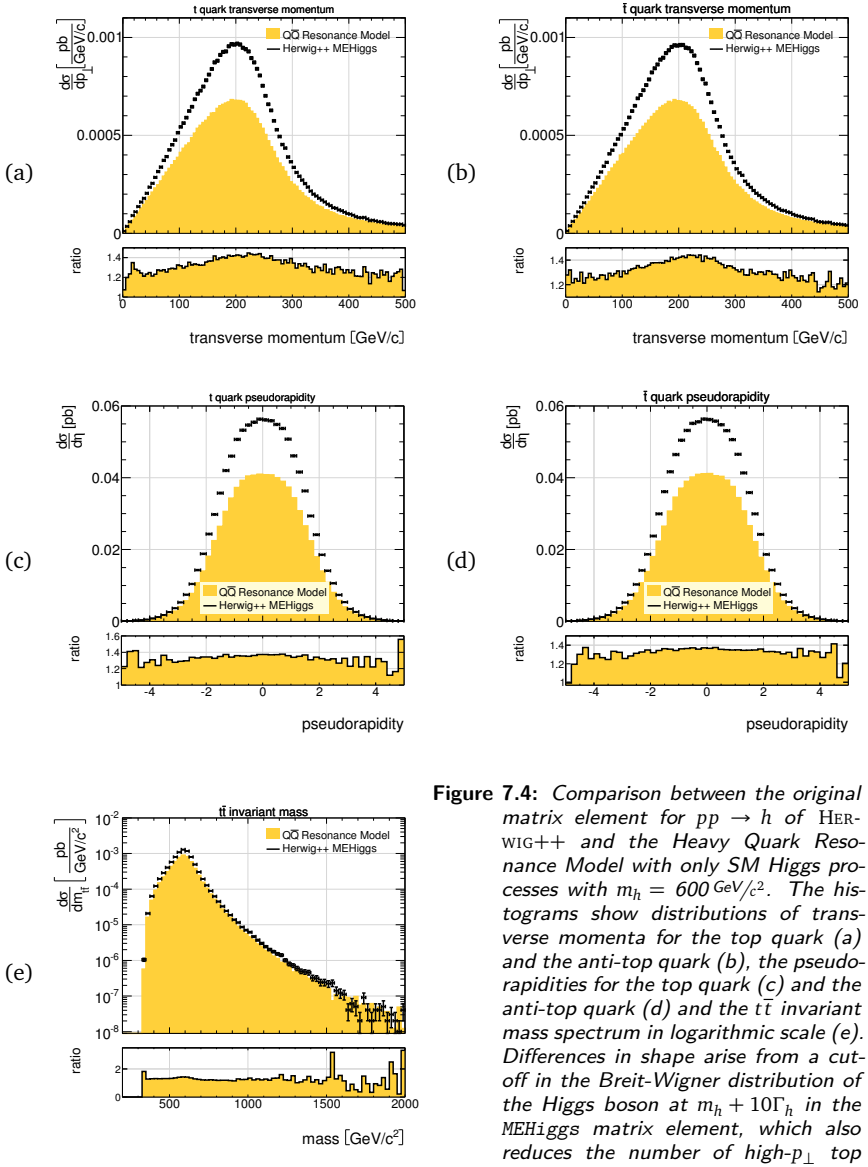

Figure 7.4: *Comparison between the original matrix element for $pp \to h$ of* HERWIG++ *and the Heavy Quark Resonance Model with only SM Higgs processes with $m_h = 600\,\mathrm{GeV}/c^2$. The histograms show distributions of transverse momenta for the top quark (a) and the anti-top quark (b), the pseudorapidities for the top quark (c) and the anti-top quark (d) and the $t\bar{t}$ invariant mass spectrum in logarithmic scale (e). Differences in shape arise from a cut-off in the Breit-Wigner distribution of the Higgs boson at $m_h + 10\Gamma_h$ in the* `MEHiggs` *matrix element, which also reduces the number of high-$p_\perp$ top quarks.*

$t\bar{t}$ cross sections of higher order calculations as well as cross sections determined in experiment, leading order results have to be rescaled in every analysis.

7.1.3 Existing Studies with Interferences and Spin Correlations

As already stated previously, the lifetime of a top quark is smaller than the typical timescale of strong interactions, which also reflects in its decay width being larger than the scale where QCD becomes strong, $\Gamma_t \approx 1.5\,\mathrm{GeV}/c^2 > \Lambda_{\mathrm{QCD}}$. Thus, it is the only quark which can be studied as a quasi-free particle. As such, also its spin information is conserved after its decay and passed on to its child particles. If the pair of top quarks originated from a resonance, they also carry information about the spin of their common parent.

This way, the top decay products also carry information about the resonance spin. Because the $W^{\pm}$ boson couples only to left-handed components of fermions, it translates the top quark spin into directions of flight of its decay products. Through this mechanism, the directions of flight of the $W^{\pm}$ child particles are 100 % correlated with the polarisation of the top quarks [151, 152, 43].

Additionally, also the children of both top quarks are correlated among each other in their directions of flight. As it turns out [151], the best way to determine the correlation between the decay products of both top quarks is given by the down-type fermions from the decays of both $W^{\pm}$ bosons.

A common quantity [153] to study spin correlations in $t\bar{t}$ events is the distribution of

$$\frac{1}{\sigma}\frac{d^2\sigma}{d(\cos\theta_+)d(\cos\theta_-)} = \frac{1}{4}\left[1 - A\cos(\theta_+)\cos(\theta_-) + b_+\cos(\theta_+) + b_-\cos(\theta_-)\right], \quad (7.1)$$

where the two angles θ_+ and θ_- are defined between the directions of flight of the top (antitop) quark in the $t\bar{t}$ centre-of-mass system and the down-type fermions in the top (antitop) rest frames, respectively.

Figure 7.5 shows the above distributions for several different models of $t\bar{t}$ production. Subfigure (e) contains the distribution for $t\bar{t}$ production in QCD. The following distributions show spin correlations for a scalar (a) and pseudoscalar (b) resonance with a mass of $m_{\mathrm{Res}} = 400\,\mathrm{GeV}/c^2$ and for a vector (c) and axial vector (d) resonance with a mass of $m_{\mathrm{Res}} = 1000\,\mathrm{GeV}/c^2$.

The distribution of the pure QCD $t\bar{t}$ production clearly shows an anti-correlation between both angles θ_+ and θ_-. If θ_+ vanishes, θ_- tends to assume values about π and also the other way round. This means, if the down-type fermion from the top quark

(a)

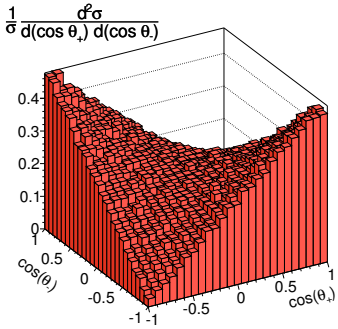

(b)

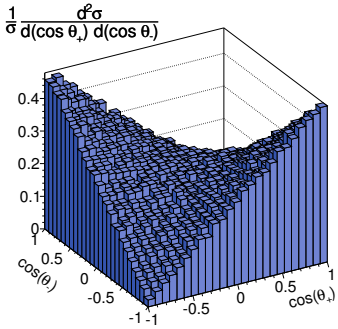

(c)

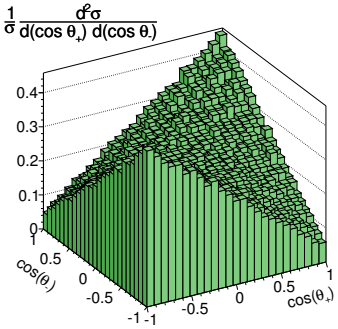

(d)

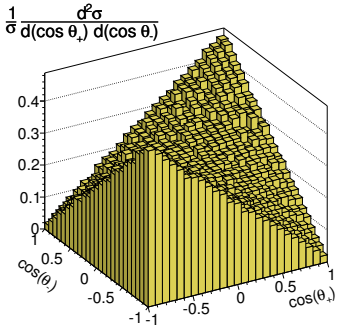

(e)

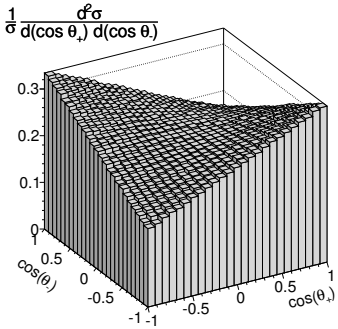

Figure 7.5: *Spin correlations for different resonance properties. Histograms show the correlation between the angles θ_+ and θ_- for scalar (a), pseudoscalar (b), vector (c), axial vector (d) resonances and QCD $t\bar{t}$ production (e)*

decay goes into the same direction as the top quark, the down-type fermion from the antitop quark tends to go into the opposite direction as the antitop quark.

The scalar and pseudoscalar resonances lead to similar effects of anti-correlation which are even stronger than in pure QCD $t\bar{t}$ production. One reason for spin correlations in QCD being weaker is because top quark pairs can be produced via three different processes, the s-, t- and u-channels. On the other hand, there is only the s-channel Feynman diagram for $t\bar{t}$ production via resonances. In this case, the pair of top quarks always inherits the spin information of the resonance in the same way.

In contrast, vector and axial vector resonances show an opposite behaviour of spin correlations. In this case, the angles θ_+ and θ_- are positively correlated. If the down-type fermion from the top quark decay goes into the same direction as the top quark, the down-type fermion from the antitop quark tends to go also into the same direction as the antitop quark. This also means, that spin correlations provide an opportunity to determine the spin of $t\bar{t}$ resonances.

Spin correlations of top quark pairs have also been investigated in previous studies [43]. Shapes of the above figures agree well with the shapes of figures 16 and 17 therein, whereas the normalisation differs significantly. Plots in this work have been normalised to unit volume. On the other hand, contrary to their description, figures 16 and 17 of [43] have not been normalised to unit volume, but also include information of the total cross sections of the respective processes [154]. Cross sections of both studies are difficult to compare because coupling parameters can be chosen arbitrarily and have been set differently.

resonance	mass $[\mathrm{GeV}/c^2]$	A	b_+	b_-	$\chi^2/\mathrm{n.d.f.}$
QCD $t\bar{t}$	—	0.36	-0.004	-0.004	0.94
scalar	400	0.98	-0.004	-0.006	1.13
pseudoscalar	400	0.98	-0.003	-0.006	1.08
vector	1000	-0.84	-0.008	-0.01	0.99
axial vector	1000	-0.98	-0.006	-0.007	0.98

Table 7.1: *Fit values of spin correlation distributions. Fits converged and lead to reasonable results which agree with values in [43].*

On the other hand, shapes can be compared easily by application of a two dimensional fit of equation 7.1 to the distributions. Values of the fit parameters have been calculated and are listed in table 7.1. Corresponding values determined in [43] and this work are consistent with each other in both independent calculations.

7.2 Determination of Mass Resolutions

The most important quantity for this work is the invariant mass of the original pair of top quarks. As their true 4-momenta are not accessible in experiment, they have to be determined from quantities measured by the detector. As explained earlier, these quantities are 4-momenta of jets, electrons or muons and the missing transverse momentum.

In order to check the accuracy of calculated invariant masses, they are also determined at different stages of the event, ranging from the original pair of top quarks to reconstructed jets after detector simulation. On each level of reconstruction, the concept remains always the same, i.e. certain partons, particles or jets are selected and their 4-momenta are summed up to receive their invariant mass m by

$$m^2c^2 = \left(\sum_{\text{partons/particles/jets}} p_i \right)^2 .$$

The general idea is to follow the decay chain of the $t\bar{t}$ pair and to reconstruct the $t\bar{t}$ invariant mass from their child particles or derived objects like jets. It is then possible to determine the accuracy of reconstructed invariant masses compared to respective partonic $t\bar{t}$ invariant masses, i.e. the mass resolution. Additionally, steps in reconstruction can be identified which introduce large statistical or systematic uncertainties.

At later stages of the event, the association of hadrons or jets to a parton is not defined unambiguously. In general, the original pair of top quarks is not neutral in colour charge, but hadrons and jets are. Therefore, the top quarks or their children have to compensate their colour charges by interactions with partons from the underlying event. At this point, the association of a hadron to either the hard event or the underlying event is not unique any more. For the following investigations, such hadrons have been considered as coming from the hard event as the energy transfer from the underlying event is considered small.

A second ambiguity arises from the association of jets to one of the quarks of the outgoing fermions of the t, $\bar{t}$, W^+ and W^- decays. Quarks are associated with available jets, such that the difference in

$$\Delta R = \sqrt{(\Delta\eta)^2 + (\Delta\varphi)^2}$$

between the 4-momenta of the quark and the jet is minimal. If two or more quarks are associated with the same jet, the jet momentum is considered only once.

In case a $W^{\pm}$ boson decays leptonically, the true 4-momenta of the charged lepton and the corresponding neutrino are included into the invariant mass reconstruction. Only in the last step, the semileptonic reconstruction of the invariant mass, a kinematical fit is applied for the z-component of the neutrino momentum using the missing transverse momentum as explained in section 6.2.

The invariant mass has been determined on the following stages of every event.

$\mathbf{t\bar{t}}$ The immediate $t\bar{t}$ invariant mass is calculated immediately from the 4-momenta of the top and antitop quarks. This is the value of reference that any other calculation has to match. Large deviations from this value indicate miscalculations, which sometimes cannot be avoided, e.g. when the wrong solution for the z-component of the neutrino momentum is chosen.

$\mathbf{W^+W^-b\bar{b}}$ The $t\bar{t}$ invariant mass is calculated from the $t\bar{t}$ decay products, after each top quark decayed into a $W^{\pm}$ boson and a $b/\bar{b}$ quark respectively.

$\mathbf{f_1\bar{f}_2f_3\bar{f}_4b\bar{b}}$ After the two $W^{\pm}$ bosons decayed into fermion-antifermion pairs, the invariant mass is calculated again. No separation is done between the different decay channels of the $W^{\pm}$ bosons.

first hadrons Only first hadrons are considered just after they have formed during hadronisation. Secondary hadrons from hadron decays are ignored. Only those hadrons are taken into the calculation of the $t\bar{t}$ invariant mass, that can be traced back to a top quark, i.e. which are child particles of an original top or antitop quark. If a $W^{\pm}$ boson decayed leptonically, the respective charged lepton and the neutrino are also considered for the invariant mass calculation.

stable $\mathbf{t\bar{t}}$ children All final state particles are taken into account for the calculation of the invariant mass, that originate from the decays of the top or antitop quarks. Particles from the underlying event are ignored.

stable $\mathbf{t\bar{t}}$ children in any jets Only final state particles with a connection to the original $t\bar{t}$ pair are considered, which additionally end up in one of all jets obtained from all final state particles with the Anti-$k_{\perp}$ jet algorithm. Particles outside any jets are ignored.

stable $\mathbf{t\bar{t}}$ children in matched jets Only final state particles with a connection to the original $t\bar{t}$ pair are considered. Additionally, they have to end up in a jet that is matched to one of the quarks of the outgoing fermions of the t, $\bar{t}$, W^+ and W^- decays. In semileptonic events, the 4-momenta of the charged lepton and the corresponding neutrino are adopted unchanged.

stable $\mathbf{t\bar{t}}$ children in highest $\mathbf{p_{\perp}}$ jets This step considers final state particles from the $t\bar{t}$ decay which end up in jets with the highest transverse momentum. In

semileptonic events, 4 jets are included which are expected to originate from the four quarks of the semileptonic $t\bar{t}$ decay.

stable particles in matched jets The 4-momenta of all final state particles are summed up, which lie inside jets that are matched to a parton from the $t\bar{t}$ decay. The matching is done as described above.

stable particles in highest $\mathbf{p}_\perp$ jets The invariant mass is determined from all final state particles which also lie inside one of the jets with highest transverse momentum.

semileptonic reconstruction The invariant mass is calculated with the semileptonic reconstruction after all events have passed the DELPHES detector simulation. The 4-momentum of the leptonically decaying $W^\pm$ boson is obtained from the kinematical fit of a charged lepton and the missing transverse momentum. The invariant mass is calculated from the sum of all 4-momenta of four jets and the fitted momentum of the $W^\pm$ boson.

On each level it is possible to check how the distribution of the invariant mass changes compared to the original $t\bar{t}$ mass distribution. Figures 7.6 and 7.7 show the development of the reconstructed invariant mass from parton level to the complete reconstruction after detector simulation. In order to be able to compare all histograms with each other, only semileptonic decays of the pair of top quarks are taken into account.

As all particles have non-vanishing decay widths, reconstruction of invariant masses cannot be perfect. Deviations in reconstruction are expected to grow with increasing level of reconstruction. In order to obtain a measure for the error made in reconstruction, the relative difference in invariant masses $\frac{m_{\text{reco}} - m_{t\bar{t}}}{m_{t\bar{t}}} = \frac{m_{\text{reco}}}{m_{t\bar{t}}} - 1$ is calculated at each reconstruction level. Widths of the distributions are measured by taking their full width at half maximum (FWHM) divided by $2\sqrt{2 \cdot \ln(2)}$ in order to obtain the equivalent width of a Gaussian distribution. All resolutions are summarised later in table 7.2.

Figure 7.6 shows relative error distributions from the direct children of the top quarks up to an invariant mass of stable final state children of the $t\bar{t}$ decay. At these levels, reconstructed invariant masses accurately match the $t\bar{t}$ invariant mass. The relative error of invariant masses calculated from all $t\bar{t}$ children is smaller than 1 %.

The last diagram in this figure shows the relative error when the invariant mass is determined only from those $t\bar{t}$ children which end up inside an arbitrary jet cone found by the Anti-$k_\perp$ jet clustering algorithm. This distribution has a width of 2.5 % which is a significant increase compared to a width of 0.5 % of the previous level. This effect shows that there are always some particles from the $t\bar{t}$ decay that end up outside

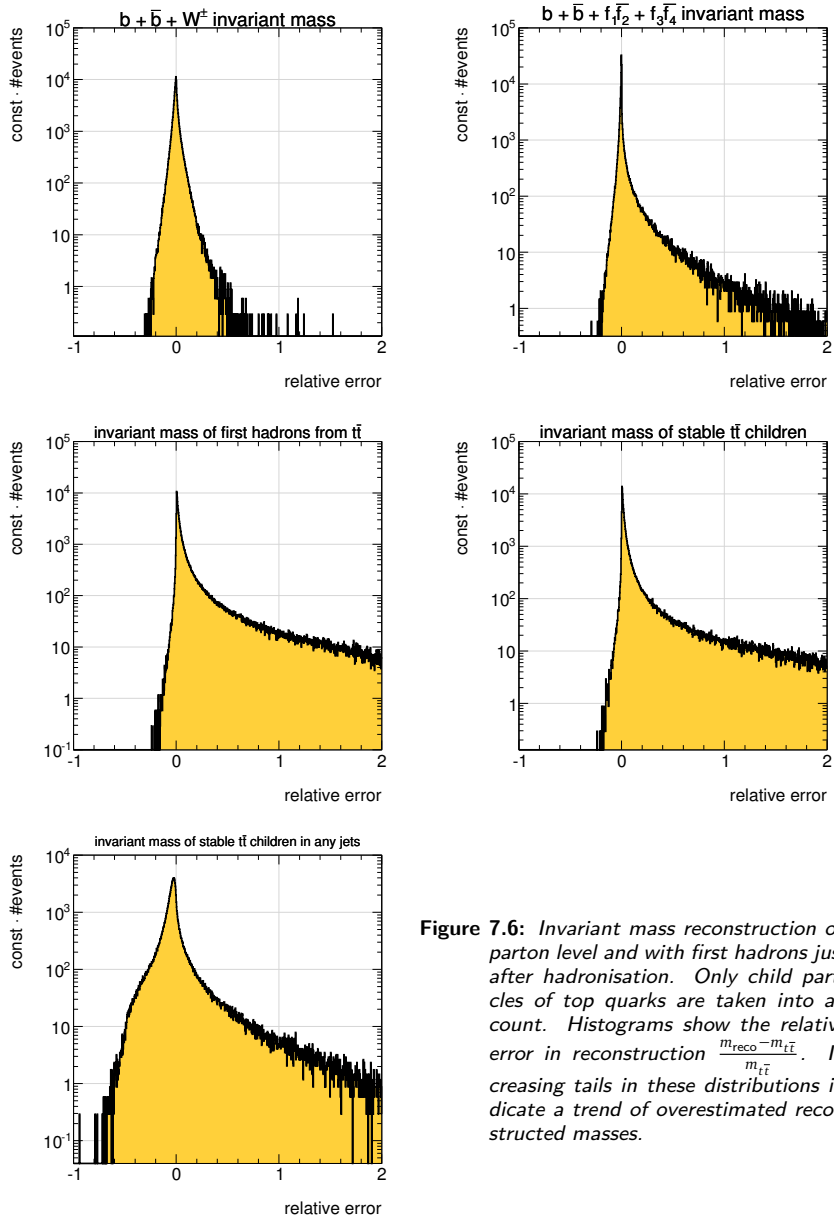

Figure 7.6: *Invariant mass reconstruction on parton level and with first hadrons just after hadronisation. Only child particles of top quarks are taken into account. Histograms show the relative error in reconstruction* $\frac{m_{\text{reco}} - m_{t\bar{t}}}{m_{t\bar{t}}}$. *Increasing tails in these distributions indicate a trend of overestimated reconstructed masses.*

of any jet cone. Neglected momenta of missing particles broaden the error distribution and also slightly shift the peak of the invariant mass to lower values.

Diagrams in figure 7.7 show further error distributions with different selections of particles and jets. The top row contains distributions of $t\bar{t}$ children whereas the middle row contains histograms of all stable particles. In the left column, only particles have been considered that end up in jets which are matched to one of the fermions of the t, $\bar{t}$ or $W^{\pm}$ decays. In the column on the right hand side, only particles within the jets with the highest transverse momenta have been considered.

The distribution of the relative error does not change much when going from stable $t\bar{t}$ children in matched jets to those in jets with highest transverse momentum. This implies, that the highest $p_{\perp}$ jets most probably are jets from the $t\bar{t}$ decay. The fact that there is a slight difference in the distributions shows some rare cases where a jet from the underlying event has a larger $p_{\perp}$ than one of the four jets of a semileptonic event.

The transition from stable $t\bar{t}$ children to all stable particles in jets matched to fermions from the $t\bar{t}$ decay also is moderate. The distribution becomes rather symmetric, which is a consequence of a particles from the underlying event ending up in a jet associated to a quark from the $t\bar{t}$ decay.

The next histogram combines the transition to all stable particles with the choice of jets with highest transverse momentum. In contrast to the two previous comparisons, the step from stable $t\bar{t}$ children in matched jets to stable particles in highest $p_{\perp}$ jets shows a large difference in distributions. This can be explained by the fact that this determination of the invariant mass does not rely on any information of partons. Particles do not have to originate from the hard event and jets do not have to be associated to partons any more. Therefore, the result is affected by the underlying event as well as initial state radiation, which can also produce jets with high transverse momentum. As a result, the peak of this distribution is also shifted slightly to a higher mass.

Although the selection of jets may by improved by constrains on dijet invariant masses, this histogram gives a good impression on the experimentally achievable mass resolution. This histogram was calculated using simulated events without any detector simulation. In experiment, any detector can only increase errors on invariant masses.

The last diagram in figure 7.7 shows the semileptonic reconstruction of the invariant mass as described in section 6.2 after all events have passed the DELPHES detector simulation. The shape of the distribution has not changed significantly, but its width has increased to 16.6 %.

Table 7.2 summarises widths of distributions of all levels of reconstruction. Many different effects are responsible for a non-vanishing resolution of the invariant mass.

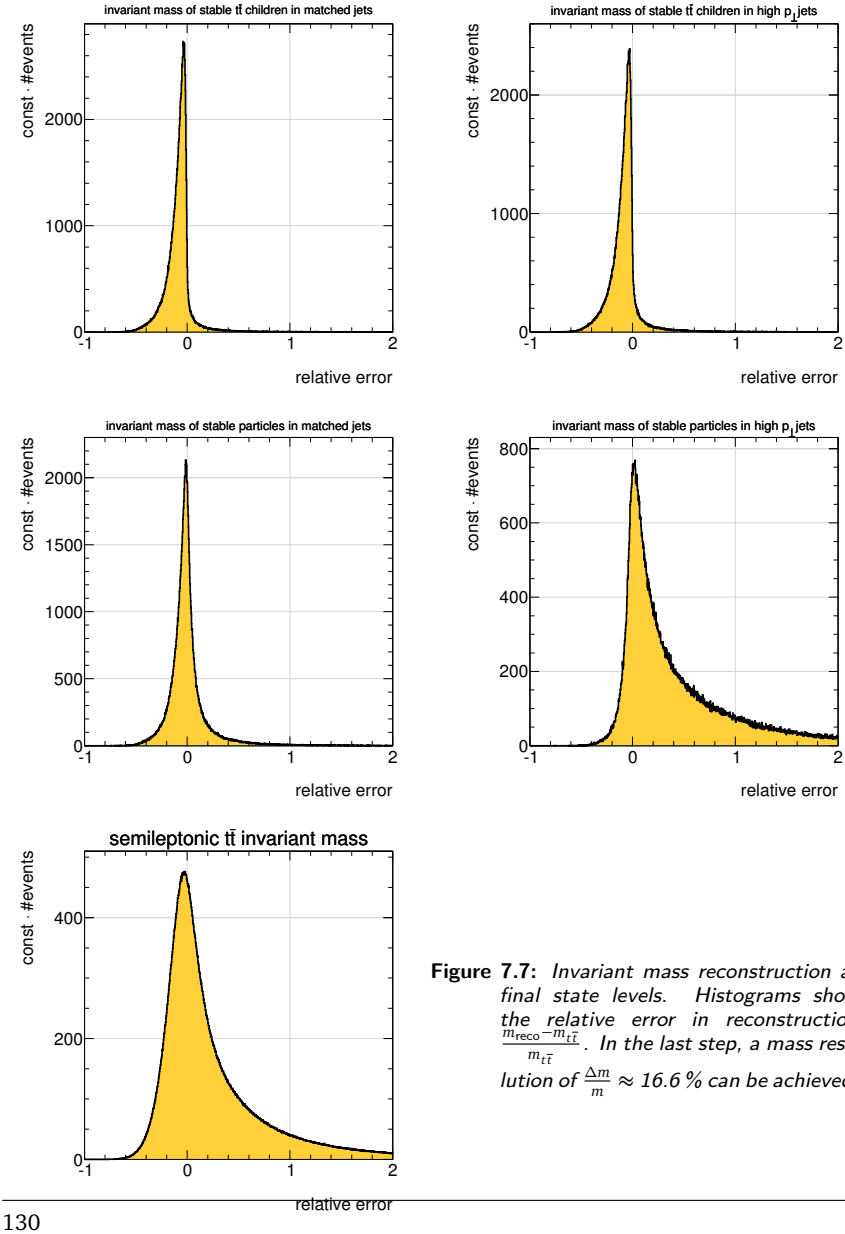

Figure 7.7: *Invariant mass reconstruction at final state levels. Histograms show the relative error in reconstruction* $\frac{m_{\text{reco}} - m_{t\bar{t}}}{m_{t\bar{t}}}$. *In the last step, a mass resolution of* $\frac{\Delta m}{m} \approx 16.6\,\%$ *can be achieved.*

level of reconstruction	mass resolution
$W^+W^-b\bar{b}$	0.9 %
$f_1\bar{f}_2f_3\bar{f}_4b\bar{b}$	0.2 %
first hadrons	0.6 %
stable $t\bar{t}$ children	0.5 %
stable $t\bar{t}$ children in jets	2.5 %
stable $t\bar{t}$ children in matched jets	4.3 %
stable $t\bar{t}$ children in high $p_\perp$ jets	4.7 %
stable particles in matched jets	4.8 %
stable particles in high $p_\perp$ jets	10.3 %
semileptonic reconstruction	16.6 %

Table 7.2: *Mass resolution on different levels of reconstruction. Largest errors in reconstruction are introduced in the latest stages by jet clustering and jet selection, detector effects and the semileptonic reconstruction.*

Main contributions to the resolution come from initial state radiation and underlying events. This error can be estimated by $\sqrt{(10.3\,\%)^2-(4.8\,\%)^2} = 9.1\,\%$. Detector effects and the reconstruction of the z-momentum of the neutrino from the lepton momentum and missing transverse momentum contribute with an error of $\sqrt{(16.6\,\%)^2-(10.3\,\%)^2} = 13.0\,\%$.

Although the exact values of resolutions at different stages of an event and its reconstruction depend on chosen algorithms and methods, the above values give an estimate of what can be achieved in experiment and which is the fundamental physical limit of mass resolution.

7.3 Example Models

This work investigates several different scenarios with $t\bar{t}$ resonances of different types of couplings and quantum numbers at several masses and decay widths. The Heavy Quark Resonance Model has been implemented as flexible as possible. It provides a large number of configurable parameters, which reflect the large number of possible $t\bar{t}$ resonances. As it is not possible for this study to cover all possible configurations, five different models with interesting properties have been chosen, which show some characteristic features. Properties of the chosen types of resonances are summarised in table 7.3.

model name	type of coupling	spin [$\hbar$]	colour representation	parities (1,γ_5)
scalar Higgs	SM Higgs-like	0	[1]	(1, 0)
pseudoscalar Higgs	SM Higgs-like	0	[1]	(0, 1)
sequential Z'	SM Z^0	1	[1]	(SM, SM)
coloron	strong	1	[8]	(1, 0)
axigluon	strong	1	[8]	(0, 1)

Table 7.3: *Models investigated in this study. Quantum numbers have been chosen to cover a wide range of possible combinations, which are also motivated by extensions of the Standard Model.*

These Models have been analysed for several different masses of the resonance. Masses have been chosen such that each model contains samples with large contributions of resonances which are easily visible and detectable as well as other samples with only small contributions of resonances which are expected hard to discover.

Couplings have been fixed equally for all masses of the same type of resonance. Although this also fixes all decay widths of the theoretical model, it is possible to define decay widths separately in HERWIG++ to account for unknown decay modes or unusual properties of the considered model. Therefore, all resonances have been assumed with a decay width of 1 % of their mass, i.e.

$$\frac{\Gamma_{\text{Res}}}{m_{\text{Res}}} = 1\,\%,$$

so that all of them can be treated as narrow resonances. As seen in section 7.2, the resolution of the invariant mass for semileptonically decaying pairs of top quarks is of the order of 15 %. Thus the decay widths of all resonances is much smaller than the experimental resolution, which means that effects from different decay widths can be ignored.

7.3.1 $t\bar{t}$ Production in QCD

Production of top quark pairs via QCD is considered as the null hypothesis in later investigations. Every model is compared to QCD production of top quarks without any resonance. For this reason, an accurate prediction of the cross section and the shape of the invariant mass spectrum is important. Samples of $t\bar{t}$ production in QCD have been generated for five different centre-of-mass energies. Information about these

samples is summarised in table 7.4. Calculated cross sections are lower than analytic

data set	centre-of-mass energy [TeV]	number of events	cross section [pb]	equivalent integrated luminosity [$^1/_{fb}$]
QCD ($p\overline{p}$)	1.96	100000	5.985	1.671
QCD	7	1000000	142.1	7.036
	8	1000000	207.7	4.815
	10	1000000	378.5	2.642
	14	25020000	871.5	28.71

Table 7.4: *QCD datasets. An increased number of events has been generated for the sample of 14 TeV centre-of-mass energy, because it is used for the subsequent analysis of $t\overline{t}$ resonances.*

calculations [155, 156, 157], measurements at Tevatron [158, 159] as well as first measurements at the LHC at a centre-of-mass energy of $\sqrt{s} = 7\,\text{TeV}$ [160, 161]. Deviations from all these determinations of cross sections are expected, because calculations of this study are limited to leading order accuracy, which are known to underestimate results at higher precision. As this work focuses on proton-proton collisions at a centre-of-mass energy of 14 TeV, this sample has been chosen to contain a much larger number of events in order to obtain accurate results for the invariant mass spectrum even at large invariant masses up to $4\,^{\text{TeV}}/_{c^2}$. Even larger invariant masses are hard to produce as can be estimated from figure 7.1(e). Only a fraction of about $2 \cdot 10^{-6}$ of all events have an invariant mass above $4\,^{\text{TeV}}/_{c^2}$.

The number of generated events directly affects the amount of resonance events that can be excluded. A large number of simulated events ensures an accurate prediction of the invariant mass spectrum. Predictions of different models can only be distinguished, if their difference is larger than statistical and systematic errors of each prediction. This has to be considered at large invariant masses, where only few events from the full mass spectrum are available.

7.3.2 The Scalar Higgs Model

The scalar Higgs model assumes couplings and quantum numbers of the Standard Model Higgs boson. Only its decay width has been defined differently. The decay width of the Standard Model Higgs boson increases according to the third power of its mass $\Gamma_h \sim m_h^3$ for $m_h > 2m_{Z^0} = 182.38\,^{\text{GeV}}/_{c^2}$. For large masses of the Higgs boson

	Higgs datasets		pure resonance			QCD $t\bar{t}$ + resonance + interference		
	mass [GeV/c^2]	width [GeV/c^2]	number of events	cross section [pb]	equivalent integrated luminosity [1/fb]	number of events	cross section [pb]	equivalent integrated luminosity [1/fb]
scalar	400	4	1010000	4.002	252.4	15015000	871.08	17.237
	500	5	1005000	5.643	178.1	15000000	874.24	17.158
	600	6	1010000	3.585	281.7	15035000	873.72	17.208
	700	7	1030000	1.953	527.4	25000000	873.00	28.637
	800	8	1000000	1.033	967.8	25000000	872.38	28.657
	900	9	1000000	0.5530	1808.2	25015000	871.93	28.689
	1000	10	1005000	0.3023	3324.1	25005000	871.75	28.684
	1500	15	1020000	0.02129	47908.3	25005000	871.51	28.686
	2000	20	1000000	0.002475	404015.9	25000000	871.45	28.688
pseudoscalar	400	4	1035000	41.90	24.70	15025000	918.8	16.35
	500	5	1020000	19.93	51.19	15035000	899.3	16.72
	600	6	1020000	8.410	121.3	15085000	885.5	17.03
	700	7	1000000	3.701	270.2	25010000	879.5	28.44
	800	8	1015000	1.727	587.9	25080000	876.3	28.62
	900	9	1000000	0.8494	1177.4	25040000	874.4	28.64
	1000	10	1030000	0.4385	2348.8	25100000	873.6	28.73
	1500	15	1005000	0.02750	36551.4	25025000	872.2	28.69
	2000	20	1015000	0.003234	313810.7	25005000	871.9	28.68

Table 7.5: *Datasets of the scalar and pseudoscalar Higgs samples. Samples of the pure resonance have been chosen to contain 1 Mio events, whereas samples of the full process contain at least 15 Mio or 25 Mio events for higher resonance masses, respectively.*

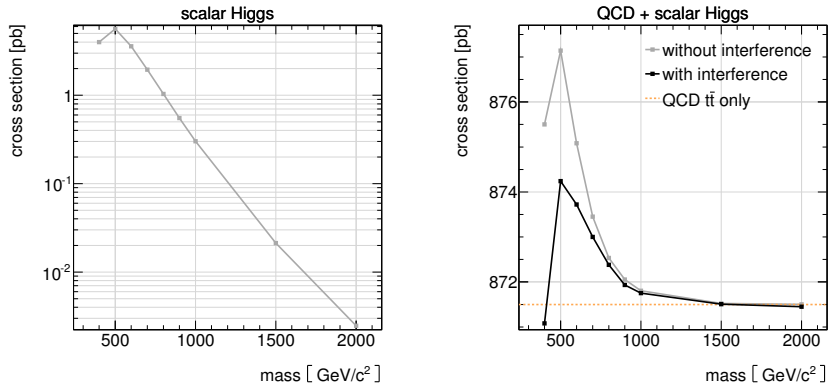

Figure 7.8: *Cross sections of the scalar Higgs boson. Cross sections of pure resonances decrease rapidly with increasing mass. The cross section of the full model is even lower than the sum of cross sections of the pure resonance and QCD $t\bar{t}$ production, indicating a negative net effect of the interference. At a resonance mass of $m_h = 400\,\mathrm{GeV}/c^2$ and above $m_h = 1500\,\mathrm{GeV}/c^2$ the cross section of the full model is even lower than for QCD $t\bar{t}$ production alone.*

$m_h \gtrsim 1\,\mathrm{TeV}/c^2$, its width becomes larger than its mass so that it will be extremely difficult to discover.

On the other hand, Higgs bosons in models with two Higgs doublets are much more narrow [162, 163]. In these models, widths of Higgs bosons can even be smaller than 1 % of their mass. For this study, widths of simulated Higgs bosons have been assumed to be 1 % of their mass.

Properties of samples of the scalar and pseudoscalar Higgs boson are shown in table 7.5. In order to obtain accurate predictions for all studied quantities, all models have been simulated with at least 1 Mio events for the pure resonance. The simulation of the full process had to be performed with an even higher number of events because it included also events of QCD $t\bar{t}$ production. Samples of the full simulation contain at least 15 Mio events for small masses of the Higgs boson and 25 Mio events for larger masses.

Especially for high resonance masses, the resonance contribution to the whole sample decreases approximately like $\frac{\sigma_{\mathrm{Res}}}{\sigma_{\mathrm{QCD+Res}}}$, which can be written as $\frac{\sigma_{\mathrm{Res}}}{\sigma_{\mathrm{QCD}}+\sigma_{\mathrm{Res}}}$ in case of negligible interference. Figure 7.8 shows the cross sections for the different masses, also

compared to the cross section of $t\bar{t}$ production without a resonance in QCD. From this it can be estimated, that the resonance fraction of the samples decreases from about 10^{-2} to about 10^{-6}. In case of a Higgs boson of $m_h = 1\,\mathrm{TeV}/c^2$, its cross section is 0.3 pb, compared to 871.5 pb for pure QCD $t\bar{t}$ production, resulting in a fraction of only $\frac{\sigma_{\mathrm{Res}}}{\sigma_{\mathrm{QCD}}+\sigma_{\mathrm{Res}}} = 3.4 \cdot 10^{-4}$ of all events of the full process. This means, that production of resonances gets increasingly inefficient for high masses. Therefore, also an increasing number of events is needed to obtain a significant amount of resonance events well above statistical fluctuations.

Figure 7.8 also shows a first effect of interferences which will be discussed in more detail later on. The cross section of the model respecting the interference is significantly lower than the cross section of the model without interference. For a mass of the Higgs boson of $m_h = 400\,\mathrm{GeV}/c^2$ the cross section is even lower than the cross section of pure QCD $t\bar{t}$ production. This effect indicates a negative interference between Feynman diagrams which is even larger in size than the pure resonance contribution for $m_h = 400\,\mathrm{GeV}/c^2$ and above $m_h = 1500\,\mathrm{GeV}/c^2$.

7.3.3 The Pseudoscalar Higgs Model

The pseudoscalar Higgs model is the same as the scalar Higgs model except for different couplings to left- and right-handed fermions. The strength of couplings is set to the coupling strengths of the Standard Model Higgs boson to all quarks, but coupling to left- and right-handed components of quarks is set corresponding to a pseudoscalar coupling. The widths of the resonances have been assumed to be 1 % of their respective masses, again.

Pseudoscalar Higgs bosons are present in every Model with more than one Higgs doublet. Accordingly, these models provide a variety of possibilities coupling the pseudoscalar Higgs boson to particles of the Standard Model. The general Two-Higgs-Doublet model describes the coupling of the pseudoscalar Higgs boson to up- and down-type fermions by a parameter $\tan(\beta)$. The model analysed in this study assumes equal couplings to up- and down-type fermions which corresponds to a value of $\tan(\beta) = 1$. As this study additionally considers decays of the resonance into a pair of top quarks only, couplings to down-type fermions only affect the production of resonances.

The primary production channel of Higgs-like particles via gluon fusion is dominated by a top quark loop, because Higgs couplings are proportional to fermion masses. Down-type quarks only contribute a small fraction to the total production of resonances with a Higgs-like coupling. The second production channel via quark-antiquark

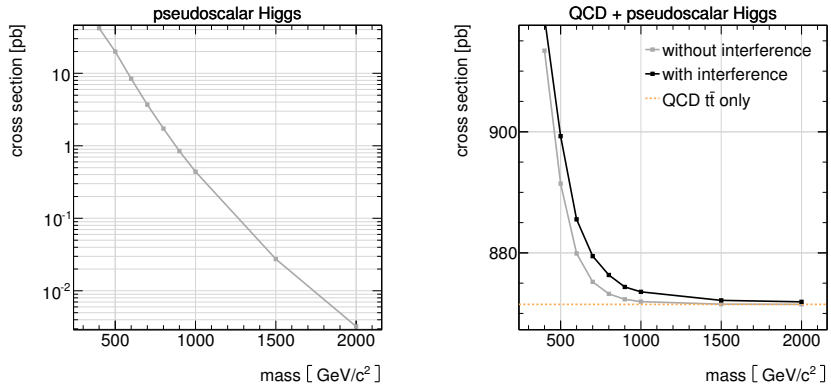

Figure 7.9: *Cross sections of the pseudoscalar Higgs boson. Cross sections of pure resonances decrease rapidly with increasing mass. The cross section of the full model is higher than the sum of cross sections of the pure resonance and QCD $t\bar{t}$ production, indicating a positive net effect of the interference.*

scattering only contributes with a negligible fraction at the LHC, because parton desities of antiquarks in protons are small compared to gluons and protons predominatly contain light quarks, which have only a small coupling to Higgs-like particles. Thus, heavy down-type quarks from this channel also have only a small impact compared to the majority of events. If all contributions of down-type quarks are ignored because of their small contributions, cross sections of resonances can just be scaled with $\tan^2(\beta)$, because all Feynman diagrams contain two vertices coupling them to quarks.

Table 7.5 lists all samples of the pseudoscalar Higgs model. Masses and widths have been chosen equal to the scalar Higgs samples, so that both models can be easily compared. Again, the numbers of events produced have been increased at large masses.

Figure 7.9 shows the graphical representation of the cross sections listed in table 7.5. In general, cross sections of the pseudoscalar Higgs boson are larger by up to one order of magnitude for low masses, compared to scalar Higgs bosons. In contrast to the latter model, the full simulation of the pseudoscalar Higgs boson results in a larger cross section than the sum of cross sections of the pure resonance and the QCD $t\bar{t}$ processes. This behaviour indicates that the interference increases the total cross section of this model.

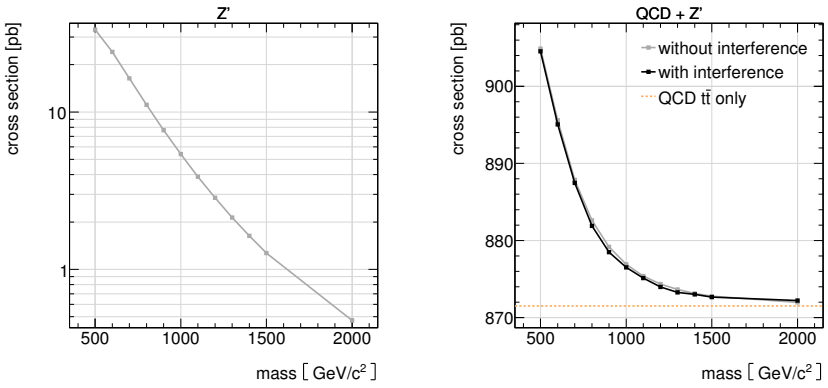

Figure 7.10: *Cross sections of the sequential Z' boson. Cross sections of pure resonances decrease moderately with increasing mass. The cross section of the full models are equal to the sum of cross sections of the pure resonance and QCD $t\bar{t}$ production, indicating negligible interference.*

7.3.4 The sequential Z′ Model

The sequential Z' model is a general model which can be easily compared between different studies. Many theoretical models provide an additional heavy vector boson which is neutral in electrical and colour charge. Although in most cases they are generally called Z', their couplings to particles of the Standard Model as well as additional particles predicted by the respective model may differ significantly between different models.

The sequential Z' model has been established as the minimal model extending the Standard Model by just one additional Z' boson with couplings of the Standard Model Z^0 boson to all other particles. The most important free parameter of this model is the mass of the Z' boson. Although the decay width of the boson is completely fixed in theory by its couplings to other particles, the decay width has also been provided as a free parameter in order to account for unknown or additional effects of a special model. This means, the actual decay width of a Z' boson could be affected by additional particles present in a certain model, but not in the Standard Model.

As in the previous models, the total decay width of the Z' boson has been chosen to be to 1 % of its mass. Properties of the Z' samples are summarised in table 7.6.

Z' datasets		pure resonance			QCD $t\bar{t}$ + resonance + interference		
mass [GeV/c^2]	width [GeV/c^2]	number of events	cross section [pb]	equivalent integrated luminosity [1/fb]	number of events	cross section [pb]	equivalent integrated luminosity [1/fb]
500	5	1005000	33.40	30.09	15005000	904.6	16.59
600	6	1000000	24.10	41.49	15015000	895.1	16.78
700	7	1000000	16.36	61.11	15030000	887.5	16.94
800	8	1020000	11.11	91.82	15015000	881.9	17.03
900	9	1010000	7.670	131.7	15015000	878.5	17.09
1000	10	1000000	5.402	185.1	15010000	876.5	17.12
1100	11	1020000	3.882	262.8	25035000	875.1	28.61
1200	12	1010000	2.852	354.1	25085000	874.0	28.70
1300	13	1005000	2.134	470.9	24990000	873.3	28.62
1400	14	1000000	1.632	612.7	25010000	873.0	28.65
1500	15	1010000	1.268	796.5	25030000	872.7	28.68
2000	20	1000000	0.4731	2113.6	25055000	872.2	28.73

Table 7.6: *Datasets of the Z' sample. Samples of the pure resonance have been chosen to contain 1 Mio events, whereas samples of the full process contain at least 15 Mio or 25 Mio events for resonance masses above 1 TeV/c^2, respectively.*

Cross sections of processes including a Z' boson are comparable to cross sections of the pseudoscalar Higgs boson for low resonance masses, but the cross section of the Z' model does not decrease as fast with higher mass. Reason for this behaviour is a different production mechanism. Higgs bosons are primarily produced via gluon fusion whereas Z' bosons are predominantly produced via quark-antiquark scattering. As a coulor-neutral particle, it can only couple to gluons via a quark loop, which is further suppressed by Furry's theorem [100, 101, 164]. Therefore, couplings of Z' bosons to gluons can be ignored.

Figure 7.10 shows the cross sections of the Z' model against the resonance mass. The right hand side of this figure shows the cross sections of the Z' model with and without consideration of the interference lying on top of each other. This indicates only a small effect of the interference, which also makes this model popular for other studies as the interference can simply be ignored without any corrections necessary. In this study, the sequential Z' model is used to establish a method for analysing models with and without a significant interference. As the model does not show an interference, both cases have to lead to same results. Thus, the Z' is used to check obtained results for consistency. Equal results in both cases, whether the interference is taken into account or not, indicate that the method of analysis can be applied to models with an interference.

7.3.5 The Coloron Model

The coloron model assumes an additional heavy particle with equal properties as the gluon. As it couples to quarks, it can be produced in quark-antiquark annihilation. As the coloron is a vector boson, Furry's theorem [100, 101] forbids its production via a quark loop in gluon-gluon scattering. Nevertheless, the coloron is a colour-octet particle. It carries colour charges and can therefore couple to gluons directly.

The strong coupling to quarks and gluons provides this model with a huge cross section for the resonance, compared to the previous models. Thus, also heavy resonances with high masses far above $m_C = 1\,\mathrm{TeV}/c^2$ can be produced and easily studied. Table 7.7 lists all coloron samples studied in this work. They include resonances with masses from $m_C = 700\,\mathrm{GeV}/c^2$ up to $m_C = 4.5\,\mathrm{TeV}/c^2$.

Even for the highest considered resonance mass, the cross section for $t\bar{t}$ production via a coloron ($\sigma_{pp\to R\to t\bar{t}} = 76.65\,\mathrm{pb}$) is still higher than any cross section of the previous Higgs or Z' models. Thus, the model is supposed to provide a clean signal for the presence of a coloron. On the other hand, the total cross section of the corresponding full sample ($\sigma_{pp(\to R)\to t\bar{t}} = 784.3\,\mathrm{pb}$) is even lower than the cross section of pure QCD

	datasets		pure resonance			QCD $t\bar{t}$ + resonance + interference		
	mass [GeV/c^2]	width [GeV/c^2]	number of events	cross section [pb]	equivalent integrated luminosity [1/fb]	number of events	cross section [pb]	equivalent integrated luminosity [1/fb]
coloron	700	7	1005000	6596.0	0.1524	15070000	7201.0	2.093
	1000	10	1005000	1515.4	0.6632	15005000	2168.3	6.920
	1500	15	1000000	310.2	3.224	15015000	994.6	15.10
	2000	20	1000000	136.6	7.319	15025000	832.5	18.05
	2500	25	1000000	96.61	10.35	15010000	797.2	18.83
	3000	30	1005000	84.53	11.89	15095000	788.3	19.15
	3500	35	1000000	79.87	12.52	15060000	785.3	19.18
	4000	40	1035000	77.91	13.28	15060000	784.5	19.20
	4500	45	1000000	76.65	13.05	15030000	784.3	19.16
axigluon	1000	10	1015000	948.8	0.8498	15020000	1816.0	7.290
	1500	15	1025000	208.9	4.400	15005000	1078.3	13.62
	2000	20	1005000	75.86	12.65	15005000	946.0	15.80
	2500	25	1000000	43.01	22.92	15130000	913.4	16.55
	3000	30	1020000	32.92	30.83	15075000	903.9	16.68
	3500	35	1035000	29.30	35.28	15020000	900.5	16.68
	4000	40	1035000	27.80	37.19	15025000	898.9	16.71
	4500	45	1000000	27.09	36.95	15030000	898.6	16.73

Table 7.7: *Datasets of the coloron and axigluon sample. Samples of the pure resonance have been chosen to contain 1 Mio events, whereas samples of the full model contain at least 15 Mio events.*

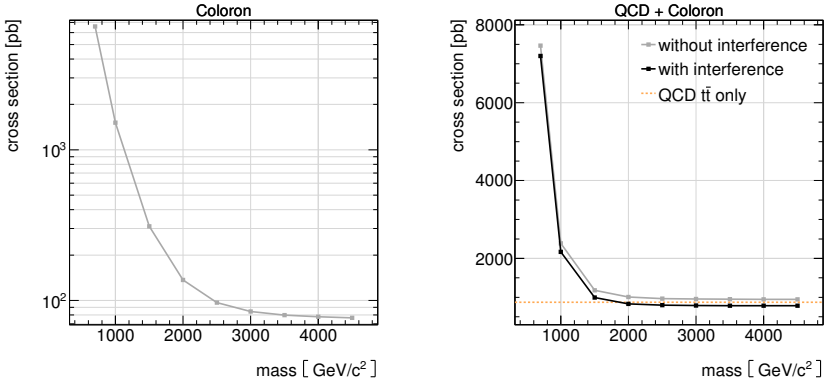

Figure 7.11: *Cross sections of the coloron model. Cross sections of pure resonances decrease with increasing mass, but with decreasing rate. Cross sections of the full models are lower than the sum of cross sections of the pure resonance and QCD $t\bar{t}$ production. For resonance masses above 2 $^{TeV}/_{c^2}$ the cross section of the full model is even lower than the cross section of QCD $t\bar{t}$ production alone.*

$t\bar{t}$ production alone, which indicates a strong negative interference lowering the total cross section even at highest resonance masses.

This effect can also been seen in figure 7.11, where both lines, for the samples of separate simulation of QCD and resonance $t\bar{t}$ production differ significantly from the full simulation including the interference.

As an additional remarkable aspect, the cross section of the pure resonance process decreases extremely slowly, especially for high masses of the resonance. Figure 7.12 shows that this is because the $t\bar{t}$ invariant mass spectrum for a pure resonance, i.e. without contributions from QCD $t\bar{t}$ production, develops not only a peak at the nominal resonance mass, but also a continuum contribution which is similar to the $t\bar{t}$ invariant mass spectrum of QCD. This means, the resonance can not only be produced resonantly, but there are also events where the $t\bar{t}$ resonance occurs only as a virtual particle. With increasing mass of the resonance, this continuum contribution remains almost constant whereas the resonance peak becomes smaller and smaller.

This effect can also be observed not only for colorons, but for all types of resonances, although in most cases the continuum is less pronounced than in this model. The strength of the continuum depends on the type and properties of the resonance.

Additionally, this effect leads to a difficulty for experimental analyses. To determine the cross section of a resonance it is necessary to subtract the underlying contribution of $t\bar{t}$ events from QCD. In order to obtain this distribution, the full spectrum is fitted to a QCD sample of $t\bar{t}$ events in regions not affected by the nominal peak of the resonance.

If the resonance also develops a continuum contribution similar to the QCD part of the $t\bar{t}$ spectrum, the resonance spectrum is no longer localised at the nominal mass of the resonance. Accordingly, there is no region of the spectrum that is not affected by the resonance. Therefore it is not possible any more to fit the QCD $t\bar{t}$ spectrum alone.

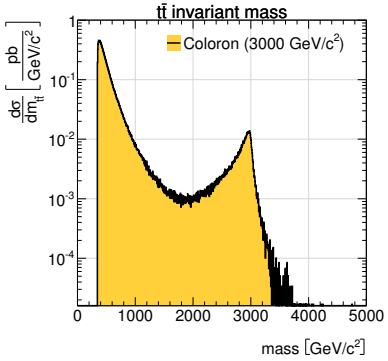

Figure 7.12: *The $t\bar{t}$ invariant mass spectrum of a coloron resonance with a mass of $m_C = 3\ \mathrm{TeV}/c^2$. The model shows not only resonant production, but also a continuum contribution from virtual colorons.*

Nevertheless, this difficulty does not apply to this work. In case of strong interferences between QCD and resonance channels of $t\bar{t}$ production, a distinction between a QCD contribution and a contribution from a pure resonance to the invariant mass distribution of top quark pairs is meaningless, because the interference tightly couples both channels. As a consequence, no attempt has been carried out in this study to separate both channels. All methods of this analysis have been chosen such that they are suitable for the case of a full model of QCD and resonance $t\bar{t}$ production.

7.3.6 The Axigluon Model

The axigluon model is rather similar to the coloron model. It assumes a heavy colour octet axial vector boson that couples directly to quarks. Couplings to gluons are suppressed because parity conservation forbids gluon-axigluon vertices with an odd number of axigluons [64]. Properties of the samples considered are summarised in table 7.7. As it turns out, all cross sections of pure resonances and the cross section of the QCD $t\bar{t}$ production add up to the respective cross sections of the full models. This already indicates a negligible interference.

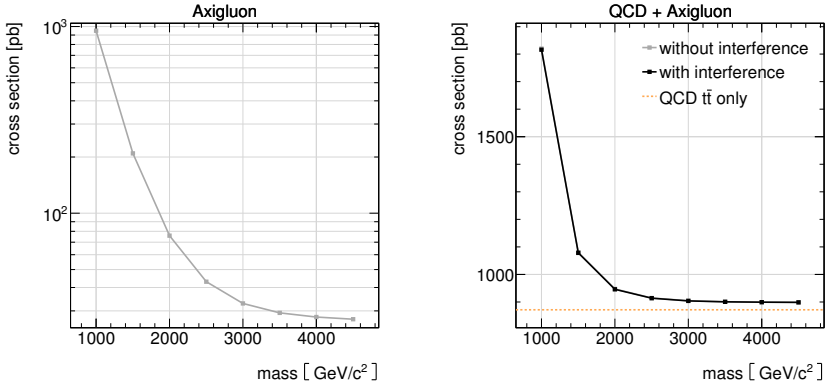

Figure 7.13: *Cross sections of the axigluon. Cross sections of pure resonances decrease with increasing mass, but seem to run towards a non-vanishing limit. The sum of cross sections of the of the pure resonance and QCD $t\bar{t}$ production add up almost exactly to the cross section of the full model, indicating a negligible interference.*

This can also been seen in figure 7.13 where cross sections of both channels always lie on top of each other for all considered resonance masses. Without a significant interference, the axigluon model also serves as a cross check to prove applied analysis methods being consistent between both cases whether interferences are taken into account or not. Therefore, with the axigluon model it is possible to check the applied methods also at higher resonance masses, where the Z' model does not provide enough events any more.

Similarly to the coloron model, Figure 7.13 also shows the tendency of the axigluon model to retain a certain cross section even if the nominal resonance mass rises strongly and the actual mass peak is not visible any more.

7.4 Interferences in the Top-Antitop invariant Mass Spectrum

As already mentioned, interferences only occur with QCD and resonance $t\bar{t}$ production calculated in the same matrix element. As such, the interference is not an observable quantity on its own. Nevertheless, as shown in figure 6.9, it can be calculated as the difference between the full simulation and the simpler model of separate simulations of QCD and pure resonance $t\bar{t}$ production.

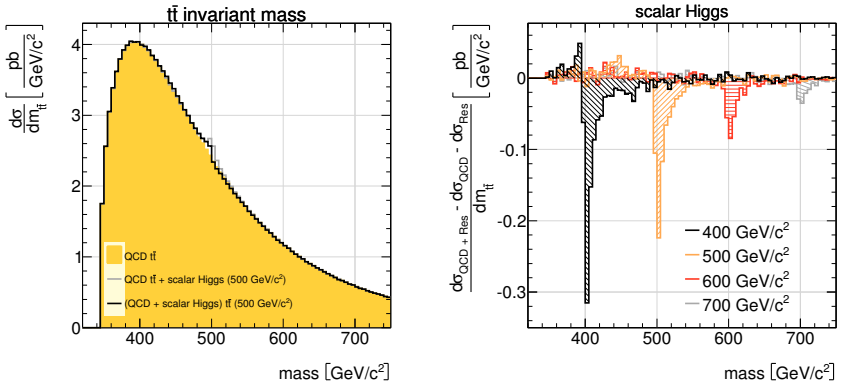

Figure 7.14: *Interference of the scalar Higgs model. The model reveals a negative interference which lowers the total cross section.*

When calculating interferences for different models, several different patterns of interference emerge, depending on the properties of the resonance. In order to get a clear picture of an interference, the $t\bar{t}$ invariant mass spectrum on parton level has been determined with a high resolution. Interferences in this section have been determined with a resolution of 5 $^{GeV}/_{c^2}$, which is considerably finer than the experimental resolution, determined in section 7.2.

Resolution also is a major difficulty in a determination of interference patters. The interference emerges as a difference of two large numbers of similar size, which additionally contain statistical errors. Therefore, differential cross sections of all models have to be determined precisely for each bin of the invariant mass spectrum so that differences become visible well above statistical uncertainties. This is the main reason why all samples have been generated with such a huge number of events, i.e. several millions of events per sample.

The following sections describe interferences calculated for the models described in the previous section.

Scalar Higgs model The scalar Higgs boson mainly shows a negative interference as already indicated by the values of the total cross sections including or ignoring the interference, respectively. Considering the full $t\bar{t}$ invariant mass distribution as shown in figure 7.14, separate calculations of QCD and resonance $t\bar{t}$ produc-

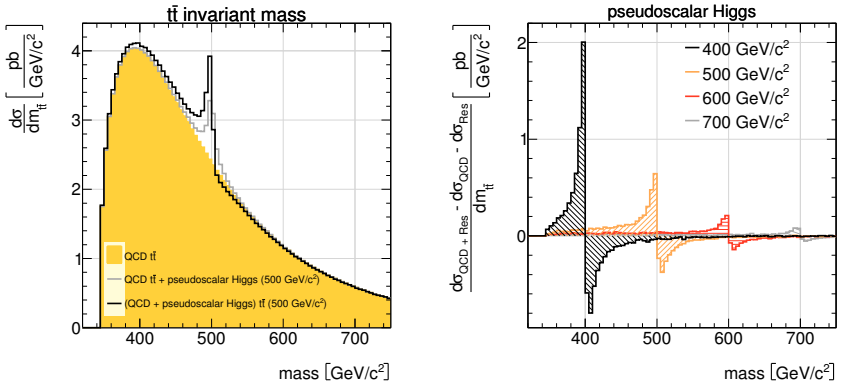

Figure 7.15: *Interference of the pseudoscalar Higgs model. A strong negative interference leads to a deficit above the nominal mass of the resonance and imprints a sharp edge into the $t\bar{t}$ invariant mass distribution which even drops below the differential cross section predicted by pure QCD $t\bar{t}$ production.*

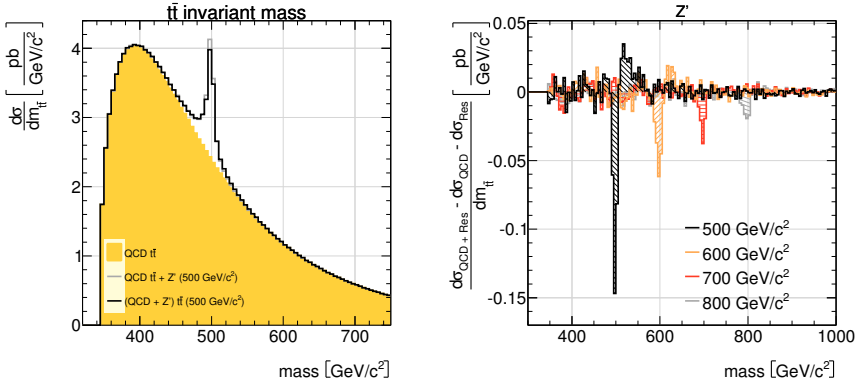

Figure 7.16: *Interference of the Z' model. Only a small interference is visible strictly localised in the region of the nominal mass of the resonance. The visible effect of the interference is mainly a small decrease of the height of the peak. The total cross section is not changed by the interference.*

tion show a small bump at the nominal resonance mass on top of the continuous distribution of QCD $t\bar{t}$ events.

The distribution of full $t\bar{t}$ production shows an even smaller bump, because of the negative interference. In its major bins at nominal resonance mass, the interference is of the same size as the pure resonance, but with an opposite sign. Compared to its small size, the strength of the resonance is reduced significantly so that the bump only appears as a small edge where the spectrum drops by a small amount.

Pseudoscalar Higgs model The pseudoscalar Higgs model shows a stronger interference than the scalar Higgs model. The peak is enhanced below the nominal resonance mass and reduced above, as can be seen in figure 7.15.

The size of the interference is of the same order as the actual resonance signal, but also negative above the nominal resonance mass. This leads to a deficit of events in this region. In this case the negative part of the interference is even stronger than the pure resonance contribution so that the appropriate region contains even less events than suggested by pure QCD.

In total, the interference slightly increases the total cross section, because it enhances resonance production at lower invariant mass and suppresses resonances

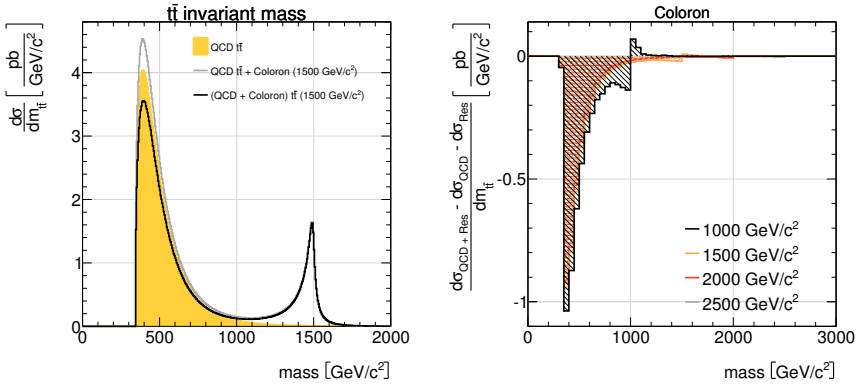

Figure 7.17: *Interference of the coloron model. The strongest effect of the interference is a large decrease of the height of the continuum peak, which also decreases the total cross section. The predicted cross section is even lower than that predicted by QCD only $t\bar{t}$ production.*

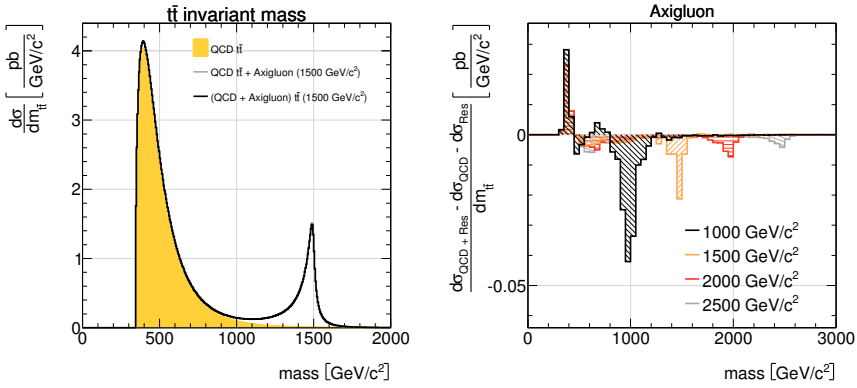

Figure 7.18: *Interference of the axigluon model. Almost no differences are visible between both cases including or ignoring an interference. Thus, all interferences can be ignored for the axigluon model.*

production at higher invariant mass compared to the nominal resonance mass. As a consequence, it is more likely to produce a resonance at slightly lower invariant mass than a heavier one. Additionally, resonance production at lower invariant mass is also prefered kinematically, because of a larger phase space. Accordingly, the cross section of resonance production rises slightly.

Z′ model The $t\bar{t}$ invariant mass distributions of the sequential Z' model including or ignoring the interference look almost the same. Nevertheless, there are some differences visible in figure 7.16.

First of all, the resonance peak is about 10 % smaller when the interference is included. On the other hand, this is compensated by a similar excess of events in the tail of the peak. These two effects nearly compensate such that total cross sections of both cases remain equal. Thus, the interference in the sequential Z' model, only changes the shape of the $t\bar{t}$ invariant mass spectrum, but not the total cross section.

Coloron model As already shown earlier in figure 7.12, the coloron develops not only a peak at its nominal mass, but also a strong continuum production of top quark pairs. This can be clearly seen in figure 7.17, where the coloron increases $t\bar{t}$ production by about 0.5 $\frac{\text{pb}}{\text{GeV/c}^2}$ at the continuum peak. Additionally, the resonance shows the usual strong peak at its nominal mass.

When considering the full model of QCD and resonance $t\bar{t}$ production, the coloron model shows the strongest interference of all models considered in this study when compared for equal nominal mass. The interference can be divided into a continuum region and a region at the nominal resonance mass. An interference only becomes relevant, if both the QCD and the resonance contributions become of equal size at a certain point in the invariant mass spectrum. Otherwise the spectrum is dominated by only one contribution and the other one can be ignored.

With the continuum part of coloron production, the resonance can also interfere strongly with QCD in the continuum region. In this case, the interference is even stronger than the pure resonance and turns the increase of the differential cross section into a deficit of similar size, i.e. $t\bar{t}$ production is decreased by about 0.5 $\frac{\text{pb}}{\text{GeV}/c^2}$ at the continuum peak. As continuum production of colorons persists with increasing mass of the coloron, so does the interference with QCD at the continuum peak.

The second region with a significant interference is located at the nominal mass of the resonance where the invariant mass spectrum first shows a small deficit below the nominal mass, followed by a small excess of differential cross section compared to a model without interference. This structure gets smaller and smaller with increasing resonance mass.

Axigluon model Compared to the strength of the pure resonance, the axigluon model shows the smallest interference of all considered models.

According to figure 7.18, the interference is of the order of 1 % of the size of the mass peak. In a comparison of both distributions of cases with or without an interference, almost no difference becomes visible. Thus, for the axigluon model, it is safe to ignore any effect of an interference.

In total, all considered models reveal quite different patterns of interference depending on the spin and parities of the resonance. Most interferences are located in a small region near the nominal mass of resonances. In order to be able to observe interferences in measurements, structures have to exceed the experimental resolution of the invariant mass of top quark pairs. Otherwise, fine structures are smeared by limited resolution of the detector and reconstruction. As determined in section 7.2, observable structures have to be larger than the experimental resolution of the respective invariant mass, which has been determined earlier to an order of about 15 %.

This means, that it will be quite difficult to observe interference in direct measurements of the $t\bar{t}$ invariant mass spectrum. Figure 7.19 shows distributions of the differential cross sections after detector simulation and semileptonic reconstruction of

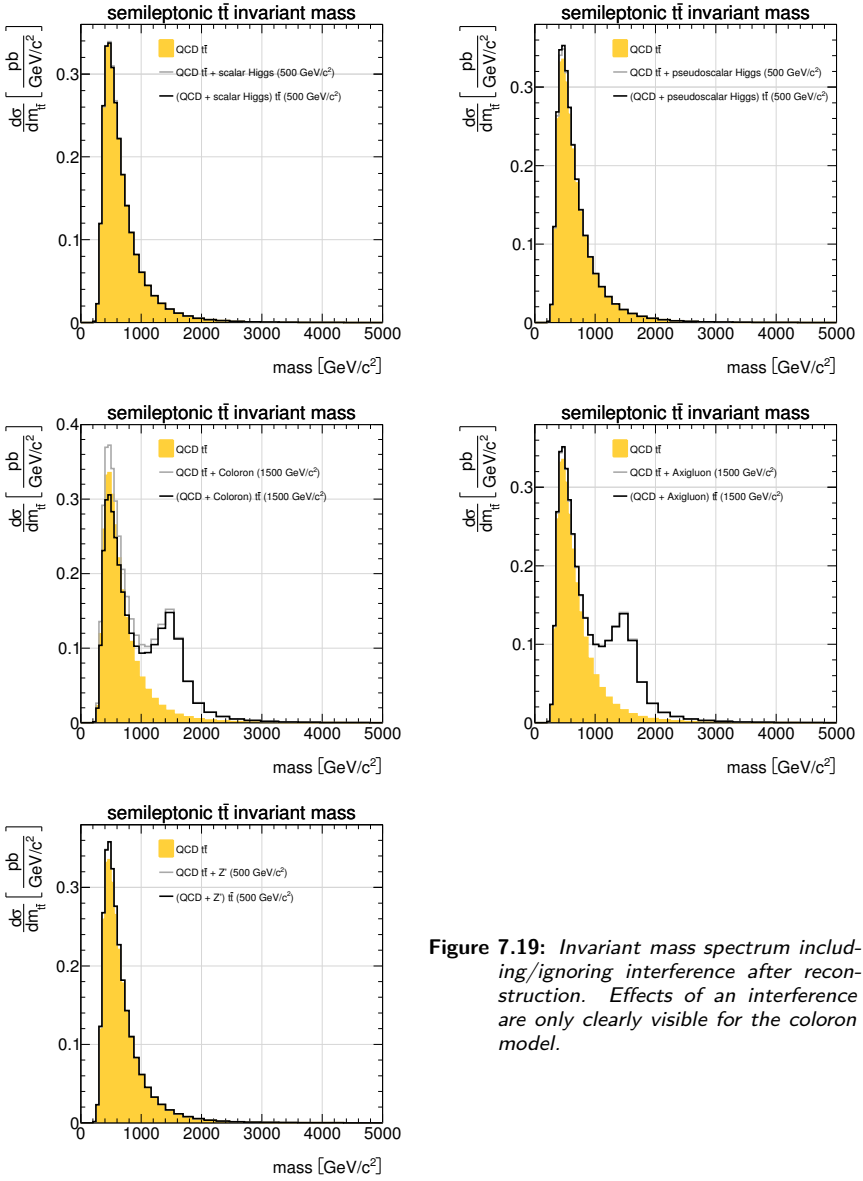

Figure 7.19: *Invariant mass spectrum including/ignoring interference after reconstruction. Effects of an interference are only clearly visible for the coloron model.*

models including an interference and without interference compared to QCD only $t\bar{t}$ production. Each of the five histograms shows distributions for a different type of resonance considered in this study.

A large difference between distributions respecting and ignoring the interference can only be seen for the Coloron model, although the major difference arises not from the peak at nominal mass of the resonance, but from the peak of the continuum. In all other distributions, the interference is hardly visible, which is the expected behaviour for structures smaller than the experimental resolution. Although most of the interferences considered in this study are not visible any more after detector simulation and semileptonic reconstruction, the full analysis is nevertheless applied also to these models, because interferences could have subtle effects for the determination of sensitivities to a certain model.

model	interference
scalar Higgs	strong negative
pseudoscalar Higgs	strong
sequential Z'	negligible
coloron	strong negative
axigluon	negligible

Table 7.8: *Scheme of interferences with respect to resonance properties.*

In summary, it is difficult to establish a general rule for the size and shape of an interference. It depends on the couplings to the left- and right-handed components of quarks as well as the strength of the coupling. Table 7.8 shows an estimation of the interferences encountered in the models presented in this section.

7.5 Systematic Uncertainties

There are some systematic uncertainties which limit the ability to distinguish the studied models from each other when considering the invariant mass spectrum of top quark pairs. The most important experimental uncertainties arise from limited precision in a measurement of the integrated luminosity, the total cross section of a specific process and the determination of the jet energy scale. Additionally, theoretical uncertainties arise from limited knowledge of parton distribution functions and the leading order approximation of matrix elements.

From these uncertainties, PDF and JES errors have been determined for all studied models separately, i.e. all events have been analysed repeatedly with different assumptions of parton distribution functions and jet energy scales. On the other hand,

luminosity or cross section uncertainties can be treated more easily by smearing the number of events in ensembles, during the calculation of sensitivities.

7.5.1 Luminosity and Cross Section Uncertainties

Uncertainties in integrated luminosity and total cross sections are strongly correlated and, in case of this study, even have identical effects. Experiments can only determine a total number of events after certain cuts. Cuts are optimised to select events matching certain criteria. In the end, it is not possible to determine the actual hard process of a single event. Only the full distribution can be measured, but not its decomposition into distinct channels.

In experiment, the total number of events after all cuts is given by the extension of equation 6.4 for several distinct processes

$$N = \mathscr{L} \cdot \left(\sigma_1 \varepsilon_1 + \ldots + \sigma_n \varepsilon_n\right) , \tag{7.2}$$

where $\mathscr{L}$ is the integrated luminosity, $\sigma_1 \ldots \sigma_n$ are respective cross sections and $\varepsilon_1 \ldots \varepsilon_n$ are respective selection efficiencies of processes $1 \ldots n$. Each of these quantities has its own uncertainty. When comparing a theoretical model to measured data, sizes of all these quantities have to be determined or fitted against measured distributions within their respective uncertainties. The above equation imposes a constraint on all quantities such that the total number of events has to agree with measurement.

In case of this study, as already stated in section 6.3, relative amounts of contributions from different processes are always fixed to predictions from the event generator. Relative values of cross sections for different contributions to the total distribution are closely coupled when taking interferences into account. The only degrees of freedom left available are the value of the integrated luminosity and one value for the total cross section of all processes combined.

For a given number of events, these two remaining degrees of freedom are 100 % anticorrelated via equation 7.2. In this case, the predicted value of the total cross section can be treated without any error and the uncertainty on luminosity accounts for variations in the total number of events.

7.5.2 PDF Uncertainties

All known parametrisations of parton distribution functions are also affected by theoretical errors as well as limited accuracy of measured data, which had been used in

fitting free parameters. As figure 3.5 shows, these bands of uncertainty become large at small values of Bjørken-x, which become only accessible with higher centre-of-mass energies.

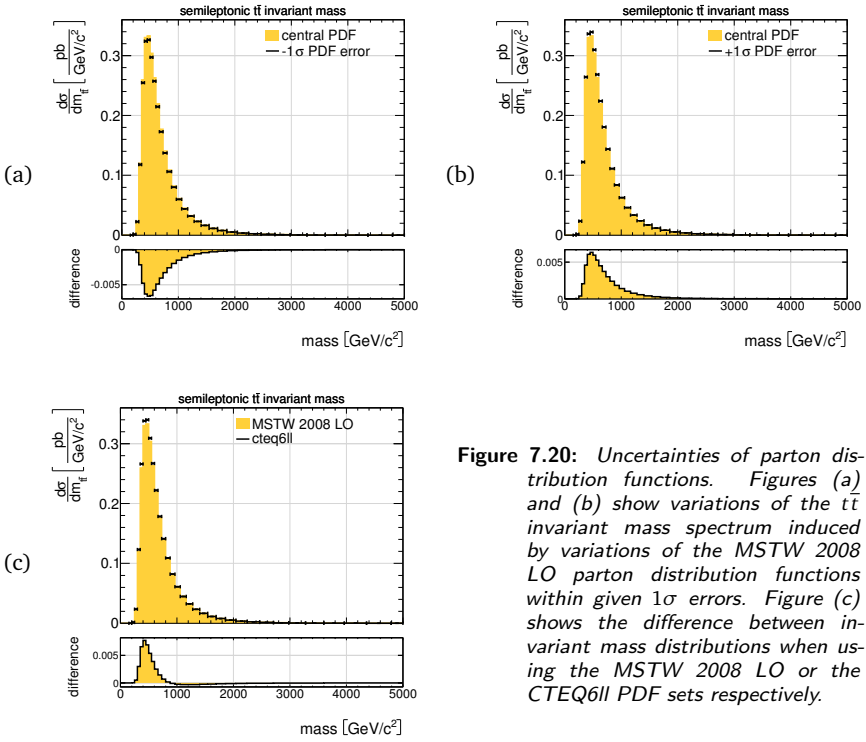

Figure 7.20: *Uncertainties of parton distribution functions. Figures (a) and (b) show variations of the $t\bar{t}$ invariant mass spectrum induced by variations of the MSTW 2008 LO parton distribution functions within given 1σ errors. Figure (c) shows the difference between invariant mass distributions when using the MSTW 2008 LO or the CTEQ6ll PDF sets respectively.*

Effects of uncertainties of parton distribution functions to the invariant mass spectrum of top quark pairs can be seen in figure 7.20. There are two contributions to the PDF uncertainties. The first one is the uncertainty of one parametrisation. To determine this error, PDF collaborations provide sets of PDFs which contain a central PDF and a number of eigenvector error sets. The error sets parametrise positive and negative errors to each parameter used in the PDF parametrisation. To determine this type of error, the MSTW 2008 LO PDF set with 68 % CL errors [75] has been used in this

study which consists of a central PDF and 20 pairs of positive and negative eigenvector parametrisations.

These 20 pairs of error eigenvectors can be treated as statistically independent errors, because they have been decorrelated. Then, to obtain only one PDF error band for all considered quantities, the overall error is a quadratic sum of these errors. Moreover, if both PDFs of one pair of error shift the invariant mass spectrum into the same direction, only the larger shift is considered as the appropriate error. The resulting difference between the central PDF and the summed PDF errors is shown in figure 7.20(a) and (b).

The second type of PDF error is the difference between two independent parametrisations, published by different PDF collaborations. To estimate the effect of this uncertainty, the invariant mass distribution has also been determined using the CTEQ6ll [165] PDF set. The difference arising between both PDF sets can be seen in the bottom distribution in figure 7.20.

Both types of PDF errors alter the invariant mass spectrum by about 2 %. The combined 20 PDF eigenvector errors together almost only affect the total rate of events, but do not change the shape of the distribution strongly. The comparison with a different PDF set also shows some changes in shape.

7.5.3 Jet Energy Scale Uncertainty

A key ingredient for an accurate reconstruction of the $t\bar{t}$ invariant mass is a precise measurement of jet energies. Errors in this measurement arise from uncertainties in determination of energy deposition in single cells of calorimeters as well as unavoidable mistakes when clustering detector hits to jets. Additional errors are introduced by matching measured jet energies to energies of partons.

To account for errors in jet energy scales, the invariant mass spectrum has also been calculated for variations of the jet energy scale by $\pm 5\,\%$, i.e. jet energies have been uniformly scaled up and down by 5 %, respectively. The invariant mass distributions with scaled jet energies are shown in figure 7.21. Scaling of jet energies is directly reflected in the invariant mass distribution. Invariant masses of fully hadronic $t\bar{t}$ events are shifted upwards or downwards linearly with the variation in jet energies. Invariant masses of semileptonic $t\bar{t}$ events only approximately scale linearly with jet energy scales because the energy of the measured charged lepton is not modified by jet energies. As a visible consequence, the invariant mass distribution appears stretched or squeezed respectively, when jet energies are scaled.

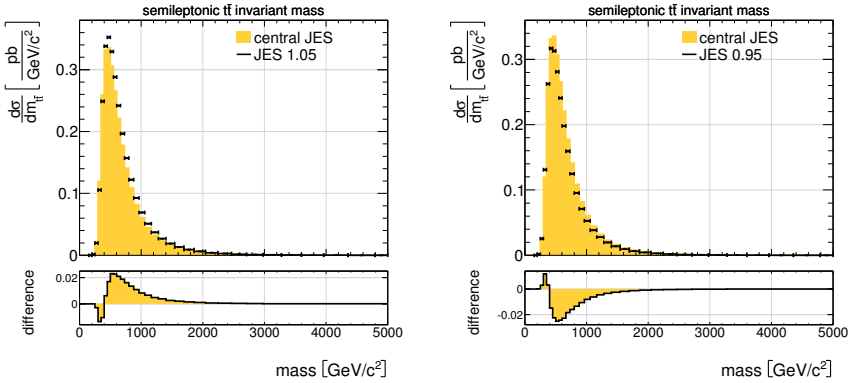

Figure 7.21: *Invariant mass distribution with scaled jet energies. Variations in jet energies stretch or squeeze the invariant mass distribution, respectively, because the semileptonic invariant mass is depends almost linearly on jet energies, except for the energy of the charged lepton. Additionally, additional or less events may pass cuts on jet energies with different jet energy scales, which results in variations of the observed total number of events.*

A second effect of a modified jet energy scale is that more or less events may pass applied cuts on jet energies. If the jet energy scale is increased, all jets are given higher energies and may pass a certain threshold required by one of the cuts. Therefore, also the number of selected events may rise, which increases the observed rate of events.

In total, the uncertainty on the jet energy scale ranges in an order of 10 %. Compared to the PDF uncertainties, this induces a larger contribution to the overall error.

7.5.4 Uncertainty of Leading Order Approximation

All simulations have been carried out considering leading order Feynman diagrams only in the hard process. As leading order calculations represent only the simplest approximation to the exact result, its error has to be estimated, which is difficult because the exact result cannot be known. Therefore, the error is estimated as the difference to a calculation in next-to-leading order carried out using MC@NLO 3.42 [166, 167]. This event generator only calculates matrix elements and has to be interfaced with an older version of HERWIG written in Fortran for hadronisation. Interfacing with HER-

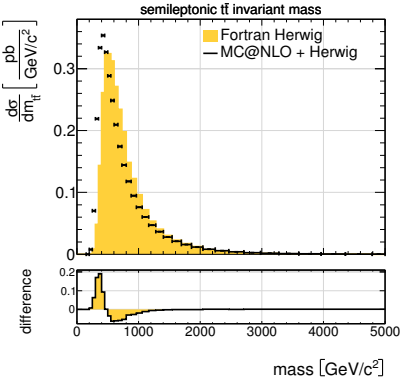

Figure 7.22: *Comparison of leading-order and next-to-leading order $t\bar{t}$ production. The LO distribution has been generated with Fortran* Herwig*, the NLO distribution with MC@NLO + Fortran* Herwig*.*

WIG++ only recently became available with MC@NLO version 4.0, which was too late for this study.

Additionally, generation of $t\bar{t}$ resonances is not implemented in MC@NLO, so that only $t\bar{t}$ production in QCD can be compared between LO and NLO calculations. Figure 7.22 shows a comparison of the invariant mass spectrum calculated with Fortran HERWIG 6.5.10 and MC@NLO + Fortran HERWIG.

The main difference is a softer spectrum for $t\bar{t}$ production in NLO, i.e. at next-to-leading order pairs of top quarks are more likely produced with a lower invariant mass than at leading order. This is caused by additional Feynman diagrams that have been calculated in the hard process. Diagrams of higher orders contribute corrections to the leading order process, which change the shape and integral of the $t\bar{t}$ invariant mass spectrum.

Above an invariant mass of $1\,\mathrm{TeV}/c^2$ uncertainty of the leading order approximation is smaller than 10 %. In the threshold region just above $2m_t$, the uncertainty grows to almost 60 %, which means that the shape of the distribution in this region is not well known.

As the real distribution of the invariant mass spectrum at infinite order of perturbation theory is not known, it is assumed to lie somewhere in between the leading order and next-to-leading order distribution. Additionally, the correction introduced by higher orders is supposed to become smaller and smaller with increasing order of perturbation theory. Accordingly, the uncertainty of the leading order approximation is not treated as a Gaussian error, but as a one-sided, uniformly distributed error.

7.6 Determination of Sensitivities

By combining a $t\bar{t}$ resonance with QCD $t\bar{t}$ production into a full process including interference, it is not possible any more to separate the resonance and QCD contributions into distinct channels. This is true for every observable. Difficulties interpreting sensitivities arise from two features of the full channel.

non-linearity of signals The resonance contribution cannot be scaled linearly any more, because the interference has to be taken into account according to equation 6.1. Thus, the size of a resonance is not proportional to a given scale factor any more. Also shapes of distributions change non-linearly with such a factor.

negative relative cross sections With strong interference between a resonance and QCD $t\bar{t}$ production, splitting observed quantities into a resonance and a QCD contribution does not have a meaningful interpretation any more. As seen in figure 7.17 for the example of a coloron, the interference could even render the resulting total cross section for a resonance negative. Without the context of an interference, this would result in a negative number of events being produced in particle collisions, which does not make any sense at all.

These properties make it cumbersome to present determined sensitivities in a consistent, model independent and easily understandable way.

7.6.1 Representation of Sensitivities

Experimental exclusion limits for considered models can be expressed in various ways. For this study, there are five characteristic quantities that, in principle, can be displayed as functions of each other.

- nominal mass of the resonance
- total cross section
- integrated luminosity
- signal scale factor
- sensitivity

As not every combination makes sense to be investigated, only four combinations will be discussed in the following. All representations are show for the sequential Z' model, because it does not show a significant interference. For this model, all considered quantities should be equal with no significant differences, whether interference is respected in simulations and analysis or not.

The first possibility to present sensitivities is to draw the sensitivity against integrated luminosity. As seen in figure 7.23, integrated luminosity needed for a given sensitivity can be easily read off the diagram. As expected, the sensitivities rise proportionally to $\sqrt{\mathscr{L}}$, because the statistical error of the ensembles of pseudodata shrinks with $1/\sqrt{N}$, where N is the total number of events.

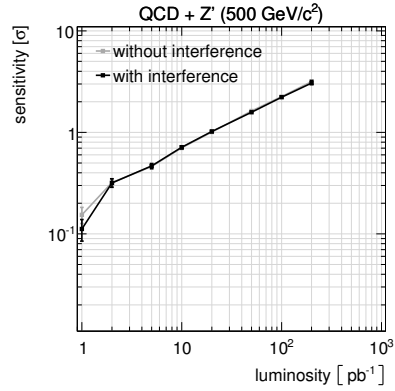

Figure 7.23: *Sensitivity against integrated luminosity. Calculations respecting interference agree with results without interference.*

In this case, a Z' boson with a mass of $m_{Z'} = 500\,\mathrm{GeV}/c^2$ could be excluded with 95 % confidence level with an integrated luminosity of about $50\,\mathrm{pb}^{-1}$. It has to be mentioned, that this diagram does not include any systematic uncertainties, which lower respective sensitivities such that more luminosity is needed for a certain exclusion limit. Additionally, calculated sensitivities agree well between models including and ignoring interference, respectively. Both calculation lead to same results for all luminosities.

The second possibility to present sensitivities is to draw the sensitivity against the signal scale factor κ. This parameter does not have a proper physical meaning, because it only scales the strong, Higgs- or Z-like coupling chosen in simulation. Thus, κ has a different meaning in every different model, whereas exclusion limits should be quoted in a model independent way, where possible.

The sensitivity for a given scale factor can be read off in figure 7.24. For a scale factor of 1, both types of calculations lead to the same sensitivity. For small values of κ, both calculations differ by a significant amount. The same is true for large values of κ, although not visible in the diagram, which can be explained by two reasons.

First, as seen in section 7.4, none of the studied models is completely free of interference. Therefore, it is not surprising that results including interference differ from the traditional approach without an interference. A second reason for the discrepancy between both approaches is the way how the distribution with a scaled resonance contribution is calculated.

As explained in section 6.3, distributions with scaled resonance contributions have been calculated only from unscaled distributions. No additional events have been generated with varied resonance coupling parameters. Instead, events have been reweighted according to their partonic $t\bar{t}$ invariant mass to emphasise events with a large resonance contribution.

Event weights have been calculated from three distinct distributions of invariant masses, namely the pure QCD $t\bar{t}$ production, the pure resonance contribution and the full distribution including the interference. In this combination, statistical errors of all distributions add up, so that the lookup distribution of event weights will contain large errors. Therefore, event weights are affected by relatively large errors. This difficulty cannot be avoided, even though all distributions have been determined with a huge number of events. As a result, extrapolations with a scale factor far away from $\kappa = 1$ should be interpreted carefully.

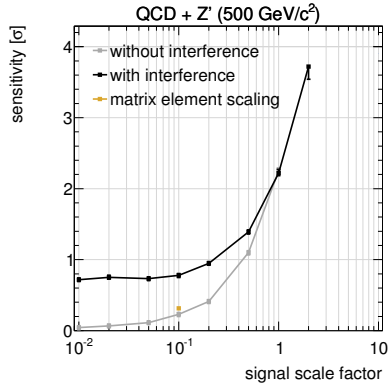

Figure 7.24: *Sensitivity against signal scale factor for a luminosity of $\mathcal{L} = 100\,pb^{-1}$. The coloured dot shows the sensitivity of a sample with scaled resonance coupling inside the matrix element, corresponding to a signal scale factor $\kappa = 0.1$.*

When extrapolating away from $\kappa = 1$, statistical fluctuations are amplified, so that the difference between two models appear larger than they actually are. The coloured dot in figure 7.24 shows the sensitivity determined from a Z' sample, where the coupling of the resonance vertex has been scaled by $\sqrt[4]{\kappa} = \sqrt[4]{0.1} \approx 0.56$ inside the matrix element. The result of this accurate calculation lies close to the result without interference. This already indicates that reweighting should not be applied when the scale factor differes from $\kappa = 1$ too much. This issue is also discussed in the next section.

A disadvantage of these two representations of results is that they only show a specific model for one particular mass of the resonance. Presenting these diagrams for all masses and all models would be confusing and it would be hard to get an overview of this amount of diagrams. Thus, it is better to show sensitivities against nominal

resonance mass for each type of resonance. Moreover, the signal scale factor κ is not a physical quantity, but only a parameter to scale couplings used during the event generation, whereas real $t\bar{t}$ resonances may have completely different and independent couplings to particles of the Standard Model.

Figure 7.25 shows the sensitivity for a Z' resonance against its mass for an integrated luminosity of $\mathscr{L} = 100\,\mathrm{pb}^{-1}$. It can be seen that both types of models, with or without interference, behave similarly, but also with some differences. The sensitivity for the pure resonance model decreases approximately linearly with increasing mass of the resonance. The full calculation including the interference shows a slightly steeper decrease.

Again, this diagram only applies for fixed values of resonance couplings and therefore only contains information for this specific model.

These examples show, that it is almost impossible to achieve agreement between both types of simulations in the complete 4-dimensional space of signal scale factor, mass, luminosity and sensitivity, although the Z' model exhibits only a small interference.

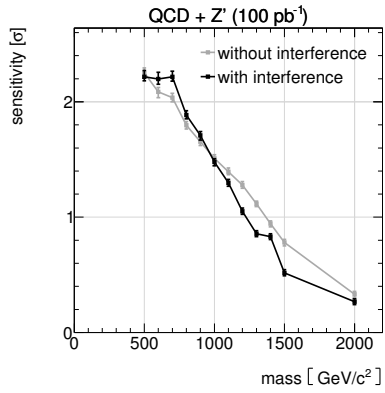

Figure 7.25: *Sensitivity against resonance mass for a luminosity of $\mathscr{L} = 100\,\mathrm{pb}^{-1}$. Error bars show the accuracy of determined sensitivities with the used number of ensembles.*

The common way to display exclusion limits is to draw the total cross section of a pure resonance times branching ratio into top quarks $\sigma_{\mathrm{Res}} \times \mathrm{BR}_{\mathrm{Res}\to t\bar{t}}$ for a 95 % confidence level against the mass of the resonance. This has the advantage of being independent from specific values of coupling parameters. Certain models can be excluded by comparing their predicted cross sections for resonances with respective exclusion limits. In case of this study, there is no value for the cross section of a pure resonances, because the resonance only appears together with QCD $t\bar{t}$ production and interference. Additionally, the cross section for top quark pair production already includes the branching ratio of a resonance into top quarks. Therefore, the branching ratio is not quoted explicitly as a separate factor.

An equivalent to the cross section times branching ratio of a pure resonance can only be given by the difference between cross sections of a full model including a resonance and the QCD model without a resonance. In case of no interference, this leads to the same value as the cross section of a resonance alone. In case of a strong interference, the resulting value is the excess of cross sections of a pure resonance with interference over the cross section of pure QCD $t\bar{t}$ production. As stated before, this excess can be negative when the full model predicts less events than expected from QCD, which makes a meaningful interpretation difficult. Nevertheless, results of this study are presented in this way in order to conform to common expectations for exclusion limits as far as possible.

7.6.2 Sensitivities without Systematic Uncertainties

A first analysis of sensitivities is done without systematic uncertainties in order to estimate the best result that can be obtained with the procedure of analysis described so far. This means, when generating ensembles for different models, only statistical uncertainties are taken into account.

Figure 7.26 shows respective cross sections needed for a 95 % CL exclusion limit for different types of resonances.

In general, all lines for models without interference are smooth across the whole mass range. Lines for models including interference show some fluctuations which can be seen best for the scalar and pseudoscalar Higgs models, because they have the smallest resonance contributions. Lines for the Z' models and models of coloured particles are rather smooth because of the larger resonances. Fluctuations originate from the difficulty in scaling a small resonance contribution to different resonance strengths. In this case, fluctuations of three different distributions add up as explained by equation 6.2, leading to large statistical errors of the calculated distribution. These arbitrary variations lead to fluctuations in shown exclusion limits when interpolating between sensitivities of models with fixed resonance strengths.

The relative behaviour of both lines of sensitivities, with or without interference, is similar for all other types of resonances. At low masses, the line of sensitivity respecting interference is always below the line of a model without interference. At high masses, both lines change positions. The lines for models respecting the interference run above lines of models without interference. The crossing point is different for each type of resonance.

This behaviour reflects the difficulty of scaling resonance contributions by reweighting events. As shown in figure 7.24, scaling of resonance contributions does not reproduce

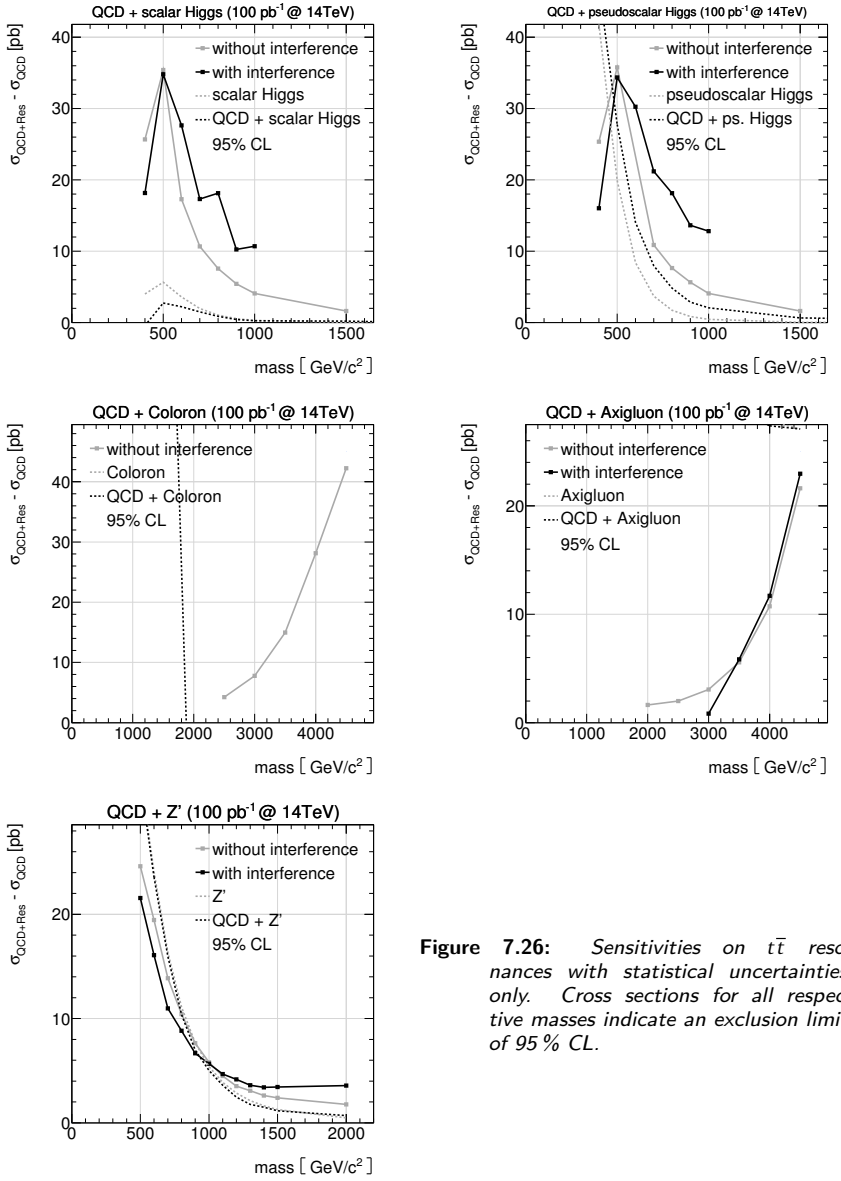

Figure 7.26: *Sensitivities on $t\bar{t}$ resonances with statistical uncertainties only. Cross sections for all respective masses indicate an exclusion limit of 95 % CL.*

corresponding sensitivities without interference when extrapolating too far from the simulated resonance strength, even in cases of negligible interference. Table 7.9 shows the scale factors needed for the Z' model to achive the 95 % CL exclusion limits shown in figure 7.26. The relative behaviour of the full model with respect to the line without interference follows the flow of scale factors. The crossing point of both lines matches the point with a scale factor of 1.

The discrepancies clearly show that reweighting of events on parton level according to the partonic invariant mass spectrum does not seem to propagate accurately through hadronisation, detector simulation, jet clustering and semileptonic reconstruction. Reweighting generates the correct $t\bar{t}$ invariant mass distribution on parton level by construction, but does not reproduce the right distribution after semileptonic reconstruction.

For accurate predictions of invariant mass spectra after reconstruction, it is necessary to simulate explicitly all variations in coupling parameters inside the matrix element, which also leads to more reliable results for sensitivities as has been shown in figure 7.24. This has to be done for each model and every mass of a resonance. This means, the number of generated events has to be multiplied by the number of different values of coupling parameters and resonance masses. Also the amount of needed computing power increases by this amount, which is far too much for the current study.

mass $[\mathrm{GeV}/c^2]$	scale factor
500	0.654
600	0.685
700	0.691
800	0.854
900	0.958
1000	1.125
1100	1.283
1200	1.632
1300	1.923
1400	2.211
1500	2.867
2000	6.351

Table 7.9: *Scale Factors of the Z' model for 95 % CL*

As most interferences investigated in this study are localised in the immediate vicinity of the nominal peak of the resonance, patterns of interference are also narrower than the experimental resolution. Therefore, it cannot be resolved in experiment by the method used in this study. As seen in section 7.4, shapes of distributions respecting or ignoring the interference hardly differ. The only measurable effect of an interference remains a change in the total cross section.

As already mentioned in section 7.3, total cross sections of the full models deviate from the sum of cross sections of the pure resonance and QCD $t\bar{t}$ production. Additionally, all simulated resonances are narrower than the experimental resolution, which is why the interference cannot be observed directly in experiment. Regarding

this situation, experimental sensitivities on total cross sections have to be equal for both cases, whether the interference is considered or ignored. Therefore, when calculated with accurate scaling of resonance contributions, all lines in figure 7.26 have to lie on top of the lines without interference.

Instead of having different sensitivities on an excess of the total cross section, theoretical predictions deviate whether interference is taken into account or not. Interference changes the total cross section of many models and, thus, increases or decreases the strength of a possible signal. In turn, interference also influences discovery potentials of these models. In total, not experimental sensitivities, but theoretical predictions of cross sections are different between both types of models.

The only exception to this situation considered in this study is the coloron model. The interference in this model introduces large differences, which are also easily visible after detector simulation and semileptonic reconstruction. Therefore, also significant differences in sensitivities are expected.

Figure 7.26 does not provide a line for the full model of a coloron with interference, because all sensitivities lie above 95 % CL for all scaled resonance contributions. This means, even if the resonance is scaled down by $\kappa = 0.01$, the sensitivity is still high enough to exclude this model with more than 95 % CL for all masses of the resonance. This changes, when systematic uncertainties are taken into account.

model	integrated luminosity $[{}^{1}/_{\mathrm{pb}}]$	exclusion limit $[{}^{\mathrm{GeV}}/_{c^2}]$ without interference	with interference
scalar Higgs	5000	400	—
pseudoscalar Higgs	500	550	800
sequential Z'	100	850	850
coloron	20	4100	4500
axigluon	20	4000	4000

Table 7.10: *Exclusion limits with only systematic uncertainties at 14 TeV centre-of-mass energy. Larger integrated luminosities are needed to exclude models with small resonance contributions like the Higgs models. Interferences can have strong impacts on the achievable exclusion limits.*

Table 7.10 shows exclusion limits obtained without systematic uncertainties. Depending on respective strengths of couplings, different integrated luminosities are needed to obtain 95 % CL exclusion limits. Cross sections of the scalar Higgs model are the smallest. This model can only be excluded because of increased sensitivity in the

threashold region of the invariant mass spectrum. The negative interference in this model decreases the cross section, so that no exclusion limit can be given, when the interference is taken into account.

7.6.3 Sensitivities including Systematic Uncertainties

The final step of this analysis includes systematic uncertainties into the calculation of sensitivities. As before, lines of sensitivities deviate between models including and without interferences.

Figure 7.27 summarises respective 95 % CL exclusion limits for the models under consideration. Again, lines of models without interference are smooth across the whole mass range. Lines of models including interference deviate slightly from these lines, which is caused by problems in scaling the resonance contribution. Apart from these difficulties, all lines are expected to lie on top of each other.

Again, the coloron model constitutes an exception, because of its large interference with the QCD continuum. In the full model including the interference, the 95 % CL exclusion limit is negative, because the interference leads to a deficit of events, which reduces the number of events compared to QCD $t\bar{t}$ production alone. In this case, exclusion limits set a lower limit on the total cross section of $t\bar{t}$ production. A stronger resonance contribution leads to a stronger interference, which would lower the observable cross section below the given threshold, which could be discovered in experiment.

In order to exclude specific extensions of the Standard Model, predictions of resonance cross sections of models described in section 7.3 have been superimposed onto figure 7.27. Apart from calculations done in this work, most other calculations of cross sections are done without paying attention to interferences. Full calculations including interferences are hardly done at all, which is why corresponding numerical values of cross sections are hardly available for the full models.

Figure 7.27 compares experimental sensitivities with the cross sections of models studied in this work. Resulting exclusion limits are summarised in table 7.11, where a larger integrated luminosity was chosen for the pseudoscalar Higgs model, because no exclusion limit could be obtained for this model with $\mathscr{L} = 100\,\mathrm{pb}^{-1}$. When systematic uncertainties are included, no exclusion limit can be established for the scalar Higgs boson, even with integrated luminosities of several fb^{-1}. Either a larger amount of data is needed to exclude this model or a model with an increased Higgs cross section could be considered, e.g. a 2HDM with $\tan(\beta) < 1$.

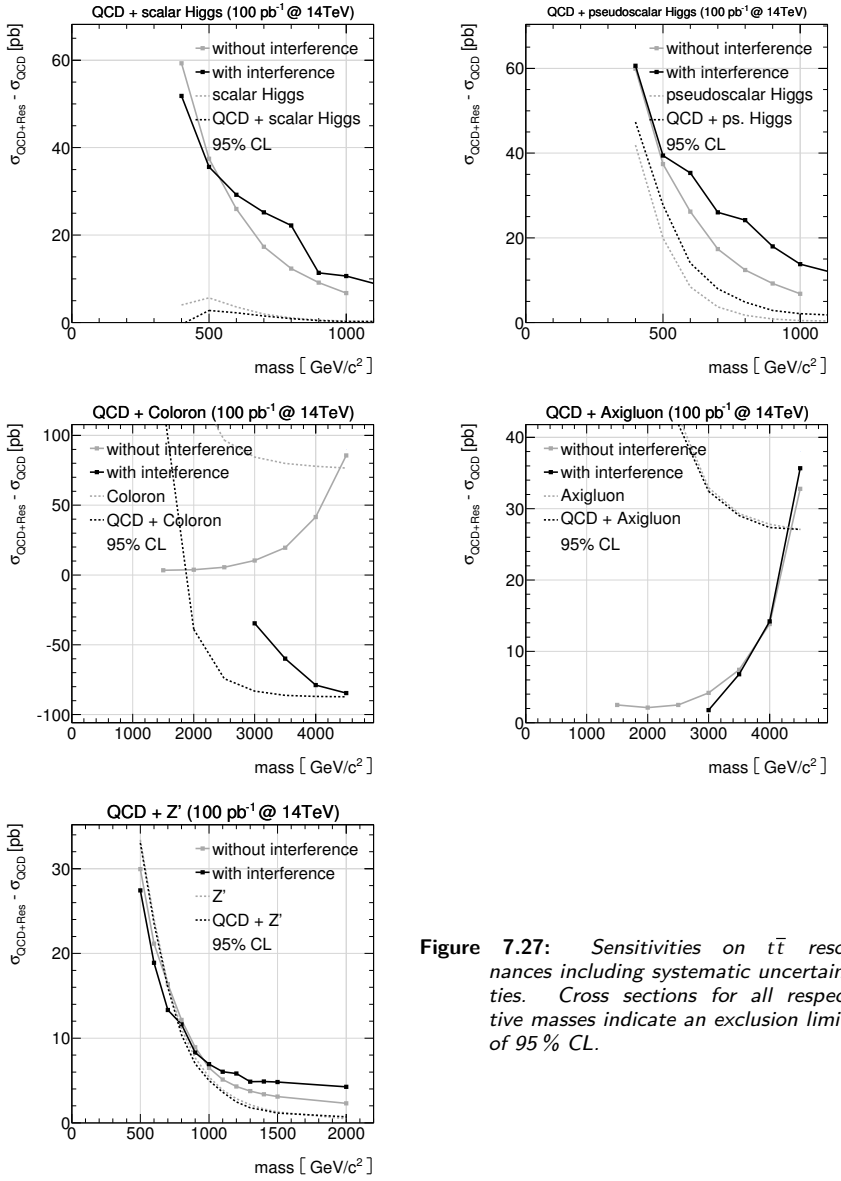

Figure 7.27: *Sensitivities on $t\bar{t}$ resonances including systematic uncertainties. Cross sections for all respective masses indicate an exclusion limit of 95 % CL.*

model	integrated luminosity $[1/\text{pb}]$	exclusion limit $[\text{GeV}/c^2]$ without interference	with interference
scalar Higgs	5000	—	—
pseudoscalar Higgs	500	500	650
sequential Z'	100	700	700
coloron	100	4400	4500
axigluon	100	4300	4300

Table 7.11: *Exclusion limits including systematic uncertainties at 14 TeV centre-of-mass energy. Larger integrated luminosities are needed to exclude models with small resonance contributions like the Higgs models. Interferences can have strong impacts on the achievable exclusion limits.*

7.7 Summary and Conclusion

This study investigated the effect of interferences of top-antitop quark pair production in QCD with a new heavy elementary boson decaying into a $t\bar{t}$ pair, which is generally called a $t\bar{t}$ resonance. Effects of interferences on the experimental data were of special interest. The determination of their influence on experimental studies involved the following steps.

- A new matrix element for the event generator HERWIG++ was developed, which calculates the full process of heavy quark-antiquark production, including the resonance as well as standard QCD $q\bar{q}$ production at the same time. The matrix element has been designed as flexible as possible, so that it is able to simulate resonances with almost every possible combinations of quantum numbers and couplings.
- Using the newly developed matrix element, five different models have been simulated, each with a different type of resonance. Studied models included a scalar and a pseudoscalar Higgs boson, a sequential Z' boson, a coloron model and an axigluon model. For each model, a huge amount of events has been generated for ∼10 different resonance masses of each model. This large number of events was necessary to distinguish interferences from statistical fluctuations even at high resonance masses of up to $4.5\,\text{TeV}/c^2$. With increasing mass of the resonance, its fraction of events on the full process decreases rapidly. In order to observe interference, which is an even smaller effect than the pure resonance signal, even more events are necessary in order to gain enough resonance events well above statistical fluctuations.

- All generated events have been processed by the free, open source detector simulation DELPHES. This is important to estimate experimentally accessible signatures. The layout and performance of the ATLAS detector has been chosen as an example of an existing detector.
- At several stages of an event, the invariant mass spectrum of top-antitop pairs has been determined. By calculating the error in reconstructing the original $t\bar{t}$ invariant mass, the mass resolution was determined at each considered stage of the event. The development of resolutions over all stages exhibited steps which introduce large errors in reconstruction of semileptonic events. The experimental resolution on the $t\bar{t}$ invariant mass in the semileptonic channel, averaged over the full mass range, was determined to be 16.6 %.
- Interferences have been calculated on parton level, revealing various patterns of interference for different types of $t\bar{t}$ resonances, depending on its quantum numbers and couplings. The pseudoscalar Higgs model exhibited the strongest interference relative to the size of the pure resonance contribution, whereas the coloron model showed the strongest absolute interference, also with the $t\bar{t}$ continuum of QCD. The sequential Z' and the axigluon model showed only negligible interference.
- A statistical analysis of expected data has been developed, taking into account the specialities of interferences. Established tools of analysis could not be used because the resonance contribution to the full $t\bar{t}$ spectrum cannot be separated into a distinct channel. The irreducible background of $t\bar{t}$ events from QCD is closely coupled to $t\bar{t}$ production via resonances. The according difficulties in a determination of sensitivities have been addressed in the context of a modified frequentistic approach.
- Systematic errors of the semileptonic reconstruction have been determined and respected in the determination of sensitivities of all considered kinds of $t\bar{t}$ resonances. Uncertainties of the leading order approximation are largest in the threshold region of $t\bar{t}$ production, but less important in higher mass regions. Jet energy scale uncertainties amount to about 10 % and PDF uncertainties to only about 3 %.
- Sensitivities to all considered models have been calculated and expected exclusion limits for all these types of resonances have been determined. In general, sensitivities to an excess of total cross sections over the standard QCD prediction of $t\bar{t}$ production do not change with interferences as long as the resonances are narrow, well below the detector resolution. Instead, theoretical predictions of total cross sections change when interference is taken into account, which renders resonances more or less likely to be discovered.

A special case is a strongly coupling resonance, which is produced directly in gluon-gluon fusion. A strong interference, which is possible in models of a vector or pseudoscalar particle, can significantly influence the continuum of the $t\bar{t}$ invariant mass spectrum, which would be clearly visible in experiment.

- With wide resonances, interferences will certainly have an effect also on the shape of the $t\bar{t}$ invariant mass distribution. In this case, a more sophisticated method of analysis, as developed in this work, has to be applied in order to take interference into account.

In summary, interferences do not affect analytical techniques significantly for narrow resonances. Instead, they change values of theoretical predictions of total cross sections. On the other hand, interferences in models of wide resonances change total cross sections as well as shapes of the $t\bar{t}$ invariant mass distributions. For this case, a method has been developed to determine experimental sensitivities, that also accounts for all difficulties arising, when $t\bar{t}$ production via a resonance and via standard QCD cannot be distinguished or separated any more.

A Calculation of the Top Resonance Colour Factors

A.1 The $\mathfrak{su}(N_C)$ Algebra

Relations of all representations

The colour matrices T^a_{ij} with $i,j = 1 \ldots N_C$ and $a = 1 \ldots \left(N_C^2 - 1\right)$ respect the (anti-)commutation relations

$$\left[T^a, T^b\right] = i f^{abc} T^c$$
$$\left\{T^a, T^b\right\} = \frac{1}{N_C} \delta^{ab} + d^{abc} T^c$$

with totally antisymmetric structure constants f^{abc}, and totally symmetric coefficients d^{abc}.

$$f^{axx} = d^{axx} = 0$$

Furthermore, the three constants C_A, C_F and T_F are defined by the following equations

$$\delta^{ab} C_A = f^{axy} f^{bxy}$$
$$\delta_{ij} C_F = (T^a T^a)_{ij}$$
$$\delta^{ab} T_F = \mathrm{Tr}\left(T^a T^b\right)$$

Products

$$T^a_{ij}T^a_{kl} = T_F\left(\delta_{il}\delta_{jk} - \frac{1}{N_C}\delta_{ij}\delta_{kl}\right)$$
$$f^{abx}f^{cdx} = \frac{2}{N_C}\left(\delta^{ac}\delta^{bd} - \delta^{ad}\delta^{bc}\right) + d^{acx}d^{bdx} - d^{adx}d^{bcx}$$

Jacobi identities

$$f^{abx}f^{cdx} - f^{acx}f^{bdx} + f^{adx}f^{bcx} = 0$$
$$f^{abx}d^{cdx} + f^{acx}d^{bdx} + f^{adx}d^{bcx} = 0$$

Casimir operators

$$\delta_{ab}T^a_{ij}T^b_{jk} = C_F\delta_{ik} = T_F\frac{N_C^2-1}{N_C}\delta_{ik}$$
$$f^{axy}f^{bxy} = C_A\delta^{ab} = N_C\delta^{ab}$$
$$d^{axy}d^{bxy} = \frac{N_C^2-4}{N_C}\delta^{ab}$$
$$f^{axy}d^{bxy} = 0$$

Further relations for the structure constants

$$f^{axy}f^{byz}f^{czx} = \frac{N_C}{2}f^{abc}$$
$$d^{axy}f^{byz}f^{czx} = -\frac{N_C}{2}d^{abc}$$
$$d^{axy}d^{byz}f^{czx} = -\frac{1}{2}\frac{N_C^2-4}{N_C}f^{abc}$$
$$d^{axy}d^{byz}d^{czx} = \frac{1}{2}\frac{N_C^2-12}{N_C}d^{abc}$$
$$f^{axy}f^{byz}f^{czu}f^{dux} = \delta^{ab}\delta^{cd} + \delta^{ad}\delta^{bc} + \frac{N_C}{4}\left(d^{abx}d^{cdx} - d^{acx}d^{bdx} + d^{adx}d^{bcx}\right)$$

Relations of special Representations

Traces of the fundamental representation

$$\begin{aligned}
\mathrm{Tr}\,(1) &= N_C \\
\mathrm{Tr}\,(T^a) &= 0 \\
\mathrm{Tr}\left(T^a T^b\right) &= T_F \delta^{ab} \\
\mathrm{Tr}\left(T^a T^b T^c\right) &= \frac{1}{2} T_F \left(d^{abc} + i f^{abc}\right) \\
\mathrm{Tr}\left(T^a T^b T^c T^d\right) &= \frac{1}{4} T_F \left[\frac{2}{N_C}\left(\delta^{ab}\delta^{cd} - \delta^{ac}\delta^{bd} + \delta^{ad}\delta^{bc}\right)\right. \\
&\quad + d^{abx} d^{cdx} - d^{acx} d^{bdx} + d^{adx} d^{bcx} \\
&\quad \left. + i\left(d^{abx} f^{cdx} + d^{acx} f^{bdx} + d^{adx} f^{bcx}\right)\right]
\end{aligned}$$

Further relations for the fundamental representation

$$\begin{aligned}
T^a T^b &= \frac{1}{2N_C}\delta^{ab} + \frac{1}{2}\left(d^{abx} + i f^{abx}\right) T^x \\
T^x T^a T^x &= \left(C_F - \frac{1}{2} C_A\right) T^a \\
f^{axy} T^x T^y &= \frac{i}{2} C_A T^a \\
f^{xyz} T^x T^y T^z &= \frac{i}{2} C_A C_F
\end{aligned}$$

For $SU(2)$, all $d^{abc} = 0$.

Following relation is only valid for $SU(3)$

$$d^{abx} d^{cdx} + d^{acx} d^{bdx} + d^{adx} d^{bcx} = \frac{1}{3}\left(\delta^{ab}\delta^{cd} + \delta^{ac}\delta^{bd} + \delta^{ad}\delta^{bc}\right)$$

Common convention is

$$T_F = \frac{1}{2}$$

For $SU(3)$ is

$$C_F = \frac{4}{3} \qquad \text{and} \qquad C_A = N_C = 3$$

Results may be extended to $U(1)$ by setting

$$T_F = C_F = 1 \qquad \text{and} \qquad C_A = 0$$

A.1.1 Multipletts of the $\mathfrak{su}(3)$ Algebra

$$\begin{aligned}
3 \otimes \overline{3} &= 8 \oplus 1 \\
3 \otimes 3 &= 6 \oplus \overline{3} \\
3 \otimes 3 \otimes 3 &= 10 \oplus 8 \oplus 8 \oplus 1 \\
3 \otimes 6 &= 10 \oplus 8 \\
\overline{3} \otimes 6 &= 12 \oplus 3 \oplus 3 \\
6 \otimes 6 &= 15 \oplus 12 \oplus \overline{6} \oplus 3 \\
6 \otimes \overline{6} &= 27 \oplus 8 \oplus 1 \\
8 \otimes 8 &= 27 \oplus 10 \oplus \overline{10} \oplus 8 \oplus 8 \oplus 1
\end{aligned}$$

A.2 Feynman Diagrams

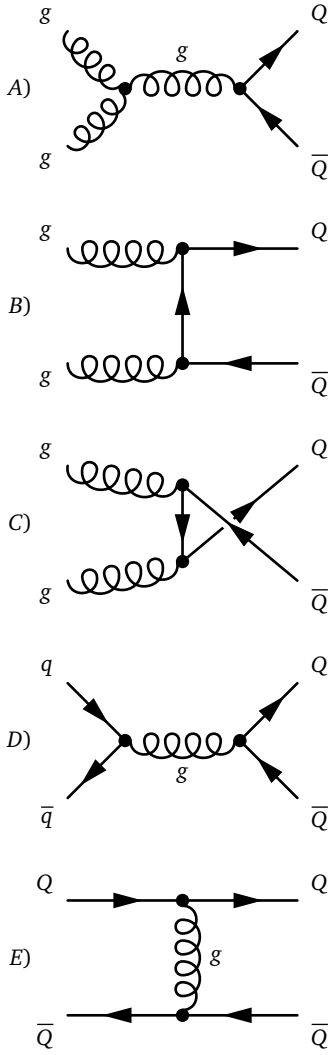

(scalar)

Note: If the direction of the fermion loop makes a difference (e.g. in colour factors), the diagram with the opposite fermion direction is labelled H'.

(colour octet)

A.3 Colour Flows

number	colour flow	Feynman diagrams	
		colour singlet resonance	colour octet resonance
1	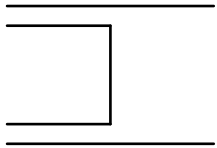	*A*, *B*	*A*, *B*, *H*, *I*
2	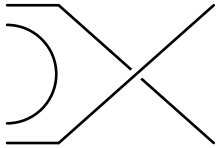	*A*, *C*	*A*, *C*, *H*, *I*
3	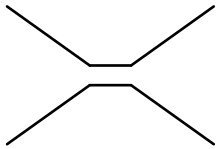	*D*, *G*	*D*, *F*
4	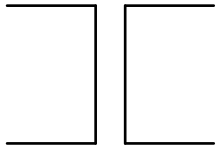	*E*, *F*	*E*, *G*
5	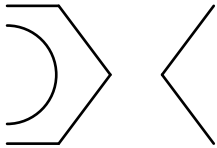	*H*, *I*	–

Table A.1: *Colour flows for implemented Feynman diagrams.*

A.4 Interferences

A.4.1 QCD Diagrams

Process	Feynman diagram	colour factor
$A\overline{A} =$	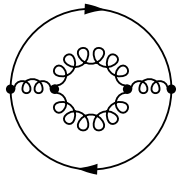	$\sim (T^a)_{ij}(-i)f_{abc}(-i)f_{bdc}(T^d)_{ji}$ $= -(i^2)f_{abc}f_{dbc}\mathrm{Tr}(T^aT^d)$ $= \delta_{ad}C_\mathrm{A}\mathrm{Tr}(T^aT^d)$ $= \delta_{ad}C_\mathrm{A}\delta^{ad}T_\mathrm{F}$ $= C_\mathrm{A}(N_\mathrm{C}^2-1)T_\mathrm{F}$ $= C_\mathrm{A}N_\mathrm{C}C_\mathrm{F} = 12$
$A\overline{B} = -A\overline{C} =$	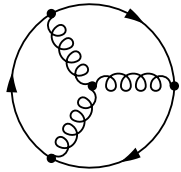	$\sim (T^a)_{ij}(T^b)_{jk}(T^c)_{ki}(-i)f_{abc}$ $= -if_{abc}\mathrm{Tr}(T^aT^bT^c)$ $= -if_{abc}\frac{1}{2}T_\mathrm{F}\left(d^{abc}+if^{abc}\right)$ $= \frac{1}{2}T_\mathrm{F}f_{abc}f^{abc}$ $= \frac{1}{2}T_\mathrm{F}C_\mathrm{A}\delta^{aa}$ $= \frac{1}{2}T_\mathrm{F}C_\mathrm{A}(N_\mathrm{C}^2-1)$ $= \frac{1}{2}C_\mathrm{A}^2C_\mathrm{F} = 6$ $-A\overline{C}$ because the fermion line flows into the opposite direction.
$B\overline{B} = C\overline{C} =$	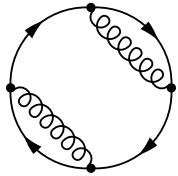	$\sim (T^a)_{ij}(T^a)_{jk}(T^b)_{kl}(T^b)_{li}$ $= (T^a)_{ij}(T^a)_{jk}C_\mathrm{F}\delta_{ki}$ $= C_\mathrm{F}(T^a)_{ij}(T^a)_{ji}$ $= C_\mathrm{F}^2\delta_{ii}$ $= N_\mathrm{C}C_\mathrm{F}^2 = \frac{16}{3}$

Process	Feynman diagram	colour factor
$B\overline{C} = D\overline{E} =$	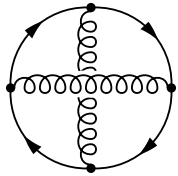	$\sim (T^a)_{ij}(T^b)_{jk}(T^a)_{kl}(T^b)_{li}$ $= \mathrm{Tr}\left(T^a T^b T^a T^b\right)$ $= \left(C_\mathsf{F} - \frac{1}{2}C_\mathsf{A}\right)\mathrm{Tr}\left(T^a T^a\right)$ $= \left(C_\mathsf{F} - \frac{1}{2}C_\mathsf{A}\right)T_\mathsf{F}(N_\mathsf{C}^2 - 1)$ $= \left(C_\mathsf{F} - \frac{1}{2}C_\mathsf{A}\right)N_\mathsf{C}C_\mathsf{F} = -\frac{2}{3}$
$D\overline{D} = E\overline{E} =$	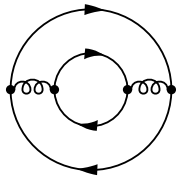	$\sim (T^a)_{ij}(T^b)_{ji}(T^a)_{kl}(T^b)_{lk}$ $= \mathrm{Tr}\left(T^a T^b\right)\mathrm{Tr}\left(T^a T^b\right)$ $= \mathrm{Tr}^2\left(T^a T^b\right)$ $= T_\mathsf{F}^2 \delta_{ab}\delta^{ab}$ $= T_\mathsf{F}^2 \delta^{aa}$ $= T_\mathsf{F}^2(N_\mathsf{C}^2 - 1)$ $= T_\mathsf{F}C_\mathsf{F}N_\mathsf{C} = 2$

A.4.2 Colour Singlet Resonance Diagrams

Process	Feynman diagram	colour factor
$D\overline{F} = E\overline{G} =$	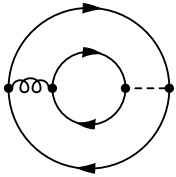	$\sim (T^a)_{ij}\delta_{ji}(T^a)_{kl}\delta_{lk}$ $= \mathrm{Tr}(T^a)\mathrm{Tr}(T^a)$ $= 0$
$D\overline{G} = E\overline{F} =$	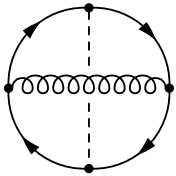	$\sim (T^a)_{ij}\delta_{jk}(T^a)_{kl}\delta_{li}$ $= (T^a)_{ik}(T^a)_{ki}$ $= C_\mathsf{F}\delta_{ii}$ $= C_\mathsf{F}N_\mathsf{C} = 4$

Process	Feynman diagram	colour factor
$F\overline{F} = G\overline{G} =$	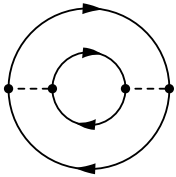	$\sim \delta_{ij}\delta_{ji}\delta_{kl}\delta_{lk}$ $= \delta_{ii}\delta_{kk}$ $= N_C^2 = 9$
$F\overline{G} =$	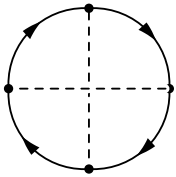	$\sim \delta_{ij}\delta_{jk}\delta_{kl}\delta_{li}$ $= \delta_{ii}$ $= N_C = 3$
$B\overline{H} = C\overline{H} =$	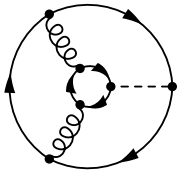	$\sim (T^a)_{ij}\delta_{jk}(T^b)_{ki}(T^a)_{lm}\delta_{mn}(T^b)_{nl}$ $= \mathrm{Tr}\left(T^aT^b\right)\mathrm{Tr}\left(T^aT^b\right)$ $= D\overline{D} = E\overline{E}$ $= T_F C_F N_C = 2$
$A\overline{H} =$	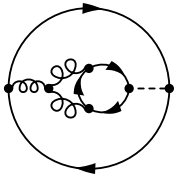	$\sim (T^a)_{ij}\delta_{ji}f^{abc}(T^b)_{kl}\delta_{lm}(T^c)_{mk}$ $= f^{abc}\mathrm{Tr}(T^a)\mathrm{Tr}\left(T^bT^c\right)$ $= 0$
$H\overline{H} =$	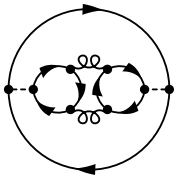	$\sim \delta_{ij}\delta_{ji}\delta_{kl}(T^a)_{lm}(T^b)_{mk}(T^a)_{np}\delta_{pq}(T^b)_{qn}$ $= \delta_{ii}\mathrm{Tr}\left(T^aT^b\right)\mathrm{Tr}\left(T^aT^b\right)$ $= N_C \cdot D\overline{D} = N_C \cdot E\overline{E}$ $= T_F C_F N_C^2 = 6$

A.4.3 Colour Octet Resonance Diagrams

Process	Feynman diagram	colour factor
$D\overline{F} = E\overline{G} =$	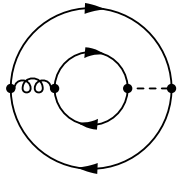	$\sim (T^a)_{ij}(T^b)_{ji}(T^a)_{kl}(T^b)_{lk}$ $= \mathrm{Tr}\left(T^a T^b\right) \mathrm{Tr}\left(T^a T^b\right)$ $= D\overline{D} = E\overline{E}$ $= T_\mathsf{F} C_\mathsf{F} N_\mathsf{C} = 2$
$D\overline{G} = E\overline{F} =$	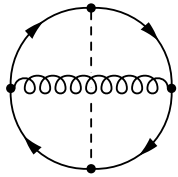	$\sim (T^a)_{ij}(T^b)_{jk}(T^a)_{kl}(T^b)_{li}$ $= \mathrm{Tr}\left(T^a T^b T^a T^b\right)$ $= B\overline{C} = D\overline{E}$ $= \left(C_\mathsf{F} - \frac{1}{2} C_\mathsf{A}\right) N_\mathsf{C} C_\mathsf{F} = -\frac{2}{3}$
$F\overline{F} = G\overline{G} =$	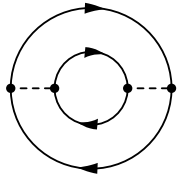	$\sim (T^a)_{ij}(T^b)_{ji}(T^a)_{kl}(T^b)_{lk}$ $= \mathrm{Tr}\left(T^a T^b\right) \mathrm{Tr}\left(T^a T^b\right)$ $= D\overline{D} = E\overline{E}$ $= T_\mathsf{F} C_\mathsf{F} N_\mathsf{C} = 2$
$F\overline{G} =$	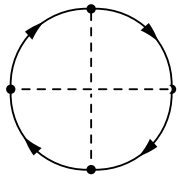	$\sim (T^a)_{ij}(T^b)_{jk}(T^a)_{kl}(T^b)_{li}$ $= \mathrm{Tr}\left(T^a T^b T^a T^b\right)$ $= B\overline{C} = D\overline{E}$ $= \left(C_\mathsf{F} - \frac{1}{2} C_\mathsf{A}\right) N_\mathsf{C} C_\mathsf{F} = -\frac{2}{3}$

Process	Feynman diagram	colour factor
$B\overline{H} =$	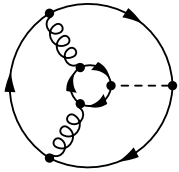	$\sim (T^a)_{ij}(T^b)_{jk}(T^c)_{ki}(T^a)_{lm}(T^b)_{mn}(T^c)_{nl}$ $= \mathrm{Tr}\left(T^a T^b T^c\right) \mathrm{Tr}\left(T^a T^b T^c\right)$ $= \left[\frac{1}{2} T_\mathrm{F}\left(d^{abc} + i f^{abc}\right)\right]^2$ $= \frac{1}{4} T_\mathrm{F}^2 \left(d^{abc} d_{abc} - f^{abc} f_{abc} + 2i d^{abc} f_{abc}\right)$ $= \frac{1}{4} T_\mathrm{F}^2 \left(\frac{N_\mathrm{C}^2 - 4}{N_\mathrm{C}} \delta^{aa} - N_\mathrm{C} \delta^{aa}\right)$ $= -T_\mathrm{F}^2 \frac{1}{N_\mathrm{C}} \left(N_\mathrm{C}^2 - 1\right)$ $= -T_\mathrm{F} C_\mathrm{F} = -\frac{2}{3}$
$C\overline{H} =$	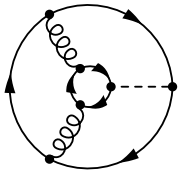	$\sim (T^c)_{ij}(T^a)_{jk}(T^a)_{ki}(T^a)_{lm}(T^b)_{mn}(T^c)_{nl}$ $= \mathrm{Tr}\left(T^c T^b T^a\right) \mathrm{Tr}\left(T^a T^b T^c\right)$ $= \left[\frac{1}{2} T_\mathrm{F}\left(d^{cba} + i f^{cba}\right)\right] \left[\frac{1}{2} T_\mathrm{F}\left(d^{abc} + i f^{abc}\right)\right]$ $= \left[\frac{1}{2} T_\mathrm{F}\left(d^{abc} - i f^{abc}\right)\right] \left[\frac{1}{2} T_\mathrm{F}\left(d^{abc} + i f^{abc}\right)\right]$ $= \frac{1}{4} T_\mathrm{F}^2 \left(d^{abc} d_{abc} + f^{abc} f_{abc}\right)$ $= \frac{1}{4} T_\mathrm{F}^2 \left(\frac{N_\mathrm{C}^2 - 4}{N_\mathrm{C}} \delta^{aa} + N_\mathrm{C} \delta^{aa}\right)$ $= \frac{1}{4} T_\mathrm{F}^2 \frac{2N_\mathrm{C}^2 - 4}{N_\mathrm{C}} \left(N_\mathrm{C}^2 - 1\right)$ $= \frac{1}{4} T_\mathrm{F} C_\mathrm{F} (2N_\mathrm{C}^2 - 4) = \frac{7}{3}$

Process	Feynman diagram	colour factor
$A\overline{H} =$	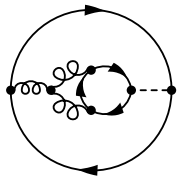	$\sim (T^a)_{ij}(T^b)_{ji}(-i)f^{acd}(T^c)_{kl}(T^b)_{lm}(T^d)_{mk}$ $= (-i)f^{acd}\mathrm{Tr}\left(T^aT^b\right)\mathrm{Tr}\left(T^cT^bT^d\right)$ $= (-i)f^{acd}T_\mathrm{F}\delta^{ab}\frac{1}{2}T_\mathrm{F}\left(d^{cbd}+if^{cbd}\right)$ $= (-i)f^{acd}T_\mathrm{F}\frac{1}{2}T_\mathrm{F}\left(d^{acd}-if^{acd}\right)$ $= -\frac{1}{2}T_\mathrm{F}^2 f^{acd}f_{acd}$ $= -\frac{1}{2}T_\mathrm{F}^2 C_\mathrm{A}\delta_{aa}$ $= -\frac{1}{2}T_\mathrm{F}^2 C_\mathrm{A}\left(N_\mathrm{C}^2-1\right)$ $= -\frac{1}{2}T_\mathrm{F}C_\mathrm{F}N_\mathrm{C}C_\mathrm{A} = -3$
$H\overline{H} =$	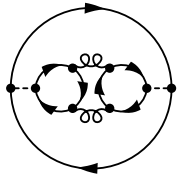	$\sim (T^a)_{ij}(T^b)_{ji}(T^a)_{kl}(T^c)_{lm}(T^d)_{mk}(T^c)_{np}(T^b)_{pq}(T^d)_{qn}$ $= \mathrm{Tr}\left(T^aT^b\right)\cdot\mathrm{Tr}\left(T^aT^cT^d\right)\cdot\mathrm{Tr}\left(T^cT^bT^d\right)$ $= T_\mathrm{F}\delta^{ab}\cdot\frac{1}{2}T_\mathrm{F}\left(d^{acd}+if^{acd}\right)\cdot\frac{1}{2}T_\mathrm{F}\left(d^{cbd}+if^{cbd}\right)$ $= \frac{1}{4}T_\mathrm{F}^3\cdot\left(d^{acd}+if^{acd}\right)\cdot\left(d^{acd}-if^{acd}\right)$ $= \frac{1}{4}T_\mathrm{F}^3\cdot\left(d^{acd}d_{acd}+f^{acd}f_{acd}\right)$ $= \frac{1}{4}T_\mathrm{F}^3\cdot\left(\frac{N_\mathrm{C}^2-4}{N_\mathrm{C}}\delta^{aa}+C_\mathrm{A}\delta^{aa}\right)$ $= \frac{1}{4}T_\mathrm{F}^3\left(N_\mathrm{C}^2-1\right)\cdot\left(\frac{N_\mathrm{C}^2-4}{N_\mathrm{C}}+N_\mathrm{C}\right)$ $= \frac{1}{2}T_\mathrm{F}^3\left(N_\mathrm{C}^2-1\right)\cdot\frac{N_\mathrm{C}^2-2}{N_\mathrm{C}}$ $= \frac{1}{2}T_\mathrm{F}^2C_\mathrm{F}\cdot\left(N_\mathrm{C}^2-2\right) = \frac{7}{6}$

Process	Feynman diagram	colour factor
$H\overline{H'} =$	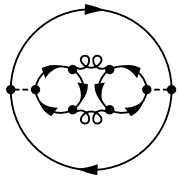	$\sim (T^a)_{ij}(T^b)_{ji}(T^a)_{kl}(T^c)_{lm}(T^d)_{mk}(T^d)_{np}(T^b)_{pq}(T^c)_{qn}$ $= \mathrm{Tr}\left(T^a T^b\right) \cdot \mathrm{Tr}\left(T^a T^c T^d\right) \cdot \mathrm{Tr}\left(T^b T^c T^d\right)$ $= T_\mathrm{F}\delta^{ab} \cdot \frac{1}{2} T_\mathrm{F}\left(d^{acd} + if^{acd}\right) \cdot \frac{1}{2} T_\mathrm{F}\left(d^{bcd} + if^{bcd}\right)$ $= \frac{1}{4} T_\mathrm{F}^3 \cdot \left(d^{acd} + if^{acd}\right) \cdot \left(d^{acd} + if^{acd}\right)$ $= \frac{1}{4} T_\mathrm{F}^3 \cdot \left(d^{acd} d_{acd} - f^{acd} f_{acd}\right)$ $= \frac{1}{4} T_\mathrm{F}^3 \cdot \left(\frac{N_\mathrm{C}^2 - 4}{N_\mathrm{C}} \delta^{aa} - C_\mathrm{A}\delta^{aa}\right)$ $= \frac{1}{4} T_\mathrm{F}^3 \left(N_\mathrm{C}^2 - 1\right) \cdot \left(\frac{N_\mathrm{C}^2 - 4}{N_\mathrm{C}} - N_\mathrm{C}\right)$ $= -T_\mathrm{F}^3 \left(N_\mathrm{C}^2 - 1\right) \cdot \frac{1}{N_\mathrm{C}}$ $= -T_\mathrm{F}^2 C_\mathrm{F} = -\frac{1}{3}$

A.5 Matrix Elements

A.5.1 Colour Singlet Resonance

$$
\begin{aligned}
\left|\mathscr{M}_{gg}\right|^2 &= \mathscr{M}_{gg}\overline{\mathscr{M}_{gg}} \\
&= \frac{1}{4}\cdot\frac{1}{64}\sum_{\text{Helicity,Colour}}\left|A+B+C+H+H'\right|^2 \\
&= \frac{1}{4}\cdot\frac{1}{64}\sum_{\text{Helicity,Colour}}\Bigg(12\cdot A\overline{A}+\frac{16}{3}\cdot B\overline{B}+\frac{16}{3}\cdot C\overline{C}+6\cdot[H+H']\overline{[H+H']} \\
&\qquad +6\cdot A\overline{B}+6\cdot B\overline{A}-6\cdot A\overline{C}-6\cdot C\overline{A}-\frac{2}{3}\cdot B\overline{C}-\frac{2}{3}\cdot C\overline{B} \\
&\qquad +0\cdot A\overline{[H+H']}+0\cdot[H+H']\overline{A} \\
&\qquad +2\cdot B\overline{[H+H']}+2\cdot[H+H']\overline{B}+2\cdot C\overline{[H+H']}+2\cdot[H+H']\overline{C}\Bigg) \\
&= \frac{1}{4}\cdot\frac{1}{64}\sum_{\text{Helicity,Colour}}\text{Re}\Bigg(12\cdot A\overline{A}+\frac{16}{3}\cdot B\overline{B}+\frac{16}{3}\cdot C\overline{C}+24\cdot H\overline{H} \\
&\qquad +12\cdot A\overline{B}-12\cdot A\overline{C}-\frac{4}{3}\cdot B\overline{C}+8\cdot B\overline{H}+8\cdot C\overline{H}\Bigg) \\
&= \frac{1}{4}\cdot\frac{1}{64}\cdot\frac{4}{3}\sum_{\text{Helicity,Colour}}\text{Re}\Big(9\cdot A\overline{A}+4\cdot B\overline{B}+4\cdot C\overline{C}+18\cdot H\overline{H} \\
&\qquad +9\cdot A\overline{B}-9\cdot A\overline{C}-B\overline{C}+6\cdot B\overline{H}+6\cdot C\overline{H}\Big)
\end{aligned}
$$

$$
\begin{aligned}
\left|\mathcal{M}_{q\bar{q}}\right|^2 &= \mathcal{M}_{q\bar{q}}\overline{\mathcal{M}_{q\bar{q}}} \\
&= \frac{1}{4}\cdot\frac{1}{9}\sum_{\text{Helicity,Colour}} |D+E+F+G|^2 \\
&= \frac{1}{4}\cdot\frac{1}{9}\sum_{\text{Helicity,Colour}} \Big(2\cdot D\overline{D} + 2\cdot E\overline{E} + 9\cdot F\overline{F} + 9\cdot G\overline{G} \\
&\qquad -\frac{2}{3}\cdot D\overline{E} - \frac{2}{3}\cdot E\overline{D} + 0\cdot D\overline{F} + 0\cdot F\overline{D} + 4\cdot D\overline{G} + 4\cdot G\overline{D} \\
&\qquad + 4\cdot E\overline{F} + 4\cdot F\overline{E} + 0\cdot E\overline{G} + 0\cdot G\overline{E} + 3\cdot F\overline{G} + 3\cdot G\overline{F} \Big) \\
&= \frac{1}{4}\cdot\frac{1}{9}\sum_{\text{Helicity,Colour}} \mathrm{Re}\Big(2\cdot D\overline{D} + 2\cdot E\overline{E} + 9\cdot F\overline{F} + 9\cdot G\overline{G} \\
&\qquad -\frac{4}{3}\cdot D\overline{E} + 8\cdot D\overline{G} + 8\cdot E\overline{F} + 6\cdot F\overline{G} \Big) \\
&= \frac{1}{4}\cdot\frac{1}{9}\cdot\frac{1}{3}\sum_{\text{Helicity,Colour}} \mathrm{Re}\Big(6\cdot D\overline{D} + 6\cdot E\overline{E} + 27\cdot F\overline{F} + 27\cdot G\overline{G} \\
&\qquad -4\cdot D\overline{E} + 24\cdot D\overline{G} + 24\cdot E\overline{F} + 18\cdot F\overline{G} \Big)
\end{aligned}
$$

A.5.2 Colour Octet Resonance

$$
\begin{aligned}
\left|\mathcal{M}_{gg}\right|^2 &= \mathcal{M}_{gg}\overline{\mathcal{M}_{gg}} \\
&= \frac{1}{4}\cdot\frac{1}{64}\sum_{\text{Helicity,Colour}}\left|A+B+C+H+H'\right|^2 \\
&= \frac{1}{4}\cdot\frac{1}{64}\sum_{\text{Helicity,Colour}}\Bigg(12\cdot A\overline{A}+\frac{16}{3}\cdot B\overline{B}+\frac{16}{3}\cdot C\overline{C} \\
&\quad +\frac{7}{6}\cdot\left[H\overline{H}+H'\overline{H'}\right]-\frac{1}{3}\cdot\left[H\overline{H'}+H'\overline{H}\right] \\
&\quad +6\cdot A\overline{B}+6\cdot B\overline{A}-6\cdot A\overline{C}-6\cdot C\overline{A}-\frac{2}{3}\cdot B\overline{C}-\frac{2}{3}\cdot C\overline{B} \\
&\quad -3\cdot A\overline{H}-3\cdot H\overline{A}-\frac{2}{3}\cdot B\overline{H}-\frac{2}{3}\cdot H\overline{B}+\frac{7}{3}\cdot C\overline{H}+\frac{7}{3}\cdot H\overline{C}\Bigg) \\
&= \frac{1}{4}\cdot\frac{1}{64}\sum_{\text{Helicity,Colour}}\text{Re}\Bigg(12\cdot A\overline{A}+\frac{16}{3}\cdot B\overline{B}+\frac{16}{3}\cdot C\overline{C}+\frac{5}{3}\cdot H\overline{H} \\
&\quad +12\cdot A\overline{B}-12\cdot A\overline{C}-\frac{4}{3}\cdot B\overline{C}-6\cdot A\overline{H}-\frac{4}{3}\cdot B\overline{H}+\frac{14}{3}\cdot C\overline{H}\Bigg) \\
&= \frac{1}{4}\cdot\frac{1}{64}\cdot\frac{1}{3}\sum_{\text{Helicity,Colour}}\text{Re}\Big(36\cdot A\overline{A}+16\cdot B\overline{B}+16\cdot C\overline{C}+5\cdot H\overline{H} \\
&\quad +36\cdot A\overline{B}-36\cdot A\overline{C}-4\cdot B\overline{C}-18\cdot A\overline{H}-4\cdot B\overline{H}+14\cdot C\overline{H}\Big)
\end{aligned}
$$

$$
\begin{aligned}
\left|\mathcal{M}_{q\bar{q}}\right|^2 &= \mathcal{M}_{q\bar{q}}\overline{\mathcal{M}_{q\bar{q}}} \\
&= \frac{1}{4}\cdot\frac{1}{9}\sum_{\text{Helicity,Colour}} |D+E+F+G|^2 \\
&= \frac{1}{4}\cdot\frac{1}{9}\sum_{\text{Helicity,Colour}} \Big(2\cdot D\overline{D}+2\cdot E\overline{E}+2\cdot F\overline{F}+2\cdot G\overline{G} \\
&\quad -\frac{2}{3}\cdot D\overline{E}-\frac{2}{3}\cdot E\overline{D}+2\cdot D\overline{F}+2\cdot F\overline{D}-\frac{2}{3}\cdot D\overline{G}-\frac{2}{3}\cdot G\overline{D} \\
&\quad -\frac{2}{3}\cdot E\overline{F}-\frac{2}{3}\cdot F\overline{E}+2\cdot E\overline{G}+2\cdot G\overline{E}-\frac{2}{3}\cdot F\overline{G}-\frac{2}{3}\cdot G\overline{F}\Big) \\
&= \frac{1}{4}\cdot\frac{1}{9}\sum_{\text{Helicity,Colour}} \text{Re}\Big(2\cdot D\overline{D}+2\cdot E\overline{E}+2\cdot F\overline{F}+2\cdot G\overline{G} \\
&\quad -\frac{4}{3}\cdot D\overline{E}+4\cdot D\overline{F}-\frac{4}{3}\cdot D\overline{G}-\frac{4}{3}\cdot E\overline{F}+4\cdot E\overline{G}-\frac{4}{3}\cdot F\overline{G}\Big) \\
&= \frac{1}{4}\cdot\frac{1}{9}\cdot\frac{2}{3}\sum_{\text{Helicity,Colour}} \text{Re}\Big(3\cdot D\overline{D}+3\cdot E\overline{E}+3\cdot F\overline{F}+3\cdot G\overline{G} \\
&\quad -2\cdot D\overline{E}+6\cdot D\overline{F}-2\cdot D\overline{G}-2\cdot E\overline{F}+6\cdot E\overline{G}-2\cdot F\overline{G}\Big)
\end{aligned}
$$

B

Migrations in Reconstruction Levels

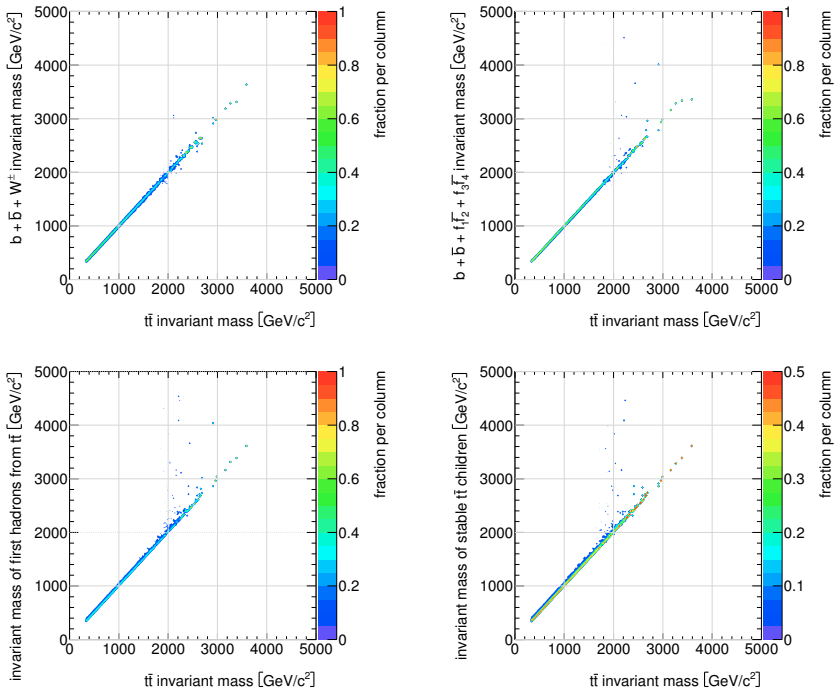

Figure B.1: *Invariant mass reconstruction on parton level and with first hadrons just after hadronisation. Only child particles of top quarks are taken into account. Histograms show the migration of the $t\bar{t}$ invariant mass from its true value to the reconstructed value. Straight diagonal lines indicate an accurate reconstruction of the invariant mass.*

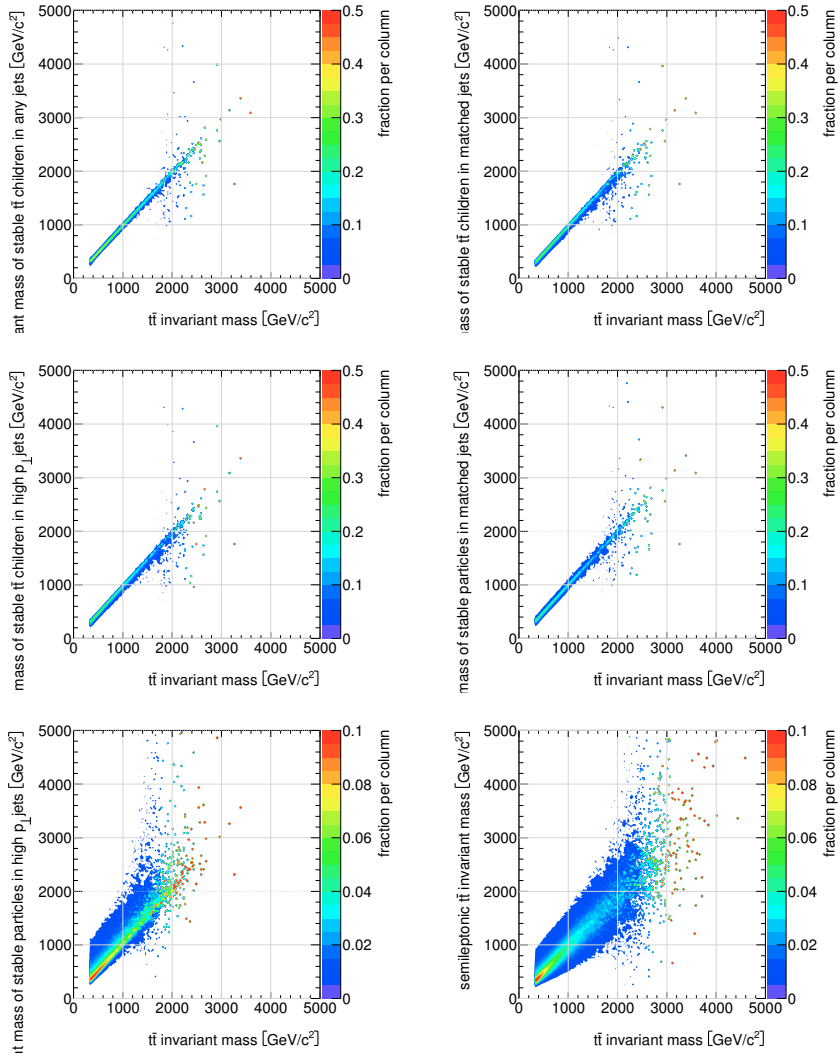

Figure B.2: *Invariant mass reconstruction at final state levels. Histograms show the migration of the $t\bar{t}$ invariant mass from its true value to the reconstructed value. Deviations from a straight diagonal line indicate misreconstructed invariant masses. In the last step, a mass resolution of $\frac{\Delta m}{m} \approx 16.6\,\%$ can be achieved.*

C

Sensitivities with Statistical Uncertainties

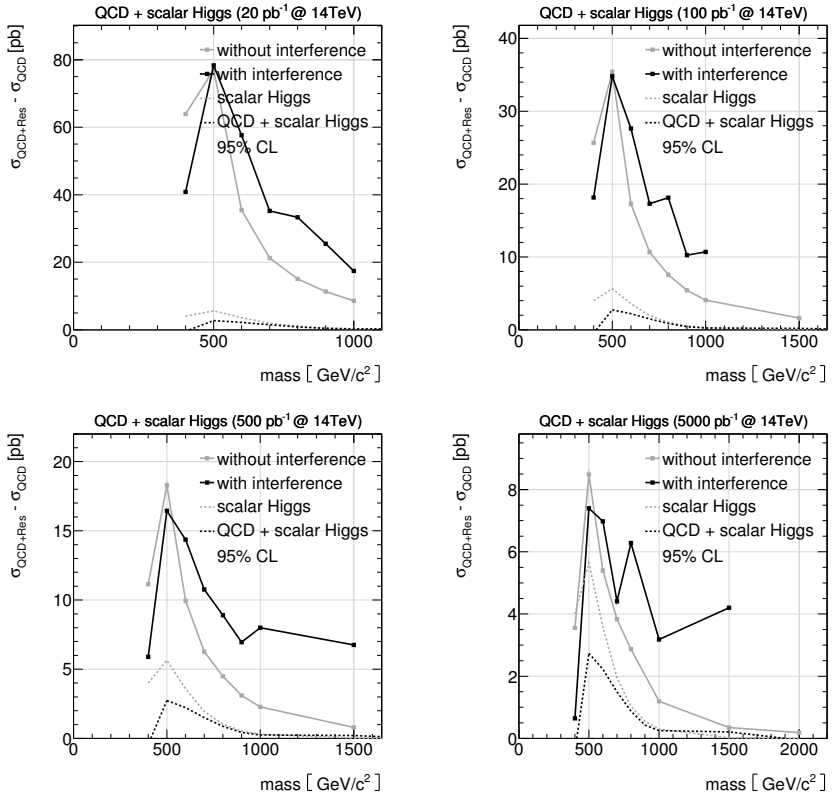

Figure C.1: *Sensitivities on scalar Higgs bosons with statistical uncertainties. Cross sections for all respective masses indicate an exclusion limit of 95 % CL.*

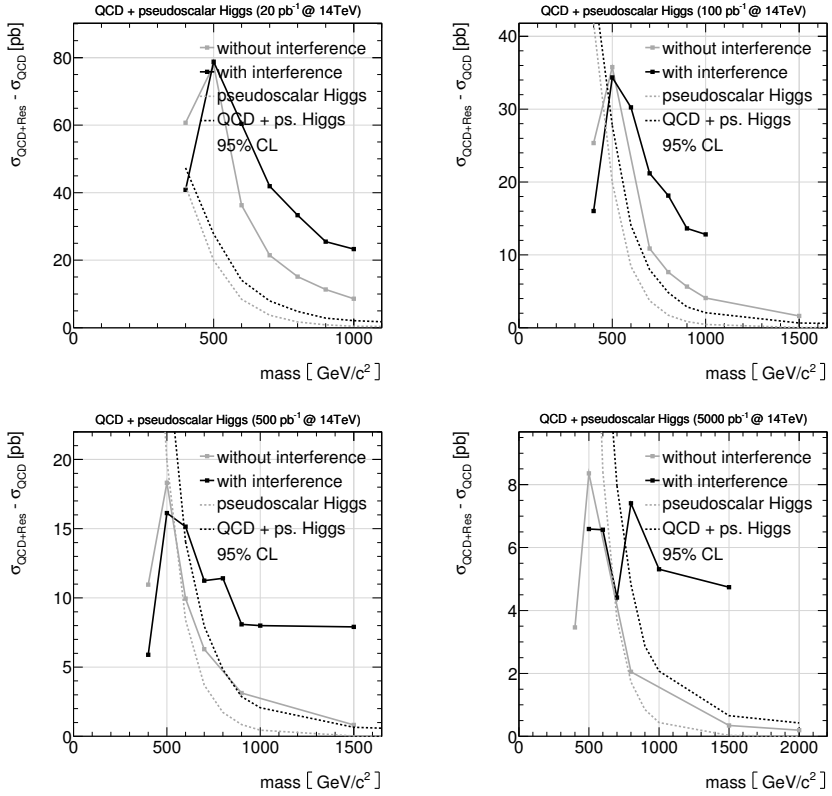

Figure C.2: *Sensitivities on pseudoscalar Higgs bosons with statistical uncertainties. Cross sections for all respective masses indicate an exclusion limit of 95 % CL.*

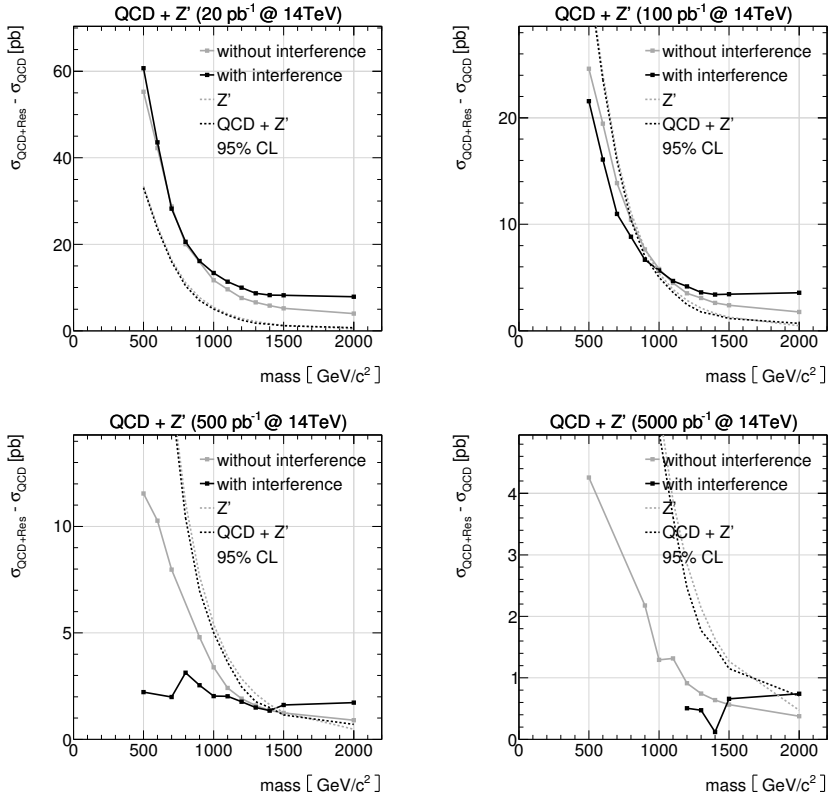

Figure C.3: *Sensitivities on Z' bosons with statistical uncertainties. Cross sections for all respective masses indicate an exclusion limit of 95 % CL.*

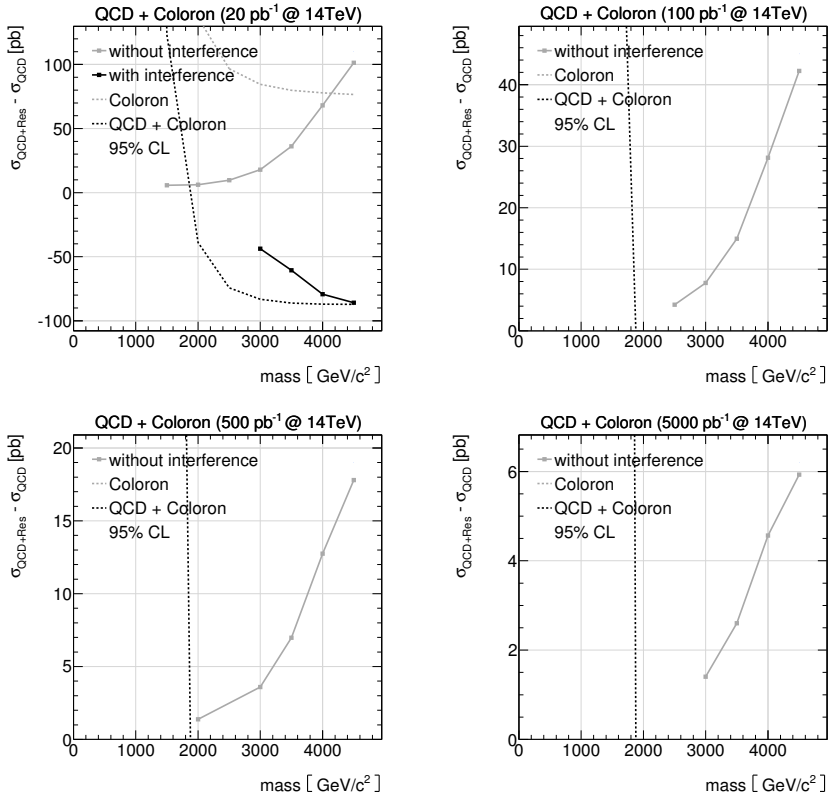

Figure C.4: *Sensitivities on colorons bosons with statistical uncertainties. Cross sections for all respective masses indicate an exclusion limit of 95 % CL.*

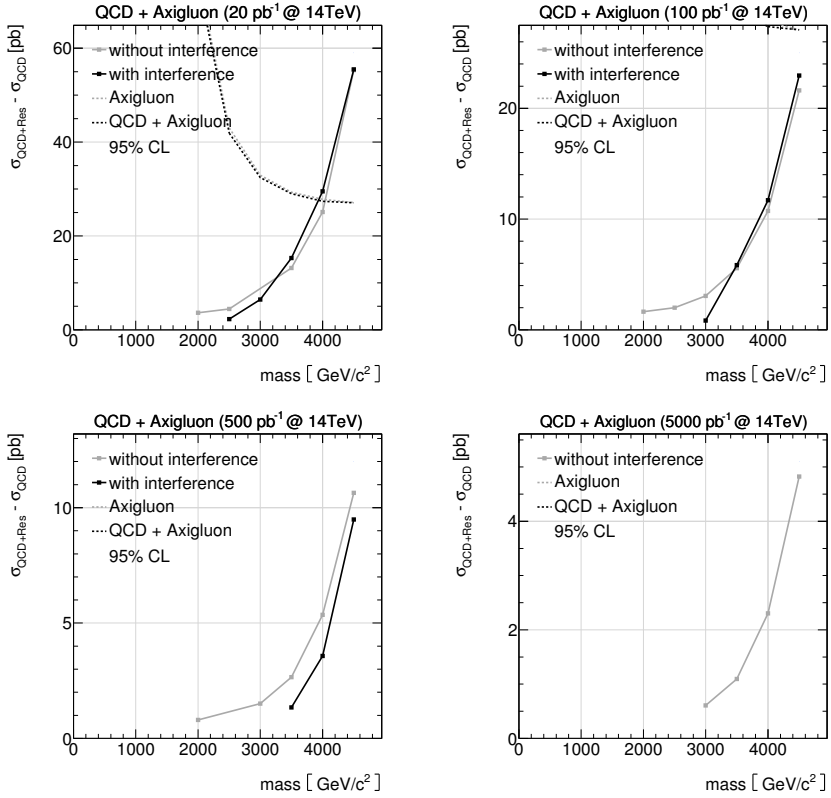

Figure C.5: *Sensitivities on axigluons with statistical uncertainties. Cross sections for all respective masses indicate an exclusion limit of 95 % CL.*

D

Sensitivities including Systematic Uncertainties

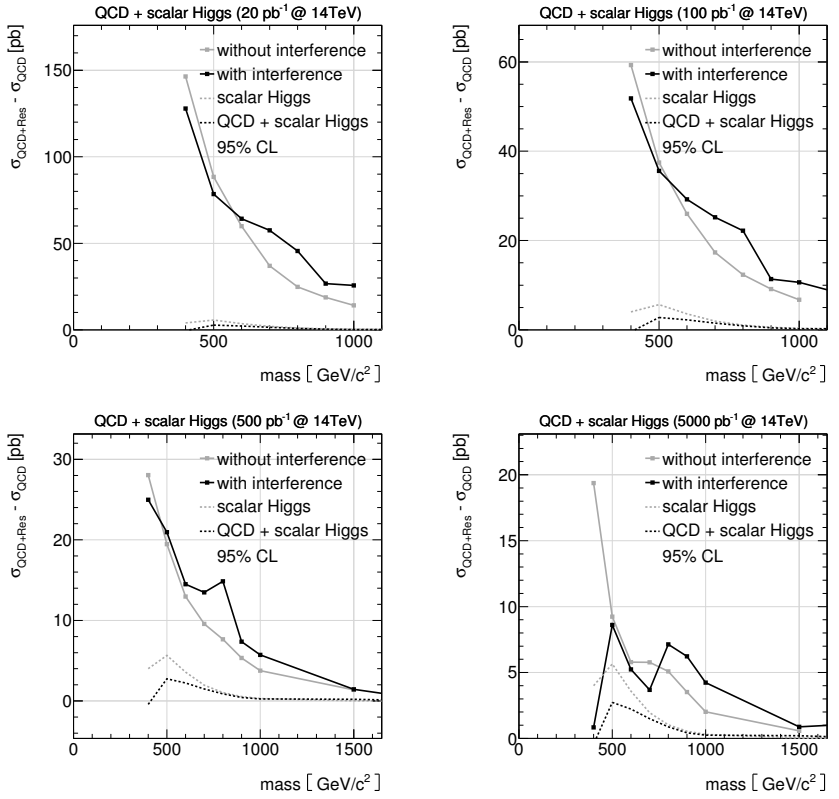

Figure D.1: *Sensitivities on scalar Higgs bosons with systematic uncertainties. Cross sections for all respective masses indicate an exclusion limit of 95 % CL.*

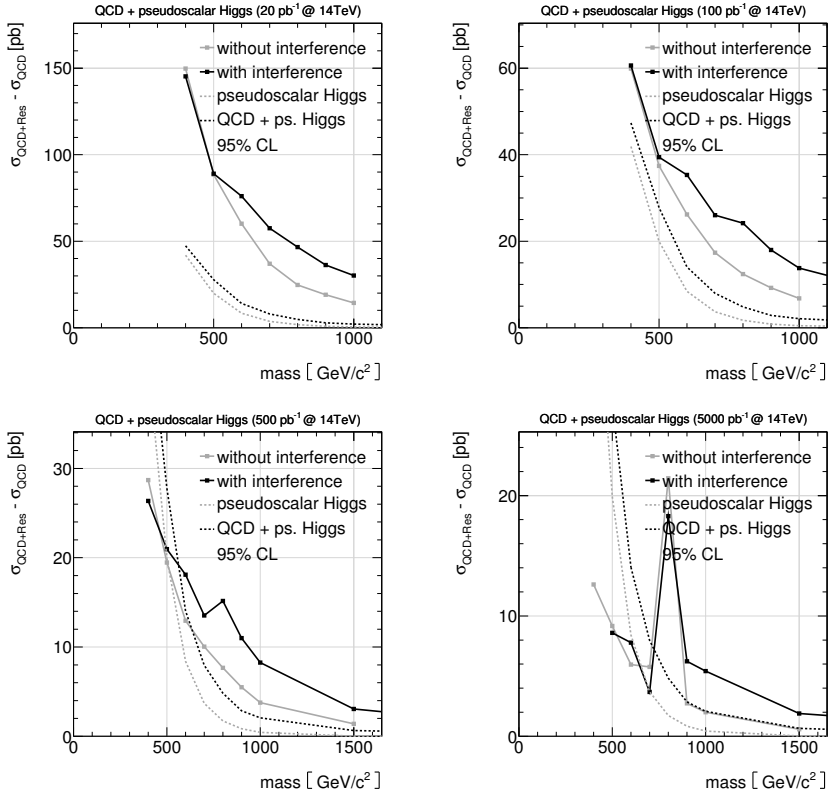

Figure D.2: *Sensitivities on pseudoscalar Higgs bosons with systematic uncertainties. Cross sections for all respective masses indicate an exclusion limit of 95 % CL.*

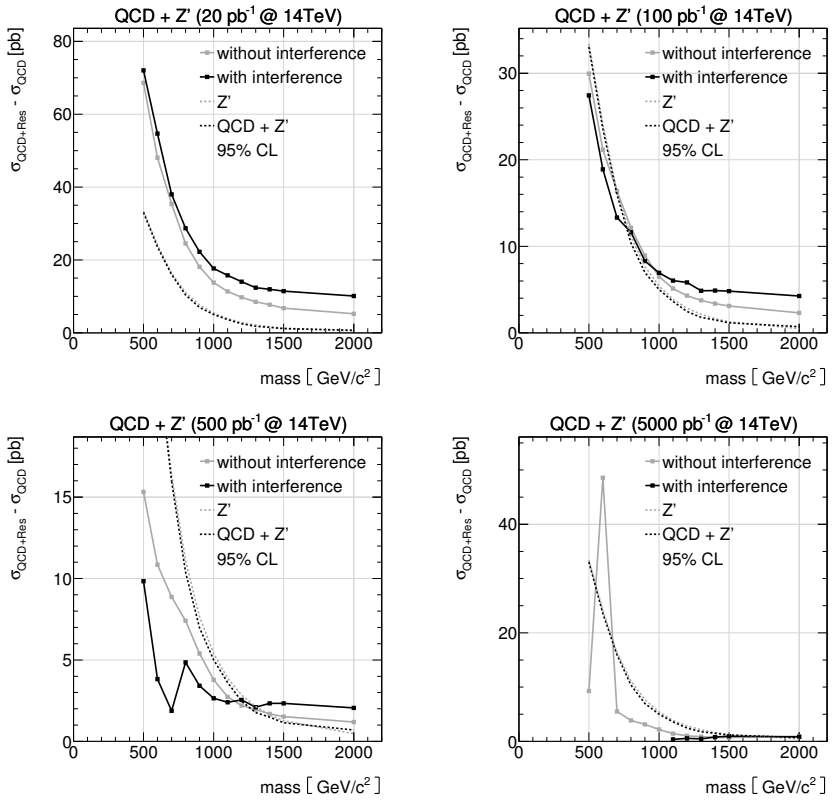

Figure D.3: *Sensitivities on Z' bosons including systematic uncertainties. Cross sections for all respective masses indicate an exclusion limit of 95 % CL.*

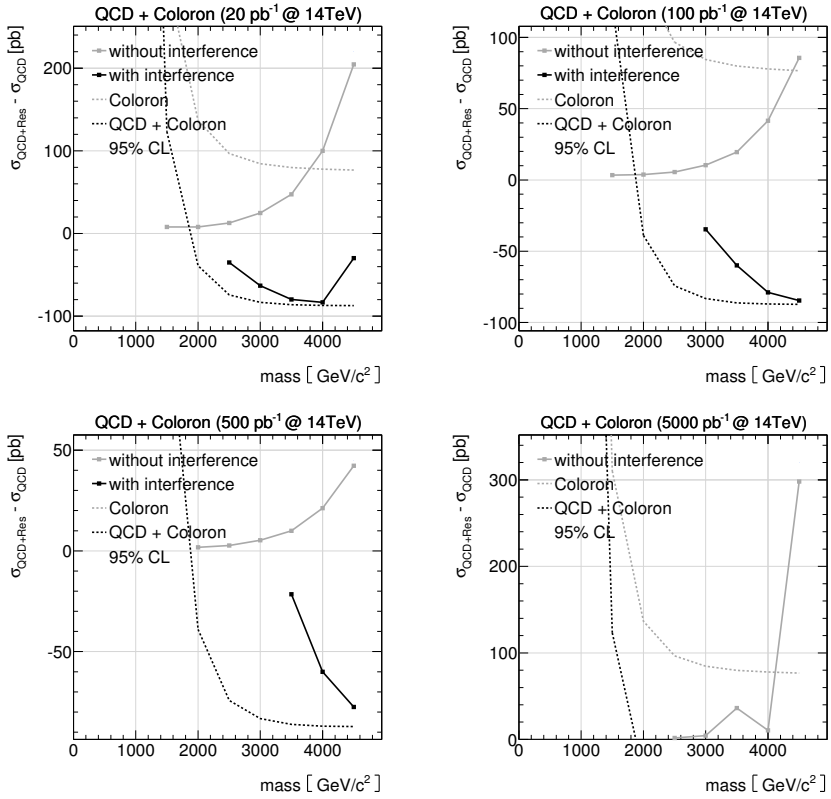

Figure D.4: *Sensitivities on colorons with systematic uncertainties. Cross sections for all respective masses indicate an exclusion limit of 95 % CL.*

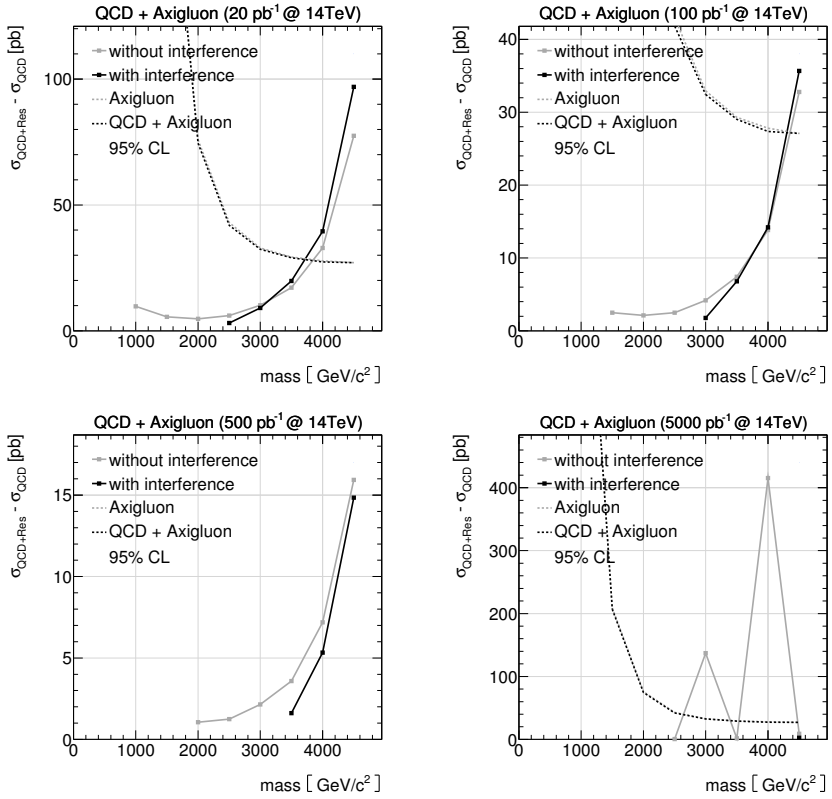

Figure D.5: *Sensitivities on axigluons with systematic uncertainties. Cross sections for all respective masses indicate an exclusion limit of 95 % CL.*

Acknowledgements

This work would not have been possible without the support of many people I would like to thank. First of all, I thank Peter Mättig for providing me the opportunity for this work and giving me the chance to work together with interesting people on various topics. I also like to thank the members of the group for high energy particle physics for their help, especially Wolfgang Wagner, Klaus Hamacher, Torsten Harenberg and Daniel Wicke, who were always supportive in answering my difficult questions.

Of cource, I thank my colleagues for having great times in Wuppertal, especially Stephan, Tatjana, Thorsten, Nicole, Jens, Kathrin, Tobias, Julia and Oskar. You always were a great company, at work as well as in spare times.

Finally, I want to express many thanks to my roommates Lena, Daniela, Nils and Tülay for their support in difficult times and huge amounts of great fun.

List of Figures

List of Tables

List of Abbreviations

Notation	Description	Page List
LEP	**L**arge **E**lectron **P**ositron Collider	20, 21, 23
ALICE	**A** **L**arge **I**on **C**ollider **E**xperiment	56–58
AOD	**A**anlysis **O**bject **D**ata	72
ATHENA	**AT**LAS realization of a **h**igh **E**nergy and **n**uclear Physics Data Analysis **A**rchitecture	72, 78, 79
ATLAS	**A** **T**oroidal **L**HC **A**pparatu**s**	3, 56–65, 69, 72, 87–91, 115, 168, 206, 209
CDF	**C**ollider **D**etector at **F**ermilab	18, 20, 24
CE	**C**omputing **E**lement	70, 71
CERN	**C**onceil **E**uropeenne pour la **R**echerche **N**ucleaire	55, 72, 73, 88, 90
CMS	**C**ompact **M**uon **S**olenoid	56–58
CSC	**C**athode-**S**trip **C**hamber	66
DESY	**D**eutsches **E**lektronen **Sy**nchrotron	73
GANGA	**G**audi **A**thena a**n**d **G**rid **A**lliance	72, 78–83, 91, 206
GEANT	**Ge**ometry **an**d **T**racking	69

Notation	Description	Page List
HELAS	**Hel**icity **A**mplitude **s**ubroutines	51
HEPCG	**H**igh **E**nergy **P**hysics **C**ommunity **G**rid	78
HERWIG++	**H**adron **E**mission **R**eactions **w**ith **i**nterfering **G**luons	2, 31, 42–46, 49, 51, 115–121, 132, 156, 167, 206
IP	**I**nteraction **P**oint	58, 59
IR	**I**nser**r**tion	57
JDL	**J**ob **D**escription **L**anguage	70, 79
JEM	**J**ob **E**xection **M**onitor	2, 72, 73, 75, 78–83, 90, 91
LCG	**L**HC **C**omputing **G**rid	69, 72, 209
LHAPDF	**L**es **H**ouches **A**ccord **P**arton **D**istribution **F**unctions	45
LHC	**L**arge **H**adron **C**ollider	2, 3, 32, 33, 55–59, 69, 70, 72, 78, 84, 116, 133, 137, 206
LHCb	**L**arge **H**adron **C**ollider **b**eauty	56–58, 72
LHCf	**L**arge **H**adron **C**ollider **f**orward	57, 58
MDT	**M**onitored **D**rift **T**ube	66
NLO	**N**ext to **L**eading **O**rder	11, 42–44, 155, 156
PDF	**P**arton **D**istribution **F**unctions	44, 45, 151, 153–155, 168

Notation	Description	Page List
QCD	**Q**uantum **C**hromo**d**ynamics	V, 3, 6, 10–12, 18, 19, 23, 24, 27–29, 32, 36–41, 44, 49, 50, 53, 54, 67, 93, 95, 96, 98, 100–103, 105, 108–113, 115–118, 122–124, 132, 133, 135–138, 140, 142–147, 149, 151, 156, 157, 159–161, 163, 165, 167–169, 206, 210
QED	**Q**uantum **E**lectro**d**ynamics	6, 12
R-GMA	**R**elational **G**rid **M**onitoring **A**rchitecture	90
RPC	**R**esistive **P**late **C**hamber	66
SE	**S**torage **E**lement	71
SM	**S**tandard **M**odel	5, 20, 54, 118–121, 132
SPS	**S**uper **P**roton **S**ynchrotron	56
TGC	**T**hin **G**ap **C**hamber	66
TOTEM	**Tot**al **e**lastic and diffractive Cross Section **M**easurement	57, 58
UI	**U**ser **I**nterface	70
WMS	**W**orkload **M**anagement **S**ystem	70, 71, 79
WN	**W**orker **N**ode	70, 71

Bibliography

[1] **T. Nakano**, **K. Nishijima**, *Charge Independence for V-particles*, Progress of Theoretical Physics **10** (1953), no. 5, 581–582.

[2] **K. Nishijima**, *Charge Independence Theory of V Particles*, Progress of Theoretical Physics **13** (1955), no. 3, 285–304.

[3] **M. Gell-Mann**, *The interpretation of the new particles as displaced charge multiplets*, Il Nuovo Cimento **4** (4, 1956) 848–866.

[4] **Particle Data Group** Collaboration**, K. Nakamura et al.**, *Review of particle physics*, J. Phys. **G37** (2010) 075021.

[5] **CDF and DØ** Collaboration**, T. E. W. Group**, *Combination of CDF and DØ Results on the Mass of the Top Quark*, [1007.3178].

[6] **B. T. Cleveland**, **T. Daily**, **R. Davis, Jr**, **J. R. Distel**, **K. Lande**, **C. K. Lee**, **P. S. Wildenhain**, **J. Ullman**, *Measurement of the Solar Electron Neutrino Flux with the Homestake Chlorine Detector*, The Astrophysical Journal **496** (1998), no. 1, 505.

[7] **Q. R. Ahmad**, **R. C. Allen**, **T. C. Andersen**, **J. D. Anglin**, **G. Bühler**, **J. C. Barton**, **E. W. Beier**, **M. Bercovitch**, **J. Bigu**, **S. Biller**, **R. A. Black**, **I. Blevis**, **R. J. Boardman**, **J. Boger**, **E. Bonvin**, **M. G. Boulay**, **M. G. Bowler**, **T. J. Bowles**, **S. J. Brice**, **M. C. Browne**, **T. V. Bullard**, **T. H. Burritt**, **K. Cameron**, **J. Cameron**, **Y. D. Chan**, **M. Chen**, **H. H. Chen**, *Measurement of the Rate of*

$\nu e + d \to p + p + e^-$ *Interactions Produced by* ^8B *Solar Neutrinos at the Sudbury Neutrino Observatory*, Phys. Rev. Lett. **87** (July, 2001) 071301.

[8] **P. W. Higgs**, *Broken symmetries, massless particles and gauge fields*, Phys. Lett. **12** (1964) 132–133.

[9] **M. Gell-Mann**, *A Schematic Model of Baryons and Mesons*, Phys. Lett. **8** (1964) 214–215.

[10] **G. Zweig**, *An* $SU(3)$ *model for strong interaction symmetry and its breaking. Part I*,.

[11] **G. Zweig**, *An* $SU(3)$ *model for strong interaction symmetry and its breaking. Part II*,.

[12] **H. Fritzsch**, **M. Gell-Mann**, **H. Leutwyler**, *Advantages of the Color Octet Gluon Picture*, Phys. Lett. **B47** (1973) 365–368.

[13] **M. Gell-Mann**, *Symmetries of baryons and mesons*, Phys. Rev. **125** (1962) 1067–1084.

[14] **T. van Ritbergen**, **J. A. M. Vermaseren**, **S. A. Larin**, *The four-loop beta function in quantum chromodynamics*, Phys. Lett. **B400** (1997) 379–384, [hep-ph/9701390].

[15] **S. Bethke**, *Experimental tests of asymptotic freedom*, Prog. Part. Nucl. Phys. **58** (2007) 351–386, [hep-ex/0606035].

[16] **S. Dürr et al.**, *Ab-Initio Determination of Light Hadron Masses*, Science **322** (2008) 1224–1227, [0906.3599].

[17] **S. L. Glashow**, *Partial Symmetries of Weak Interactions*, Nucl. Phys. **22** (1961) 579–588.

[18] **S. Weinberg**, *A Model of Leptons*, Phys. Rev. Lett. **19** (1967) 1264–1266.

[19] **A. Salam**, *Gauge Unification of Fundamental Forces*, Rev. Mod. Phys. **52** (July, 1980) 525–538.

[20] **N. Cabibbo**, *Unitary Symmetry and Leptonic Decays*, Phys. Rev. Lett. **10** (June, 1963) 531–533.

[21] **M. Kobayashi**, **T. Maskawa**, *CP Violation in the Renormalizable Theory of Weak Interaction*, Prog. Theor. Phys. **49** (1973), no. 2, 652–657.

[22] **B. Pontecorvo**, *Electron and muon neutrinos*, Sov. Phys. JETP **10** (1960) 1236–1240.

[23] **Z. Maki**, **M. Nakagawa**, **S. Sakata**, *Remarks on the unified model of elementary particles*, Prog. Theor. Phys. **28** (1962) 870–880.

[24] **CDF** Collaboration**, F. Abe et al.**, *Evidence for top quark production in $\overline{p}p$ collisions at $\sqrt{s} = 1.8\,TeV$*, Phys. Rev. **D50** (1994) 2966–3026.

[25] **D0** Collaboration**, S. Abachi et al.**, *Observation of the top quark*, Phys. Rev. Lett. **74** (1995) 2632–2637, [hep-ex/9503003].

[26] **H. Georgi**, **A. Pais**, *Vacuum Symmetry and the PseudoGoldstone Phenomenon*, Phys. Rev. **D12** (1975) 508.

[27] **N. Arkani-Hamed**, **A. G. Cohen**, **E. Katz**, **A. E. Nelson**, *The littlest Higgs*, JHEP **07** (2002) 034, [hep-ph/0206021].

[28] **C. T. Hill**, *Topcolor: Top quark condensation in a gauge extension of the standard model*, Phys. Lett. **B266** (1991) 419–424.

[29] **C. T. Hill**, *Topcolor assisted technicolor*, Phys. Lett. **B345** (1995) 483–489, [hep-ph/9411426].

[30] **R. M. Harris**, **C. T. Hill**, **S. J. Parke**, *Cross section for topcolor Z'_t decaying to $t\bar{t}$*, [hep-ph/9911288].

[31] **B. A. Dobrescu**, **C. T. Hill**, *Electroweak symmetry breaking via top condensation seesaw*, Phys. Rev. Lett. **81** (1998) 2634–2637, [hep-ph/9712319].

[32] **R. S. Chivukula**, **B. A. Dobrescu**, **H. Georgi**, **C. T. Hill**, *Top quark seesaw theory of electroweak symmetry breaking*, Phys. Rev. **D59** (1999) 075003, [hep-ph/9809470].

[33] **H.-J. He**, **C. T. Hill**, **T. M. P. Tait**, *Top quark seesaw, vacuum structure and electroweak precision constraints*, Phys. Rev. **D65** (2002) 055006, [hep-ph/0108041].

[34] **C. D. McMullen**, **S. Nandi**, *Collider implications of Kaluza-Klein excitations of the electroweak gauge bosons*, [hep-ph/0110275].

[35] **K. Agashe**, **A. Delgado**, **M. J. May**, **R. Sundrum**, *RS1, custodial isospin and precision tests*, JHEP **08** (2003) 050, [hep-ph/0308036].

[36] **K. Agashe**, **A. Belyaev**, **T. Krupovnickas**, **G. Perez**, **J. Virzi**, *LHC signals from warped extra dimensions*, Phys. Rev. **D77** (2008) 015003, [hep-ph/0612015].

[37] **B. Lillie**, **L. Randall**, **L.-T. Wang**, *The Bulk RS KK-gluon at the LHC*, JHEP **09** (2007) 074, [hep-ph/0701166].

[38] **A. Djouadi**, **G. Moreau**, **R. K. Singh**, *Kaluza–Klein excitations of gauge bosons at the LHC*, Nucl. Phys. **B797** (2008) 1–26, [0706.4191].

[39] **R. Ghavri**, **C. D. McMullen**, **S. Nandi**, *Collider implications of multiple non-universal extra dimensions*, Phys. Rev. **D74** (2006) 015012, [hep-ph/0602014].

[40] **G. Burdman**, **B. A. Dobrescu**, **E. Ponton**, *Resonances from two universal extra dimensions*, Phys. Rev. **D74** (2006) 075008, [hep-ph/0601186].

[41] **B. Lillie**, **J. Shu**, **T. M. P. Tait**, *Kaluza-Klein Gluons as a Diagnostic of Warped Models*, Phys. Rev. **D76** (2007) 115016, [0706.3960].

[42] **K. Agashe et al.**, *LHC Signals for Warped Electroweak Neutral Gauge Bosons*, Phys. Rev. **D76** (2007) 115015, [0709.0007].

[43] **R. Frederix**, **F. Maltoni**, *Top pair invariant mass distribution: a window on new physics*, JHEP **01** (2009) 047, [0712.2355].

[44] **LEP Working Group for Higgs boson searches** Collaboration, **R. Barate et al.**, *Search for the standard model Higgs boson at LEP*, Phys. Lett. **B565** (2003) 61–75, [hep-ex/0306033].

[45] **CDF** Collaboration, *Combined CDF and DØ Upper Limits on Standard Model Higgs-Boson Production with 2.1-5.4 fb^{-1} of Data*, [0911.3930].

[46] **CDF and DØ** Collaboration, *Combined CDF and DØ Upper Limits on Standard Model Higgs- Boson Production with up to 6.7 fb^{-1} of Data*, [1007.4587].

[47] **T. D. Lee**, *A Theory of Spontaneous T Violation*, Phys. Rev. **D8** (1973) 1226–1239.

[48] **Y. Grossman**, *Phenomenology of models with more than two Higgs doublets*, Nucl. Phys. **B426** (1994) 355–384, [hep-ph/9401311].

[49] **J. F. Gunion**, **H. E. Haber**, **G. L. Kane**, **S. Dawson**, *The Higgs Hunter's Guide*,. SCIPP-89/13.

[50] **G. C. Branco**, **A. J. Buras**, **J. M. Gerard**, *CP Violation in Models with two and three scalar Doublets*, Nucl. Phys. **B259** (1985) 306.

[51] **J. Wess**, **B. Zumino**, *Supergauge Transformations in Four-Dimensions*, Nucl. Phys. **B70** (1974) 39–50.

[52] **ALEPH, DELPHI, L3, OPAL** Collaboration, **S. Schael et al.**, *Search for neutral MSSM Higgs bosons at LEP*, Eur. Phys. J. **C47** (2006) 547–587, [hep-ex/0602042].

[53] **Tevatron New Phenomena & Higgs Working Group** Collaboration, **D. Benjamin et al.**, *Combined CDF and DØ upper limits on MSSM Higgs boson production in tau-tau final states with up to 2.2 fb-1*, [1003.3363].

[54] **J. Schechter**, **J. W. F. Valle**, *Neutrino Masses in SU(2) x U(1) Theories*, Phys. Rev. **D22** (1980) 2227.

[55] **T. P. Cheng**, **L.-F. Li**, *Neutrino Masses, Mixings and Oscillations in SU(2) x U(1) Models of Electroweak Interactions*, Phys. Rev. **D22** (1980) 2860.

[56] **S. Weinberg**, *Implications of Dynamical Symmetry Breaking: An Addendum*, Phys. Rev. **D19** (1979) 1277–1280.

[57] **L. Susskind**, *Dynamics of Spontaneous Symmetry Breaking in the Weinberg-Salam Theory*, Phys. Rev. **D20** (1979) 2619–2625.

[58] **S. Dimopoulos**, **L. Susskind**, *Mass Without Scalars*, Nucl. Phys. **B155** (1979) 237–252.

[59] **E. Eichten**, **K. D. Lane**, *Dynamical Breaking of Weak Interaction Symmetries*, Phys. Lett. **B90** (1980) 125–130.

[60] **DØ** Collaboration, *Search for $t\bar{t}$ Resonances in the Lepton+Jets Final State in $p\overline{p}$ Collisions at $\sqrt{s} = 1.96\,TeV$*,. DØ note 5882-CONF.

[61] **CDF** Collaboration, *Search for resonant $t\bar{t}$ production in $p\overline{p}$ Collisions at $\sqrt{s} = 1.96\,TeV$*,. CDF note 9844.

[62] **C. T. Hill**, **S. J. Parke**, *Top production: Sensitivity to new physics*, Phys. Rev. **D49** (1994) 4454–4462, [hep-ph/9312324].

[63] **P. H. Frampton**, **S. L. Glashow**, *Chiral Color: An Alternative to the Standard Model*, Phys. Lett. **B190** (1987) 157.

[64] **J. Bagger**, **C. Schmidt**, **S. King**, *Axigluon production in hadronic collisions*, Phys. Rev. D **37** (Mar., 1988) 1188–1196.

[65] **D. Choudhury**, **R. M. Godbole**, **R. K. Singh**, **K. Wagh**, *Top production at the Tevatron/LHC and nonstandard, strongly interacting spin one particles*, Phys. Lett. **B657** (2007) 69–76, [0705.1499].

[66] **T. Kaluza**, *Zum Unitätsproblem der Physik*, Sitzungsber. Preuss. Akad. Wiss. Berlin (Math. Phys.) **1921** (1921) 966–972.

[67] **O. Klein**, *Quantentheorie und fünfdimensionale Relativitätstheorie*, Z. Phys. **37** (1926) 895–906.

[68] **M. Guchait**, **F. Mahmoudi**, **K. Sridhar**, *Tevatron constraint on the Kaluza-Klein gluon of the bulk Randall-Sundrum model*, JHEP **05** (2007) 103, [hep-ph/0703060].

[69] **A. D. Martin**, **W. J. Stirling**, **R. S. Thorne**, **G. Watt**, *Uncertainties on α_s in global PDF analyses*, Eur. Phys. J. **C64** (2009) 653–680, [0905.3531].

[70] **S. Catani**, **M. Ciafaloni**, **F. Hautmann**, *High-energy factorization and small x heavy flavor production*, Nucl. Phys. **B366** (1991) 135–188.

[71] **J. C. Collins**, **R. K. Ellis**, *Heavy quark production in very high-energy hadron collisions*, Nucl. Phys. **B360** (1991) 3–30.

[72] **E. M. Levin**, **M. G. Ryskin**, **Y. M. Shabelski**, **A. G. Shuvaev**, *Heavy quark production in semihard nucleon interactions*, Sov. J. Nucl. Phys. **53** (1991) 657.

[73] **J. C. Collins**, **J.-W. Qiu**, *k_T factorization is violated in production of high-transverse-momentum particles in hadron-hadron collisions*, Phys. Rev. **D75** (2007) 114014, [0705.2141].

[74] **M. A. Dobbs**, **J. B. Hansen**, *The HepMC C++ Monte Carlo event record for High Energy Physics*, Comput. Phys. Commun. **134** (2001) 41–46.

[75] **A. D. Martin**, **W. J. Stirling**, **R. S. Thorne**, **G. Watt**, *Parton distributions for the LHC*, Eur. Phys. J. **C63** (2009) 189–285, [0901.0002].

[76] **Y. L. Dokshitzer**, *Calculation of the Structure Functions for Deep Inelastic Scattering and e+ e- Annihilation by Perturbation Theory in Quantum Chromodynamics*, Sov. Phys. JETP **46** (1977) 641–653.

[77] **V. N. Gribov**, **L. N. Lipatov**, *Deep inelastic e p scattering in perturbation theory*, Sov. J. Nucl. Phys. **15** (1972) 438–450.

[78] **G. Altarelli**, **G. Parisi**, *Asymptotic Freedom in Parton Language*, Nucl. Phys. **B126** (1977) 298.

[79] **V. V. Sudakov**, *Vertex parts at very high-energies in quantum electrodynamics*, Sov. Phys. JETP **3** (1956) 65–71.

[80] **D. Amati**, **G. Veneziano**, *Preconfinement as a Property of Perturbative QCD*, Phys. Lett. **B83** (1979) 87.

[81] **Y. I. Azimov**, **Y. L. Dokshitzer**, **V. A. Khoze**, **S. I. Troian**, *The String Effect and QCD Coherence*, Phys. Lett. **B165** (1985) 147–150.

[82] **Y. I. Azimov**, **Y. L. Dokshitzer**, **V. A. Khoze**, **S. I. Troian**, *Similarity of Parton and Hadron Spectra in QCD Jets*, Z. Phys. **C27** (1985) 65–72.

[83] **Y. Aoki**, **Z. Fodor**, **S. D. Katz**, **K. K. Szabo**, *The QCD transition temperature: Results with physical masses in the continuum limit*, Phys. Lett. **B643** (2006) 46–54, [hep-lat/0609068].

[84] **Y. Aoki et al.**, *The QCD transition temperature: results with physical masses in the continuum limit II*, JHEP **06** (2009) 88, [0903.4155].

[85] **Wuppertal-Budapest** Collaboration**, S. Borsanyi et al.**, *Is there still any T_c mystery in lattice QCD? Results with physical masses in the continuum limit III*, [1005.3508].

[86] **N. Attig et al.**, *Demonstration of string breaking in quantum chromodynamics by large-scale eigenvalue computations*, Comput. Phys. Commun. **169** (2005) 382–385.

[87] **G. S. Bali et al.**, *String breaking*, Nucl. Phys. Proc. Suppl. **153** (2006) 9–16, [hep-lat/0512018].

[88] **P. M. Nadolsky et al.**, *Implications of CTEQ global analysis for collider observables*, Phys. Rev. **D78** (2008) 013004, [0802.0007].

[89] **M. R. Whalley**, **D. Bourilkov**, **R. C. Group**, *The Les Houches Accord PDFs (LHAPDF) and Lhaglue*, [hep-ph/0508110].

[90] **Y. I. Azimov**, **Y. L. Dokshitzer**, **S. I. Troian**, **V. A. Khoze**, *Coherent Effects in QCD Jets: New Theory and Experiments*,. Presented at 20th Leningrad Winter School, 1985.

[91] **L. Lönnblad**, *Matching and merging Matrix Elements with Parton Showers*, 2008. Lecture at the MCnet/CTEQ summer school 2008, Debrecen.

[92] **S. Gieseke**, **P. Stephens**, **B. R. Webber**, *New formalism for QCD parton showers*, JHEP **12** (2003) 045, [hep-ph/0310083].

[93] **M. Bahr et al.**, *Herwig++ Physics and Manual*, Eur. Phys. J. **C58** (2008) 639–707, [0803.0883].

[94] **S. Catani**, **S. Dittmaier**, **Z. Trocsanyi**, *One-loop singular behaviour of QCD and SUSY QCD amplitudes with massive partons*, Phys. Lett. **B500** (2001) 149–160, [hep-ph/0011222].

[95] **Y. L. Dokshitzer**, **V. A. Khoze**, **S. I. Troian**, *On specific QCD properties of heavy quark fragmentation ('dead cone')*, J. Phys. **G17** (1991) 1602–1604.

[96] **R. D. Field**, **S. Wolfram**, *A QCD Model for e+ e- Annihilation*, Nucl. Phys. **B213** (1983) 65.

[97] **B. Andersson**, *The Lund String Model*,. In *Durham 1984, Proceedings, Antiproton 1984*, 447-462.

[98] **B. R. Webber**, *Fragmentation and hadronization*, [hep-ph/9912292].

[99] **W. Bernreuther**, *Top quark physics at the LHC*, J. Phys. **G35** (2008) 083001, [0805.1333].

[100] **W. H. Furry**, *A Symmetry Theorem in the Positron Theory*, Phys. Rev. **51** (Jan., 1937) 125–129.

[101] **K. Nishijima**, *Generalized Furry's Theorem for Closed Loops*, Progress of Theoretical Physics **6** (1951), no. 4, 614–615.

[102] **H. Murayama**, **I. Watanabe**, **K. Hagiwara**, *HELAS: HELicity Amplitude Subroutines for Feynman diagram evaluations*,. KEK-91-11.

[103] **T. S. Pettersson**, **P. Lefèvre**, *The Large Hadron Collider: conceptual design*, Tech. Rep. CERN-AC-95-05 LHC, CERN, Geneva, Oct., 1995.

[104] **J.-L. Caron**, *Layout of the LEP tunnel including future LHC infrastructures / L'ensemble du tunnel LEP avec les futures infractrustures LHC*,. AC Collection. Legacy of AC. Pictures from 1992 to 2002.

[105] **S. Dailler**, *Cross section of LHC dipole / Dipole LHC: coupe transversale*,. AC Collection. Legacy of AC. Pictures from 1992 to 2002.

[106] **ATLAS** Collaboration**, G. Aad et al.**, *The ATLAS Experiment at the CERN Large Hadron Collider*, JINST **3** (2008) S08003.

[107] **J. Pequenao**, *Event Cross Section in a computer generated image of the ATLAS detector*,.

[108] **ATLAS Electromagnetic Barrel Calorimeter** Collaboration**, M. Aharrouche et al.**, *Energy linearity and resolution of the ATLAS electromagnetic barrel calorimeter in an electron test-beam*, Nucl. Instrum. Meth. **A568** (2006) 601–623, [physics/0608012].

[109] **M. Schram**, *Electron and pion results from the ATLAS forward calorimeter 2003 test beam*,. Prepared for 9th ICATPP Conference on Astroparticle, Particle, Space Physics, Detectors and Medical Physics Applications, Villa Erba, Como, Italy, 17-21 Oct 2005.

[110] **Y. A. Kulchitsky**, **M. V. Kuzmin**, **J. A. Budagov**, **V. B. Vinogradov**, **M. Nessi**, *Hadron energy reconstruction for the ATLAS barrel prototype combined calorimeter in the framework of the non-parametrical method*, [hep-ex/0004009].

[111] **M. Cacciari**, **G. P. Salam**, **G. Soyez**, *The anti-k_T jet clustering algorithm*, JHEP **04** (2008) 063, [0802.1189].

[112] **G. C. Blazey et al.**, *Run II jet physics*, [hep-ex/0005012].

[113] **S. Ovyn**, **X. Rouby**, **V. Lemaitre**, *Delphes, a framework for fast simulation of a generic collider experiment*, [0903.2225].

[114] **GEANT4** Collaboration**, S. Agostinelli et al.**, *GEANT4: A simulation toolkit*, Nucl. Instrum. Meth. **A506** (2003) 250–303.

[115] **CDF** Collaboration**, F. Abe et al.**, *The Topology of three jet events in $\overline{p}p$ collisions at $\sqrt{s} = 1.8\,TeV$*, Phys. Rev. **D45** (1992) 1448–1458.

[116] **G. P. Salam**, **G. Soyez**, *A practical Seedless Infrared-Safe Cone jet algorithm*, JHEP **05** (2007) 086, [0704.0292].

[117] **S. Catani**, **Y. L. Dokshitzer**, **M. H. Seymour**, **B. R. Webber**, *Longitudinally invariant K_t clustering algorithms for hadron hadron collisions*, Nucl. Phys. **B406** (1993) 187–224.

[118] **S. D. Ellis**, **D. E. Soper**, *Successive combination jet algorithm for hadron collisions*, Phys. Rev. D **48** (Oct., 1993) 3160–3166.

[119] **Y. L. Dokshitzer**, **A. Lucenti**, **G. Marchesini**, **G. P. Salam**, *On the QCD analysis of jet broadening*, JHEP **01** (1998) 011, [hep-ph/9801324].

[120] **M. Wobisch**, **T. Wengler**, *Hadronization corrections to jet cross sections in deep-inelastic scattering*, [hep-ph/9907280].

[121] **C. Eck**, **J. Knobloch**, **L. Robertson**, **I. Bird**, **K. Bos**, **N. Brook**, **D. Düllmann**, **I. Fisk**, **D. Foster**, **B. Gibbard**, **C. Grandi**, **F. Grey**, **J. Harvey**, **A. Heiss**, **F. Hemmer**, **S. Jarp**, **R. W. L. Jones**, **D. Kelsey**, **M. Lamanna**, **H. Marten**, **P. Mato-Vila**, **F. Ould-Saada**, **B. Panzer-Steindel**, **L. Perini**, **Y. Schutz**, **U. Schwickerath**, **J. Shiers**, **T. Wenaus**, *LHC computing Grid: Technical Design Report. Version 1.06 (20 Jun 2005)*. Technical Design Report LCG. CERN, Geneva, 2005.

[122] **M. Cecchi et al.**, *The gLite workload management system*, J. Phys. Conf. Ser. **219** (2010) 062039.

[123] **D. Cooper**, **S. Santesson**, **S. Farrell**, **S. Boeyen**, **R. Housley**, **W. Polk**, *Internet X.509 Public Key Infrastructure Certificate and Certificate Revocation List (CRL) Profile*,.

[124] **J. T. Mościcki**, **F. Brochu**, **J. Ebke**, **U. Egede**, **J. Elmsheuser**, **K. Harrison**, **R. W. L. Jones**, **H. C. Lee**, **D. Liko**, **A. Maier**, **A. Muraru**, **G. N. Patrick**, **K. Pajchel**, **W. Reece**, **B. H. Samset**, **M. W. Slater**, **A. Soroko**, **C. L. Tan**, **D. C. van der Ster**, **M. Williams**, *GANGA: A tool for computational-task management and easy access to Grid resources*, Computer Physics Communications **180** (Nov., 2009) 2303–2316, [0902.2685].

[125] **ATLAS** Collaboration, *ATLAS computing: Technical Design Report*, vol. 17 of *Technical Design Report ATLAS*. CERN, Geneva, 2005. CERN-LHCC-2005-022 (2005).

[126] **G. Barrand et al.**, *GAUDI - A software architecture and framework for building HEP data processing applications*, Comput. Phys. Commun. **140** (2001) 45–55.

[127] **S. Borovac et al.**, *Overview over the high energy physics community Grid in Germany's D-Grid inititative*, PoS **ACAT** (2007) 025.

[128] **R. Müller-Pfefferkorn**, **R. Neumann**, **S. Borovac**, **A. Hammad**, **T. Harenberg**, **M. Hüsken**, **P. Mättig**, **M. Mechtel**, **D. Meder-Marouelli**, **P. Ueberholz**, *Moni-*

toring of Jobs and their Execution for the LHC Computing Grid, Proceedings of Cracow Grid Workshop (CGW) 2006 (2006) 224–231. ISBN: 83-915141-7-X.

[129] **R. Müller-Pfefferkorn**, **R. Neumann**, **S. Borovac**, **T. Harenberg**, **M. Hüsken**, **P. Mättig**, **M. Mechtel**, **D. Meder-Marouelli**, **P. Ueberholz**, **P. Buchholz**, **D. Lorenz**, **C. Uebing**, **W. Walkowiak**, **R. Wismüller**, *User-Centric Monitoring and Steering of the Execution of Large Job Sets*, in *Proceedings of the German e-Science Conference 2007*. Baden-Baden, Germany, May, 2007.

[130] **D. Lorenz**, **S. Borovac**, **P. Buchholz**, **H. Eichenhardt**, **T. Harenberg**, **P. Mättig**, **M. Mechtel**, **R. Müller-Pfefferkorn**, **R. Neumann**, **K. Reeves**, **C. Uebing**, **W. Walkowiak**, **T. William**, **R. Wismüller**, *Job monitoring and steering in D-Grid's High Energy Physics Community Grid*, Future Gener. Comput. Syst. **25** (March, 2009) 308–314.

[131] **E. Ehses et al.**, *Job centric monitoring for ATLAS jobs in the LHC Computing Grid*, PoS **ACAT08** (2008) 042.

[132] **M. Rau**, *Erweiterung der Benutzerschnittstelle für LHC Grid Jobs um die Monitoring-Funktionalität*,. diploma thesis.

[133] **T. dos Santos**, *Schematic Component View of the Job Execution Monitor*,.

[134] **D. Igdalov**, *Entwicklung eines Systems zur Analyse und Überwachung der Verarbeitung von Rechenanforderungen im LHC Computing-Grid*,. diploma thesis.

[135] **A. Hammad**, *Entwicklung eines Überwachungssystems für verteilte Prozesse im LHC Computing Grid*,. diploma thesis.

[136] **A. Baldeau**, *Skriptüberwachung im Job Execution Monitor für das LHC Computing Grid*,. bachelor thesis.

[137] **C. L. Forgy**, *Rete: a fast algorithm for the many pattern/many object pattern match problem*, Expert systems: a software methodology for modern applications (1990) 324–341.

[138] **T. Henß**, *Entwurf und Implementation eines Expertensystems für das Detektorkontrollsystem des ATLAS-Pixeldetektors*,. PhD thesis.

[139] **RedHat Corporation**, *JBoss Rules (Drools) Homepage*,. http://www.jboss.org/drools/.

[140] **D. Huning**, *Entwicklung einer Rich Client basierten GUI für Experten Systeme*,. bachelor thesis.

[141] **F. Iker**, *Entwicklung einer Abstraktionsschicht für regelbasierte Expertensysteme am CERN Grid-Cluster*,. bachelor thesis.

[142] **A. W. Cooke et al.**, *Relational Grid monitoring architecture (R-GMA)*, [cs/0308024].

[143] **D. D. Chamberlin**, **R. F. Boyce**, *SEQUEL: A structured English query language*, in *Proceedings of the 1974 ACM SIGFIDET (now SIGMOD) workshop on Data description, access and control*, SIGFIDET '74, pp. 249–264. ACM, New York, NY, USA, 1974.

[144] **D. D. Chamberlin**, **M. M. Astrahan**, **K. P. Eswaran**, **P. P. Griffiths**, **R. A. Lorie**, **J. W. Mehl**, **P. Reisner**, **B. W. Wade**, *SEQUEL 2: a unified approach to data definition, manipulation, and control*, IBM J. Res. Dev. **20** (November, 1976) 560–575.

[145] **J. Andreeva**, **M. Boehm**, **B. Gaidioz**, **E. Karavakis**, **L. Kokoszkiewicz**, **E. Lanciotti**, **G. Maier**, **W. Ollivier**, **R. Rocha**, **P. Saiz**, **I. Sidorova**, *Experiment Dashboard for Monitoring Computing Activities of the LHC Virtual Organizations*, Journal of Grid Computing **8** (2010) 323–339. 10.1007/s10723-010-9148-x.

[146] **R. A. Fisher**, *Statistical methods for research workers*. Oliver & Boyd, Edinburgh, 11th ed.(rev.) ed., 1950.

[147] **J. Neyman**, **E. S. Pearson**, *On the Problem of the Most Efficient Tests of Statistical Hypotheses*, Royal Society of London Philosophical Transactions Series A **231** (1933) 289–337.

[148] **A.-M. Siebel**, *Study of the Potential of the ATLAS dDetector to observe a Higgs Decay into $t\bar{t}$ in the fully hadronic Decay Mode*,. PhD thesis.

[149] **T. Schliephake**, *Resonance Searches with the $t\bar{t}$ Invariant Mass Distribution measured with the DØ Experiment at $\sqrt{s} = 1.96$ TeV*,. PhD thesis.

[150] **T. Lenz**, *Prospects for $t\bar{t}$ resonance searches at ATLAS*,. PhD thesis.

[151] **M. Jezabek**, **J. H. Kuhn**, *V-A tests through leptons from polarized top quarks*, Phys. Lett. **B329** (1994) 317–324, [hep-ph/9403366].

[152] **A. Czarnecki**, **M. Jezabek**, **J. H. Kuhn**, *LEPTON SPECTRA FROM DECAYS OF POLARIZED TOP QUARKS*, Nucl. Phys. **B351** (1991) 70–80.

[153] **M. Beneke et al.**, *Top quark physics*, [hep-ph/0003033].

[154] **R. Frederix**, **F. Maltoni**. private communication, Okt, 2010.

[155] **M. Cacciari**, **S. Frixione**, **M. L. Mangano**, **P. Nason**, **G. Ridolfi**, *Updated predictions for the total production cross sections of top and of heavier quark pairs at the Tevatron and at the LHC*, JHEP **09** (2008) 127, [0804.2800].

[156] **N. Kidonakis**, **R. Vogt**, *The Theoretical top quark cross section at the Tevatron and the LHC*, Phys. Rev. **D78** (2008) 074005, [0805.3844].

[157] **U. Langenfeld**, **S. Moch**, **P. Uwer**, *Measuring the running top-quark mass*, Phys. Rev. **D80** (2009) 054009, [0906.5273].

[158] **CDF** Collaboration**, G. Compostella**, *Top cross section measurement at CDF*, PoS **DIS2010** (2010) 151.

[159] **DØ** Collaboration**, V. M. Abazov et al.**, *Combination of $t\bar{t}$ cross section measurements and constraints on the mass of the top quark and its decays into charged Higgs bosons*, Phys. Rev. **D80** (2009) 071102, [0903.5525].

[160] **CMS** Collaboration**, V. Khachatryan et al.**, *First Measurement of the Cross Section for Top-Quark Pair Production in Proton-Proton Collisions at sqrt(s)=7 TeV*, Phys. Lett. **B695** (2011) 424–443, [1010.5994].

[161] **ATLAS** Collaboration**, G. Aad et al.**, *Measurement of the top quark-pair production cross section with ATLAS in pp collisions at $\sqrt{s} = 7$ TeV*, [1012.1792].

[162] **A. Djouadi**, *The Anatomy of electro-weak symmetry breaking. I: The Higgs boson in the standard model*, Phys. Rept. **457** (2008) 1–216, [hep-ph/0503172].

[163] **A. Djouadi**, *The Anatomy of electro-weak symmetry breaking. II. The Higgs bosons in the minimal supersymmetric model*, Phys. Rept. **459** (2008) 1–241, [hep-ph/0503173].

[164] **A. A. Andrianov**, **P. Osland**, **A. A. Pankov**, **N. V. Romanenko**, **J. Sirkka**, *On the phenomenology of a Z' coupling only to third family fermions*, Phys. Rev. **D58** (1998) 075001, [hep-ph/9804389].

[165] **P. M. Nadolsky**, **H.-L. Lai**, **Q.-H. Cao**, **J. Huston**, **J. Pumplin**, **D. Stump**, **W.-K. Tung**, **C.-P. Yuan**, *Implications of CTEQ global analysis for collider observables*, Phys. Rev. D **78** (July, 2008) 013004.

[166] **S. Frixione**, **B. R. Webber**, *Matching NLO QCD computations and parton shower simulations*, JHEP **06** (2002) 029, [hep-ph/0204244].

[167] **S. Frixione**, **P. Nason**, **B. R. Webber**, *Matching NLO QCD and parton showers in heavy flavour production*, JHEP **08** (2003) 007, [hep-ph/0305252].

[168] **R. J. Scherrer**, *Time variation of a fundamental dimensionless constant*, [0903.5321].

[169] **DELPHI** Collaboration**, P. Abreu et al.**, *Production characteristics of K^0 and light meson resonances in hadronic decays of the Z^0*, Z. Phys. **C65** (1995) 587–602.

[170] **R. Ticciati**, *Quantum field theory for mathematicians*,. Cambridge, UK: Univ. Pr. (1999) 699 p.

[171] **M. E. Peskin**, **D. V. Schroeder**, *An Introduction to quantum field theory*,. Reading, USA: Addison-Wesley (1995) 842 p.